NOVEL APPROACHES IN NOBLE-GAS CHEMISTRY: MECHANOCHEMICAL SYNTHESIS AND HIGH-PRESSURE CHEMISTRY

Erik Uran

Doctoral Dissertation
Jožef Stefan International Postgraduate School
Ljubljana, Slovenia

Supervisor: Asst. Prof. Matic Lozinšek, Jožef Stefan Institute, Ljubljana, Slovenia

Evaluation Board:
Prof. Tadej Rojac, Chair, Jožef Stefan Institute, Ljubljana, Slovenia
Asst. Prof. Marta Počkaj, Member, Faculty of Chemistry and Chemical Technology, University of Ljubljana, Slovenia
Dr. Nikola Biliškov, Member, Ruđer Bošković Institute, Zagreb, Croatia

MEDNARODNA PODIPLOMSKA ŠOLA JOŽEFA STEFANA
JOŽEF STEFAN INTERNATIONAL POSTGRADUATE SCHOOL



Erik Uran

NOVEL APPROACHES IN NOBLE-GAS CHEMISTRY: MECHANOCHEMICAL SYNTHESIS AND HIGH-PRESSURE CHEMISTRY

Doctoral Dissertation

NOVI PRISTOPI V KEMIJI ŽLAHTNIH PLINOV: MEHANOKEMIJSKA SINTEZA IN KEMIJA POD VISOKIMI TLAKI

Doktorska disertacija

Supervisor: Asst. Prof. Matic Lozinšek

Ljubljana, Slovenia, February 2026

Acknowledgments

I would first like to acknowledge the supervisor, Asst. Prof. Matic Lozinšek, for enabling me to work within the newly-equipped facilities of the Extreme Conditions Chemistry Laboratory on the exotic, fascinating and challenging field of fluorine- and noble-gas chemistry. His help regarding X-ray structural analysis and scientific text writing was crucial for this dissertation, whereas fruitful discussions about the science significantly changed my way of thinking about scientific problems. Of course, his investment in (proof)reading this dissertation is also acknowledged.

I am also indebted to Dr. Kristian Radan, a fluorine-chemistry and Raman spectroscopy expert, as well as science and coffee enthusiast. His skillfulness in many aspects of inorganic synthesis and willingness to help even during the late night/early morning experimentation helped enlarge the opus of this dissertation.

Asst. Prof. Mirela Dragomir has to be acknowledged for all her help with analysis of powder X-ray diffraction data, and, who in the beginning of this PhD, provided necessary mechanochemical equipment to perform preliminary experiments regarding mechanochemical synthesis.

I am also indebted to Dr. Miha Virant, without whom the quantum-chemical calculations would be non-existent. His dedicated work in improving overall quality of work, especially in the terms of high-pressure research, significantly accelerated many important discoveries.

Many thanks go to Klemen Motaln, for his help in preparing publication-level quality results regarding the research of hydrostatic properties of the oxidatively resistant fluorinated liquids at high pressure. Moreover, his expertise about many technical aspects of the work in the laboratory was also helpful.

Olha Sanko, whose kind spirit made otherwise elaborate and hard work much more bearable, and with whom I had (and still have) privilege to share many interesting and challenging projects which required formidable patience from her side, is also acknowledged.

I was also happy to share moments with ECCL team members and visitors: Dr. Valentina Milašinović, Dr. Ana Siljanovska Virant, Dr. Lewis Clough, Dr. Kristina Smokrović, Dr. Luka Fotović, Dr. Mateja Pisačić and Dr. Katarina Lisac. Of course, I am grateful for conversation with Dr. Matic Belak Vivod and Lia Šibav from K5 department. Thanks also goes to Dr. Jan Gnidovec, Marko Jeran, Tomaž Mržljak, Žan Zakošek with whom I had opportunity to discuss many interesting topics. Thanks also to all other colleagues from K1 department, with whom I had interesting discussions during 4.5 years.

Many thanks go to Prof. Dominik Kurzydłowski and his group in Warsaw. His expertise in Raman spectroscopy under high pressure and computational analysis of high-pressure structures provided many important insights. I would also like to thank him and Sylwia Olszewska for their hospitality during my two-week Warsaw visit in 2024.

Acknowledgments also go to Dr. rer. nat. Lukáš Palatinus, Dr. Petr Brázda and Dr. Ksihtij Gurung in Prague for their expertise in 3D electron diffraction.

I would also like to thank Prof. Sebastian Riedel at Freie Universität in Berlin. During 1-month stay in his laboratory within Erasmus+ programme, I learnt many new techniques

and met fantastic scientists, in particular Dr. Alexander Millanvois for giving me opportunity to collaborate on his project.

Beamline scientists, Dr. Nico Giordano (DESY), Dr. Björn Wehinger (ESRF) and Dr. Mohamed Mezouar (ESRF), are also acknowledged for their help in taming the synchrotron radiation and for helpful discussions regarding collection and analysis of high-pressure data.

The help provided from Prof. Maxim Bykov and Prof. Elena Bykova for high-pressure data analysis is also acknowledged, especially in terms of analysis of high-pressure data of XeF_6 and $XeF_2{\cdot}XeF_4$ samples.

I am also grateful for hospitality of Prof. Simon Parsons during my stay in Edinburgh in 2023, with whom I had the opportunity to discuss many topics in high-pressure science.

Expectedly, enormous thanks go to Dr. Nikola Jakupec, the "cyanide virtouso", not only for his, in my opinion, major contribution to our many joint projects, but also for deep, interesting, and long conversations about science, philosophy, and life. Damjan Šinjori is also acknowledged for his conversations during these 4.5 years.

I am also indebted to Dr. Clara von Randow, which provided me with big inspiration during the PhD work and has shown me the fascinating field of electride chemistry.

I am also grateful for interesting conversations with Prof. Vladimir Stilinović and Prof. Dominik Cinčić, whose halogen-bond chemistry still found me in Ljubljana. Of course, Dr. Lidija Posavec and Dr. Darko Vušak from PMF in Zagreb are also acknowledged for many insightful discussions.

I would also like to thank Dr. Krunoslav Užarević and his group for conversations regarding mechanochemistry.

Thanks also goes to all committee members: Prof. Tadej Rojac, Asst. Prof. Marta Počkaj, and Dr. Nikola Biliškov for their (extremely fast) reading of this dissertation.

Finally, the biggest thanks go my family, without whom this dissertation would not be possible.

The author of this thesis acknowledges the funding from the European Research Council (ERC) under the European Union's Horizon 2020 Research and Innovation Programme (Starting Grant 950625), Slovenian Research and Innovation Agency (ARIS) (J1-60022, N1-0225), as well as the Jožef Stefan Institute Director's Fund.

"Po mogućnosti stvaralaštva, po nemogućnosti da se predvide rezultati, i po igri mašte, znanstvena je spoznaja srodna s umjetnošću."

Ivan Supek, *Filozofija, znanost, humanizam*

Abstract

The chemistry of noble-gas compounds is fundamentally important because it challenges concepts of reactivity and bonding, providing also valuable insight in the valence shell electron pair repulsion model of molecular structure. However, the synthesis and handling of these compounds is a difficult task, which places their rich chemistry beyond the reach of most laboratories.

To broaden access to noble-gas chemistry, mechanochemistry has been introduced as a viable method for synthesis of noble-gas compounds. It has been demonstrated that compounds containing the xenon in the oxidation state +1/2, +2, and +4 can be readily prepared using commercially available equipment, with purities comparable to those obtained through classical synthetic routes.

Reaction of NCCN with $[XeF][AsF_6]$ has been investigated for the first time and it enabled the synthesis of $[FXeNCCNXeF][AsF_6]_2$, which represents the first example of a bis-$[XeF]^+$-coordinated nitrogen base. This compound converts to $[XeNC(F)C(F)NXe][AsF_6]_2$ at room temperature. The $[XeNC(F)C(F)NXe]^{2+}$ cation contains the first example of C=N−Xe bonding modality and exhibits a σ-hole on the xenon atoms. The presence of a σ-hole in the cation was exploited for the synthesis of the adduct-cations $[RCN\cdots XeNC(F)C(F)NXe\cdots NCR][AsF_6]_2$ (R = CH_3, H), which feature rare examples of an N−Xe−N linkage.

To investigate the propensity of XeF_2 to act as a hydrogen-bond donor, the salt cocrystals $(RC(OH)NH_2)[AsF_6]\cdot XeF_2$ (R = CF_3, C_2F_5, C_3F_7) were prepared and crystallographically characterized at low temperature. These represent the first crystallographically characterized examples of NH···FXeF hydrogen bonds. Additionally, the crystal structures of hemiprotonated amide salts $(CF_3CONH_2)_2H[AsF_6]$ and $(C_3F_7CONH_2)_2H[AsF_6]$, as well as the salt cocrystal $H_3O[AsF_6]\cdot 2CF_3CONH_2$ were elucidated.

Protonated decafluorobenzophenone, $(C_6F_5)_2COH^+$, isolated as a $(C_6F_5)_2COH^+[AsF_6]^-$, as well as $(C_6F_5)_2CO\cdot AsF_5$ adduct have been synthesized and crystallographically characterized for the first time, with latter representing a rare case of ketone acting as a ligand toward AsF_5. In both compounds, the geometry of $(C_6F_5)_2CO$ moiety is perturbed relative to that of the neutral molecule.

The hydrostatic properties of several oxidatively resistant fluorinated liquids have been investigated under high pressure. They have been shown to be truly hydrostatic up to 1.7 GPa and remain nearly hydrostatic even at 4 GPa, making them suitable for high-pressure studies of noble-gas compounds.

Finally, high-pressure studies of XeF_6 and $XeF_2\cdot XeF_4$ have been carried out. XeF_6 has been found to form a one-dimensional polymer already above 1 GPa. $XeF_2\cdot XeF_4$ undergoes structural changes at lower pressures, as indicated by Raman spectroscopy.

Overall, the results of this thesis demonstrate the richness of the chemistry of noble-gas compounds over the large temperature and pressure range and show that many new insights can be gained by introducing novel methodologies in the chemistry of so-called inert gases.

Povzetek

Kemija spojin žlahtnih plinov je temeljnega pomena, saj postavlja ustaljene koncepte reaktivnosti in kemijske vezi na preizkušnjo ter hkrati nudi dragocen vpogled v teorijo odboja valenčnih elektronskih parov. Sinteza in rokovanje s temi spojinami pa sta eksperimentalno zahtevna, zaradi česar njihova bogata kemija ostaja zunaj dosega večine laboratorijev.

Za razširitev dostopa do spojin žlahtnih plinov je bila kot sintezna metoda uvedena mehanokemija. Pokazano je bilo, da je mogoče spojine, ki vsebujejo ksenon v oksidacijskih številkah +1/2, +2, in +4 zlahka pripraviti z uporabo komercialno dostopne opreme, pri čemer so dosežne čistosti sintetiziranih vzorcev primerljive z vzorci, pripravljenimi s klasičnimi sinteznimi postopki.

Prvič je bila raziskana tudi reakcija NCCN s $[XeF][AsF_6]$, ki je omogočila sintezo spojine $[FXeNCCNXeF][AsF_6]_2$, kar predstavlja prvi primer dušikove baze, koordinirane z dvema $[XeF]^+$ kationoma. Ta spojina se pri sobni temperaturi pretvori v $[XeNC(F)C(F)NXe][AsF_6]_2$, pri čemer kation $[XeNC(F)C(F)NXe]^{2+}$, ki predstavlja prvi primer vezave C=N−Xe, izkazuje prisotnost σ-lukenj na atomih ksenona. Lewisova kislost tega kationa je bila izkoriščena za sintezo kationskih aduktov $[RCN\cdots XeNC(F)C(F)NXe\cdots NCR][AsF_6]_2$ (R = CH_3, H), ki vsebujejo redek primer N−Xe−N povezave.

Za preučevanje XeF_2 kot akceptorja vodikove vezi, so bili pripravljeni kokristali soli $(RC(OH)NH_2)[AsF_6]\cdot XeF_2$ (R = CF_3, C_2F_5, C_3F_7) in kristalografsko okarakterizirani pri nizki temperaturi. Ti rezultati predstavljajo prve kristalografsko karakterizirane primere vodikovih vezi tipa NH···FXeF. Poleg tega so bile določene kristalne strukture hemiprotoniranih amidnih soli $(CF_3CONH_2)_2H[AsF_6]$ in $(C_3F_7CONH_2)_2H[AsF_6]$ ter kokristal soli $H_3O[AsF_6]\cdot 2CF_3CONH_2$.

Protonirani dekafluorobenzofenon, $(C_6F_5)_2COH^+$, izoliran kot $(C_6F_5)_2COH^+[AsF_6]^-$, in adukt $(C_6F_5)_2CO\cdot AsF_5$ sta bila sintetizirana in kristalografsko okarakterizirana; slednji predstavlja redek primer ketona, ki je kot ligand vezan na AsF_5. V obeh spojinah je geometrija fragmenta $(C_6F_5)_2CO$ opazno popačena v primerjavi z nevtralno molekulo.

Hidrostatične lastnosti več oksidativno odpornih fluoriranih tekočin so bile raziskane pri visokem tlaku. Pokazalo se je, da so te tekočine resnično hidrostatične do 1,7 GPa, ostanejo pa deloma hidrostatične tudi pri 4 GPa, zaradi česar so primerne za visokotlačne raziskave spojin žlahtnih plinov.

Izvedene so bile tudi visokotlačne študije XeF_6 in $XeF_2\cdot XeF_4$. Ugotovljeno je bilo, da XeF_6 že pri tlaku nad 1 GPa tvori enodimenzionalni polimer. Kokristal $XeF_2\cdot XeF_4$ pri nižjih tlakih verjetno tudi izkazuje strukturne spremembe, kar je razvidno iz rezultatov Ramanske spektroskopije.

Rezultati te doktorske naloge potrjujejo bogastvo kemije spojin žlahtnih plinov v širokem temperaturnem in tlačnem območju ter kažejo, da uvajanje novih metodoloških pristopov v kemijo tako imenovanih inertnih plinov omogoča pridobivanje pomembnih novih spoznanj.

Contents

List of Figures **xi**

List of Tables **xiv**

Abbreviations **xv**

1 Introduction **1**
1.1 Definition of the Problem ... 1
1.2 Noble-Gas Compounds ... 1
1.2.1 The chemistry of krypton ... 1
1.2.2 The chemistry of xenon ... 3
1.2.2.1 Xenon as a ligand ... 3
1.2.2.2 Xenon in oxidation states lower than +2 ... 3
1.2.2.3 Xenon in the +2 oxidation state ... 4
1.2.2.4 Xenon in the +4 oxidation state ... 8
1.2.2.5 Xenon in the +6 oxidation state ... 10
1.2.2.6 Xenon in the +8 oxidation state ... 12
1.3 Mechanochemistry ... 13
1.4 High Pressure Chemistry ... 13
1.4.1 Diamond anvil cell ... 14
1.4.2 Hydrostaticity ... 15
1.4.3 Noble-gas chemistry under high pressure ... 15
1.4.3.1 Xenon oxides under high pressure ... 16
1.4.3.2 Xenon interaction with halogens ... 16

2 Aims and Hypotheses **19**

3 Materials and Methods **21**
3.1 Materials ... 21
3.2 Methods ... 24
3.2.1 Synthesis ... 24
3.2.1.1 Mechanochemical syntheses ... 24
3.2.1.2 Syntheses in the solution ... 25
3.2.1.3 Solid-state reactions ... 25
3.2.2 High-pressure experiments ... 26
3.2.3 Characterization ... 28
3.2.3.1 Powder X-ray diffraction (PXRD) ... 28
3.2.3.2 Single-crystal X-ray diffraction (SCXRD) ... 28
3.2.3.3 Raman and infrared spectroscopy ... 28
3.2.3.4 3D electron diffraction ... 29
3.2.3.5 Synchrotron X-ray diffraction ... 29

4 Results and Discussion **30**
4.1 Mechanochemical Synthesis of Noble-Gas Compounds 30
4.1.1 Synthesis of compounds containing xenon in the +2 oxidation state by mechanochemistry 30
4.1.2 Synthesis of the dixenon ($[Xe_2]^+$) cation by mechanochemistry 37
4.1.3 Synthesis of compounds containing xenon in the +4 oxidation state by mechanochemistry 39
4.1.4 Employing 3D electron diffraction for characterization of mechanochemically synthesized noble-gas compounds 42
4.1.5 Conclusions of the mechanochemical results 42
4.2 Xenon(II)–Nitrogen Bonded Compounds Derived from Cyanogen 44
4.3 Hydrogen-Bonded Salt Cocrystals of Xenon Difluoride and Protonated Perfluoroamides 54
4.4 Synthesis of Protonated Decafluorobenzophenone and Decafluorobenzophenone−AsF_5 Adduct 86
4.5 Hydrostatic Limits of Selected Inert Fluids 99
4.6 High-Pressure Behavior of Noble-Gas Fluorides 113
4.6.1 High-pressure behavior of XeF_6 113
4.6.2 High-pressure behavior of $XeF_2{\cdot}XeF_4$ 118

5 Conclusions **121**

References **123**

Bibliography **141**

Biography **143**

List of Figures

Figure 1.1: Structures of a) $[KrF][SbF_6]$ (Lehmann, Dixon, & Schrobilgen, 2001); b) $[Kr_2F_3]^+$ cation in $[Kr_2F_3][SbF_6]\cdot KrF_2$ (Lehmann, Dixon, & Schrobilgen, 2001); c) $[Mg(KrF_2)_4][AsF_6]_2$ (Lozinšek, Mercier, Brock, Žemva, & Schrobilgen, 2017). 2
Figure 1.2: Structure of $[AuXe_4]^{2+}$ cation in the $[AuXe_4][Sb_2F_{11}]_2$ (Seidel & Seppelt, 2000). 3
Figure 1.3: Crystal structure of $[Xe_2][Sb_4F_{21}]$ (Drews & Seppelt, 1997). 4
Figure 1.4: Structure of a) XeF_2 (Elliot, Lehmann, Mercier, Jenkins, & Schrobilgen, 2010); b) $[XeF][Sb_2F_{11}]$ (Elliot, Lehmann, Mercier, Jenkins, & Schrobilgen, 2010) and c) $[Xe_2F_3]^+$ cation in $[Xe_2F_3][SbF_6]$ (Bortolus, Mercier, Nguyen, & Schrobilgen, 2021);. 4
Figure 1.5: Crystal structures of a) $[XeF]_2[Ti_9F_{38}]$ (Radan, Goreshnik, & Žemva, 2014) and b) $XeF_2\cdot MnF_4$ (Motaln, et al., 2024). Broken of bonds show continuation of fluoride-bridged polyfluoridotitanate(IV). 5
Figure 1.6: Xenon(II) oxy(fluoro) cations: a) $[FXeOXeFXeF]^+$ (Gerken, et al., 2009), b) $[CH_3CN\cdots XeOXe\cdots NCCH_3]^{2+}$ (De Backere, Bortolus, & Schrobilgen, 2016) and c) $[XeOXeOXe]^{2+}$ cation (Ivanova, Mercier, & Schrobilgen, 2015). 6
Figure 1.7: Structures of the compounds featuring xenon(II)−nitrogen bonds. a) $[F_3SNXeF]^+$ adduct-cation (Smith, Mercier, & Schrobilgen, 2007); b) $[F_4SNXe][AsF_6]$ (Smith, Mercier, & Schrobilgen, 2009), c) $[F_5SN(H)Xe][AsF_6]$ (Smith, Mercier, & Schrobilgen, 2008) and d) $[F_4SNXe\cdots NSF_3]^+$ cation in $[F_4SNXeNSF_3][AsF_6]$ (Smith & Schrobilgen, 2009). 7
Figure 1.8: Structure of the $[Zn(XeF_2)_6]^{2+}$ cation (Tavčar, Goreshnik, & Mazej, 2006). 8
Figure 1.9: Structure of a) XeF_4 (Bortolus, Mercier, Nguyen, & Schrobilgen, 2021); b) $[XeF_3][SbF_6]$ (Brock, Mercier, & Schrobilgen, 2013) and c) $[Mg(XeF_4)(XeF_2)][AsF_6]_2$ (Tavčar & Žemva, 2009). 9
Figure 1.10: Structure of a) $[XeF_5]^-$ anion (Christe, et al., 1991); b) $XeOF_2\cdot NCCH_3$ (Brock, Bilir, Mercier, & Schrobilgen, 2007) and c) $[C_6F_5XeF_2]^+$ cation (Koppe, Haner, Mercier, Frohn, & Schrobilgen, 2014) coordinated with two acetonitrile molecules. 10
Figure 1.11: Crystal structure of a) $(XeF_6)_4$tetramer (contacts between two $[XeF_5]^+$ moieties which are bridged by fluoride anion are denoted as orange dashed lines) (Hoyer, Emmler, & Seppelt, 2006); b) $[XeF_5]^+$ cation (Goettel, Bortolus, Stuart, Mercier, & Schrobilgen, 2019) and c) $[Xe_2F_{11}]^+$ cation (Goettel, Bortolus, Stuart, Mercier, & Schrobilgen, 2019). 10
Figure 1.12: Molecular geometries of a) $[XeF_7]^-$, b) $[Xe_2F_{13}]^-$ (Ellern, Mahjoub, & Seppelt, 1996) and c) $[XeF_8]^{2-}$ anions (Adam, Ellern, & Seppelt, 1996). In c), shaded polyhedron faces outline square antiprism. 11
Figure 1.13: Crystal structure of a) Propionitrile adduct with XeO_3 (Goettel, Matsumoto, Mercier, & Schrobilgen, 2016) b) Crown-ether complex with XeO_3 (Marczenko, Mercier, & Schrobilgen, 2018). 11
Figure 1.14: Structures of a) $XeOF_4$ molecule; b) $[XeOF_3]^+$ cation in $[XeOF_3][SbF_6]$ (Mercier, Sanders, Schrobilgen, & Tsai, 1993); c) $[XeO_2F]^+$ cation in $[XeO_2F][SbF_6]$ (Pointner, Suontamo, & Schrobilgen, 2006). 12
Figure 1.15:Schematic view of diamond anvil cell (courtesy of dr. Miha Virant). 14

Figure 3.1: Vacuum line used for synthetic work presented in this thesis. 21
Figure 3.2: Different FEP vessels used. a) FEP vessel made out of the main and side arm (8 mm o.d.; 6 mm i.d.) equipped with PTFE valve encased in brass body; b) FEP vessel (6 mm o.d.; 4.7 mm i.d.) equipped with PCTFE -valve encased in aluminum body, typically used for low-temperature syntheses. o.d. is abbreviation for outer diameter, whereas i.d. is abbreviation for inner diameter..... 22
Figure 3.3: Anhydrous HF (aHF) with $K_2[NiF_6]$ in FEP vessel (o.d. 19 mm, i.d. 16 mm) equipped with PTFE valve encased in brass. 23
Figure 3.4: Mechanochemical equipment used for research work described in this thesis. a) PTFE milling vessels with the PTFE milling balls inside; b) An example of closed PTFE milling vessel for transfer in glovebox; c) Milling vessel used for the reaction performed on the Fritsch Pulverisette 23 mill; d) Retsch MM 400 mill; e) Fritsch Pulverisette 23 mill. 25
Figure 3.5: a) SSDAC-80 and b) Merrill-Bassett diamond anvil cell..... 26
Figure 3.6: Fitted ruby fluorescence spectrum with important parameters obtained after fitting procedure. Black squares represent measured, whereas red lines represent fitted spectrum. Fitting was performed using *CrimsonCalc* software (Virant & Lozinšek, 2025). 27
Figure 3.6: Diamond peak and the first derivative of the diamond peak..... 27
Figure 4.1: Comparison of synthetic methods for $[XeF][Ta_2F_{11}]$. The asterisk (*) denotes $[XeF][TaF_6]$ as a secondary phase, whereas the plus sign (+) denotes TaF_5. 31
Figure 4.2: Asymmetric unit of $[XeF][Ta_2F_{11}]$. All atoms are depicted with 50 % probability ellipsoids. 32
Figure 4.3: Comparison of synthetic methods for $[XeF][TaF_6]$. The asterisk (*) denotes a $[Xe_2F_3][TaF_6]$ as a secondary phase, whereas the plus sign (+) denotes a PTFE impurity originating from the milling vessel. 34
Figure 4.4: Asymmetric unit of $[XeF][TaF_6]$. All atoms are depicted with 50 % probability ellipsoids. 35
Figure 4.5: a) Comparison of synthetic methods for $[Xe_2F_3][TaF_6]$. The asterisk (*) denotes $[XeF][TaF_6]$ as a secondary phase. b) Rietveld refinement of mechanochemically prepared $[Xe_2F_3][TaF_6]$. The red points represent the experimental data, the black line the refined profile, and blue tick marks indicate the positions of the Bragg reflections. The difference plot is shown as a green line. Rietveld analysis was performed in *GSAS*-II (Toby & Von Dreele, 2013) by Asst. Prof. Mirela Dragomir. 35
Figure 4.6: Asymmetric unit of $[Xe_2F_3][TaF_6]$. All atoms are depicted with 50 % probability ellipsoids. 36
Figure 4.7: Results of time-dependent milling for XeF_2:TaF_5 in a 2:1 ratio. The plus sign (+) denotes $[TaF_6]^-$ anion of $[Xe_2F_3][TaF_6]$, the asterisk (*) denotes the $[TaF_6]$ moiety of $[XeF][TaF_6]$, and the hash symbol (#) denotes $[Ta_2F_{11}]$ moiety of $[XeF][Ta_2F_{11}]$. All spectra correspond to separate experiments; that is, once a milling vessel was opened, it was not closed again for continuation of the experiment. 37
Figure 4.8: Raman spectra of products obtained after one hour of grinding of XeF_2:SbF_3 mixture in different ratios. The asterisk (*) represents unreacted XeF_2, whereas the plus sign (+) likely corresponds to $[Xe_2F_3][SbF_6]\cdot XeF_2$ cocrystal (Frlec & Holloway, 1975). The inset shows the green powder obtained after grinding the XeF_2:SbF_3 mixture in a 1.25:1 ratio. 38
Figure 4.9: Raman spectra of the product obtained after 20 minutes of grinding XeF_2 and XeF_4 in a 1:1 molar ratio. For comparison, Raman spectra of $XeF_2\cdot XeF_4$ cocrystal prepared by solid-state synthesis, XeF_2, and XeF_4 are also shown for comparison. 39
Figure 4.10: Raman spectra of mechanochemically synthesized $[XeF_3][Ta_2F_{11}]$. The asterisk (*) denotes unreacted TaF_5. 40

Figure 4.11: Asymmetric unit of $[XeF_3][Ta_2F_{11}]$. All atoms are depicted with 50% probability ellipsoids. Short F4···Xe1 and F11···Xe1 contacts are shown as a dashed orange lines. 42
Figure 4.12: Raman spectra of XeF_6 collected up to 1.68 GPa. Insets show the photographs of the sample chamber at the indicated pressure points..... 114
Figure 4.13: One-dimensional polymer in the $P2_1/c$ polymorph of XeF_6 at 1.9 GPa. Essentially the same 1D polymer is observed in the $P\bar{1}$ and $P2_1/m$ polymorphs. 115
Figure 4.14: a) Interchain Xe···F contacts (blue dashed lines) and b) packing in the $P2_1/c$ polymorph. In a), orange dashed lines indicate the continuation of the 1D polymer..... 116
Figure 4.15: Raman spectra of XeF_6 collected up to 5.17 GPa. Insets show the sample chamber. Black streaks observed in the sample are attributed to synchrotron radiation damage. 117
Figure 4.16: Raman spectra of the sample at 7.8 GPa. Inset shows the sample chamber. Arrows indicate the areas from which the Raman spectra were collected. The asterisk (*) denotes the XeF_2 peak, which is in good agreement with the values reported in literature (Liu, et al., 2024). 118
Figure 4.17: Comparison of Raman spectra of the $XeF_2{\cdot}XeF_4$ cocrystal at ambient pressure and at 7.12 GPa. 119
Figure 4.18: a) Raman spectra of the $XeF_2{\cdot}XeF_4$ cocrystal during compression up to 32 GPa; b) Raman spectra of the $XeF_2{\cdot}XeF_4$ cocrystal during decompression down to 1.95 GPa. 120

List of Tables

Table 3.1: Used chemicals in this thesis and their stated purity or reference to their synthesis..... 24
Table 4.1: Comparison of results from different synthethic methods in terms of secondary phases present. The phases in bold are the major phases present, whereas the non-bolded are secondary phases. Solid-state synthesis referes to synthesis at elevated temperature..31
Table 4.2: Summary of crystal data and structure refinements for [XeF][Ta_2F_{11}], [XeF][TaF_6] and [Xe_2F_3][TaF_6]. All data was measured with Ag Kα raddiation. 33
Table 4.3: Summary of crystal data and structure refinements for [XeF_3][Ta_2F_{11}]. 41
Table 4.4: Summary of crystal data and structure refinements for different polymorphs of XeF_6 obtained at 1.68 GPa ($P\bar{1}$ and $P2_1/m$) and 1.90 GPa ($P2_1/c$). The radiation wavelength for all measurements was 0.2898 Å. 116

Abbreviations

aHF ... anhydrous hydrogen fluoride
SCXRD ... single-crystal X-ray diffraction
PXRD ... powder X-ray diffraction
DAC ... diamond anvil cell
HP ... high pressure
HT ... high temperature
LH ... laser heating
LT ... low temperature
FEP ... fluorinated ethylene propylene
3D ED ... three-dimensional electron diffraction

Chapter 1

Introduction

1.1 Definition of the Problem

The chemistry of noble gases is a fundamental area of chemical research that stands at the forefront of exploring core concepts of chemical reactivity, bonding and structure. It therefore does not seek any immediate application. The intertwined nature of fluorine chemistry and chemistry of noble gases, however, makes exploration a particular challenge, as the required synthetic methods are highly specialized and practiced in only a limited number of laboratories worldwide. Consequently, the expertise required to prepare, isolate, and characterize noble-gas compounds is readily transferable to the synthesis and handling of other highly unstable or reactive species across chemical research.

1.2 Noble-Gas Compounds

Reaction of xenon with platinum hexafluoride, which is considered to be "one of the most beautiful chemical experiments" (Ball, 2005), affords $XePtF_6$ (Bartlett, 1962; Graham, Graudejus, Jha, & Bartlett, 2000). Following this discovery by Neil Bartlett, the synthesis of many xenon and krypton compounds has ensued, therefore showing the rich chemical reactivity of group 18 in periodic table of elements.

In essence, noble-gas chemistry can be divided into the chemistry of krypton and xenon. The lighter noble gases (He, Ne, and Ar) have not been observed to form compounds in macroscopic quantities. Radon has been found to react with fluorine, forming radon fluoride(s), but its high radioactivity and short half-life hinders full characterization of these compounds (Stein, 1983).

1.2.1 The chemistry of krypton

Krypton forms only one binary fluoride, KrF_2, which is unstable at room temperature but is stable at low temperatures (Lehmann, Mercier, & Schrobilgen, 2002). Consequently, krypton chemistry has been explored far less extensively than that of xenon.

KrF_2 can be synthesized in several ways, of which three are known to give particularly good yields (Lehmann, Mercier, & Schrobilgen, 2002): UV-photolysis of solid krypton in liquid fluorine at −196 °C (Slivnik, Šmalc, Lutar, Žemva, & Frlec, 1975); reaction of fluorine radicals generated by a hot-wire reactor with solid krypton (Bezmel'nitsyn, Legasov, & Chaivanov, 1977; Kinkead, FritzPatrick, Foropoulos, Kissane, & Purson, 1994; Lehmann, Dixon, & Schrobilgen, 2001); and electric discharge of gaseous krypton and fluorine at cryogenic temperatures (Schreiner, Malm, & Hindman, 1965).

KrF_2 adopts a linear geometry and crystallizes in two polymorphs (Burbank, Falconer, & Sunder, 1972; Lehmann, Dixon, & Schrobilgen, 2001), both of which exhibit essentially identical Kr−F bond distances. In addition to being one of the strongest oxidizers known, KrF_2 also acts as a fluoride-ion donor. This behavior is exemplified by the synthesis of $[KrF][MF_6]$ tight-ion pairs (Figure 1.1, a) (M = Nb, Ta, As, Sb, Au) (Selig & Peacock, 1964; Frlec & Holloway, 1973; Frlec & Holloway, 1974; Gillespie & Schrobilgen, 1974; Frlec & Holloway, 1976). In crystal structure, the asymmetric F−Kr−F moiety is present, reflecting the ionization of KrF_2 to $[KrF]^+$ cation and F^- anion. (Lehmann, Dixon, & Schrobilgen, 2001; Lehmann & Schrobilgen, 2003). Adducts of KrF_2 with MOF_4, i.e., $KrF_2{\cdot}nMOF_4$ (M = Cr, Mo, W; n = 1,2) adducts (Mecier, Breddemann, Brock, Bortolus, & Schrobilgen, 2019; Bortolus, Mercier, Brock, & Schrobilgen, 2022) are also known, although in these KrF_2 can also act as a bridging ligand.

The $[KrF][MF_6]$ tight-ion pairs can further react with additional KrF_2 to form $[Kr_2F_3][MF_6]$ salts (Frlec & Holloway, 1973; Frlec & Holloway, 1974; Gillespie & Schrobilgen, 1974; Lehmann, Dixon, & Schrobilgen, 2001). The $[Kr_2F_3]^+$ cation adopts a V-shaped geometry (Figure 1.1, b) and can be described as KrF_2 coordinated to a $[KrF]^+$ cation. KrF_2 can also act as ligand toward "naked" metal cations (Lozinšek, Mercier, Brock, Žemva, & Schrobilgen, 2017; De Backere & Schrobilgen, 2018) (Figure 1.1, c), as well as toward $[XeF_5]^+$ (Lozinšek, Mercier, & Schrobilgen, 2021) and $[XeF]^+$ cations (Bortolus, Mercier, Nguyen, & Schrobilgen, 2021), resulting in mixed noble-gas compounds. KrF_2 also forms cocrystals with $XeOF_4$ (Hughes, 2010) and XeF_4 (Bortolus, Mercier, Nguyen, & Schrobilgen, 2021).

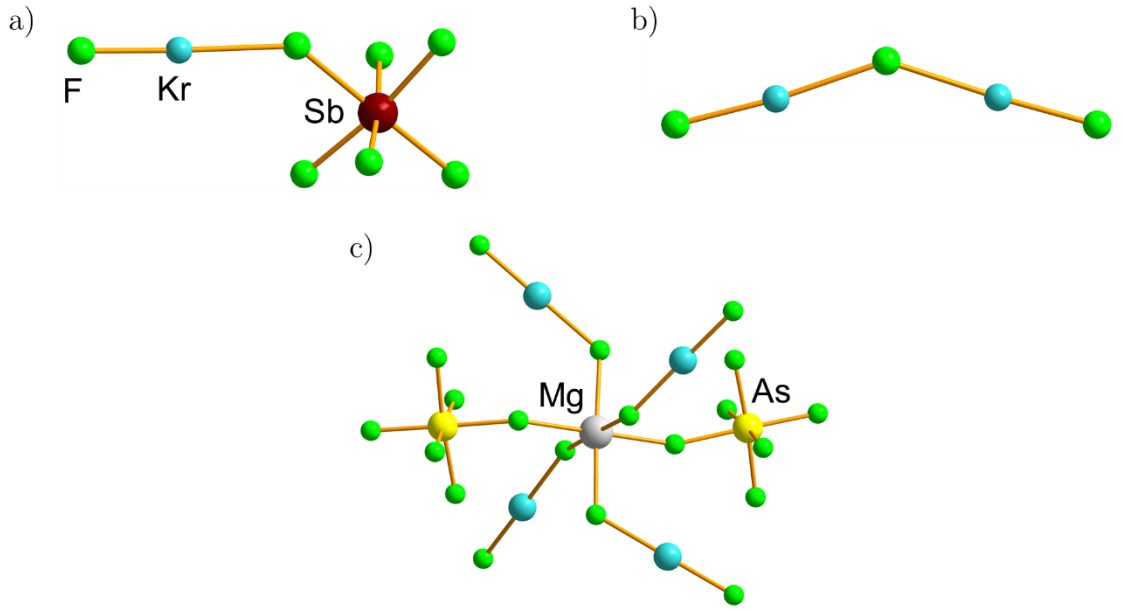


Figure 1.1: Structures of a) $[KrF][SbF_6]$ (Lehmann, Dixon, & Schrobilgen, 2001); b) $[Kr_2F_3]^+$ cation in $[Kr_2F_3][SbF_6]{\cdot}KrF_2$ (Lehmann, Dixon, & Schrobilgen, 2001); c) $[Mg(KrF_2)_4][AsF_6]_2$ (Lozinšek, Mercier, Brock, Žemva, & Schrobilgen, 2017).

Although rare, compounds in which krypton is bonded to another highly electronegative element, such as oxygen or nitrogen, are known.

The $[KrF]^+$ cation (from $[KrF][AsF_6]$) can coordinate to oxidatively resistant nitrogen bases, such as HCN and CF_3CN (Schrobilgen, 1988*a*; Schrobilgen, 1988*b*). The formation of these $[RCNKrF]^+$ adduct cations has been confirmed by low-temperature NMR and

Raman spectroscopy. As expected, these compounds are highly unstable; for example, $[HCNKrF][AsF_6]$ decomposes readily above −50 °C.

Currently, the only known example of a krypton–oxygen bond is $Kr(OTeF_5)_2$, which is formed upon reaction of $B(OTeF_5)_3$ with KrF_2 in SO_2ClF. It was characterized in solution by low-temperature NMR spectroscopy. The compound is highly unstable, decomposing already at −90 °C (Sanders & Schrobilgen, 1989). The reaction of KrF_2 with $HOTeF_5$ or $HOSeF_5$ in ClO_3F yields hydrogen-bonded cocrystals that are stable up to −10 °C or −40 °C, respectively (Jacob, Lentz, Seppelt, & Simon, 1981).

1.2.2 The chemistry of xenon

The chemistry of xenon, unlike that of krypton, spans through several oxidation states.

1.2.2.1 Xenon as a ligand

Noble gases were originally found to act as ligands to metal carbonyls under matrix conditions or in supercritical fluids (Simpson, Poliakoff, Turner, Maier II, & McLaughlin, 1983; Weiller, 1992; Wells & Weitz, 1992; Ehlers, Frenking, & Baerends, 1997). However, the first example in the condensed state has been observed in the tetraxenongold(II) cation (Figure 1.2) in the $[AuXe_4][Sb_2F_{11}]_2$ salt (Seidel & Seppelt, 2000). The short Au—Xe bonds (2.728(1)–2.750(1) Å) are indicative of bonding, with xenon considered a σ-donor toward Au^{2+}. Several other gold–xenon complexes have also been obtained and characterized by single-crystal X-ray diffraction (Drews, Seidel, & Seppelt, 2002; Hwang, Seidel, & Seppelt, 2003). The mercury(II) cation has also been found to form a coordination compound with xenon in $[HgXe][SbF_6][Sb_2F_{11}]$ (Hwang, Seidel, & Seppelt, 2003).

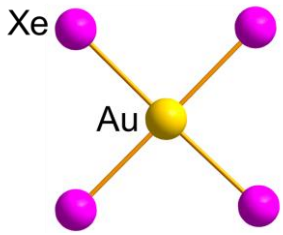


Figure 1.2: Structure of $[AuXe_4]^{2+}$ cation in the $[AuXe_4][Sb_2F_{11}]_2$ (Seidel & Seppelt, 2000).

1.2.2.2 Xenon in oxidation states lower than +2

The green dixenon cation, $[Xe_2]^+$, is obtained by reacting xenon with $[XeF][Sb_2F_{11}]$ in liquid SbF_5 (Brown, et al., 1992). The crystal structure of $[Xe_2][Sb_4F_{21}]$ has been determined (Drews & Seppelt, 1997) and features the $[Xe_2]^+$ cation with an Xe—Xe bond distance of 3.087(2) Å (Figure 1.3). The cation decomposes upon addition of HF or removal of xenon pressure (Brown, et al., 1992). A further increase of xenon pressure (above 50 bar) under similar condition produces a blue solution, presumably containing the $[Xe_4]^+$ cation (Seidel, Seppelt, van Wulle, & Sun, 2007). However, all crystallization attempts, which require cooling, result in a decrease of xenon pressure, leading to the formation of the green $[Xe_2]^+$ cation.

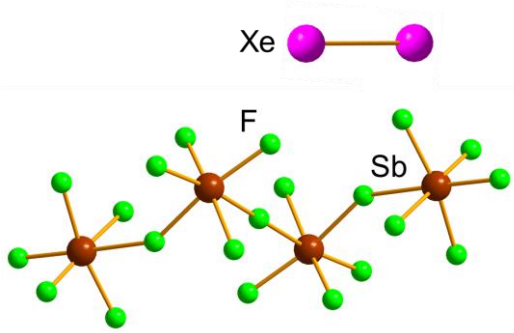


Figure 1.3: Crystal structure of $[Xe_2][Sb_4F_{21}]$ (Drews & Seppelt, 1997).

1.2.2.3 Xenon in the +2 oxidation state

The chemistry of xenon in oxidation state +2 has been studied extensively, owing to the stability and relative inertness of the starting material, XeF_2 (Tramšek & Žemva, 2006). Similar to KrF_2, the XeF_2 molecule has linear, centrosymmetric geometry (Figure 1.4, a) with an Xe—F bond length of 1.999(4) Å (Elliot, Lehmann, Mercier, Jenkins, & Schrobilgen, 2010). It is a potent oxidizer, capable of oxidizing certain metals to their highest oxidation state. It is also a relatively good fluoride-ion donor (Tramšek & Žemva, 2006). Both of these properties were also explored in the context of organic chemistry (Tius, 1995). Nevertheless, XeF_2 is considerably less reactive than other noble-gas fluorides, as evidenced by its stability in water for several hours and in many dry organic solvents, such as acetonitrile and dichloromethane (Tramšek & Žemva, 2006).

There are many synthesis pathways to XeF_2. Xenon and fluorine react thermally under excess of xenon to form XeF_2 (Slivnik, Šmalc, Žemva, & Mosevič, 1968), but the highest purity is achieved via photochemical synthesis of XeF_2 using traces of HF as catalyst (Lutar & Šmalc, 1989).

In inorganic fluorine chemistry, XeF_2 has primarily been studied as a fluoride-ion donor (Žemva, 1988; Tramšek & Žemva, 2006). This behavior is illustrated by its reaction with metal pentafluorides, yielding $[XeF][MF_6]$ or $[XeF][M_2F_{11}]$ (Figure 1.4, b) (M = Nb, Ta, As, Sb, Pt, Bi) tight-ion pairs (Sladky, Bulliner, & Bartlett, 1969; Žemva, 1988; Elliot, Lehmann, Mercier, Jenkins, & Schrobilgen, 2010), which are analogous to the corresponding $[KrF][MF_6]$ tight-ion pairs. As expected, the F—Xe—F fragment is asymmetric, reflecting the ionization of XeF_2 into $[XeF]^+$ and F^- (Žemva, et al., 1987). These tight-ion pairs can further react with XeF_2 to form $[Xe_2F_3][MF_6]$ salts, in which the $[Xe_2F_3]^+$ cation adopts a V-shaped geometry, similar to the $[Kr_2F_3]^+$ cation (Figure 1.4, c).

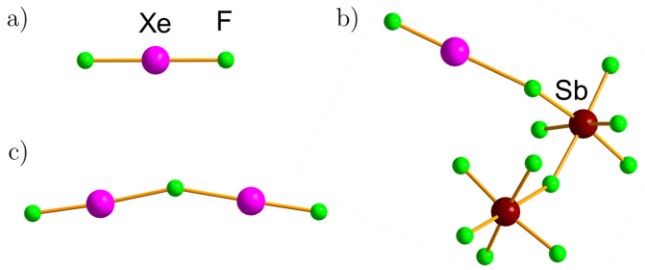


Figure 1.4: Structure of a) XeF_2 (Elliot, Lehmann, Mercier, Jenkins, & Schrobilgen, 2010); b) $[XeF][Sb_2F_{11}]$ (Elliot, Lehmann, Mercier, Jenkins, & Schrobilgen, 2010) and c) $[Xe_2F_3]^+$ cation in $[Xe_2F_3][SbF_6]$ (Bortolus, Mercier, Nguyen, & Schrobilgen, 2021);.

Metal tetrafluorides (MnF_4, TiF_4, SnF_4, PtF_4, PdF_4, CrF_4) also react with XeF_2, forming $n XeF_2 \cdot m MF_4$ adducts, where n and m can vary (Družina & Žemva, 1986; Lutar, Leban, Ogrin, & Žemva, 1992; Lutar, Borrmann, & Žemva, 1998; Radan, Goreshnik, & Žemva, 2014; Radan, 2017; Motaln, et al., 2024; Motaln, et al., 2025). Unlike XeF_2 adducts with pentafluorides, the crystal structures of $n XeF_2 \cdot m MF_4$ adducts can be described as fluoride-bridged oligomers or polymers, consisting of anionic fluoridometalates to which $[XeF]^+$ is bonded (Figure 1.5). Interestingly, when TiF_4, is used as a Lewis acid, the $[Xe_2F_3]^+$ cation is formed even when XeF_2 is not present in excess (Radan, Goreshnik, & Žemva, 2014). Metal oxyfluorides, such as $CrOF_4$ (Mecier, Breddemann, Brock, Bortolus, & Schrobilgen, 2019), $MoOF_4$ and WOF_4 (Bortolus, Mercier, Brock, & Schrobilgen, 2022) also act as fluoride-ion acceptors and form discrete units.

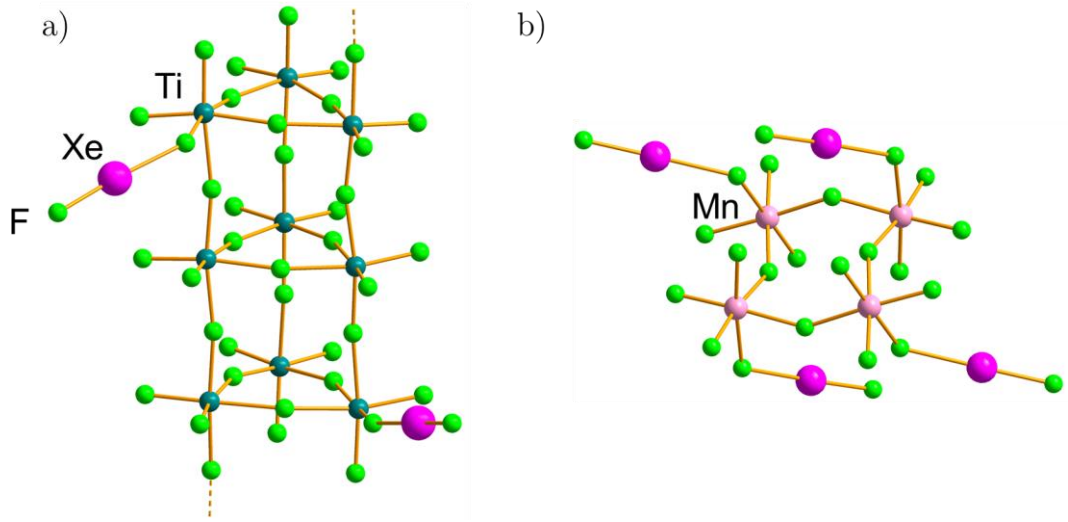


Figure 1.5: Crystal structures of a) $[XeF]_2[Ti_9F_{38}]$ (Radan, Goreshnik, & Žemva, 2014) and b) $XeF_2 \cdot MnF_4$ (Motaln, et al., 2024). Broken of bonds show continuation of fluoride-bridged polyfluoridotitanate(IV).

Oxyfluoroxenon(II) cations can be formed upon reaction of $[XeF]^+$ with water at low temperatures. Reaction of $[XeF][AsF_6]$ or $[XeF][SbF_6]$ with H_2O in anhydrous HF (aHF) at −40 °C leads to the formation of $[FXeOXeFXeF]^+$ cation (Figure 1.6, a) (Gerken, et al., 2009). This cation can subsequently decompose in the presence of acetonitrile at −60 °C to yield the $[XeOXe]^{2+}$ cation (De Backere, Bortolus, & Schrobilgen, 2016) which is coordinated with two acetonitrile molecules (Figure 1.6, b). Another xenon–oxygen cation is the $[XeOXeOXe]^{2+}$ cation (Ivanova, Mercier, & Schrobilgen, 2015) (Figure 1.6, c), which is obtained from the reaction of ReO_3F_2 with XeF_2.

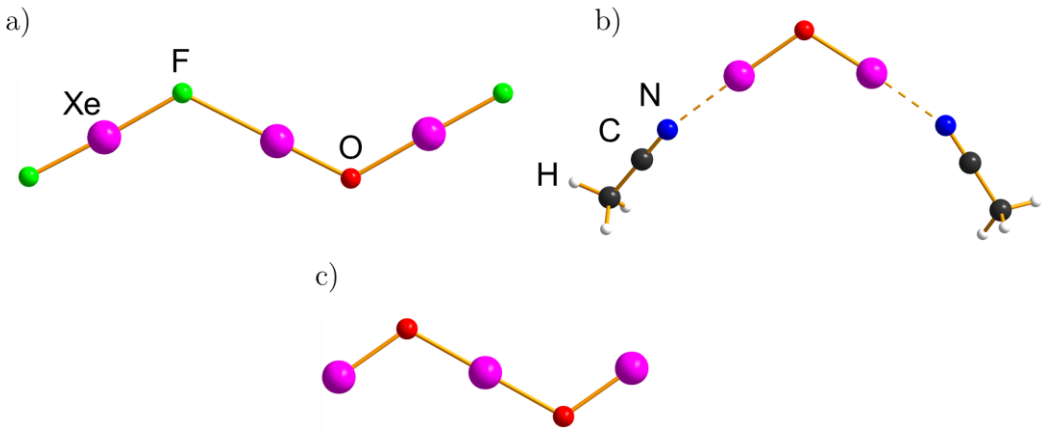


Figure 1.6: Xenon(II) oxy(fluoro) cations: a) $[FXeOXeFXeF]^+$ (Gerken, et al., 2009), b) $[CH_3CN{\cdots}XeOXe{\cdots}NCCH_3]^{2+}$ (De Backere, Bortolus, & Schrobilgen, 2016) and c) $[XeOXeOXe]^{2+}$ cation (Ivanova, Mercier, & Schrobilgen, 2015).

Numerous other compounds containing xenon(II)–oxygen bonds are known – $FXeOTeF_5$, $Xe(OTeF_5)_2$, $FXeOSeF_5$, $Xe(OSeF_5)_2$, $Xe(OSO_2F)_2$, etc. (Seppelt, 1979). The compounds are in principle less reactive than $[XeF][MF_6]$, but still act as potent oxidizers. The $FXeOTeF_5$ and $FXeOSeF_5$ can also act as fluoride-ion donors, forming $[XeOTeF_5]^+$ and $[XeOSeF_5]^+$ cations. Coordination of oxygen bases to $[XeF]^+$ cation has also been reported (Minkwitz & Molsbeck, 1992; Schrobilgen & Whalen, 1994) and $FXeONO_2$ (Moran, Brock, Mercier, & Schrobilgen, 2010), $FXeClO_4$, and $Xe(ClO_4)_2$ (Wechsberg, Bulliner, Sladky, Mews, & Bartlett, 1972) are also known.

The chemistry of compounds containing nitrogen–xenon bonds has also been extensively studied. First compound which was synthesized and contained nitrogen–xenon bond was $(FSO_2)_2NXeF$ (LeBlond & DesMarteu, 1974; DesMarteu, LeBlond, Hossain, & Nothe, 1981; Sawyer, Schrobilgen, & Sutherland, 1982). $(FSO_2)_2NXe^+$ derivatives can be obtained by fluoride abstraction from xenon atom. Compounds containing nitrogen–xenon bonds can also be prepared by the reaction of $[XeF][AsF_6]$ with oxidatively resistant nitrogen Lewis bases, such as HCN, CH_3CN, F_3SN, and pyridine derivatives (Emara & Schrobilgen, 1987; Schrobilgen, 1988*b*; Smith, Mercier, & Schrobilgen, 2007). The formation of N—Xe bond arises from the presence of a σ-hole on the xenon atom in the $[XeF]^+$ cation, which acts as a Lewis acid towards the electron-donating nitrogen atom (MacDougall, Schrobilgen, & Bader, 1989; Politzer, Murray, Clark, & Resnati, 2017). To prepare such compounds, the nitrogen bases must have an ionization potential (IE) equal to or greater than the estimated electron affinity of $[XeF]^+$ cation (~10.8 eV) (Sladky, Bulliner, & Bartlett, 1969; Emara & Schrobilgen, 1992). Syntheses of such adduct-cations is generally carried out in aHF or BrF_5 at low temperatures.

With the exception of $[s\text{-}C_3F_3N_2N{-}XeF][AsF_6]$ (Schrobilgen, 1988*b*) and $(FSO_2)_2NXeF$ (LeBlond & DesMarteu, 1974; DesMarteu, LeBlond, Hossain, & Nothe, 1981; Sawyer, Schrobilgen, & Sutherland, 1982), $[RNXeF][AsF_6]$ compounds are unstable at room temperature (Emara, 1991) and decompose to release xenon gas. The decomposition of $[F_3SNXeF][AsF_6]$ (Figure 1.7, a), however, proceeds through a series of reactions. The $[F_3SNXeF][AsF_6]$ (Smith, Mercier, & Schrobilgen, 2007) undergoes fluoride rearrangement at room temperature, either in solution (aHF, BrF_5) or in the solid state, to form $[F_4SNXe][AsF_6]$ (Fig 1.7, b), in which the xenon atom is coordinated to the $[AsF_6]^-$ anion via Xe···F contact (Smith, Mercier, & Schrobilgen, 2009). This compound undergoes further solvolysis in HF to yield $[F_5SN(H)Xe][AsF_6]$ (Smith, Mercier, & Schrobilgen, 2008) (Figure

1.7, c), which is structurally analogous to the tellurium analogue, $[F_5TeN(H)Xe][AsF_6]$ (Fir, Whalen, Mercier, Dixon, & Schrobilgen, 2006). Finally, $[F_5SN(H)Xe][AsF_6]$ decomposes at room temperature to give xenon, $NH_4[AsF_6]$ and SF_6.

When the fluoride-transfer reaction of $[F_3SNXeF][AsF_6]$ to $[F_4SNXe][AsF_6]$ is carried out in F_3SN, $[F_4SNXeNSF_3][AsF_6]$ (Figure 1.7, d) is formed (Smith & Schrobilgen, 2009), providing a rare example of crystallographically characterized N−Xe−N linkage. A similar linkage has also been observed in $[(FSO_2)_2N]_2Xe$ (DesMarteau, LeBlond, Hossain, & Nothe, 1981) and $[(CF_3SO_2)_2N]_2Xe$ (Foropoulos & DesMarteau, 1982), although the crystal structures of these compounds have not yet been determined.

Other xenon(II) cations can also serve as Lewis acids, such as $[XeOTeF_5]^+$, which forms an adduct cation with pentafluoropyridine (Toraman, et al., 2024).

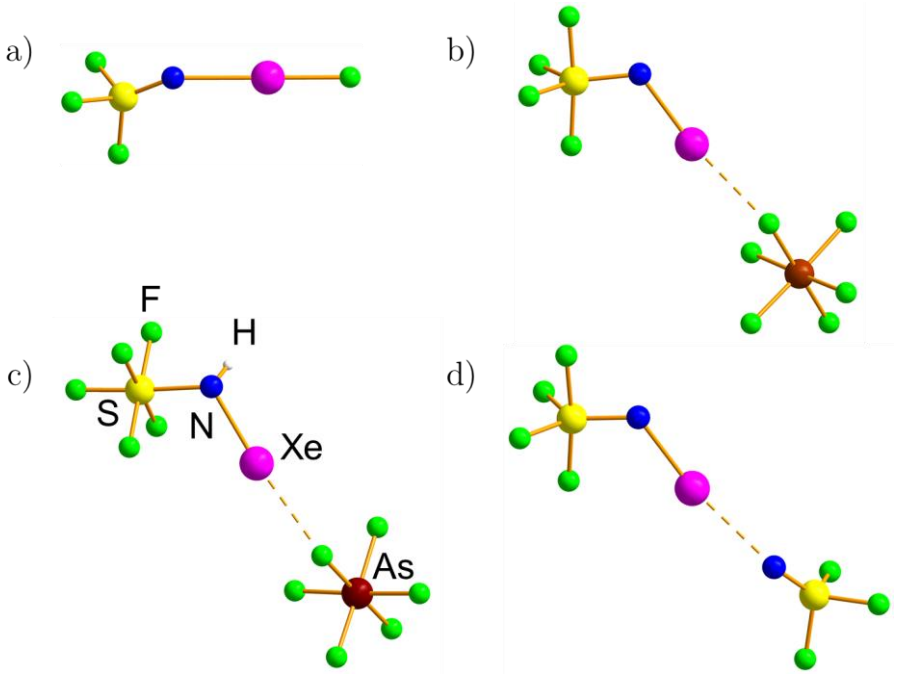


Figure 1.7: Structures of the compounds featuring xenon(II)−nitrogen bonds. a) $[F_3SNXeF]^+$ adduct-cation (Smith, Mercier, & Schrobilgen, 2007); b) $[F_4SNXe][AsF_6]$ (Smith, Mercier, & Schrobilgen, 2009), c) $[F_5SN(H)Xe][AsF_6]$ (Smith, Mercier, & Schrobilgen, 2008) and d) $[F_4SNXe\cdots NSF_3]^+$ cation in $[F_4SNXeNSF_3][AsF_6]$ (Smith & Schrobilgen, 2009).

The chemistry of xenon in oxidation state +2 has also been explored in compounds featuring Xe−C bonds, i.e., organoxenon(II) compounds (Frohn & Bardin, 2001). A prototypical example is $[C_6F_5Xe]^+$ cation. These compounds have been found to be useful organic reagents and are generally less oxidative than the corresponding $[XeF]^+$ cation. The $[C_6F_5Xe]^+$ also features a σ-hole, as evident by synthesis of species featuring C−Xe−O (Bilir, Blaser, Boese, & Frohn, 2009) and C−Xe−N (Frohn, Jakobs, & Henkel, 1989) linkage.

Xenon in oxidation state +2 is also known to form bonds with chlorine. The C_6F_5XeCl and $[(F_5C_6Xe)_2Cl][AsF_6]$ are known (Frohn, Schroer, & Henkel, 1999), and the Xe−Cl bond is also found in the $[XeCl]^+$ cation in $[XeCl][Sb_2F_{11}]$ (Seidel & Seppelt, 2001).

XeF_2 has also been extensively used as a ligand. Apart of typical adducts, such as $FXeF{-}RuF_5$ (i.e., $[XeF][RuF_6]$) and $XeF_2{\cdot}MOF_4$ (M = Cr, Mo, W), XeF_2 can also be coordinated to "naked" metal cations. The first such compound, $[Ag(XeF_2)_2][AsF_6]$, was

obtained serendipitously during the oxidation of xenon in aHF with solvated Ag^{2+} cations (Hagiwara, Hollander, Maines, & Bartlett, 1991). Since then, numerous such compounds have been synthesized and crystallographically characterized. The metal cation can carry formal charges of 1+, 2+, and 3+, and the number of coordinated XeF_2 molecules varies depending on the metal (Tavčar & Tramšek, 2015). Both heteroleptic and homoleptic (Figure 1.8) coordination spheres around the cations have been observed (Tramšek, Benkič, & Žemva, 2004; Tavčar, Goreshnik, & Mazej, 2006), and XeF_2 can also act as a bridging ligand between two metal centers (Matsumoto, Hagiwara, Ito, & Tamada, 2002).

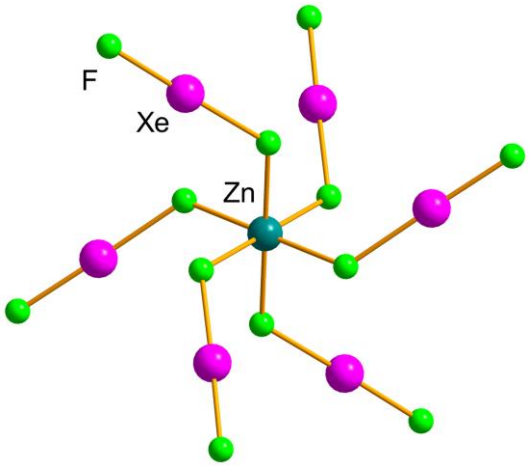


Figure 1.8: Structure of the $[Zn(XeF_2)_6]^{2+}$ cation (Tavčar, Goreshnik, & Mazej, 2006).

XeF_2 has also been observed to act as a hydrogen-bond acceptor in hydrogen-bonded (salt) cocrystals with $H_3O[AsF_6]$ (Gerken, et al., 2009), HNO_3 (Moran, Brock, Mercier, & Schrobilgen, 2010), protonated trifluoroacetamide, $[CF_3C(OH)NH_2]^+$ (Schrobilgen & Whalen, 1994) and in the crystal structures of $[Cd(FH)_2XeF_2][MF_6]_2$ (M = Ta, Nb) (Lozinšek, 2013; Tavčar & Tramšek, 2015). XeF_2 has also been found to coordinate halogen cations, such as $[BrOF_2]^+$ (Brock, Casalis de Pury, Mercier, Schrobilgen, & Silvi, 2010), $[BrO_2]^+$ (Bortolus, LaChapelle, Mercier, Haner, & Schrobilgen, 2023), and $[ClO_2]^+$ (Bortolus, Ellwanger, Haner, & Schrobilgen, 2021).

Unlike XeF_4 and XeF_6, XeF_2 is not a fluoride-ion acceptor, and all attempts to generate the $[XeF_3]^-$ anion have been unsuccessful (Vasdev, et al., 2010).

1.2.2.4 Xenon in the +4 oxidation state

XeF_4, like XeF_2, is a molecular compound. It adopts square planar geometry (Figure 1.9, a) with Xe—F bond distances of 1.9449(6) and 1.9509(6) Å (Bortolus, Mercier, Nguyen, & Schrobilgen, 2021). The higher oxidation state of xenon in XeF_4 makes it a much more powerful oxidizing and fluorinating agent than XeF_2. It reacts readily with water forming yellow XeO_2 and $XeOF_2$ and, subsequently, shock-sensitive XeO_3. XeF_4 forms cocrystal with XeF_2, $XeF_2{\cdot}XeF_4$, either by co-sublimation of starting reagents (Burns, Ellison, & Levy, 1965) or via solid-state synthesis at 90 °C (Adams, 1974; Ogrin, Bohinc, & Slivnik, 1973). This cocrystal also makes separation of XeF_2 and XeF_4 difficult when XeF_4 is obtained thermally (Žemva, 1988). Highly pure XeF_4 can be prepared by UV-irradiation of F_2/XeF_2 mixture in aHF (Tavčar & Žemva, 2009).

XeF_4 acts as a fluoride-ion donor with metal pentafluorides, yielding $[XeF_3][MF_6]$ or $[XeF_3][M_2F_{11}]$ tight-ion pairs (Haner & Schrobilgen, 2015). However, it is the weakest fluoride-ion donor in the series of xenon fluorides ($XeF_6 > XeF_2 >> XeF_4$). The $[XeF_3]^+$

cation exhibits AX_3E_2 geometry (Figure 1.9, b), as predicted by the VSEPR model of molecular geometry (Gillespie & Hargittai, 2012).

XeF_4 can also coordinate metal cations, although this is rare; examples include $[Mg(XeF_4)(XeF_2)][AsF_6]_2$ (Tavčar & Žemva, 2009) (Figure 1.9, c) and $XeF_4{\cdot}WOF_4$ (Bortolus, Mercier, & Schrobilgen, 2022). Additionally, XeF_4 has been observed as a cocrystallized molecule in some noble-gas compounds, arising either from the partial decomposition of xenon(VI) compounds or from the oxidation of XeF_2 with KrF_2. Notable examples include $[XeF_5][CrF_6]{\cdot}XeF_4$ (Lutar, Leban, Ogrin, & Žemva, 1992) and $[Xe_2F_3][SbF_6]{\cdot}XeF_4$ (Bortolus, Mercier, Nguyen, & Schrobilgen, 2021).

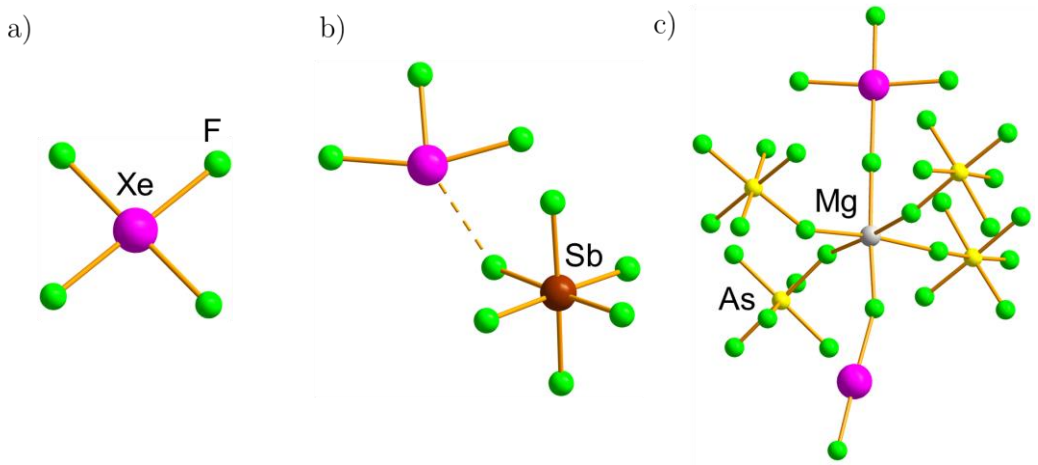


Figure 1.9: Structure of a) XeF_4 (Bortolus, Mercier, Nguyen, & Schrobilgen, 2021); b) $[XeF_3][SbF_6]$ (Brock, Mercier, & Schrobilgen, 2013) and c) $[Mg(XeF_4)(XeF_2)][AsF_6]_2$ (Tavčar & Žemva, 2009).

Unlike XeF_2, XeF_4 can act as a fluoride-ion acceptor, forming the $[XeF_5]^-$ anion, which represents a rare example of AX_5E_2 geometry predicted by VSEPR theory (Gillespie & Hargittai, 2012) (Figure 1.10, a). This anion can be isolated either by reacting XeF_4 with alkali-metal fluorides at elevated temperatures or by reacting XeF_4 with tetramethylammonium fluoride in acetonitrile (Christe, et al., 1991). Previous claims of a $[XeF_6]^{2-}$ anion (Spitzin, Kiselev, Fadeeva, Popov, & Tchumaevsky, 1988) were later shown to correspond to $[XeF_5]^-$ (Christe, et al., 1991).

The only isolable oxide of xenon(IV) is XeO_2, a transient intermediate formed during the reaction of XeF_4 with water at 0 °C. XeO_2 is a yellow, amorphous solid that is presumed to be polymeric (Brock & Schrobilgen, 2011). When XeF_4 reacts with water at lower temperatures, $XeOF_2$ is produced instead (Gillespie & Schrobilgen, 1977), whereas in the superacidic medium, oxyfluoroxenon(IV) cations are formed (Brock, Mercier, & Schrobilgen, 2013). Owing to the presence of a σ-hole on the xenon atom, $XeOF_2$ can interact with Lewis bases such as acetonitrile to form $XeOF_2{\cdot}NCCH_3$ adduct (Figure 1.10, b), which represents a rare example of a Xe^{IV}—N bond (Brock, Bilir, Mercier, & Schrobilgen, 2007).

The chemistry of organoxenon(IV) compounds has also been investigated. The salt $[C_6F_5XeF_2][BF_4]$ has been isolated (Frohn, LeBlond, Lutar, & Žemva, 2000), along with its acetonitrile adduct-cation (Koppe, Haner, Mercier, Frohn, & Schrobilgen, 2014) (Figure 1.10, c) The $[C_6F_5XeF_2][BF_4]$ salt is significantly less stable than its xenon(II) counterpart.

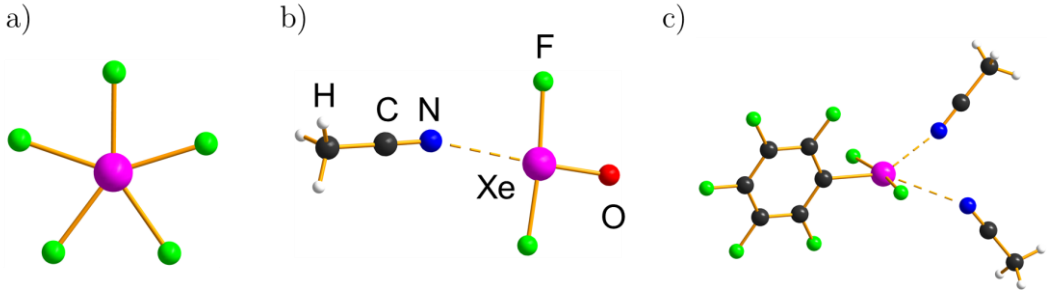


Figure 1.10: Structure of a) $[XeF_5]^-$ anion (Christe, et al., 1991); b) $XeOF_2{\cdot}NCCH_3$ (Brock, Bilir, Mercier, & Schrobilgen, 2007) and c) $[C_6F_5XeF_2]^+$ cation (Koppe, Haner, Mercier, Frohn, & Schrobilgen, 2014) coordinated with two acetonitrile molecules.

1.2.2.5 Xenon in the +6 oxidation state

Xenon hexafluoride, XeF_6, is the last binary fluoride of xenon to be synthesized. It was independently prepared in several laboratories (Malm, Sheft, & Chernick, 1963; Eugene Weaver, Weinstock, & Knop, 1963), including the laboratory from Jožef Stefan Institute, by reacting xenon gas with an excess of fluorine at elevated temperature (Slivnik, et al., 1962; Slivnik, Šmalc, Žemva, & Mosevič, 1968). XeF_6 represents the highest oxidation state of xenon in an exclusively fluorine environment. In all polymorphs, XeF_6 is found as tetrameric or hexameric cluster consisting of $[XeF_5]^+$ cations bridged by fluoride anion (Hoyer, Emmler, & Seppelt, 2006) (Figure 1.11, a). "Molecular" XeF_6 has been observed in $XeF_6{\cdot}n NCCH_3$ (n = 1,2), in which the XeF_6 molecule adopts a geometry close to C_{3v} (Matsumoto, Haner, Mercier, & Schrobilgen, 2015), and such geometry is also retained under matrix conditions (Gawrilow, Beckers, Riedel, & Cheng, 2018).

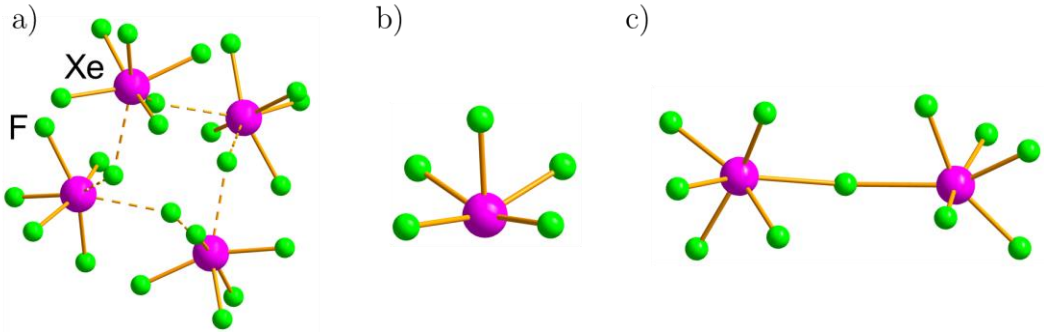


Figure 1.11: Crystal structure of a) $(XeF_6)_4$ tetramer (contacts to bridging fluoride anions are denoted as orange dashed lines) (Hoyer, Emmler, & Seppelt, 2006); b) $[XeF_5]^+$ cation (Goettel, Bortolus, Stuart, Mercier, & Schrobilgen, 2019) and c) $[Xe_2F_{11}]^+$ cation (Goettel, Bortolus, Stuart, Mercier, & Schrobilgen, 2019).

XeF_6 is the strongest fluoride-ion donor among the binary noble-gas fluorides. It reacts readily with metal or pnictogen Lewis-acidic fluorides and metal (oxy)tetrafluorides, forming $[XeF_5]^+$ and $[Xe_2F_{11}]^+$ cations (Figure 1.11, b, c), depending on the molar ratio (Žemva, 1988; Bortolus, Mercier, & Schrobilgen, 2020; Bortolus, Mercier, & Schrobilgen, 2024). The $[XeF_5]^+$ cation possesses a stereochemically active electron pair, that pushes the fluoride atoms out of the equatorial plane, resulting in a distorted square pyramidal geometry. It also features a σ-hole, which can be coordinated by XeF_2 (Žemva, et al., 1987), KrF_2, or HF (Lozinšek, Mercier, & Schrobilgen, 2021). $[XeF_5]^+$ and $[Xe_2F_{11}]^+$ salts can also

be prepared by the reaction of XeF_2, F_2 and corresponding metal tetrafluoride or pentafluoride in aHF under UV irradiation (Mazej, et al., 2017; Mazej & Goreshnik, 2023).

XeF_6 can also act as a fluoride-ion acceptor. When reacted with fluoride-ion donors such as RbF, CsF, NOF or NO_2F, the compounds containing $[XeF_7]^-$, $[Xe_2F_{13}]^-$ (Ellern, Mahjoub, & Seppelt, 1996) as well as $[XeF_8]^{2-}$ (Peterson, Holloway, Coyle, & Williams, 1971; Adam, Ellern, & Seppelt, 1996) anions can be isolated (Figure 1.12). Among these, the most stable is the $[XeF_8]^{2-}$ anion, which adopts a square-antiprismatic geometry. The $[XeF_7]^-$ anion adopts capped octahedral geometry, and can further act as a Lewis base toward another XeF_6 molecule, forming the $[Xe_2F_{13}]^-$ anion (Ellern, Mahjoub, & Seppelt, 1996). The XeF_6 moiety in the $[Xe_2F_{13}]^-$ anion exhibits a geometry close to C_{3v}.

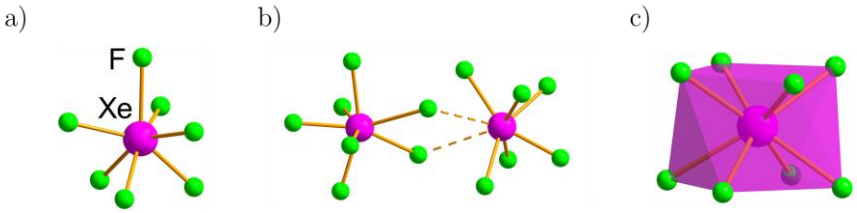


Figure 1.12: Molecular geometries of a) $[XeF_7]^-$, b) $[Xe_2F_{13}]^-$ (Ellern, Mahjoub, & Seppelt, 1996) and c) $[XeF_8]^{2-}$ anions (Adam, Ellern, & Seppelt, 1996). In c), shaded polyhedron faces outline square antiprism.

Xenon in the oxidation state +6 readily forms bonds with oxygen atom. The most well-known example is xenon(VI) oxide, XeO_3, which crystallizes as a white solid (Smith, 1963) and the molecule features trigonal pyramidal geometry. It is highly sensitive and decomposes violently even upon the slightest contact (Bartlett & Rao, 1963). It has been characterized in three different polymorphs (Goettel & Schrobilgen, 2016). The xenon atom features three σ-holes, which have been exploited in the formation of XeO_3 adducts with nitrogen bases (Goettel, Matsumoto, Mercier, & Schrobilgen, 2016) (Figure 1.13, a), oxygen bases (Marczenko, Mercier, & Schrobilgen, 2018; Marczenko, Mercier, Goettel, & Schrobilgen, 2025) (Figure 1.13, b), and halides (Hodgson & Ibers, 1969; Jaselskis, Huston, & Spittler, 1969; LaBonville, Ferraro, & Spittler, 1971; Willet, Peterson, & Coyle, 1977; Goettel, Haensch, & Schrobilgen, 2017)

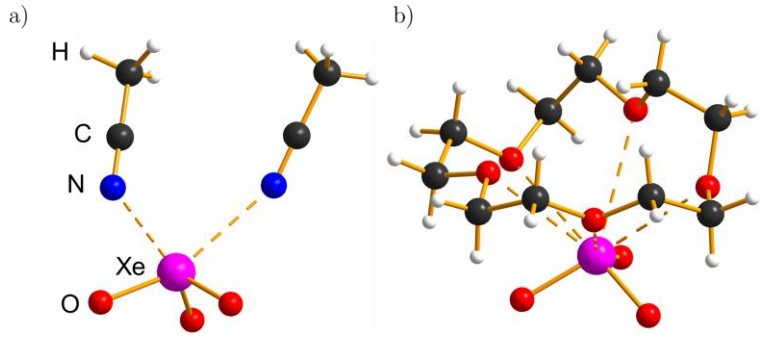


Figure 1.13: Crystal structure of a) Propionitrile adduct with XeO_3 (Goettel, Matsumoto, Mercier, & Schrobilgen, 2016) b) Crown-ether complex with XeO_3 (Marczenko, Mercier, & Schrobilgen, 2018).

Xenon(VI) oxyfluorides, $XeOF_4$ and XeO_2F_2, are also known. The crystal structure of $XeOF_4$ is unknown, although it has been observed as a cocrystallized molecule in crystal structures (Pointner, Suontamo, & Schrobilgen, 2006; Hughes, Brock, Mercier, &

Schrobilgen, 2011). $XeOF_4$ adopts square-pyramidal AX_5E geometry (Figure 1.14, a), in accordance with VSEPR theory (Gillespie & Hargittai, 2012). It is a liquid at room temperature and vigorously reacts with moisture forming XeO_3 and HF. The $[XeOF_3]^+$ cation (Figure 1.14, b), obtained by reacting $XeOF_4$ with strong Lewis acid such as SbF_5 (Mercier, Sanders, Schrobilgen, & Tsai, 1993), exhibits a seesaw geometry. $XeOF_4$ can also act as a fluoride-ion acceptor, forming $[XeOF_5]^-$ anion (Gillespie & Schrobilgen, 1977; Ellern & Seppelt, 1995). Reaction of CsF with $XeOF_4$ yields unique $[F(XeOF_4)_3]^-$ anion (Holloway, et al., 1985). Finally, $XeOF_4$ can interact with other Lewis bases, such as XeF_2 and KrF_2, forming $NgF_2{\cdot}XeOF_4$ cocrystals (Ng = Kr, Xe) (Bartlett & Wechsberg, 1971; Hughes, 2010; Hughes, Brock, Mercier, & Schrobilgen, 2011), or with acetonitrile (Gerken & Schrobilgen, 2000; Gawrilow, Beckers, Riedel, & Cheng, 2018).

XeO_2F_2, which can be synthesized from XeF_6 and XeO_3 (Huston, 1967) has been characterized by neutron diffraction and it features seesaw geometry (Peterson, Willett, & Huston, 1973). When reacted with AsF_5 or SbF_5, it forms the $[XeO_2F]^+$ (Figure 1.14, c) or $[O_2FXeFXeFO_2]^+$ cation (Pointner, Suontamo, & Schrobilgen, 2006), whereas the reaction with a fluoride-ion source results in the formation of $[XeO_2F_3]^-$ anion (Gillespie & Schrobilgen, 1977; Christe & Wilson, 1988). XeO_2F_2 can coordinate acetonitrile in solution (Gerken & Schrobilgen, 2000) and also forms a cocrystal with XeF_2 (Goettel, 2017).

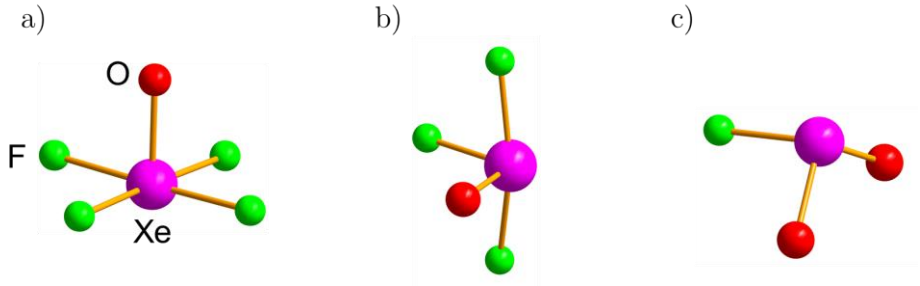


Figure 1.14: Structures of a) $XeOF_4$ molecule; b) $[XeOF_3]^+$ cation in $[XeOF_3][SbF_6]$ (Mercier, Sanders, Schrobilgen, & Tsai, 1993); c) $[XeO_2F]^+$ cation in $[XeO_2F][SbF_6]$ (Pointner, Suontamo, & Schrobilgen, 2006).

1.2.2.6 Xenon in the +8 oxidation state

All attempts to synthesize xenon(VIII) fluoride, XeF_8, have been unsuccessful. However, the neutral oxide, XeO_4, is known (Selig, Claassen, Chernick, Malm, & Huston, 1964) and it exhibits a tetrahedral geometry, as confirmed by crystal structure analysis (Goettel, 2017). XeO_4 is highly unstable, decomposing rapidly above −20 °C with detonation. The chemistry of xenon(VIII) is mainly explored in perxenates, $[XeO_6]^{4-}$, with sodium (Hamilton, Ibers, & Mackenzie, 1963; Forgeron, Wasylishen, Gerken, & Schrobilgen, 2007), potassium (Zalkin, Forrester, Templeton, Williamson, & Koch, 1964; Britvin, Kashtanov, Krivovichev, & Chukanov, 2016), calcium, strontium, barium (Britvin, et al., 2015), and even americium (Marcus & Cohen, 1966) serving as cations.

Other two xenon(VIII) oxide fluorides have also been observed, XeO_3F_2 and XeO_2F_4. Both were prepared in small concentrations, by reaction of XeO_4 or Na_4XeO_6 with XeF_6. They have been characterized by mass spectrometry and, under matrix condition, with infrared and Raman spectroscopy (Huston, 1968; Claassen & Huston, 1971; Huston, 1971). They have also been characterized in solution by low-temperature NMR spectroscopy (Gerken, 2000)

1.3 Mechanochemistry

IUPAC defines a mechanochemical reaction as "a chemical reaction that is induced by the direct absorption of mechanical energy" (Horie, et al., 2004). More broadly, mechanochemistry refers to the induction of chemical changes by mechanical means such as comminution, shear, or strain (Baláž, et al., 2013). Its origins can be traced back to ancient times, while systematic investigation began in the late 19th century. However, mechanochemistry gained its current status as an alternative, environmentally friendly synthetic methodology only at the end of the 20th and the beginning of the 21st century (Takacs, 2013).

The simplicity of the mechanochemical synthesis lies in the fact that it does not require soluble precursors, unlike typical solution-based methods, nor does it necessitate high-temperature conditions. Moreover, because there is no dilution of reactants as in solution, reactions generally proceed faster. In the absence of solvent, reaction pathways can differ, allowing products that are unstable in solution to sometimes be isolated in bulk via mechanochemical route (Friščić, Mottillo, & Titi, 2020).

Central to mechanochemistry is the grinding of the reactants in the mixture. This process produces smaller particles, thereby increasing the surface area and enhancing reactivity (Boldyrev, 2006). To achieve homogeneous grinding, the reactants are typically processed in a mechanochemical vessel using grinding balls. Typically, milling is performed in vibrational and planetary mills (Colacino, et al., 2018), but other methods for inducing mechanochemical changes are also known, such as acoustic-resonant mixing (RAM) (Osorio & Muzzio, 2015) and extrusion (Crawford & Casaban, 2016).

Apart from the milling device, several other important parameters influence the outcome of mechanochemical synthesis. These include the vessel and ball materials, which can be either hard (tungsten carbide, stainless-steel, ZrO_2) or soft (PTFE), as well as the size, mass and the number of balls in the mechanochemical vessel, and the size of the vessel itself (Mateti, et al., 2024). Changes in other parameters, such as temperature, gas pressure, or light source, can also alter the reaction landscape (Martinez, Stolar, Karadeniz, Brekalo, & Užarević, 2022).

Mechanochemistry has been successfully applied in inorganic, metallo-organic, organometallic, and organic synthesis, in particular for the preparation of air-sensitive compounds (Reynes, Leon, & Garcia, 2024). To date, however, no examples of mechanochemical synthesis involving noble-gas compounds have been reported (Tan & García, 2019). However, mechanochemistry has been applied extensively in fluorine chemistry (Scholz, 2021). Notably, it has enabled access to otherwise inaccessible fluoride glasses (Ruprecht, Wilkening, Feldhoff, Steuernagel, & Heitjans, 2009; Preishuber-Pflügl & Wilkening, 2016) and to mixed-valent Ag^{I}–Ag^{II} fluorides (Belak Vivod, et al., 2024). Grinding elemental sodium with PTFE has been shown to yield sodium fluoride (alongside carbon), which can subsequently be used in organic fluorination reactions, offering a promising route for recycling otherwise "forever" chemicals (Lowe, et al., 2025). Additional mechanochemical methods for recycling fluoropolymers are also available (Hattori, Saha, Bacho, & Shibata, 2025; Yang, et al., 2025). Mechanochemical activation of CaF_2 with phosphate has also been demonstrated as an effective route for organofluorine synthesis (Patel, et al., 2023).

1.4 High Pressure Chemistry

Pressure, alongside the temperature, is a fundamental thermodynamic variable. The free-energy change corresponding to the pressure of 100 GPa (10^6 bar) is in the range of 10 eV

(965 kJ mol^{-1}), which is in the range of strongest chemical bonds (Hemley, 2000). Under such high-pressure conditions, a variety of unusual and fascinating phenomena can occur (Grochala, Hoffmann, Feng, & Ashcroft, 2007; Miao, Sun, Zurek, & Lin, 2020). For example, chlorine, which is a typical example of non-metal, becomes metallic at 200 GPa (Dalladay-Simpsons, et al., 2019). Hydrogen sulfide becomes conventional superconductor at 100 GPa (Drozdov, Eremets, Troyan, Ksenofontov, & Shylin, 2015). Sodium metal forms electride at 100 GPa, enabled by inclusion of helium atoms in the structure (Dong, et al., 2017). Even one of the most inert elements, nitrogen, polymerizes at high pressure (Eremets, Gavriliuk, Trojan, Dzivenko, & Boehler, 2004; Eremets, et al., 2004). Oxygen forms O_8 units already below 20 GPa (Lundegaard, Weck, McMahon, Desgreniers, & Loubeyre, 2006).

In order to further facilitate reactivity under high pressure, laser heating can be performed, with which the temperatures above 1000 K can be reached (Boehler, 2000; Anzellini & Boccato, 2020). In this way, numerous nitrides (Wang, et al., 2022), nitridocarbonates such as $[CN_3]^{5-}$ (Brüning, et al., 2023), carbonates (Kovalev, et al., 2025), (per)oxides (Flosbach, et al., 2025; Lavina, et al., 2011) and even novel compositions in sodium–chlorine system (Zhang, et al., 2013) can be synthesized at high pressure.

To reach such extreme pressures and to study materials under these conditions, a diamond anvil cell (DAC) is used.

1.4.1 Diamond anvil cell

The schematic view of the diamond anvil cell is shown in Figure 1.15. The main part of the cell (the body) is constructed from two metal parts, made usually from stainless steel or copper-beryllium alloy (for magnetic measurements). Each of these two metal parts has one diamond anvil, which is placed on a backing plate, typically made of tungsten carbide.

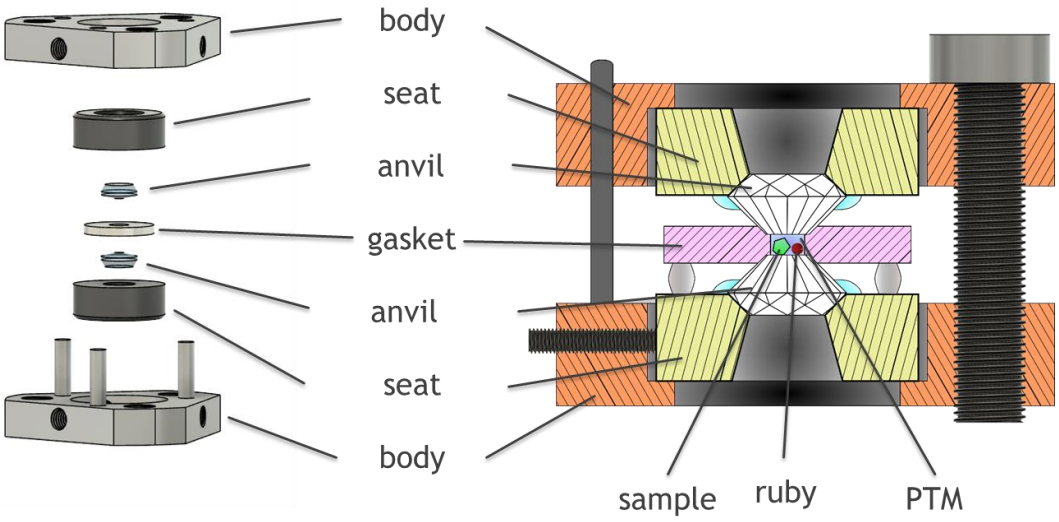


Figure 1.15: Schematic view of diamond anvil cell (courtesy of dr. Miha Virant).

Diamond is particularly useful material for generating high pressure. This is due to its hardness. Moreover, diamond is transparent, which enables inspection of changes within the sample chamber. As diamond is carbon, an element with low atomic number, it is essentially transparent for X-rays, and is therefore suitable for diffraction experiments (Katrusiak, 2019). Many designs of diamond anvils can be used for reaching high pressure, and the culet (part of the diamond anvil pressing on the gasket and sample chamber)

diameter is directly proportional to the maximum pressure which can be reached (O'Bannon III, Jenei, Cynn, Lipp, & Jeffries, 2018).

Between two diamond anvils the gasket is inserted. The gasket is usually made of a thin metal plate made of stainless-steel, rhenium, Inconel etc. Apart of providing sample chamber, the gasket also provides additional stabilization of the cell. The gasket hole is placed in the center of the diamond culet. The gasket hole is prepared by first indenting the thin metal foil with the diamond anvils to desired thickness, and then the hole is drilled in the indented part. Increasing the pressure should result in reducing the diameter of the hole. If the gasket hole starts expanding, the cells is considered to be unstable and further increase of pressure might result in the breakage of the diamond anvils.

1.4.2 Hydrostaticity

The body is under hydrostatic compression when the pressure on all sides of the body is equal and the fluid is at rest. When different pressures are felt by the body, then the body is under non-hydrostatic conditions, and shear or strain can start appearing. Such non-hydrostatic condition may inhibit or promote phase transitions (Takemura, 2021); however, in those situations, it is difficult to assess if the phase transition is only a consequence of pressure. In order to obtain hydrostatic conditions, a hydrostatic medium is usually placed with the sample in the gasket hole. The most common media are ethanol−methanol 4/1 mixture, isopentane-pentane 1/1 mixture, but also solidified gases such as nitrogen and helium (Klotz, Chervin, Munsch, & Le Marchand, 2009). The hydrostatic conditions are considered to be present when the pressure gradient throughout the cell is absent. The term “quasi-hydrostatic” is also sometimes used. This implies that the medium solidified, but the shear forces in such solid are small and pressure gradient is minimal, rendering the solid to behave as a hydrostatic media (Takemura, 2021).

The absence or presence of pressure gradient can easily be probed with the ruby fluorescence method (Piermarini, Block, & Barnett, 1973; Klotz, Chervin, Munsch, & Le Marchand, 2009). Four or more rubies are placed roughly evenly in the gasket hole and the pressure is slowly increased. When hydrostatic conditions are present, the standard pressure deviation versus pressure is constant and close to zero. When standard deviation starts increasing, this shows the presence of a pressure gradient which in turn indicates non-hydrostatic conditions. The pressure in the diamond anvil cell can also be probed by the first derivation of the Raman diamond band. This is especially convenient, as the diamond anvil is essential part of cell and pressure can be probed throughout the whole gasket hole (Eremets, et al., 2023; Akahama & Kawamura, 2010) It is typically used for pressures above 10 GPa. Finally, the pressure can also be determined by measuring unit-cell parameters of a pressure gauge; however, in this case, the equation-of-state of the gauge under same conditions must be known (Takemura, 2021).

1.4.3 Noble-gas chemistry under high pressure

The chemistry of noble gases under high pressure has been shown to be rich (Miao, 2020). Helium interacts with sodium at pressures above 110 GPa, by promoting the 8-centre-2-electron bonding in sodium electride (Dong, et al., 2017). Argon has also been found to react with nickel above 140 GPa and 3500 K, forming ArNi (Adeleke, et al., 2019). Nickel and iron have also been found to react with xenon above 100 GPa, forming XeM_3 (M = Ni, Fe), with the reaction between xenon and nickel occurring at lower temperatures (Dewaele, Pepin, Geneste, & Gabarino, 2017; Stavrou, et al., 2018). In both cases, laser heating ($T > 1000$ K) is required to form these phases.

Another class of solids based on noble gases, stabilized at high pressures, are the so-called van der Waals (vdW) solids, in which only vdW interactions are present (Ewing, 1975). Argon, krypton and xenon were found to form such solids with hydrogen. Whereas $Ar(H_2)_2$ forms only above 150 GPa (Loubeyre, Letoullec, & Pinceaux, 1994), $Kr(H_2)_4$ (Kleppe, Amboage, & Jephcoat, 2014) and $Xe(H_2)_x$ (x = 7, 8) (Somayazulu, et al., 2010) are formed already around 5 GPa. In both $Kr(H_2)_4$ and $Xe(H_2)_8$, short Ng—Ng distances are observed, but no Ng—H bonding has been confirmed by computational analyses. Interestingly, crystal structure predictions have found that the only stable stoichiometry in Xe–H_2 system is XeH_2 (Somayuzulu, Dera, Smith, & Hemley, 2015), which has not been observed experimentally.

Analogous to xenon-hydrogen mixtures, nitrogen has been found to interact with xenon already at 5 GPa, forming $Xe(N_2)_2$, in which xenon atoms form diamond-like structure with four rotationally disordered nitrogen molecules (Howie, et al., 2016; Niwa, Matsuzaki, & Hasegawa, 2017; Laniel, Weck, & Loubeyre, 2016). This phase undergoes polymorphic transition at 14 GPa, but no indication of bonding is observed even above 100 GPa. Interestingly, crystal structure predictions indicate that above 150 GPa, XeN_6 can be formed, in which hexamer rings of single-bonded nitrogen are predicted to exist (Peng, Wang, Wang, Zhang, & Ma, 2015).

1.4.3.1 Xenon oxides under high pressure

Xenon does not react with oxygen under ambient conditions, although hydrolysis of xenon fluorides leads to xenon oxyfluorides or xenon oxides (see Chapters 1.2.2.3–1.2.2.6). Below 10 GPa, xenon forms a vdW solid with oxygen, $Xe(O_2)_2$, in which no bonding is observed (Weck, Dewaele, & Loubeyre, 2010). Increasing the pressure above 80 GPa, together with laser heating, yields two new xenon oxides, Xe_3O_2 and Xe_2O_5 (Dewaele, et al., 2016). Xe_3O_2 features xenon in oxidation state +4 and 0, with xenon(IV) centres adopting a square-planar geometry. $(Xe^{IV}O_4)_n$ squares combine in infinite layers, with xenon(0) atoms intercalated between them. Xe_2O_5 represent another mixed-valent xenon oxide, containing both Xe^{IV} and Xe^{VI}, with each xenon atom adopting the geometry typical for its oxidation state: xenon(IV) centers adopt square-planar, whereas xenon(VI) centers adopt square-pyramidal geometry, similar to that of $[XeF_5]^+$ cation (see Chapter 1.2.2.5). Other Xe_xO_y stoichiometries have been predicted in addition to the known xenon oxides (XeO_2, XeO_3, XeO_4), including XeO, Xe_2O, and Xe_7O_2 (Hermann & Schwerdtfeger, 2014; Zhu, et al., 2013). XeO_3 has also been predicted to exhibit interesting structural chemistry under high pressure (Hou, Wang, Botana, & Miao, 2017).

Krypton oxides have been investigated only theoretically (Zaelski-Ejgierd & Lata, 2016) It was predicted that at pressures above 200 GPa, KrO is formed; this is the only predicted krypton oxide exhibiting Kr—O bonding, featuring a *zig-zag* polymeric chain.

1.4.3.2 Xenon interaction with halogens

Xenon interacts with chlorine at pressures as low as 5 GPa and temperatures of 800 K, forming a pink solid that can be indexed to a tetragonal cell similar to XeF_2 (Somayuzulu, Gramsch, Mao, & Hemley, 2007). The new bands in the Raman spectrum can be assigned to Xe—Cl vibrations. However, the true nature of the compound is still unknown. Computational studies (Zarifi, Liu, Tse, & Zurek, 2018), however, suggest that only vdW solids are formed, consisting of layers of xenon and chlorine atoms. The $XeCl_4$ has been predicted to form above 100 GPa, although it is also predicted to be a vdW solid. Xenon dibromide is predicted to adopt a polymeric structure similar to $MoSi_2$, with xenon coordinated to eight bromine atoms (Grochala, 2007). Xenon has also been observed to interact with iodine at 20 GPa, as indicated by Raman spectroscopy (Somayuzulu,

Gramsch, Mao, & Hemley, 2007), but no structure solutions or cell indexing have been reported.

Of all known noble-gas compounds, only XeF_2 has been investigated experimentally. Early studies reported that the XeF_2 undergoes continuous compression up to 50 GPa, as indicated by the reduction of the c/a ratio in its tetragonal crystal structure (Schwarz & Syassen, 1992). In 2010, PXRD measurements suggested several phase transitions up to 50 GPa, with XeF_2 becoming metallic above 70 GPa (Kim, Debessai, & Yoo, 2010). Subsequent work, however, showed that XeF_2 undergoes only two polymorphic transitions (Wu, et al., 2017), and no metallic phase was detected up to 86 GPa, which was also shown from computational studies (Kurzydłowski, Zaleski-Ejgierd, Grochala, & Hoffmann, 2011). The most recent experimental study confirms this conclusion, showing that above 80 GPa, with laser heating, two novel stoichiometries are formed: Xe_2F and XeF_4 (Liu, et al., 2024). These were also predicted to be stable at high pressures (Peng, Botana, Wang, Ma, & Miao, 2016).

XeF_2 has also been found to be fluorinating agent at high pressure, The reaction of rhenium or tungsten gaskets with XeF_2 at 100 °C in the presence of pressure-transmitting medium (nitrogen or oxygen) has led to the formation of ReF_6 and WF_6 as indicated by Raman spectroscopy (Guan, et al., 2024).

KrF_4 has been predicted to form above 15 GPa (Kurzydlowski, Soltysiak, Džoleva, & Zaleski-Ejgierd, 2017), whereas above 80 GPa, Kr_4F and Kr_6F should exist. Above 180 GPa, KrF_2 should disproportionate to KrF and KrF_4. Krypton hexafluoride, however, is not predicted to be stable even up to 200 GPa.

Argon fluorides have also been investigated computationally, with ArF_2 and ArF_4 (predicted as $ArF_2{\cdot}F_2$) stable only above 50 and 100 GPa, respectively (Kurzydlowski & Zaleski-Ejgierd, 2015).

Chapter 2

Aims and Hypotheses

The aims of this dissertation are to: i) expand the range of synthetic methods in noble-gas chemistry by introducing mechanochemistry; ii) advance the chemistry of compounds featuring Xe−N bonds; iii) study of hydrogen-bonding propensity of XeF_2; iv) investigate novel hydrostatic media for single-crystal X-ray diffraction of noble-gas compounds up to 10 GPa, and v) explore the behavior of xenon fluorides under high pressure.

In Chapter 4.1, the mechanochemical synthesis of compounds containing xenon in oxidation state +2 (Section 4.1.1), +1/2 (Section 4.1.2), and in +4 (Section 4.1.2) is presented. These findings open new possibilities for the synthesis of noble-gas compounds and broaden access to the field for laboratories without access to vacuum-line techniques. To assess whether mechanochemically prepared compounds can be studied using 3D electron diffraction (3D ED), the structures of $XeF_2{\cdot}XeF_4$, XeF_2 and XeF_4 were determined by 3D ED. The results from 3D ED are summarized in Section 4.1.4 and have been published.

In Chapter 4.2, the crystallographic characterization of the first example of a single ditopic nitrogen base coordinating two $[XeF]^+$ cations is presented, along with the first example of a C=N−Xe bonding modality. Novel compounds featuring an N−Xe−N linkage have also been synthesized and crystallographically characterized. All of these results significantly expand the chemistry of compounds featuring xenon-nitrogen bonds and are presented as a single publication.

In Chapter 4.3, the crystallographic investigation of xenon difluoride as a hydrogen-bond acceptor toward protonated perfluoroamides is presented. These compounds provide rare examples of hydrogen-bonded cocrystals where XeF_2 acts as a hydrogen-bond acceptor. This study also reports three new crystal structures of protonated amides and two hemiprotonated amide salts, showing diverse hydrogen-bonding motifs. The results of this investigation have been reported in a single publication and indicate that the noble-gas compounds can be used as hydrogen-bond acceptors in crystal engineering.

In Chapter 4.4, the crystallographic characterization of the $(C_6F_5)_2COH^+[AsF_6]^-$ is presented, along with a $(C_6F_5)_2CO{\cdot}AsF_5$ adduct. The results of this investigation provide a rare example of a crystallographically characterized protonated aromatic ketone and a rare example of a ketone acting as a Lewis base toward AsF_5. The results have been published in a single publication.

In Chapter 4.5, selected perfluorinated liquids were investigated as potential hydrostatic media up to 10 GPa for strong oxidative fluorinators such are the noble-gas compounds. The results show that these liquids possess modest hydrostatic properties but may still be useful even above their strict hydrostatic limits. The findings of this investigation have been published in a single article.

In Chapter 4.6., spectroscopic and structural investigations of XeF_6 and $XeF_2{\cdot}XeF_4$ under high pressure are presented, in which the first example of a polymeric noble-gas fluoride is observed. These two studies represent rare examples of high-pressure investigations of xenon compounds in the +4 and +6 oxidation states.

Chapter 3

Materials and Methods

3.1 Materials

All safety regulations must be followed during all manipulations and isolations of the compounds described in this dissertation. Calcium gluconate and other first-aid materials were kept within reach at all times (Peters & Mietchen, 1996; Segal, 2000; Möbs & Kraus, 2025). Handling small quantities is strongly recommended. Residual material should be destroyed using a large amount of water, and a suspension of $Ca(OH)_2$, $CaCO_3$ and CaO in water can be used to remove fluoride, as the hydrolysis of HF in this suspension produces insoluble CaF_2 and CO_2 from $CaCO_3$.

All manipulations involving solid reagents were performed in an N_2-filled glovebox (Vigor SG1200/750E-SG1500/750E; $H_2O < 0.02$ ppm; $O_2 < 2$ ppm) whereas syntheses requiring volatile materials were carried out on a fluorine-resistant metal vacuum line (Figure 3.1) equipped with FEP (copolymer of tetrafluoroethylene and hexafluoropropylene) manifolds, a Monel Helicoid pressure gauges, a soda lime scrubber, liquid-nitrogen-cooled traps and a rotary-vane vacuum pump.



Figure 3.1: Vacuum line used for synthetic work presented in this thesis.

All vessels were made of FEP, whereas the valves were made of either polychlorotrifluoroethylene (PCTFE) with an aluminum casing or polytetrafluoroethylene (PTFE) encased in brass (Figure 3.2). All components were passivated with F_2 overnight (200–600 Torr) prior to use. Quartz capillaries were vacuum-dried at 650 °C for several hours and subsequently passivated with F_2 (200–300 Torr) overnight.

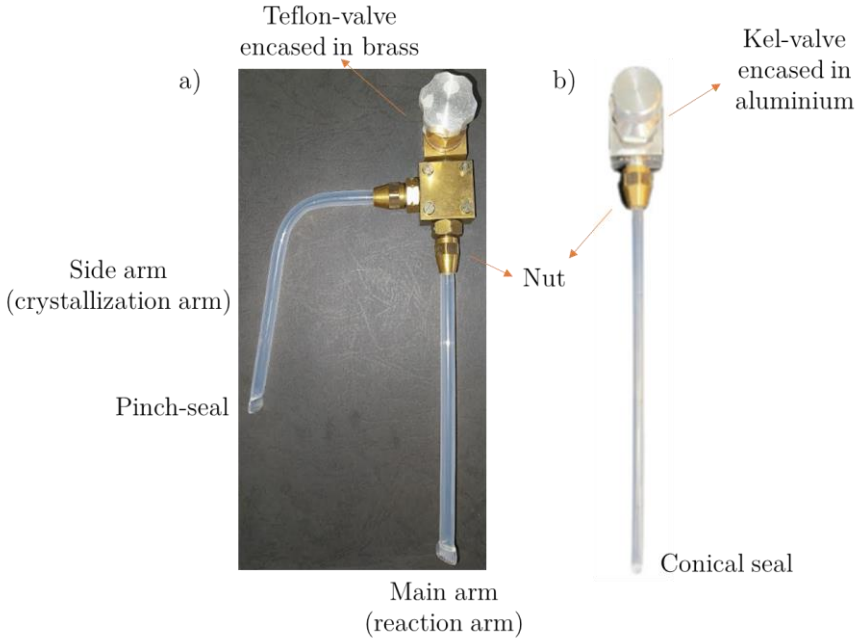


Figure 3.2: Different FEP vessels used. a) FEP vessel made out of the main and side arm (8 mm o.d.; 6 mm i.d.) equipped with PTFE valve encased in brass body; b) FEP vessel (6 mm o.d.; 4.7 mm i.d.) equipped with PCTFE -valve encased in aluminum body, typically used for low-temperature syntheses. o.d. is abbreviation for outer diameter, whereas i.d. is abbreviation for inner diameter.

Fluorine (Solvay Fluor, 98–99%) was used as supplied. Anhydrous HF (aHF; Linde, 99.995%) was first distilled into an F_2-passivated nickel vessel and then further distilled into a pre-passivated FEP vessel (o.d. 19 mm, i.d. 16 mm) containing $K_2[NiF_6]$ (Advance Research Chemicals, Inc, 99.9%). The resulting violet-blue solution (Figure 3.2), indicative of dissolved $[NiF_6]^{2-}$ anion, was thoroughly shaken for at least one day before use.



Figure 3.3: Anhydrous HF (aHF) with $K_2[NiF_6]$ in FEP vessel (o.d. 19 mm, i.d. 16 mm) equipped with PTFE valve encased in brass.

Xenon difluoride (XeF_2) was synthesized by UV irradiation of an Xe–F_2 mixture according to a literature procedure (Šmalc, Lutar, & Kinkead, 1992).

Xenon tetrafluoride (XeF_4) was prepared by UV-irradiation of an XeF_2–F_2 mixture in anhydrous HF (Tavčar & Žemva, 2009).

Xenon hexafluoride (XeF_6) was prepared by reacting xenon with fluorine at elevated temperatures in a nickel high-pressure vessel according to the literature (Slivnik, et al., 1962). $XeOF_4$ was detected as an impurity in XeF_6. Therefore, the XeF_6 required purification. This was accomplished by distilling a small amount of the mixture into an FEP vessel that was then connected to a U-trap made of FEP. The vessel was cooled to −20 °C, while the U-trap was cooled to −196 °C. After approximately one day under dynamic vacuum, the FEP vessel contained pure XeF_6, whereas the U-trap contained the XeF_6·$XeOF_4$·HF cocrystal, which had been previously characterized (Goettel, 2017).

Arsenic pentafluoride (AsF_5) was prepared by reacting As_2O_3 with F_2 at elevated temperatures in a nickel high-pressure vessel according to a literature procedure (Mazej & Žemva, 2003). Antimony trifluoride (SbF_3; Sigma-Aldrich, 99%) was used as received.

Tantalum pentafluoride (TaF_5) was either used as received (AlfaAesar, 99%) or purified. For xenon(II) chemistry, the small amount of water present in commercial TaF_5, likely in the form of an oxonium salt, did not cause any problems; however, for xenon(IV) chemistry, purified TaF_5 was required. Purification was performed by adding 2 bar of fluorine to commercial TaF_5 (~1 g) suspended in aHF in a T-shaped FEP vessel (Figure 3.2a). The mixture was stirred overnight. The F_2 was removed at −196 °C, and solution was slowly decanted into the side arm. This aHF was subsequently redistilled into the main arm, and the procedure was repeated several times. Finally, the aHF was removed at room temperature under dynamic vacuum. The absence of oxonium species in the main arm was confirmed by ATR-IR spectroscopy, as no bands around 3000 cm^{-1} were observed.

Acetonitrile (Honeywell, Riedel-de-Haën, chromatography grade, ≥99.9%) was purified using a Vigor solvent purification system and then stored over molecular sieves for at least one day before use.

Cyanogen (NCCN; Matheson) was used as supplied. Hydrogen cyanide (HCN) was prepared in reaction of dried KCN (Sigma-Aldrich, 97 %) with an excess of aHF for several minutes and co-distilled together with HF directly onto the reaction mixture. Drying of KCN was performed by placing it under dynamic vacuum for four days.

Sulfur(IV) dioxide, SO_2, was obtained from Ruše and was purified by storage over calcium hydride in a glass bulb.

Trifluoroacetamide (CF_3CONH_2; Fluorochem, 99.0%), pentafluoropropionamide ($C_2F_5CONH_2$; Apollo Scientific, 97%), heptafluorobutyramide ($C_3F_7CONH_2$; Fluorochem, 97.0%), and decafluorobenzophenone ($(C_6F_5)_2CO$; Thermo Scientific, 97 %) were used as received.

Table 3.1 contains all specifications regarding chemicals used in this dissertation.

Table 3.1: Used chemicals in this thesis and their stated purity or reference to their synthesis.

Chemical	**Producer**	**Declared purity / reference**
F_2	Solvay Fluor	98–99%
HF	Linde	99.995%
$K_2[NiF_6]$	Advance Research Chemicals, Inc.	99.9%
XeF_2	Synthesis according to literature	(Šmalc, Lutar, & Kinkead, 1992)
XeF_4	Synthesis according to literature	(Tavčar & Žemva, 2009)
XeF_6	Synthesis according to literature	(Slivnik, et al., 1962)
AsF_5	Synthesis according to literature	(Mazej & Žemva, 2003)
TaF_5	AlfaAesar	99%
CH_3CN	Honeywell, Riedel-de-Haën, chromatography grade	≥99.9%
NCCN	Matheson	not specified
KCN	Sigma-Aldrich	97 %
SO_2	Ruše	not specified
CF_3CONH_2	Fluorochem	99.0%
$C_2F_5CONH_2$	Apollo Scientific	97%
$C_3F_7CONH_2$	Fluorochem	97.0%
$(C_6F_5)_2CO$	Thermo Scientific	97 %

3.2 Methods

3.2.1 Synthesis

3.2.1.1 Mechanochemical syntheses

Mechanochemical reactions were performed in PTFE milling vessels (10 mL) with two PTFE balls (6.4 mm in diameter, 0.29 g) or in 5 mL PTFE milling vessels with a single PTFE ball (6.7 mm in diameter, 0.39 g; 7 mm in diameter, 0.56 g).

All PTFE equipment was dried in an oven at 120 °C for at least 6 hours before transfer into the glovebox. The antechamber containing milling equipment was evacuated for 45 minutes, and the milling vessels were allowed to cool for at least two hours prior to the reaction.

Milling was carried out either outside the glovebox using a Retsch MM 400 mixer mill at a frequency of 30 Hz or inside an N_2-filled glovebox using a Fritsch vibration mill (Mini-Mill PULVERISETTE 23) at 50 Hz. To prevent the milling vessels from opening due to vacuum in the antechamber during transfer, the two parts were secured with insulating tape. No modification to the milling vessels were performed for the Fritsch vibration mill.

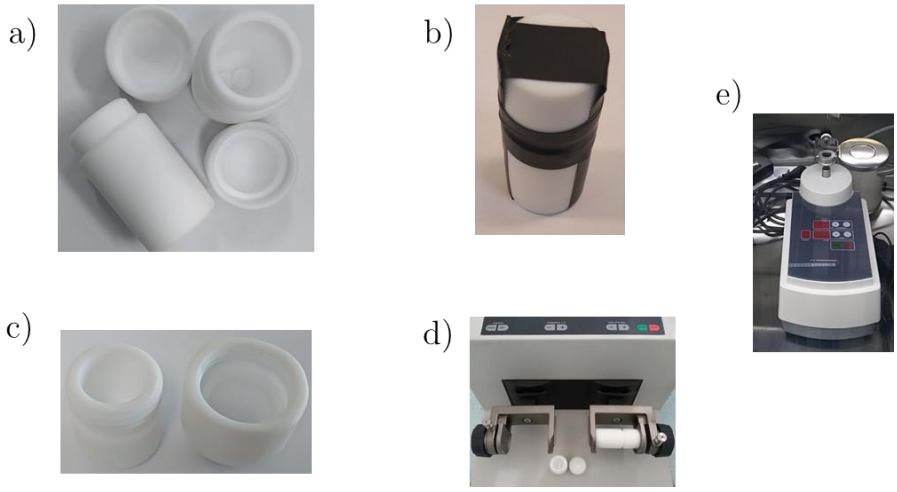


Figure 3.4: Mechanochemical equipment used for research work described in this thesis. a) PTFE milling vessels with the PTFE milling balls inside; b) An example of closed PTFE milling vessel for transfer in glovebox; c) Milling vessel used for the reaction performed on the Fritsch Pulverisette 23 mill; d) Retsch MM 400 mill; e) Fritsch Pulverisette 23 mill.

3.2.1.2 Syntheses in the solution

After attaching the FEP vessel to the vacuum line, the cross-section was evacuated for 30 minutes. When compounds containing xenon in oxidation state +4 or +6 were used, the cross-section was additionally passivated with 200–400 Torr of F_2 for approximately 30 minutes before condensing any solvent or reagent into the vessel.

The cross-section was then typically flushed twice with approximately 200 Torr of aHF. The vessels were then cooled to −196 °C and nitrogen inside the vessel was removed, after which the desired amount of aHF was condensed. Slow warming of the vessel resulted in thawing of the aHF. Other volatile reagents (e.g., SO_2, AsF_5, NCCN, CH_3CN) were condensed into the vessel in a similar manner.

Cooling baths used were either dry ice (solid CO_2, −78 °C) or ethanol cooled with liquid nitrogen (down to −118 °C). Vessels containing thermally unstable compounds were kept in dry ice and backfilled with >900 Torr of nitrogen (99.999 %) at −78 °C.

3.2.1.3 Solid-state reactions

A FEP reactor (8 mm o.d., 6 mm i.d.) was loaded with solid material inside a nitrogen-filled glovebox. The vessel was either connected to the vacuum line and evacuated under dynamic vacuum while immersed in liquid N_2, or it was sealed with nitrogen atmosphere. In both cases, the portion of the vessel containing the sample was kept in liquid nitrogen, while the upper part of the FEP was pinch-sealed using a heat gun at 650 °C and pliers. After warming to room temperature, the ampoule was placed in an oven and heated at various temperatures for different durations, depending on the experiment. The ampoule was then cooled and transferred back into the glovebox for further analysis.

3.2.2 High-pressure experiments

All high-pressure experiments were conducted using either Merrill–Bassett (Merrill & Bassett, 1974) or SSDAC-80 diamond anvil cells (Figure 3.5).

Merrill–Bassett or SS-DAC80 type cell bodies were paired with Boehler–Almax design type Ia or IIas diamond anvils with 300–700 µm diameter culets. Diamonds in Merrill–Bassett cell bodies were mounted on tungsten carbide seats (Almax easyLab) (Moggach, Allan, Parsons, & Warren, 2008), whereas in SS-DAC80 cell bodies on Vascomax. Inconel X750 plates (Goodfellow, Ni74/Cr15/Fe7/Ti/Al/Nb, annealed) with an initial thickness of 250 µm, were employed as gaskets and pre-indented to a thickness of 30–100 µm. Gasket holes with diameters of 100–250 µm were then drilled using a spark eroder (LOTO-eng SEC-400). Prior to use, the gaskets were cleaned in an ultrasonic bath containing ethanol.

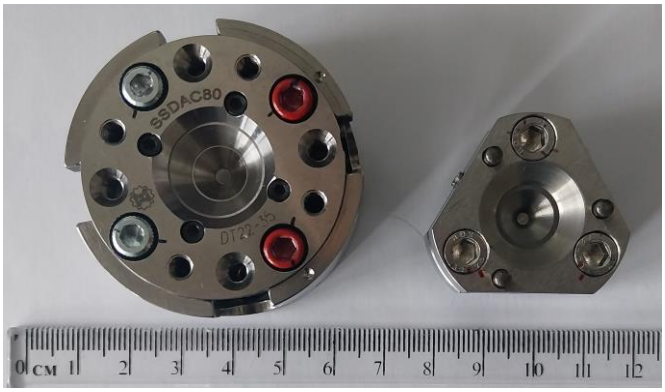


Figure 3.5: a) SSDAC-80 and b) Merrill-Bassett diamond anvil cell.

Pressure was determined by fitting the measured ruby fluorescence with Voigt profile using *CrimsonCalc* (Virant & Lozinšek, 2025). The most distinct feature of the spectrum of the ruby are the two sharp peaks, R_1 and R_2 (Forman, Piermarini, Barnett, & Block, 1972). Both peak positions move to higher wavenumbers with the increase of pressure (Piermarini, Block, & Barnett, 1973). In order to obtain the values from the ruby spectrum, such as peak position, full-width at half maximum (fwhm) and difference between peak position of R_1 and R_2, the peaks are fitted with Voigt or Pearson-VII function (Syassen, 2008) (Figure 3.6).

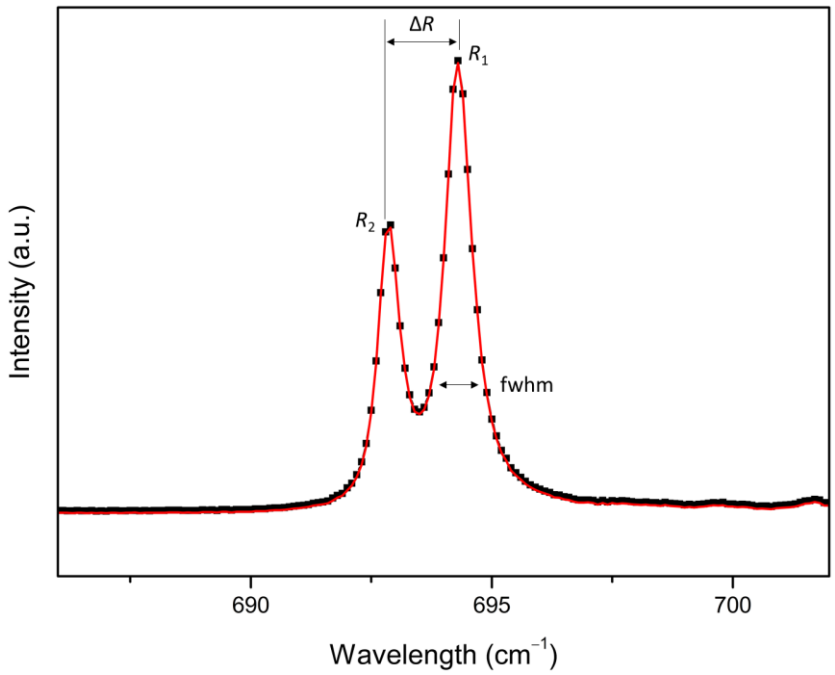


Figure 3.6: Fitted ruby fluorescence spectrum with important parameters obtained after fitting procedure. Black squares represent measured, whereas red lines represent fitted spectrum. Fitting was performed using *CrimsonCalc* software (Virant & Lozinšek, 2025).

The pressure determination by determining the minimum of the first derivation of the Raman diamond band (Figure 3.7) was performed in *OPUS* 8.7. software suite (Bruker, 2022). Diamond is quite convenient pressure gauge as it is an essential part of the cell (Eremets, et al., 2023; Akahama & Kawamura, 2010) and it covers the whole gasket hole; therefore, deviations in the pressure throughout the cell can be observed. However, it is not typically used below 5 GPa.

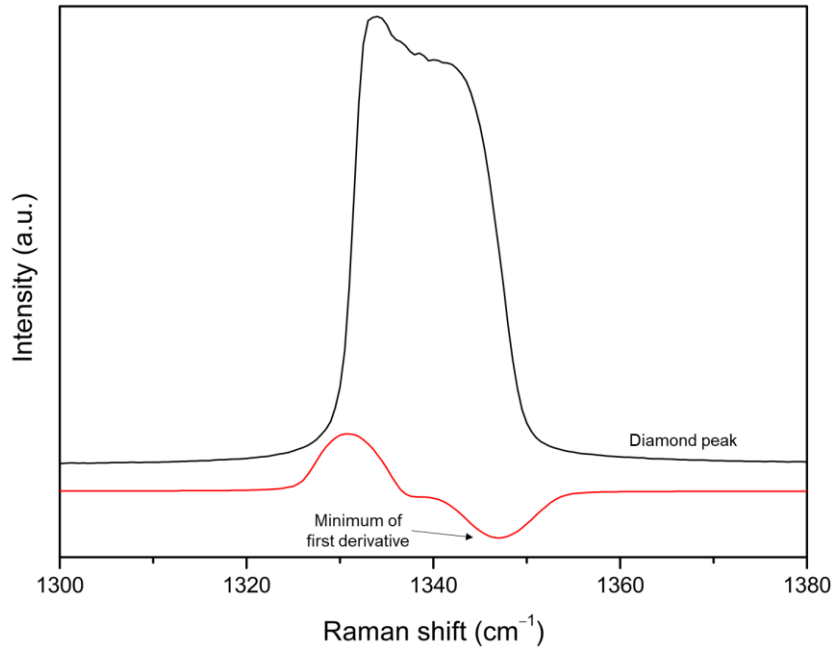


Figure 3.7: Diamond peak and the first derivative of the diamond peak.

3.2.3 Characterization

3.2.3.1 Powder X-ray diffraction (PXRD)

Powder X-ray diffraction (PXRD) data were obtained on a Rigaku OD XtaLAB Synergy-S diffractometer equipped with a Dectris Eiger2 R CdTe 1M detector, using either Cu Kα ($\lambda = 1.54184$ Å) or Ag Kα ($\lambda = 0.56087$ Å) radiation. Gandolfi movement for powders was employed to enhance the random orientation of the crystallites. A typical measurement consisted of six frames, each with an exposure time of 300 s per frame, with the detector positioned 90 mm away from the sample. Data were collected either at room temperature or at 100 K. Low temperatures were achieved with the cold N_2 stream supplied by an Oxford Cryosystems 800 Series Cryostream. Two-dimensional powder diffraction frames were reduced to standard profiles using *CrysAlisPro* software (Rigaku OD, 2025). The structural refinements and quantitative phase analyses were carried out using the Rietveld method with *GSAS-II* (Toby & Von Dreele, 2013). For thermally unstable materials, powder measurements were obtained by mounting large number of crystallites from the trough onto a MiTeGen MicroLoop or MicroMount, which was then transferred to the X-ray diffractometer in the same manner as single crystals (*vide infra*).

3.2.3.2 Single-crystal X-ray diffraction (SCXRD)

Provided that the sample was stable at room temperature under inert conditions, it was transferred from the glovebox in a short piece of FEP tube (o.d. 6.0 mm; i.d. 4.7 mm) closed with an FEP cap (o.d. 8.0 mm; i.d. 6.0 mm) and then deposited onto the aluminium trough.

Thermally unstable solids were isolated directly from the reaction vessel using the following procedure. After complete removal of the solvent, the vessel was backfilled with nitrogen (1 bar) at approximately −78 °C and detached from the vacuum system. The vessel was then tapped with a plastic stick to dislodge the crystals from the walls and subsequently cut, allowing the crystals to fall onto the aluminium trough of the low-temperature crystal mounting apparatus, which was cooled by a stream of cold nitrogen (−70 to −100 °C) (Veith & Bärnighausen, 1974; Lozinšek, Mercier, & Schrobilgen, 2021; Motaln, et al., 2024).

Suitable crystals were selected under a microscope and attached to the tip of a MiTeGen loop using Fomblin oil (Z25, SynQuest). The loop assembly was picked up with cryo pin tongs cooled to −196 °C and quickly transferred to the goniometer head, where it was cooled and protected by the stream of cold nitrogen at 100 K.

All datasets were processed with empirical and numerical absorption corrections using *CrysAlisPro* software (Rigaku OD, 2025). Crystal structures were solved with the charge flipping method using *olex2.solve* (Bourhis, Dolomanov, Gildea, Howard, & Puschmann, 2015) or with *SHELXT* (Sheldrick, 2015), and were refined with *SHELXL* (Sheldrick, 2015) within *Olex2* software (Dolomanov, Bourhis, Gildea, Howard, & Puschmann, 2009). Figures were drawn using *DIAMOND* software (Brandenburg, 2022).

3.2.3.3 Raman and infrared spectroscopy

Raman spectroscopy was performed either on a Horiba Jobin Yvon Labram-HR spectrometer coupled with an Olympus BXFM-ILHS microscope or on a Bruker Sentera II confocal Raman microscope, using red (632 or 785 nm) or green (532 nm) laser, depending on the sample. The typical resolution was 1.5 cm^{-1} or 4 cm^{-1}. Samples stable at room temperature under inert conditions were loaded into quartz capillaries, temporarily sealed with 25-5S Halocarbon grease, and then flame-sealed using an H_2–O_2 flame.

Low-temperature measurements for samples in capillaries were performed on the Bruker Sentera II Raman spectrometer equipped with a Linkam LTS420 low-temperature stage cell, with temperature controlled by a stream of liquid nitrogen contained in a separate Dewar. For thermally unstable compounds, Raman spectra at low temperatures were measured directly on the aluminium trough (see 3.2.3.2) using the Horiba Jobin Yvon Labram-HR spectrometer.

ATR-IR measurements were carried out on a Bruker Alpha II spectrometer placed in a N_2-filled glovebox, with a resolution of 2 cm^{-1} or 4 cm^{-1} depending on the sample. Typically, 24 scans were collected. The solid was placed on the diamond surface, gently pressed with a clamping device, and then measured.

Baseline subtraction was performed using *OPUS* 8.7. software suite (Bruker, 2022) with 15 iterations and 50 baseline points.

3.2.3.4 3D electron diffraction

All 3D electron diffraction (3D ED) measurements performed in Chapter 4.1.4. were performed at Institute of Physics of the Czech Academy of Sciences. All sample handling, data acquisition and data processing were processed by Dr. rer. nat. Lukáš Palatinus, Dr. Petr Brázda and Dr. Kshitij Gurung.

The FEI Tecnai G2 20 transmission electron microscope, equipped with a LaB_6 cathode and a Medipix 3 hybrid pixel detector ASI CheeTah, was operated at 200 kV. Datasets were collected at 100 K using a continuous rotation electron diffraction (cRED) method at certain tilt angle ranges with a step size of 0.25° or 0.30°. Indexing, determination of lattice parameters, and peak integration were performed using *PETS2* (Palatinus, et al., 2019). The processed data were imported into *Jana2020* software (Petříček, Palatinus, Plašil, & Dušek, 2023), and the crystal structures were determined using *Sir2014* (Burla, et al., 2015), which uses the standard direct methods for the ab initio phasing of the electron diffraction data. The resulting structures were then refined both kinematically and dynamically in *Jana2020* (Palatinus, Petříček, & Corrêa, 2015; Klar, et al., 2023).

3.2.3.5 Synchrotron X-ray diffraction

Synchrotron multigrain micro-single crystal X-ray diffraction was performed at the PETRA III synchrotron (DESY) on the Extreme Conditions Beamline P02.2 (Liermann, et al., 2015). The beam size on the sample was approximately 2 × 2 μm^2. Diffraction data were collected using a PerkinElmer XRD1621 detector with the wavelength of 0.2898 Å (42.8 keV) and 0.2906 Å (42.7 keV). Multigrain single-crystal data were obtained while rotating the sample by ±35° around the axis perpendicular to the beam, with frames collected in 0.5° steps and 1 s acquisition time per frame. Synchrotron multigrain micro-single crystal X-ray diffraction was also performed at the ESRF High Pressure Beamline ID27 (Mezouar, et al., 2024), using a beam size of 0.7 × 0.7 μm^2. Diffraction data were collected using an Eiger2 X CdTe 9M detector at a wavelength of 0.3738 Å (33.2 keV). The DAC was rotated by ±35° around the axis perpendicular to the beam, with frames collected in 0.5° steps and 1 s acquisition time per frame

Single crystal diffraction data were integrated using *CrysAlisPro* (Rigaku OD, 2025), and *DAFi* software (Aslandukov, Aslandukov, Dubrovinskaia, & Dubrovinsky, 2022) was used to index reflections to individual domains. Crystal structures were solved using *SHELXT* (Sheldrick, 2015) and refined with *SHELXL* (Sheldrick, 2015) within *Olex2* software (Dolomanov, Bourhis, Gildea, Howard, & Puschmann, 2009).

Chapter 4

Results and Discussion

4.1 Mechanochemical Synthesis of Noble-Gas Compounds

In this chapter, the results on the mechanochemical reactivity of noble-gas compounds are discussed. As these results are currently being prepared for publication, only a brief overview is presented.

4.1.1 Synthesis of compounds containing xenon in the +2 oxidation state by mechanochemistry

The XeF_2–MF_5 systems are among the most thoroughly studied in xenon(II) chemistry (Sladky, Bulliner, & Bartlett, 1969; Žemva, 1988; Elliot, Lehmann, Mercier, Jenkins, & Schrobilgen, 2010). The known stoichiometries include $[XeF][M_2F_{11}]$, $[XeF][MF_6]$, $[Xe_2F_3][MF_6]$, and $[Xe_2F_3][MF_6]\cdot n XeF_2$. Of particular interest for the mechanochemical investigation of noble-gas chemistry is the XeF_2–TaF_5 system (Holloway & Knowles, 1969; Frlec & Holloway, 1975; Frlec & Holloway, 1976), as both XeF_2 and TaF_5 are solid reagents that can be conveniently handled in mechanochemical experiments and are also commercially available.

In a typical reaction, 75 mg of a mixture of XeF_2 and TaF_5 was used. Two PTFE balls (6.4 mm in diameter, 0.29 g each) were placed inside a 10 mL PTFE milling vessel. The mixture was ground for 5, 15, 30, or 60 minutes at 30 Hz. Due to the fact that XeF_2 sublimes, a small excess of XeF_2 with regards to TaF_5 was used within defined ratios (i.e., instead 1:1, the ratio was 1.2:1). Such a small excess was also employed in previously reported solid-state reactions (Frlec & Holloway, 1975). The overview of phases obtained by different synthetic approaches is given in Table 4.1

Table 4.1: Comparison of results from different synthethic methods in terms of secondary phases present. The bolded phases are the major, whereas the non-bolded are secondary phases. Solid-state synthesis referes to synthesis at elevated temperatures.

XeF_2 : TaF_5 ratio	**1 : 2**	**1 : 1**	**2 : 1**
Mechanochemical synthesis (60 minutes)	**$[XeF][Ta_2F_{11}]$** + $[XeF][TaF_6]$	**$[XeF][TaF_6]$**	**$[Xe_2F_3][TaF_6]$** + $[XeF][TaF_6]$
Solid-state synthesis	**$[XeF][Ta_2F_{11}]$** + TaF_5	**$[XeF][TaF_6]$** + $[Xe_2F_3][TaF_6]$	**$[Xe_2F_3][TaF_6]$** + $[XeF][TaF_6]$
Solution synthesis	**$[XeF][Ta_2F_{11}]$** + TaF_5	**$[XeF][TaF_6]$**	**$[Xe_2F_3][TaF_6]$**

$[XeF][Ta_2F_{11}]$ was obtained either with residual TaF_5 or, upon increasing the XeF_2/TaF_5 ratio above 0.6, with $[XeF][TaF_6]$ as an impurity (Figure 4.1) by mechanochemical method even after 60 minutes. Solid-state synthesis of $[XeF][Ta_2F_{11}]$ at 93 °C yielded $[XeF][TaF_6]$ and TaF_5 as secondary phases, and similar results were also obtained from synthesis in solution using aHF as the solvent.

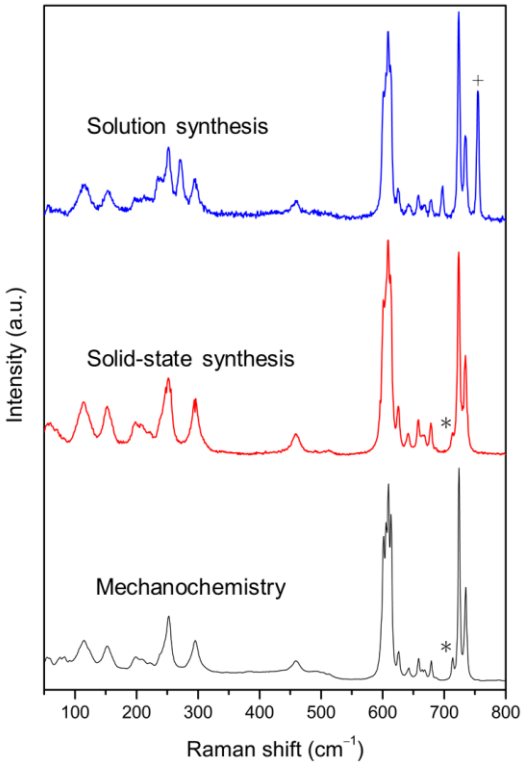


Figure 4.1: Comparison of synthetic methods for $[XeF][Ta_2F_{11}]$. The asterisk (*) denotes $[XeF][TaF_6]$ as a secondary phase, whereas the plus sign (+) denotes TaF_5.

Excluding the most intense band attributed to TaF_5 (755 cm^{-1}) (Beattie, Livingston, Ozin, & Reynolds, 1969), the Raman spectrum of $[XeF][Ta_2F_{11}]$ is in good agreement with previously reported data (Frlec & Holloway, 1975). The most distinct features are the peaks around 610 cm^{-1}, corresponding to the ionized $[XeF]^+$ fragment, which compare well

with those observed in other [XeF][M_2F_{11}] and [XeF][MF_6] compounds (Sladky, Bulliner, & Bartlett, 1969; Elliot, Lehmann, Mercier, Jenkins, & Schrobilgen, 2010; Žemva, 1988). Two peaks attributed to $[Ta_2F_{11}]^-$ are observed at 721, 730 cm^{-1} and occur at slightly lower values than in $Cd[Ta_2F_{11}]_2$ and $Hg[Ta_2F_{11}]_2$ (Tavčar & Goreshnik, 2016).

The crystal structure of [XeF][Ta_2F_{11}] (Figure 4.2, Table 4.1) consists of isolated [XeF][Ta_2F_{11}] units. The Xe1—F1 (1.8963(14) Å) and Xe—F2 (2.2504(15) Å) bond lengths are consistent with those observed for similar tight-ion pairs (Elliot, Lehmann, Mercier, Jenkins, & Schrobilgen, 2010; Radan, Goreshnik, & Žemva, 2014). The F1—Xe1—F2 angle is close to linear (176.73(7)°). The Ta—F bond distances within the $[Ta_2F_{11}]^-$ anion (1.8417(15)–2.1113(14) Å) are comparable to those reported previously for this anion, as is the Ta—F—Ta angle (164.46(8)°) (Tavčar & Goreshnik, 2016; Scheibe, et al., 2020). Interestingly, [XeF][Ta_2F_{11}] crystallizes in a different space group than both [XeF][Sb_2F_{11}] ($P2_1$) and [XeF][Bi_2F_{11}] ($P2_12_12_1$) (Elliot, Lehmann, Mercier, Jenkins, & Schrobilgen, 2010).

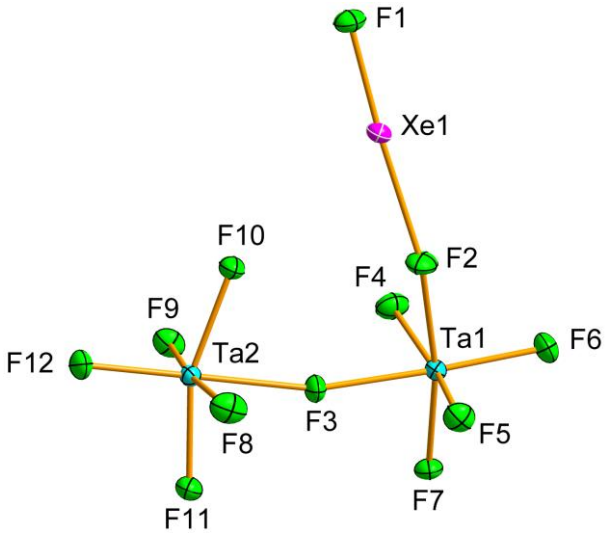


Figure 4.2: Asymmetric unit of [XeF][Ta_2F_{11}]. All atoms are depicted with 50 % probability ellipsoids.

Table 4.2: Summary of crystal data and structure refinements for $[XeF][Ta_2F_{11}]$, $[XeF][TaF_6]$ and $[Xe_2F_3][TaF_6]$. All single-crystal data was measured with Ag Kα radiation.

Compound	$\mathbf{[XeF][Ta_2F_{11}]}$	$\mathbf{[XeF][TaF_6]}$	$\mathbf{[Xe_2F_3][TaF_6]}$§
Chemical formula	$XeTa_2F_{12}$	$XeTaF_7$	Xe_2TaF_9
M_r	712.20	445.25	614.55
Crystal system	Monoclinic	Monoclinic	Monoclinic
Space group	$P2_1/n$	$P2_1/c$	Ia
T / K	100	100	100
a / Å	7.71079(7)	5.38135(5)	11.0668(1)
b / Å	8.40398(7)	10.93986(9)	8.12389(8)
c / Å	15.34986(13)	10.90195(9)	9.88950(11)
α / °	90	90	90
β / °	93.6167(8)	94.1123(8)	92.7712(9)
γ / °	90	90	90
V / Å^3	992.71(2)	640.16(1)	888.08(2)
Z	4	4	4
μ / mm^{-1}	13.68	12.00	10.66
Crystal size	0.29 × 0.17 × 0.16	0.29 × 0.17 × 0.16	0.29 × 0.2 × 0.11
T_{min}, T_{max}	0.300, 0.476	0.021, 0.603	0.136, 0.918
No. of measured, independent and observed $[I > 2\sigma(I)]$ reflections	115988, 8305, 7474	121892, 6458, 6075	64645, 5765, 5659
R_{int}	0.092	0.126	0.050
$\sin(\theta/\lambda)_{max}$ / Å^{-1}	1.000	1.064	0.957
$R[F^2 > 2\sigma(F^2)]$, $wR(F^2)$, S	0.020, 0.046, 1.03	0.023, 0.061, 1.17	0.017, 0.038, 1.08
No. of reflections	8305	6458	5765
No. of parameters	136	83	111
No. of restraints	–	–	2
$\Delta\rho_{max}$, $\Delta\rho_{min}$ / e Å^{-3}	2.76, −1.96	2.28, −2.63	1.16, −0.81

§ Refined as two-component inversion twin; scales: 0.403(6), 0.597(6).

Pure $[XeF][TaF_6]$ was obtained after 60 minutes of grinding with a slight excess of XeF_2, as indicated by the absence of peaks corresponding to TaF_5 and other compounds in this system (Figure 4.3). The pure product can also be obtained from aHF, although an excess of XeF_2 is again required. This excess can be removed under dynamic vacuum at room temperature, as $[Xe_2F_3][TaF_6]$ is unstable under these conditions. Although solid-state synthesis at elevated temperature represents a possible route to $[XeF][TaF_6]$, it has often been found to produce small amounts of $[Xe_2F_3][TaF_6]$ as a byproduct when two reactants were heated at 90 °C.

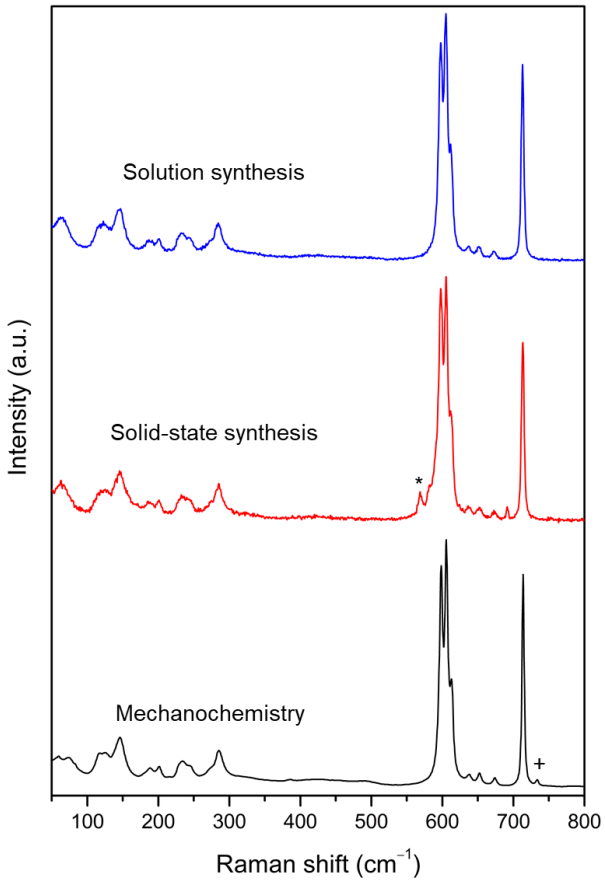


Figure 4.3: Comparison of synthetic methods for $[XeF][TaF_6]$. The asterisk (*) denotes a $[Xe_2F_3][TaF_6]$ as a secondary phase, whereas the plus sign (+) denotes a PTFE impurity originating from the milling vessel.

The Raman spectrum of $[XeF][TaF_6]$ (Figure 4.3) is in good agreement with previously reported (Frlec & Holloway, 1975). The most prominent feature corresponds to the $[XeF]^+$ vibration, located around 600 cm^{-1}. The other prominent peak appears at 714 cm^{-1} and is attributed to the $[TaF_6]^-$ anion. The crystal structure (Figure 4.4, Table 4.1) consists of isolated $[XeF][TaF_6]$ tight-ion pairs. The Xe1−F1 (1.9053(16) Å) and Xe1−F2 (2.2072(15) Å) bond lengths are consistent with those observed for similar tight-ion pairs (Elliot, Lehmann, Mercier, Jenkins, & Schrobilgen, 2010; Radan, Goreshnik, & Žemva, 2014), and the F1−Xe1−F2 angle is nearly linear (178.49(7)°). The Ta−F bond distances within the $[TaF_6]^-$ anion (1.8503(16)–1.8895(14) Å), excluding the Ta−F_b(Xe) bond (2.0467(15) Å), are also in good agreement with previously reported values for this anion. (Radan, Lozinšek, Goreshnik, & Žemva, 2011; Tavčar & Goreshnik, 2016; Groom, Bruno, Lightfoot, & Ward, 2016; Scheibe, et al., 2020).

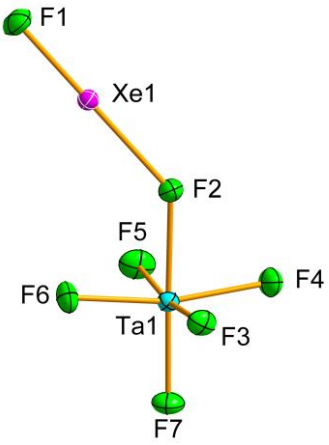


Figure 4.4: Asymmetric unit of [XeF][TaF_6]. All atoms are depicted with 50 % probability ellipsoids.

[Xe_2F_3][TaF_6] was obtained essentially pure after grinding for 60 minute (Figure 4.5). Small amounts of [XeF][TaF_6] as an impurity might arise due to the rapid liberation of XeF_2 from [Xe_2F_3][TaF_6] during the sample preparation, a process likely promoted by a high surface area of the mechanochemically synthesized sample. Liberation of XeF_2 is also observed during prolonged storage of [Xe_2F_3][TaF_6] in a closed vessel. The pure product can also be obtained from aHF by solvent removal at low temperatures (−20 °C). Solid-state synthesis performed at (83 °C) also produces [XeF][TaF_6] or XeF_2 as secondary phases.

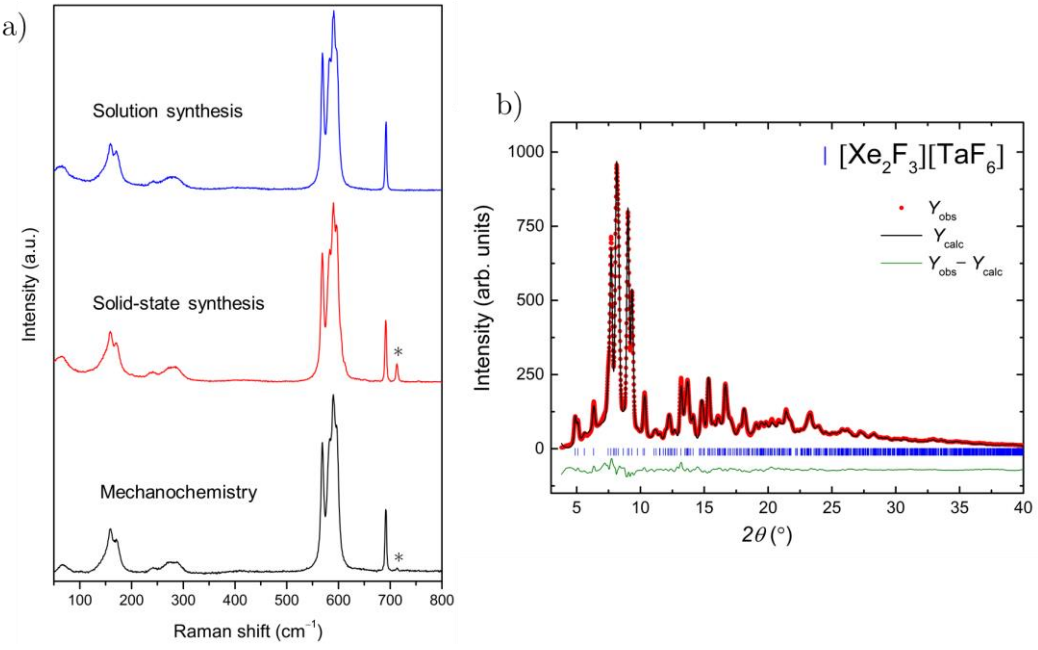


Figure 4.5: a) Comparison of synthetic methods for [Xe_2F_3][TaF_6]. The asterisk (*) denotes [XeF][TaF_6] as a secondary phase. b) Rietveld refinement of mechanochemically prepared [Xe_2F_3][TaF_6]. The red points represent the experimental data, the black line the refined profile, and blue tick marks indicate the positions of the Bragg reflections. The difference plot is shown as a green line. Rietveld analysis was performed in *GSAS*-II (Toby & Von Dreele, 2013) by Asst. Prof. Mirela Dragomir.

The Raman spectrum of $[Xe_2F_3][TaF_6]$ is in excellent agreement with spectra reported in the literature (Frlec & Holloway, 1975). Its main features are three peaks around 590 cm^{-1}, typical for the $[Xe_2F_3]^+$ cation, and a peak at 682 cm^{-1} corresponding to the nearly octahedral $[TaF_6]^-$ anion.

The crystal structure (Figure 4.6, Table 4.1) consists of isolated $[Xe_2F_3]^+$ cations and $[TaF_6]^-$ anions. The Xe1—F1 and Xe2—F3 (1.917(3), 1.922(3) Å) as well as Xe1—F2 and Xe2—F2 (2.153(3) Å, 2.144(3) Å) bond lengths in the $[Xe_2F_3]^+$ cation are in good agreement with those observed for $[Xe_2F_3][AsF_6]$ (Fir, et al., 2000), $[Xe_2F_3][SbF_6]$ (Bortolus, Mercier, Nguyen, & Schrobilgen, 2021) and $[Xe_2F_3][Ti_8F_{33}]$ (Radan, Goreshnik, & Žemva, 2014) as well as is Xe—F—Xe angle (157.21(14)°). The bond distances in the $[TaF_6]^-$ anion (1.893(2)–1.905(2) Å) are in good agreement with other examples of this anion (Radan, Lozinšek, Goreshnik, & Žemva, 2011; Tavčar & Goreshnik, 2016; Groom, Bruno, Lightfoot, & Ward, 2016).

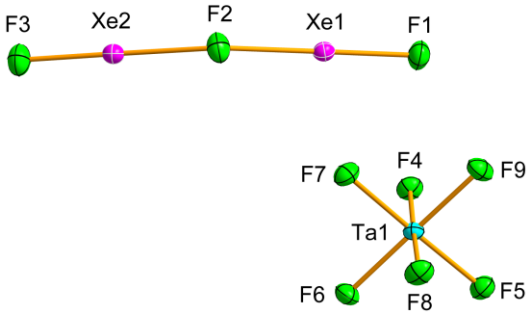


Figure 4.6: Asymmetric unit of $[Xe_2F_3][TaF_6]$. All atoms are depicted with 50 % probability ellipsoids.

Time-dependent grinding of a 2:1 molar mixture of XeF_2 and TaF_5 (Figure 4.7) indicates that the formation of $[Xe_2F_3][TaF_6]$ occurs sequentially. The starting TaF_5, which exists as a tetramer (Ta_4F_{20}) in the solid state (Edwards, 1964; Brewer, et al., 2005; Tavčar & Goreshnik, 2016), is likely broken down to a dimer (Ta_2F_{10}) upon addition of XeF_2, forming $[XeF][Ta_2F_{11}]$. After five minutes, this phase is essentially fully converted to $[XeF][TaF_6]$, which subsequently transforms into $[Xe_2F_3][TaF_6]$.

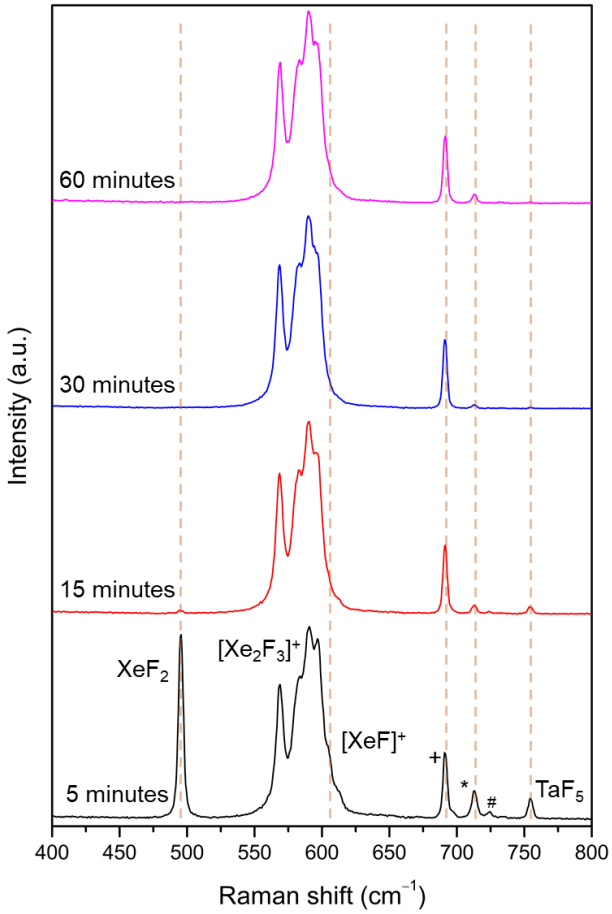


Figure 4.7: Results of time-dependent milling for XeF_2:TaF_5 in a 2:1 ratio. The plus sign (+) denotes $[TaF_6]^-$ anion of $[Xe_2F_3][TaF_6]$, the asterisk (*) denotes the $[TaF_6]$ moiety of $[XeF][TaF_6]$, and the hash symbol (#) denotes $[Ta_2F_{11}]$ moiety of $[XeF][Ta_2F_{11}]$. All spectra correspond to separate experiments; that is, once a milling vessel was opened, it was not closed again for continuation of the experiment.

4.1.2 Synthesis of the dixenon ($[Xe_2]^+$) cation by mechanochemistry

The XeF_2–SbF_5 system is among the best-studied systems in xenon(II) chemistry, with several phases fully characterized: $[Xe_2F_3][SbF_6]$, $[XeF][SbF_6]$ and $[XeF][Sb_2F_{11}]$ (Frlec & Holloway, 1975; Elliot, Lehmann, Mercier, Jenkins, & Schrobilgen, 2010; Bortolus, Mercier, Nguyen, & Schrobilgen, 2021). In contrast, the reaction of oxidation of SbF_3 with XeF_2 has been studied only once. It was reported that, upon heating these two components, only $[XeF][SbF_6]$ and $[Xe_2F_3][SbF_6]$ are formed (Popov, Scharabarin, Sukhoverkhov, & Tchumaevsky, 1989). To investigate if compounds observed in XeF_2–SbF_5 can be obtained mechanochemically by *in situ* oxidation od SbF_3, XeF_2 was ground with SbF_3 at room temperature for 60 minutes in different molar ratios. For all reactions, 75 mg of the XeF_2–SbF_3 mixture was used and the mixture was ground in a 10 mL PTFE milling vessel equipped with two PTFE balls (6.4 mm in diameter, 0.27 g) at 30 Hz.

Grinding the mixture in a 4:1 molar ratio (XeF_2:SbF_3) yielded $[Xe_2F_3][SbF_6]$ and presumably $[Xe_2F_3][SbF_6]\cdot XeF_2$,[1] as indicated by the presence of vibrations at 505 and 514 cm^{-1} (Figure 4.8), alongside unreacted XeF_2. Grinding the mixture in a 3:1 ratio produced

[1] Dr. Melita Tramšek is acknowledged for sharing the Raman spectrum and the crystal structure of this phase.

pure $[Xe_2F_3][SbF_6]$, as confirmed by Raman spectroscopy (Frlec & Holloway, 1975) (Figure 4.8).

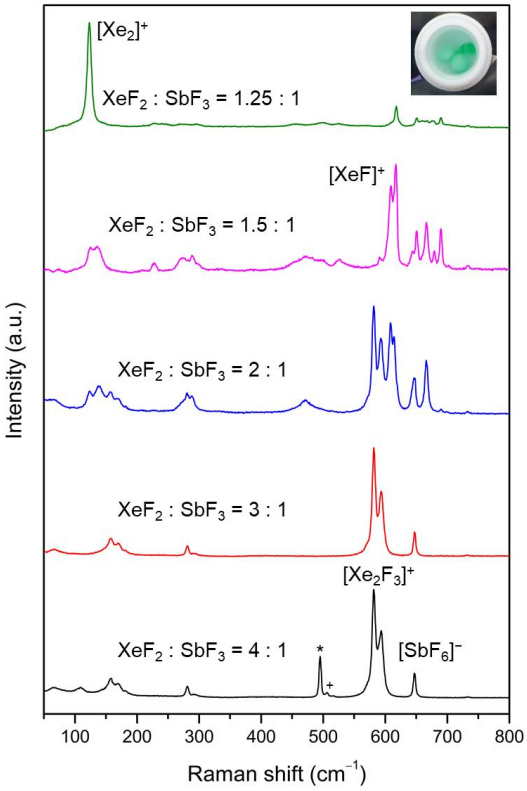


Figure 4.8: Raman spectra of products obtained after one hour of grinding of XeF_2:SbF_3 mixture in different ratios. The asterisk (*) represents unreacted XeF_2, whereas the plus sign (+) likely corresponds to $[Xe_2F_3][SbF_6]{\cdot}XeF_2$ cocrystal (Frlec & Holloway, 1975). The inset shows the green powder obtained after grinding the XeF_2:SbF_3 mixture in a 1.25:1 ratio.

Reducing the grinding ratio toward 1:1 resulted in the appearance of a green color (Figure 4.8) with concomitant appearance of a sharp peak at 123 cm^{-1}. This peak, along with the green color, can be unambiguously assigned to the $[Xe_2]^+$ cation (Brown, et al., 1992; Drews & Seppelt, 1997). Unfortunately, the green solid, which appears to form in the largest quantity when XeF_2:SbF_3 ratio is 1.25:1, is amorphous, precluding full structural analysis and elucidation of the anion by X-ray diffraction. Another phase present in this reaction is $[XeF][Sb_2F_{11}]$, along with residual SbF_3. All attempts to redissolve the green compound in either aHF (−80 °C) or acetonitrile (−40 °C) were unsuccessful. Upon contact with aHF, the green color disappeared immediately, accompanied by gas evolution. The reaction with acetonitrile was also rapid, yielding a yellow-orange amorphous product stable at room temperature, likely an organic polymer.

The two other phases, $[XeF][Sb_2F_{11}]$ and $[XeF][SbF_6]$ could also be obtained via a mechanochemical approach, as indicated by Raman spectroscopy, but never as pure phases, likely due to the equilibrium with the $[Xe_2]^+$-containing compound.

Although impurities are present in the sample containing $[Xe_2]^+$ cation, the synthetic procedure for obtaining such cation in solid state is nevertheless safer and milder than solution method in which HF/SbF_5 solution, large excess of xenon with regards to $[XeF][Sb_2F_{11}]$ is required, as well as low temperature. Importantly, solution-based method also requires significant overpressure of xenon which can lead to explosion of the vessel.

Moreover, solution method also produces, alongside $[Xe_2][Sb_4F_{21}]$, secondary phases: unreacted $[XeF][Sb_2F_{11}]$ and $[H_xF_y][Sb_2F_{11}]$ ($x = 2,3$; $y = 1,2$) salts (Drews & Seppelt, 1997).

4.1.3 Synthesis of compounds containing xenon in the +4 oxidation state by mechanochemistry

The $XeF_2{\cdot}XeF_4$ cocrystal was first obtained via co-sublimation of both reagents (Burns, Ellison, & Levy, 1965), and it was later shown that it can be synthesized by fusing XeF_2 and XeF_4 at 90 °C (Adams, 1974). Further studies revealed that the system melts congruently at 90 °C and that the only stable phase is the 1:1 cocrystal (Ogrin, Bohinc, & Slivnik, 1973). To investigate whether this cocrystal can also be obtained mechanochemically, XeF_2 and XeF_4 were grinded in a 5 mL PTFE milling vessel equipped with one PTFE ball (7 mm in diameter, 0.56 g) at 50 Hz.

The cocrystal forms as the sole product after 15 minutes of grinding when the total mass of the mixture is 75 mg. Scaling the synthesis to 200 mg of powder, the reaction yields a pure product in only 20 minutes, as confirmed by PXRD and Raman spectroscopy (Figure 4.9). The mechanochemical approach offers an advantage over a solid-state thermal method, which requires heating at 90 °C, and solution synthesis, which has been shown to produce mixtures of phases (Bortolus, Mercier, Nguyen, & Schrobilgen, 2021).

In a separate study, it was found that the powder obtained in this manner is suitable for 3D electron diffraction (Chapter 4.1.4).

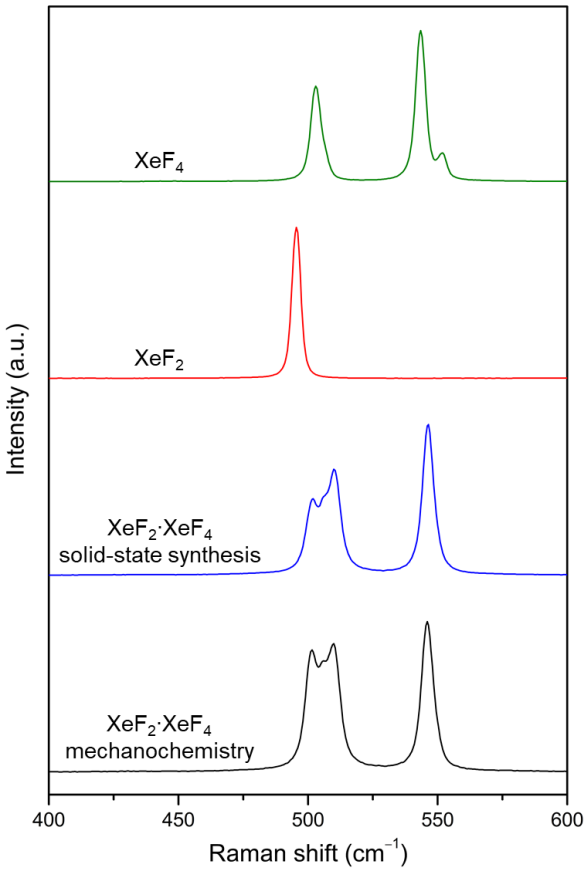


Figure 4.9: Raman spectra of the product obtained after 20 minutes of grinding XeF_2 and XeF_4 in a 1:1 molar ratio. For comparison, Raman spectra of $XeF_2{\cdot}XeF_4$ cocrystal prepared by solid-state synthesis, XeF_2, and XeF_4 are also shown for comparison.

XeF_4 can act as a fluoride-ion donor in the presence of strong Lewis acids (Žemva, 1988; Haner & Schrobilgen, 2015). Surprisingly, the reaction of XeF_4 and TaF_5 has never been confirmed to yield either $[XeF_3][Ta_2F_{11}]$ or $[XeF_3][TaF_6]$; only the formation of $[XeF][Ta_2F_{11}]$ has been reported (Edwards, Holloway, & Peacock, 1963), likely due to the presence of XeF_2 in the sample of XeF_4. To scrutinize the nature of this reaction, both mechanochemical and solution-based synthetic methods were explored.

Mechanochemical reaction of purified TaF_5 (Experimental section) and XeF_4 in 1:0.6 ratio in a 5 mL PTFE vessel equipped with one PTFE ball (6.7 mm in diameter, 0.39 g) at 50 Hz, yielded highly pure $[XeF_3][Ta_2F_{11}]$, with only traces of TaF_5 in 60 minutes (Figure 4.10).

The $[XeF_3]^+$ vibrations are clearly observable in the Raman spectrum (557, 620 cm^{-1}) (Haner & Schrobilgen, 2015) as well as those from $[Ta_2F_{11}]^-$ anion (575, 721, 734 cm^{-1}) (Tavčar & Goreshnik, 2016). More importantly, the absence of peaks attributable to $[XeF]^+$ cation (610 cm^{-1}) (Tramšek & Žemva, 2006) which could form as partial reduction product, demonstrates that even a potent oxidizer such as $[XeF_3]^+$ can be safely handled with standard mechanochemical equipment without pre-passivating the vessels.

To confirm the nature of the product, reaction of XeF_4 with TaF_5 in aHF followed by slow crystallization, provided crystals suitable for low-temperature single-crystal X-ray diffraction.

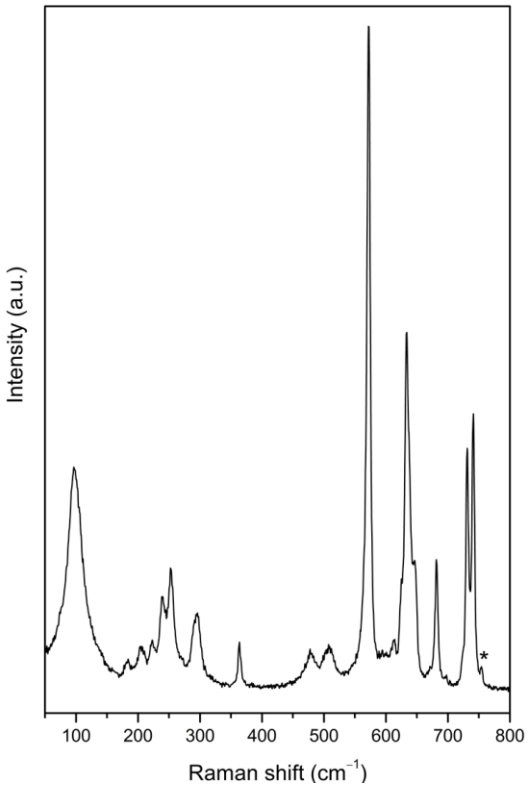


Figure 4.10: Raman spectra of mechanochemically synthesized $[XeF_3][Ta_2F_{11}]$. The asterisk (*) denotes unreacted TaF_5.

The geometry of the $[XeF_3]^+$ cation (1.842(3), 1.894(3), 1.904(3) Å) as well as the Xe–F(Ta) bond length (2.456(3) Å), is in good agreement with that observed for $[XeF_3][SbF_6]$, $[XeF_3][Sb_2F_{11}]$ and $[XeF_3][BiF_6]$ (Gillespie, Martin, Schrobilgen, & Slim, 1977; McKee, Zalkin, & Bartlett, 1973; Brock, Mercier, & Schrobilgen, 2013). The Xe1–F4 (2.456(3) Å) distance in $[XeF_3][Ta_2F_{11}]$ differs substantially from that in $XeF_4 \cdot WOF_4$

(2.068(5) Å) (Bortolus, Mercier, & Schrobilgen, 2022), consistent with the higher ionization of XeF_4 molecule and the higher Lewis acidity of Ta_2F_{10} compared to WOF_4. The bond lengths (1.826(3)–2.071(3) Å) and angles (Ta1−F5−Ta2 = 153.62(17)°) in the $[Ta_2F_{11}]^-$ anion are similar to those reported before (Tavčar & Goreshnik, 2016; Scheibe, et al., 2020) and are in excellent agreement with those in $[XeF][Ta_2F_{11}]$. The shortest Xe···F contact from the F11 to Xe1 atom (2.950(3) Å) (Figure 4.11) is consistent with previously reported values (McKee, Zalkin, & Bartlett, 1973; Gillespie, Martin, Schrobilgen, & Slim, 1977, Brock, Mercier, & Schrobilgen, 2013).

Table 4.3: Summary of crystal data and structure refinements for $[XeF_3][Ta_2F_{11}]$.

Compound	$\mathbf{[XeF_3][Ta_2F_{11}]}$
Chemical formula	$XeTa_2F_{14}$
M_r	759.20
Crystal system	Monoclinic
Space group	$P2_1/c$
T / K	100
a / Å	8.46061(18)
b / Å	15.4528(2)
c / Å	8.91049(19)
α / °	90
β / °	116.522(3)
γ / °	90
V / Å^3	1042.36(4)
Z	4
μ / mm^{-1}	13.05
Crystal size	0.29 × 0.17 × 0.16
T_{min}, T_{max}	0.256, 0.554
No. of measured, independent and observed $[I > 2\sigma(I)]$ reflections	74251, 5914, 5501
R_{int}	0.054
$\sin(\theta/\lambda)_{max}$ / Å^{-1}	0.916
$R[F^2 > 2\sigma(F^2)]$, $wR(F^2)$, S	0.034, 0.072, 1.18
No. of reflections	5914
No. of parameters	154
$\Delta\rho_{max}$, $\Delta\rho_{min}$ / e Å^{-3}	3.12, −2.21

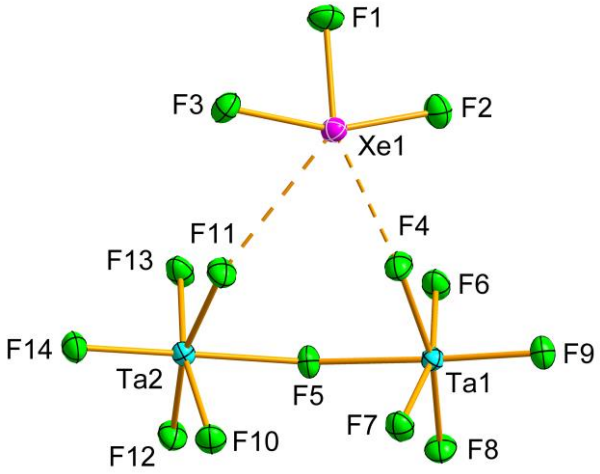


Figure 4.11: Asymmetric unit of $[XeF_3][Ta_2F_{11}]$. All atoms are depicted with 50% probability ellipsoids. Short F4···Xe1 and F11···Xe1 contacts are shown as a dashed orange lines.

Attempts to synthesize $[XeF_3][TaF_6]$, either mechanochemically or in aHF, yielded only $[XeF_3][Ta_2F_{11}]$ and XeF_4. This indicates that the $[TaF_6]^-$ anion is not sufficiently basic to stabilize the $[XeF_3]^+$ cation. Mechanochemical agitation of XeF_4 with NbF_5 under similar conditions did not result in the formation of new compound.

4.1.4 Employing 3D electron diffraction for characterization of mechanochemically synthesized noble-gas compounds

To investigate whether mechanochemically synthesized noble-gas compounds can be studied using 3D ED, the $XeF_2{\cdot}XeF_4$ cocrystal prepared mechanochemically was chosen as a suitable candidate for several reasons. The presence of XeF_4 in the sample makes it highly sensitive to even traces of moisture. At the same time, the vapor pressure of the cocrystal and its constituents makes them suitable candidates for assessing whether such compounds can be handled under the high vacuum conditions in the TEM column required for 3D ED experiments. The experimental work on 3D ED was performed by Dr. Kshitij Gurung, Dr. Petr Brázda and Dr. rer. nat. Lukáš Palatinus.

It was found that all three phases, XeF_2, XeF_4 and $XeF_2{\cdot}XeF_4$, can be measured using 3D ED. This result further validates the sample handling and cryotransfer procedure previously used for the XeF_2–MnF_4 system (Motaln, et al., 2024). Overall, the structural analyses are in good agreement with previous single-crystal X-ray diffraction studies (Burns, Ellison, & Levy, 1965; Bortolus, Mercier, Nguyen, & Schrobilgen, 2021) in terms of unit-cell parameters and bond lengths.

The results of this work have been published in: *J. Appl. Cryst.*, 2025, 58, 1079–1084. Erik Uran carried out the mechanochemical synthesis of the $XeF_2{\cdot}XeF_4$ cocrystal and assisted in revision and editing of the manuscript.

4.1.5 Conclusions of the mechanochemical results

Although all compounds prepared herein are readily obtained using classical synthetic methods familiar to the fluorine community (i.e., solution synthesis from aHF or solid-state methods), the main goal of this work has been to demonstrate that mechanochemistry can achieve essentially the same outcomes.

The synthesis of $[XeF][Ta_2F_{11}]$, $[XeF][TaF_6]$ and $[Xe_2F_3][TaF_6]$ shows that mechanochemical conditions can be finely tuned solely on the basis of time and XeF_2/TaF_5 ratio. Moreover, these compounds provide access to $[XeF]^+$-based compounds, which can lead to interesting new discoveries in noble-gas chemistry.

The investigation of the reactivity of XeF_2 with SbF_3 showed that $[Xe_2F_3][SbF_6]$ can be obtained essentially pure after only one hour of grinding. Moreover, decreasing of the ratio of XeF_2 to SbF_3 to close to equimolar leads to the solid-state synthesis of dixenon cation, $[Xe_2]^+$, which provides much more convenient synthesis than previously reported.

Moreover, as observed with the mechanochemically synthesized $XeF_2{\cdot}XeF_4$ cocrystal, which is formed rapidly, crystalline compounds obtained mechanochemically can be analyzed using 3D ED, thus avoiding the time-consuming procedure of crystal growth. The synthesis of $[XeF_3][Ta_2F_{11}]$ shows that even highly potent oxidizers such as $[XeF_3]^+$ can be safely handled in the mechanochemical equipment, further indicating the robustness of the method.

Further studies under varying atmospheres and/or temperatures, as well as introduction of other type of milling materials (ZrO_2, stainless-steel etc.) may lead to the discovery of novel noble-gas compounds. Combined with *in situ* XRD and *in situ* Raman spectroscopy, these approaches will facilitate a deeper understanding of the solid-state reactivity of these fundamentally important compounds.

4.2 Xenon(II)–Nitrogen Bonded Compounds Derived from Cyanogen

In this chapter, the results of studies on the chemistry of cyanogen (NCCN) and $[XeF][AsF_6]$ are presented and summarized in the attached article. The article has been prepared for submission to a journal. The chapter is therefore written in the format of the journal. Erik Uran performed most of the synthesis experiments, prepared and measured both single-crystal and powder samples, recorded the Raman spectra, and analyzed the results. He wrote the first draft of the manuscript and contributed to subsequent revisions.

The $[XeF]^+$ ion, typically found in $[XeF][MF_6]$ tight-ion pairs (M = Sb, As, Bi, Ta, etc.) (Tramšek & Žemva, 2006), is a strong Lewis acid featuring σ-hole (MacDougall, Schrobilgen, & Bader, 1989). It readily coordinates with Lewis bases such as XeF_2 to form the $[Xe_2F_3]^+$ cation, as well as with oxygen- (Minkwitz & Molsbeck, 1992; Schrobilgen & Whalen, 1994) and nitrogen-donor bases (Emara & Schrobilgen, 1987)

Nitriles are the most common nitrogen-donor Lewis bases employed in the reactions with the $[XeF]^+$ salts for the synthesis of xenon-nitrogen bonded adduct cations. $[RCNXeF]^+$ adduct cations have been characterized in solution (Emara & Schrobilgen, 1987), but only $[HCNXeF]^+$, $[CH_3CNXeF]^+$, $[(CH_3)_3CCNXeF]^+$ have been crystallographically characterized (Fir B. A., 1999). Furthermore, most studies focus on monotopic nitrogen bases, whereas polytopic bases are used only rarely (Schrobilgen, 1988).

To investigate whether a compound containing two $[XeF]^+$ cations coordinated to a ditopic nitrogen base could be synthesized, NCCN was employed as the simplest ditopic nitrile ligand. NCCN is resistant to oxidation (ionization energy = 13.37 eV) and has previously been shown to act as a ligand in the synthesis of coordination compounds (Corain, 1982) and to coordinate to cations such as $[Te_4]^{2+}$ (Beck & Zink, 2009).

The reaction of NCCN with $[XeF][AsF_6]$ in a large excess of NCCN yields $[FXeNCCN][AsF_6]$, whereas near-stoichiometric ratios yield $[FXeNCCNXeF][AsF_6]_2$. Both compounds feature a highly ionized $[XeF]^+$ fragment, with the Xe−F bonds in the cations being the shortest observed so far among compounds containing an N−Xe−F linkage. $[FXeNCCN][AsF_6]$ partially converts to $[FXeNCCNXeF][AsF_6]_2$ even at −78 °C, whereas $[FXeNCCNXeF][AsF_6]_2$, a first example of bis-coordinated nitrogen base with $[XeF]^+$ cation, remains stable at 0 °C. To further investigate how coordination to a Lewis acid affects the overall geometry of NCCN, $NCCNH[AsF_6]$ was also crystallographically characterized.

$[FXeNCCNXeF][AsF_6]$ converts at room temperature, in solution or in the solid state via the fluoride-ion rearrangement, to the room-temperature–stable $[XeNC(F)C(F)NXe][AsF_6]_2$. The $[XeNC(F)C(F)NXe]^{2+}$ cation represents the first example of a C=N−Xe bonding modality. The cation is coordinated to the $[AsF_6]^-$ anion through short Xe···F contacts. The coordination of the weakly coordinating anion to a xenon atom, which features a σ-hole, suggests that it may also interact with stronger Lewis bases.

$[XeNC(F)C(F)NXe][AsF_6]_2$ reacts with acetonitrile or hydrogen cyanide in aHF at low temperatures (< −30 °C), forming $[RCN\cdots XeNC(F)C(F)NXe\cdots NCR][AsF_6]_2$ (R = CH_3, H). These thermally unstable compounds represent rare examples of a crystallographically characterized N−Xe−N linkage (Smith & Schrobilgen, 2009).

Xenon(II)–Nitrogen-Bonded Compounds Derived from Cyanogen

Erik Uran,[1,2] Kristian Radan,[1] Miha Virant,[1] Mirela Dragomir,[2,3] Matic Lozinšek*[1,2]

[1] Extreme Conditions Chemistry Laboratory (ECCL K2), Jožef Stefan Institute, Jamova cesta 39, 1000 Ljubljana, Slovenia
[2] Jožef Stefan International Postgraduate School, Jamova cesta 39, 1000 Ljubljana, Slovenia
[3] Electronic Ceramics Department, Jožef Stefan Institute, Jamova cesta 39, 1000 Ljubljana, Slovenia

*Corresponding author: matic.lozinsek@ijs.si

Abstract: The reaction of $[XeF][AsF_6]$ with NCCN in anhydrous HF at low temperatures yields $[NCCNXeF][AsF_6]$ and $[FXeNCCNXeF][AsF_6]_2$, the latter representing the first example of a nitrogen base coordinated to two $[XeF]^+$ cations and exhibiting the longest N−Xe bond among compounds with an N−Xe−F linkage. $[FXeNCCNXeF][AsF_6]_2$ converts to $[XeNC(F)C(F)NXe][AsF_6]_2$ at room temperature, constituting the first example of a C=N−Xe bonding modality. The $[XeNC(F)C(F)NXe]^{2+}$ cation serves as a xenon(II) Lewis acid due to its σ-hole, as demonstrated by the synthesis of the nitrile adducts, $[RCN\cdots XeNC(F)C(F)NXe\cdots NCR][AsF_6]_2$ (R = CH_3, H), which represent rare examples of N−Xe−N linkages.

Introduction

Among all known noble-gas compounds, xenon difluoride (XeF_2) has been the most extensively studied.[1–4] XeF_2 has been employed as an oxidant[1Error! Bookmark not defined.] and as f luoride-donor, as exemplified by reactions with strongly acidic metal pentafluorides, forming tight-ion pairs $[XeF][MF_6]$ (M = As, Sb, Nb, Bi, Ta, Ru, Ir, Pt).[4,5] The resulting $[XeF]^+$ cation is isoelectronic with IF and exhibits a σ-hole[6] on the xenon atom,[7] a feature commonly observed for halogen atoms and widely utilized in materials design.[8–10] Although σ-hole interactions involving noble-gas atoms were first described in detail in 1989,[7] interest in this topic has been renewed by the synthesis of XeO_3 adducts with nitrogen[11,12] and oxygen[13,14] bases, as well as by computational studies.[15]

The significance of the σ-hole in the chemistry of the $[XeF]^+$ cation is most clearly illustrated by the formation of the well-known V-shaped $[Xe_2F_3]^+$ cation, which can be viewed as XeF_2 coordinated to $[XeF]^+$.[1] Other Lewis bases can interact with the σ-hole on Xe^{II}, with nitrogen bases in particular being employed to synthesize compounds containing N−Xe bonds.[16–22] Certain prerequisites, however, must be met to obtain such compounds. Specifically, the nitrogen base must be resistant to oxidation, with an ionization energy (IE) comparable to or exceeding the estimated electron affinity (EA) of the $[XeF]^+$ cation (~10.8 eV).[4,18] Additionally, the reaction should be conducted at low temperatures, as many of these compounds decompose at room temperature.[19] Xenon(II) cations bound to an electron-withdrawing group, such as $[XeOXe]^{2+}$,[23] $[XeOTeF_5]^+$,[24] and $[C_6F_5Xe]^+$,[25,26] also form adducts with nitrogen bases, demonstrating the versatility of xenon(II) as a σ-hole donor.

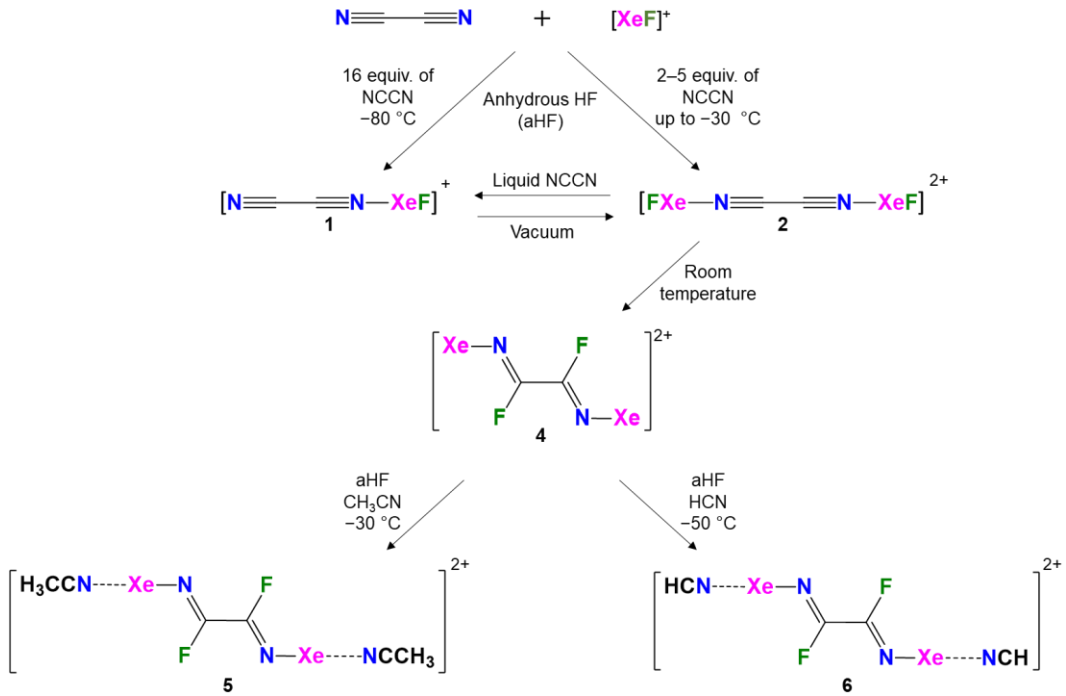
Until now, predominantly monotopic nitrogen Lewis bases have been investigated as ligands for $[XeF]^+$.[16–22] Even in cases where polytopic bases such as *s*-trifluorotriazine (*s*-$C_3F_3N_3$) were employed,[20,22] coordination of more than one $[XeF]^+$ cation to the same base

has not been reported. Therefore, cyanogen (N≡C−C≡N; IE = 13.37 eV),[27] as the simplest ditopic nitrogen bases, was selected as the molecule of choice to investigate whether it can coordinate two $[XeF]^+$ cations. The ability of NCCN to coordinate metal centers,[28] polyatomic cations,[29] and the methyl cation,[30] further supports this decision.

Results and Discussion

[NCCNXeF][AsF$_6$] and [FXeNCCNXeF][AsF$_6$] Adduct-Cation Salts and the Crystal Structure of NCCNH[AsF$_6$]

An overview of the reaction pathways is shown in Scheme 1. The reaction of a 16-fold excess of NCCN with [XeF][AsF$_6$] in anhydrous HF (aHF) at low temperatures (< −80 °C) yields tiny, colourless platelets of the [NCCNXeF][AsF$_6$] salt (**1**). When NCCN is present in 3 : 1 ratio relative to [XeF][AsF$_6$] and the solvent is removed at higher temperatures (up to −30 °C), large, colourless plates of the [FXeNCCNXeF][AsF$_6$]$_2$ salt (**2**) are obtained as the sole product (Figures S1–S3). The bis-coordinated adduct-cation in **2** represents the first example of a nitrogen base coordinated to multiple $[XeF]^+$ cations. Compound **1** partially converts to **2** at −78 °C, whereas the addition of liquid NCCN to **2** leads to the formation of **1** (Scheme 1).



Scheme 1. Observed reactions of [XeF][AsF$_6$] with NCCN. The counterion $[AsF_6]^-$ has been omitted for clarity.

The crystal structures of [NCCNXeF][AsF$_6$] and [FXeNCCNXeF][AsF$_6$]$_2$ were determined by low-temperature single-crystal X-ray diffraction (LT SCXRD) (Table 1 and S1).

Table 1. Summary of crystal data and refinement results for compounds $[NCCNXeF][AsF_6]$ (**1**), $[FXeNCCNXeF][AsF_6]_2$ (**2**), $NCCNH[AsF_6]$ (**3**), $[XeNC(F)C(F)NXe][AsF_6]_2$ (**4**), $[CH_3CN\cdots XeNC(F)C(F)NXe\cdots NCCH_3][AsF_6]_2$ (**5**) and $[HCN\cdots XeNC(F)C(F)NXe\cdots NCH][AsF_6]_2$ (**6**).

Compound	1	2	3	4	5	6
Space group	*I*2	$P2_1/c$	$P2_12_12_1$	$P2_1/c$	$P2_1/n$	*Pbca*
a **(Å)**	10.4494(3)	9.05086(14)	7.78096(8)	5.30743(6)	8.0638(2)	14.5234(2)
b **(Å)**	7.7425(2)	7.79613(10)	7.90024(9)	13.44541(15)	14.3506(4)	8.09522(11)
c **(Å)**	10.1084(3)	10.43770(18)	10.52780(12)	9.68749(10)	8.1101(2)	14.9470(2)
α (°)	90	90	90	90	90	90
β (°)	90.994(3)	112.8156(19)	90	96.8051(10)	95.204(3)	90
γ (°)	90	90	90	90	90	90
V **(Å³)**	817.70(4)	678.88(2)	647.16(1)	686.43(1)	934.63(5)	1757.32(4)
M	391.26	730.48	241.97	730.48	812.59	784.54
Z	4	2	4	2	2	4
T **(K)**	100	100	100	100	100	100
R_1	0.030	0.017	0.021	0.018	0.040	0.035
wR_2	0.067	0.039	0.055	0.049	0.077	0.077

As the adduct-cation in **1** is disordered (Figure 1, Figure S4), it exhibits relatively high uncertainties in bond lengths. Nevertheless, the N–Xe bond in **1** (2.284(5) Å) is consistent with values observed for N–Xe bonds in related $[RCNXeF]^+$ compounds (Table S2). In **2** (Figure 1, S5) this bond is longer (2.3413(13) Å) and is currently the longest among crystallographically characterized compounds featuring an N–Xe–F linkage (Table S2). The Xe–F bond distances in **1** (1.903(3) Å) and **2** (1.9051(9) Å) are similar to those observed in $[XeF][Bi_2F_{11}]$ (1.909(6) Å) and $[XeF][BiF_6]$ (1.913(7) Å),[5] indicating a high degree of $[XeF]^+$ cation ionization. The long N–Xe and short Xe–F bond lengths observed in both **1** and **2** can be attributed to the low basicity of NCCN.[31] The substantially longer N–Xe bond in **2** relative to **1** can be explained by the reduced basicity of the remaining C≡N group in **1** after the coordination of first $[XeF]^+$ cation. The N–Xe–F angle is nearly linear in both compounds (Table S2). The C–C bonds in **1** (1.418(8) Å) and **2** (1.396(3) Å) are elongated relative to that in free NCCN (1.3768(3) Å).[31] The shortening of the C≡N(Xe) bond in **1** (1.105(8) Å) and **2** (1.1370(19) Å), relative to NCCN (1.1509(3) Å), is consistent with previously characterized $[RNXeF]^+$ adduct-cations.[20,21] The length of the non-coordinated C≡N bond in **1** (1.152(8) Å) remains essentially unchanged compared to NCCN. The cations deviate slightly from linearity due to interactions with the $[AsF_6]^-$ anions, which adopt slightly distorted octahedral geometries (Table S3).

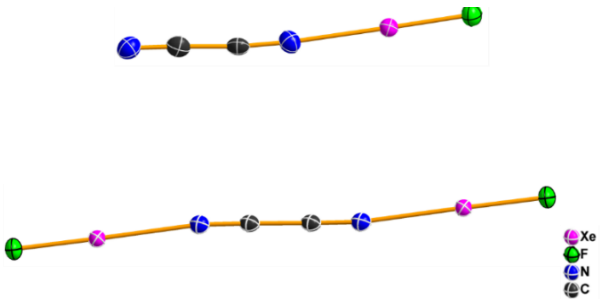


Figure 1. a) $[NCCNXeF]^+$ and $[FXeNCCNXeF]^{2+}$ cations. Anions are omitted for clarity and only the major component of disordered $[NCCNXeF]^+$ cation is shown. Displacement ellipsoids are shown at the 50 % probability level.

To better understand how coordination to a Lewis acid affects the geometry of the NCCN molecule, the previously reported $NCCNH[AsF_6]$ salt (**3**)[30] was crystallographically characterized (Table 1 and S1; Figure S6). The $NCCNH^+$ cation exhibits a C≡N(H) bond length (1.1346(14) Å), which is similar to those in adduct-cations **1** and **2**, whereas the C–C bond (1.3831(15) Å) is substantially shorter. The N–H···F hydrogen bond is short

(d(N···F) = 2.4676(12) Å) and lies barely within the 3σ range of the average N···F distance reported for other protonated nitriles, whereas the F···H distance (1.49(3) Å) is among the shortest reported so far (Table S4),[32,33] which can be attributed to the weak basicity of NCCN.[27] The As–F(···H) bond length (1.7988(7) Å) is consistent with values reported for other RC≡NH[AsF_6] salts (Table S4)[32,33] and is significantly longer than the remaining As–F bonds in **3** (1.7027(8)–1.7988(7) Å). The $NCCNH^+$ cation has been shown to be linear in the gas phase,[34] and its slight deviation from linearity in **3** likely arises from hydrogen bonding and other interactions present in the crystal structure. The experimentally determined molecular geometry of the $NCCNH^+$ cation is also of astrochemical significance, as this species has been detected in cold dark clouds.[35]

The Raman spectra of compounds **1** and **2** (Figure S7 and S8; Table S5 and S6) provide further insight into the bonding in these compounds. In **1**, the C≡N stretching vibration appears at 2370 cm^{-1}, whereas in **2** is observed at 2394 cm^{-1}. Both values are significantly shifted than that of free NCCN (2330 cm^{-1})[37] and are comparable to shifts observed for NCCN adducts with Lewis acids (Table S7). The Xe–F vibrations in **1** (588 and 595 cm^{-1}) and in **2** (592 and 600 cm^{-1}) are substantially shifted relative to that of XeF_2 (497 cm^{-1})[36] and other $[RNXeF]^+$ cations,[16–22] and approach the values reported for [XeF][MF_6] and [XeF][M_2F_{11}] (Table S7).[1,4] These shifts, together with the Xe–F bond distances obtained from crystal-structure analysis, further indicate that the $[XeF]^+$ cation is highly ionized and that NCCN is a weak Lewis base.

A sharp peak around 500 cm^{-1} in both **1** and **2** likely corresponds to the ν_4 vibrational mode of NCCN.[38] The bands at 682 cm^{-1}, 575 cm^{-1}, and around 370 cm^{-1} in both spectra originate from the $[AsF_6]^-$ anion, as similar bands are observed in [O_2][AsF_6][38] and in other [RNXeF][AsF_6] salts.[16–22] This indicates that the $[AsF_6]^-$ anions do not interact significantly with the cations. The N–Xe stretching frequencies in **1** (187 and 196 cm^{-1}) and in **2** (226 and 250 cm^{-1}) are in good agreement with the value reported for [F_3S≡NXeF][AsF_6] (194 cm^{-1}).[21] The calculated (VWN) and experimental Raman spectra of **1** and **2** are also in good agreement (Table S5, S6).

Formation of [XeNC(F)C(F)NXe][AsF_6]$_2$ – the First C=N–Xe Bonding Modality.

[FXeNCCNXeF][AsF_6]$_2$ in aHF solution at room temperature undergoes a 1,3-fluoride shift and converts to [Xe–N=CF–CF=N–Xe][AsF_6]$_2$ (**4**) (Scheme 1, Figure 3; Figure S10–S12), which crystallizes as a pale yellow solid (Figure S13). Complete conversion of **2** to **4** occurs in the solid state at room temperature over the course of one month (Figure S14) and is completed within 10 minutes at 75 °C (Figure S15). Although a similar rearrangement reaction has been observed for $[F_3S{\equiv}NXeF]^+$ transforming into $[F_4S{=}NXe]^+$,[39] this is the first example of such a conversion in a molecule containing only carbon and nitrogen.

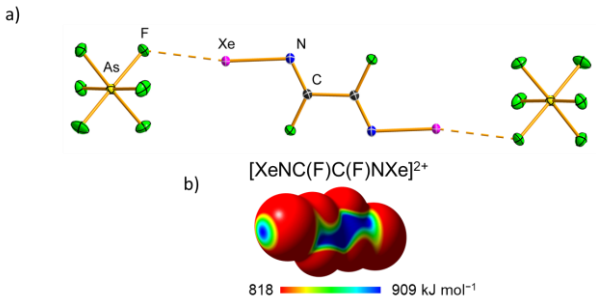


Figure 2. a) Crystal structure of **4**. Thermal ellipsoids are drawn at 50 % probability level. Xe···F contacts are represented by orange dashed lines; b) MEPS of the cation in **4** (0.001 au).

LT SCXRD of **4** (Table 1 and S1, Figure 3, Figure S10) reveals the first example of the C=N−Xe bonding modality. The N−Xe bond length (2.0620(9) Å) is similar to those observed in $[F_5S{-}N(H)Xe]^+$ (2.069(4) Å),[40] and is somewhat shorter than the N−Xe bond in $[F_4S{=}NXe]^+$ (2.084(3) Å)[39] and $[(FO_2S)_2NXe]^+$ (2.12(1) Å).[41] The C=N−Xe angle (113.11(6)°) is slightly smaller than the S=N−Xe angle (118.0(2)°) in $[F_4S{=}NXe]^+$.[39] The xenon atom is coordinated by the $[AsF_6]^-$ anion with a relatively long Xe···F distance (2.6455(8) Å), comparable to that observed in $[F_5S{-}N(H)Xe][AsF_6]$.[40] This distance is 75 % relatively shorter than the sum of the van der Waals (vdW) radii of xenon and fluorine (3.52 Å).[42] The nearly linear N−Xe···F contact (170.05(3)°) is consistent with values reported in other structures (Table S2) and also distorts the $[AsF_6]^-$ anion from an ideal octahedral geometry, a common feature in related compounds[39,40] Both the linearity and t he short Xe···F distance indicate polarization of the xenon atom, which is further supported by the molecular electrostatic potential of the $[XeNC(F)C(F)NXe]^{2+}$ cation (Figure 3) where σ-hole is evident on xenon atom. The electrostatic potential is somewhat smaller than on xenon atom in $[XeF]^+$, but it is larger than in $[XeOTeF_5]^+$ cation. The coordination of the cation in **4** with the weakly coordinating $[AsF_6]^-$ anion, together with its stability at room temperature, makes it an attractive new noble-gas-based Lewis acid. Although the ethandiimidoyldifluoride moiety is novel in noble-gas chemistry, it has previously been observed in the crystal structure of *N*,*N*′-dibromoethandiimidoyldifluoride, BrNCFCFNBr.[43] The overall geometry of moiety is similar, with only C−C bond in **4** (1.502(2) Å) being significantly longer than in BrNCFCFNBr (1.451(11) Å). The C=N (1.2689(14) Å) and C−F (1.3005(13) Å) bonds in **4** fall within 3σ of those in BrNCFCFNBr, whereas the C=N−Xe angle in **4** (113.09(7)°) is slightly smaller than C=N−Br angle in BrNCFCFNBr (116.5(6)°, 117.4(6)°).

The Raman spectrum of **4** (Figure S16, Table S10) is dominated by the strong vibrations of the $[AsF_6]^-$ anion, with peaks at 368, 374, 549, and 585 cm^{-1}, as well as a broader set of peaks in the 630–745 cm^{-1} region, all of which indicate a significant deviation from the ideal octahedral geometry. The N−Xe vibration (218 cm^{-1}) is lower than in $[F_4S{=}NXe][AsF_6]$ (253 cm^{-1}) and is comparable to $[F_5S{-}N(H)Xe][AsF_6]$ (224 cm^{-1}). Comparison of the Raman spectrum of BrNCFCFNBr[43] with that of **4** shows that both the C=N vibrations (1654, 1674 cm^{-1} in **4**; 1659 cm^{-1} in BrNCFCFNBr) and the C−C vibrations (1338, 1330 cm^{-1} in **4**; 1321 cm^{-1} in BrNCFCFNBr) are similar. Similarities are also evident in the infrared spectrum (Figure S1, Table S11), where the C−F vibration in **4** (1162 cm^{-1}) is close to that in BrNCFCFNBr (1140 cm^{-1}).[43]

Synthesis of Adduct-Cations Containing N−Xe−N Linkage From $[XeNC(F)C(F)NXe][AsF_6]_2$

To investigate the Lewis acidic properties of $[XeNC(F)C(F)NXe]^{2+}$ cation, **4** was reacted with two Lewis bases: CH_3CN and HCN. These bases were chosen because of their high IE (calculated EA(**4**) = 12.6 eV) and their prior use in the synthesis of compounds containing Xe−N bonds, such as $[HCNXeF][AsF_6]$[16,18,20] $[CH_3CN{\cdots}XeOXe{\cdots}NCCH_3][AsF_6]_2$,[23] $CH_3CN{\cdots}XeOF_2$,[44] and $CH_3CN{\cdots}XeF_6$.[45]

The reaction of **4** with an excess of CH_3CN or HCN in aHF at low temperatures yielded $[RCN{\cdots}XeNC(F)C(F)NXe\cdots NCR][AsF_6]_2$ adduct-cations, where R is CH_3 (**5**) (Figure 4a, Figure S18 and S19) or H (**6**) (Figure 4b, Figures S21 and S22), both featuring the rare N−Xe−N linkage.

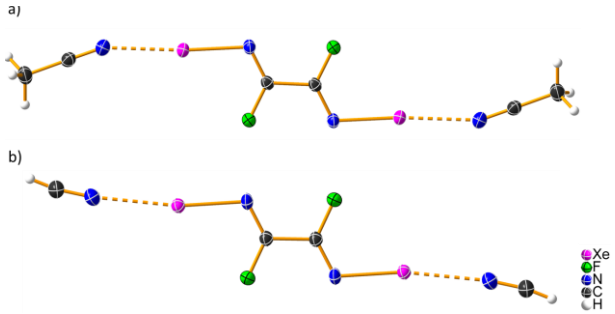


Figure 3. Adduct-cations featuring N—Xe—N linkage in the structures of **5** and **6** a) $[CH_3CN\cdots XeNC(F)C(F)NXe\cdots NCCH_3]^{2+}$ adduct-cation in **5**; b) $[HCN\cdots XeNC(F)C(F)NXe\cdots NCH]^{2+}$ adduct-cation in **6**. Thermal ellipsoids are drawn at 50 % probability level.

Other known compounds featuring this type of linkage include $Xe[N(SO_2F)_2]_2$,[46] $Xe[N(SO_2CF_3)_2]_2$[47] and $[F_4S{=}NXe\cdots N{\equiv}SF_3][AsF_6]$,[48] with only the $[F_4S{=}NXe\cdots N{\equiv}SF_3][AsF_6]$ being crystallographically characterized. In both **5** and **6**, the Xe—N(=C) bond length (2.081(3) Å in **5**; 2.078 (3) Å in **6**) is slightly elongated relative to that in **4** (2.0620(9) Å). The Xe···N(≡C) contact in **5** (2.513(3) Å) is shorter than in **6** (2.589(3) Å), consistent with HCN being a weaker base than CH_3CN,[27] in $[F_4S{=}NXe\cdots N{\equiv}SF_3]^+$ (2.583(3) Å),[48] and $[C_6F_5{-}Xe\cdots NCCH_3]^+$ (2.610(11)–2.681(8) Å)[25,26] but considerably longer than in $[CH_3CN\cdots XeOXe\cdots NCCH_3]^{2+}$ (2.294(2), 2.304(2) Å).[23] The C≡N bond length in the coordinated nitrile (1.139(5) Å in **5**; 1.130(5) Å in **6**) is essentially the same as in the crystal structures of CH_3CN (1.141(5) Å)[49] and HCN (1.19(15) Å).[50] The N—Xe···N angle in **5** (175.27(11)°) is closer to linearity than in **6** (170.57(11)°) and in $[F_4S{=}NXe\cdots N{\equiv}SF_3][AsF_6]$ (168.4(1)°).[48]

The Raman spectra of **5** and **6** (Figure S20 and S23; Table S12, S13) show vibrations arising from the $[AsF_6]^-$ anions (372, 643, 681 cm^{-1} for **5**; 372, 579, 646, 680 cm^{-1} for **6**, as well as sharp nitrile vibrations (2273, 2302 cm^{-1} for **5**; 2123 cm^{-1} for **6**. These nitrile bands are blue-shifted relative to the corresponding non-coordinated nitriles (2248 cm^{-1} in CH_3CN; 2104 cm^{-1} in HCN).[26,51] The shifts in **5** and **6** are smaller than those in the $[CH_3CNXeF]^+$ (2330 cm^{-1}) and $[HCNXeF]^+$ (2159, 2163 cm^{-1}) adduct-cations.[16,18,19] The C≡N Raman shift in **5** is smaller than in $[CH_3CN\cdots XeOXe\cdots NCCH_3]^{2+}$ (2284, 2290 cm^{-1}),[23] but closely matches those of $[C_6F_5{-}Xe\cdots NCCH_3]^+$ (2273, 2278 cm^{-1}).[26] The N—Xe stretching frequencies in **5** (221 cm^{-1}) and **6** (222 cm^{-1}) are similar to that reported for $[F_5S{-}N(H)Xe]^+$ (224 cm^{-1}),[40] but significantly lower than in $[F_4S{=}NXe]^+$ (253, 259 cm^{-1})[39] and $[F_4S{=}NXe\cdots N{\equiv}SF_3]^+$ cations (284 cm^{-1}).[48] The (C)N···Xe vibration in **5** (123 cm^{-1}) and **6** (126 cm^{-1}) are slightly higher than in $[F_4S{=}NXe\cdots N{\equiv}SF_3]^+$ (113 cm^{-1}).

Conclusions

In this work, the reactivity of NCCN with $[XeF][AsF_6]$ is reported for the first time. The isolation and crystallographic characterization of **2** provide the first example of a nitrogen base coordinated to two $[XeF]^+$ cations. The rearrangement of **2**, both in solution and in the solid state, yields **4**, featuring an unprecedented —C=N—Xe bonding motif. Compound **4** features a polarized xenon atom that functions as a novel noble-gas Lewis acid, as illustrated by the isolation of **5** and **6**, which contain rare examples of the N—Xe—N linkage.

Supporting Information

The authors have cited additional references within the Supporting Information.[52–68]

Acknowledgment

Funding for this research was provided by: European Research Council (ERC) under the European Union's Horizon 2020 research and innovation programme (Grant agreement No. 950625); Jožef Stefan Institute Director's Fund.

Keywords

Noble-gas chemistry • xenon-nitrogen bonds • solid-state reactivity • σ-hole interactions

References

[1] M. Tramšek, B. Žemva, *Acta Chim. Slov.* **2006**, *53*, 105–116.
[2] D. S. Brock, G. J. Schrobilgen, B. Žemva in *Comprehensive Inorganic Chemistry II, From Elements to Applications, Vol. 1 (Eds. J. Reedijk, K. Poeppelmeier),* Elsevier, Netherlands, **2013**, pp. 755–822.
[3] H. P. A Mercier, M. R. Bortolus, G. J. Schrobilgen in *Comprehensive Inorganic Chemistry III, Vol. 3 (Eds. J. Reedijk, K. Poeppelmeier),* Elsevier, Netherlands, **2023**, pp. 439–526.
[4] B. Žemva, *Croat. Chem. Acta* **1988**, 163–187.
[5] H. S. A. Elliott, J. F. Lehmann, H. P. A. Mercier, H. D. B. Jenkins, G. J. Schrobilgen, *Inorg. Chem.* **2010**, *49*, 8504–8523.
[6] P. Politzer, J. S. Murray, T. Clark, *Phys. Chem. Chem. Phys.* **2013**, *15*, 11178–11189.
[7] P. J. MacDougall, G. J. Schrobilgen, R. F. W. Bader, *Inorg. Chem.* **1989**, *28*, 763–769.
[8] G. Cavallo, P. Metrangolo, R. Milani, T. Pilati, A. Priimagi, G. Resnati, G. Terraneo, *Chem. Rev.* **2016**, *116*, 2478–2601.
[9] V. Nemec, K. Lisac, N. Bedeković, L. Fotović, V. Stilinović, D. Cinčić, *CrystEngComm* **2021**, *23*, 3063–3083.
[10] L. Brammer, A. Peuronen, T. M. Roseveare, *Acta Crystallogr.* **2023**, *C79*, 204–216.
[11] J. T. Goettel, K. Matsumoto, H. P. A. Mercier, G. J. Schrobilgen, *Angew. Chem. Int. Ed.* **2016**, *128*, 13780–13783; *Angew. Chem.* **2016**, *128*, 13984–13987.
[12] J. T. Goettel, H. P. A. Mercier, G. J. Schrobilgen, *J. Fluorine Chem.* **2018**, *211*, 60–69.
[13] K. M. Marczenko, H. P. A. Mercier, G. J. Schrobilgen, *Angew. Chem. Int. Ed.* **2018**, *57*, 12448–12452; *Angew. Chem.* **2018**, *38*, 12628–12632
[14] K. M. Marczenko, H. P. A. Mercier, J. T. Goettel, G. J. Schrobilgen, *Angew. Chem. Int. Ed.* **2025**, e202425216; *Angew. Chem.* e202425216.
[15] A. Bauzá, A. Frontera, *Angew. Chem. Int. Ed.* **2015**, *54*, 7340–7343; *Angew. Chem.* **2015**, *127*, 7448–7451.
[16] A. A. A. Emara, G. J. Schrobilgen, *J. Chem. Soc., Chem. Commun.* **1987**, 1644–1646.
[17] A. A. A. Emara, G. J. Schrobilgen, *J. Chem. Soc., Chem. Commun.* **1988**, 257–259.
[18] A. A. A. Emara, G. J. Schrobilgen, *Inorg. Chem.* **1992**, *31*, 1323–1332.
[19] A. A. A. Emara, PhD Thesis, McMaster University, Ontario, 1991 (CAN)
[20] B. A. Fir, Master Thesis, McMaster University, Ontario, 1991 (CAN)
[21] G. L. Smith, H. P. A. Mercier, G. J. Schrobilgen, *Inorg. Chem.* **2007**, *46*, 1369–1378.
[22] G. J. Schrobilgen, *J. Chem. Soc., Chem. Commun.* **1988**, 1506–1508.
[23] J. R. DeBackere, M. R. Bortolus, G. J. Schrobilgen, *Angew. Chem. Int. Ed.* **2016**, *55*, 11917–11920; *Angew. Chem.* **2016**, *128*, 12096–12098.
[24] A. N. Toraman, L. Fischer, A. Pérez-Bitrián, A. Wiesner, K. F. Hoffmann, S. Riedel, *Chem. Commun.* **2024**, *60*, 1711–1714.
[25] H. J. Frohn, S. Jakobs, G. Henkel, *Angew. Chem. Int. Ed.* **1989**, *28*, 1506–1507.

[26] K. Koppe, H. J. Frohn, H. P. A. Mercier, G. J. Schrobilgen, *Inorg. Chem.* **2008**, *47*, 3205–3217.
[27] Computational Chemistry Comparison and Benchmark DataBase, *National Institute of Standards and Technology*, can be found under https://webbook.nist.gov/cgi/inchi?ID=C460195&Mask=20#Ion-Energetics, (accessed: 27. 11. 2025)
[28] B. Corain, *Coord. Chem. Rev.* **1982**, 165–200.
[29] J. Beck, M. Zink, *Z. Anorg. Allg. Chem.* **2009**, *635*, 692–699.
[30] R. Minkwitz, W. Meckstroth, *Z. Anorg. Allg. Chem.* **1992**, *618*, 139–134.
[31] B. H. Torrie, B. M. Powell, *J. Phys.: Condens. Matter* **1989**, *1*, 5827–5835.
[32] R. Haiges, A. F. Baxter, N. R. Goetz, J. A. Axhausen, T. Soltner, A. Kornath, K. O. Christe, *Dalton Trans.* **2016**, *45*, 8494–8499.
[33] N. R. Goetz, J. A. H. Axhausen, T. Soltner, C. Rotter, A. J. Kornath, *ChemistrySelect*, **2016**, *1*, 5517–5520.
[34] G. Cazzoli, C. D. Esposti, F. Scappini, *J. Chem. Phys.* **1992**, *97*, 6187–6190.
[35] M. Agúndez, J. Cernicharo, P. de Vicente, N. Marcelino, E. Roueff, A. Fuente, M. Gerin, M. Guélin, C. Albo, A. Barcia, L. Barbas, R. Bolaño, F. Colomer, M. C. Diez, J. D. Gallego, J. Gómez-González, I. López-Fernández, J. A. López-Fernández, J. A. López-Pérez, I. Malo, J. M. Serna, F. Tercero, *Astron. Astrophys.* **2015**, *579*, article number L10
[36] P. A. Agron, G. M. Begun, H. A. Levy, A. A. Mason, C. G. Jones, D. F. Smith, *Science* **1963**, *139*, 842–844.
[37] H. G. M. Edwards, *J. Mol. Struct.* **1997**, *415*, 37–44.
[38] J. E. Griffiths, W. A. Sunder, *J. Chem. Phys.* **1982**, *77*, 1087–1092.
[39] G. L. Smith, H. P. A. Mercier, G. J. Schrobilgen, *J. Am. Chem. Soc.* **2009**, *131*, 7272–7286.
[40] G. L. Smith, H. P. A. Mercier, G. J. Schrobilgen, *Inorg. Chem.* **2008**, *47*, 4173–4184.
[41] R. Faggiani, D. K. Kennepohl, C. J. L. Lock, G. J. Schrobilgen, *Inorg. Chem.* **1986**, *25*, 563–571.
[42] S. Alvarez, *Dalton Trans.* **2013**, *42*, 8617–8636.
[43] A.Waterfeld, W. Isenberg, R. Mews, W. Clegg, G. M. Sheldrick, *Chem. Ber.* **1983**, *116*, 724–731.
[44] D. S. Brock, V. Bilir, H. P. A. Mercier, G. J. Schrobilgen, *J. Am. Chem. Soc.* **2007**, *129*, 3598–3611.
[45] K. Matsumoto, J. Haner, H. P. A. Mercier, G. J. Schrobilgen, *Angew. Chem. Int. Ed.* **2015**, *54*, 14169–14173; *Angew. Chem.* **2015**, *127*, 14375–143799.
[46] D. D. DesMarteau, R. D. LeBlond, S. F. Hossain, D. Nothe, *J. Am. Chem. Soc.* **1981**, *103*, 7734–7739.
[47] J. Foropoulos Jr., D. D. DesMarteau, *J. Am. Chem. Soc.* **1982**, *104*, 4260–4261.
[48] G. L. Smith, G. J. Schrobilgen, *Inorg. Chem.* **2009**, *48*, 7714–7728.
[49] R. Enjalbert, J. Galy, *Acta Crystallogr., Sect. B* **2002**, *B58*, 1005–1010.
[50] W. J. Dulmage, W. N. Lipscomb, *Acta Crystallogr.* **1951**, *4*, 330–334.
[51] M. Pézolet, R. Savoie, *Can. J. Chem.* **1969**, *47*, 3041–3048.
[52] A. Šmalc, K. Lutar, S. A. Kinkead in *Inorganic Syntheses*, *Vol. 29* (Eds. R. N. Grimes), John Wiley & Sons, New York, **1992**. pp 1–4.
[53] Z. Mazej, B. Žemva, *J. Fluorine Chem.* **2005**, *126*, 1432–1434.
[54] R. J. Gillespie, B. Landa, *Inorg. Chem.* **1973**, *12*, 1383–1388.
[55] Rigaku OD (2025). CrysAlis PRO. Rigaku Corporation, Wrocław, Poland.
[56] Toby, B. H. Toby, R. B. Von Dreele, *J. Appl. Crystallogr.* **2013**, 46, 544–549.
[57] M, Veith, H. Bärnighausen, Acta Crystallogr. B, **1974**, 30, 1806–1813.

[58] M. Lozinšek, H. P. A. Mercier, G. J. Schrobilgen **2021**, *60*, 8149–8156.
[59] K. Motaln, K. Gurung, P. Brazda, A. Kokalj, K. Radan, M. Dragomir, B. Žemva, L. Palatinus, M. Lozinšek, *ACS Cent. Sci.* **2024**, *10*, 1733–1741.
[60] L. J. Bourhis, O. V. Dolomanov, R. J. Gildea, J. A. K. Howard, H. Puschmann, *Acta Cryst.* **2015**, A*71,* 59–75.
[61] O. V. Dolomanov, L. J. Bourhis, R. J. Gildea, J. A. K. Howard, H. Puschmann, *J. Appl. Crystallogr.* **2009**, *42*, 339–341.
[62] G. M. Sheldrick, *Acta Crystallogr. C* **2015**, 71, 3–8.
[63] K. Brandeburg, Diamond – Crystal and Molecular Structure Visualization, Crystal Impact GbR, Bonn, Germany, 2022
[64] J. F. Sawyer, G. J. Schrobilgen, S. J. Sutherland, *Inorg. Chem.* **1982**, *21*, 4064–4072.
[65] M. Schickinger, Y. Morgenstern, K. Stierstorfer, A. Kornath, *Z. Anorg. Allg. Chem.* **2017**, *643*, 1431–1435.
[66] I. C. Tornieporth-Oetting, T. M. Klapötke, T. S. Cameron, J. Valkonen, P. Rademacher, K. Kowski, *J. Chem. Soc. Dalton Trans.* **1992**, 537–543.
[67] J. Beck, M. Zink, *Z. Anorg. Allg. Chem.* **2009**, *635*, 687–691.
[68] N. Bartlett, M. Gennis, D. D. Gibler, B. K. Morrell, A. Zalkin, *Inorg. Chem.* **1973**, *12*, 1717–1721.

4.3 Hydrogen-Bonded Salt Cocrystals of Xenon Difluoride and Protonated Perfluoroamides

In this chapter, the results of the structural study of XeF_2 as a hydrogen-bond acceptor are presented. These results are described in the attached manuscript, which has been published in *CrystEngComm*. Erik Uran performed the experiments, analyzed the data, and contributed to both the interpretation of the results and the writing of the manuscript.

XeF_2 is a Lewis base and readily acts as a fluoride-ion donor. This behavior is most evident in the formation of tight-ion pairs $[XeF][MF_6]$, and coordination complexes in which XeF_2 functions as a ligand (Tramšek & Žemva, 2006). XeF_2 presumably forms [FXeF···HF] hydrogen bonds in aHF, as indicated by spectroscopic measurements (Nabiev, 1998). These hydrogen bonds are not only responsible for the high solubility of XeF_2 in aHF, but also enhance its oxidizing properties.

A systematic investigation of XeF_2 as a hydrogen-bond acceptor in the solid state has not yet been carried out, and only few examples have been characterized so far. These include the salt cocrystal $H_3O[AsF_6]\cdot 2XeF_2$ (Gerken, et al., 2009), the cocrystal $HNO_3\cdot XeF_2$ (Moran, Brock, Mercier, & Schrobilgen, 2010), and the coordination compounds $[Cd(FH)_2(XeF_2)(AF_6)_2]$ (A = Nb, Ta) (Tavčar & Tramšek, 2015; Lozinšek, 2013), in which O—H···F(Xe) and F—H···F(Xe) hydrogen bonds are observed. Another known example is $(CF_3C(OH)NH_2)[AsF_6]\cdot XeF_2\cdot n$HF which has been characterized in the solid state only by Raman spectroscopy. It has been suggested that the hydrogen-bonding motifs ROH···FXeF···HOR, R(H)NH···FXeF···HOR, and R(H)NH···FXeF···HN(H)R may exist in this salt cocrystal, together with solvated HF (Schrobilgen & Whalen, 1994).

To investigate the propensity of XeF_2 as a hydrogen-bond acceptor in greater detail, as understanding this behavior is important for the chemistry of XeF_2, two other salts based on protonated amides, $(C_2F_5C(OH)NH_2)[AsF_6]$ and $(C_3F_7C(OH)NH_2)[AsF_6]$, were cocrystallized with XeF_2. The previously known $(CF_3C(OH)NH_2)[AsF_6]\cdot XeF_2$ cocrystal was also synthesized. In addition, the crystal structures of protonated amides, $(CF_3C(OH)NH_2)[AsF_6]$, $(C_2F_5C(OH)NH_2)[AsF_6]$, and $(C_3F_7C(OH)NH_2)[AsF_6]$, as well as $(CF_3CONH_2)_2H[AsF_6]$ and $(C_3F_7CONH_2)_2H[AsF_6]$, were elucidated, as well as that of $H_3O[AsF_6]\cdot 2CF_3CONH_2$ salt cocrystal.

Single-crystal X-ray diffraction analysis shows that all amides are O-protonated, in agreement with previous observations of amide protonation in superacidic media (Axhausen, Ritter, & Kornath, 2013; Saal, Haiges, & Christe, 2023). O—H···F(As) and N—H···F(As) hydrogen bonds are present between cations and anions. In the hemiprotonated salts, $(CF_3CONH_2)_2H[AsF_6]$ and $(C_3F_7CONH_2)_2H[AsF_6]$, a short but asymmetric O—H···O hydrogen bond is observed. The crystal structure of $H_3O[AsF_6]\cdot 2CF_3CONH_2$ features a neutral amide molecule that acts as a hydrogen-bond donor towards $[AsF_6]^-$ anion via N—H···F(As) interactions and as a hydrogen-bond acceptor toward the oxonium cation via O—H···O hydrogen bonds.

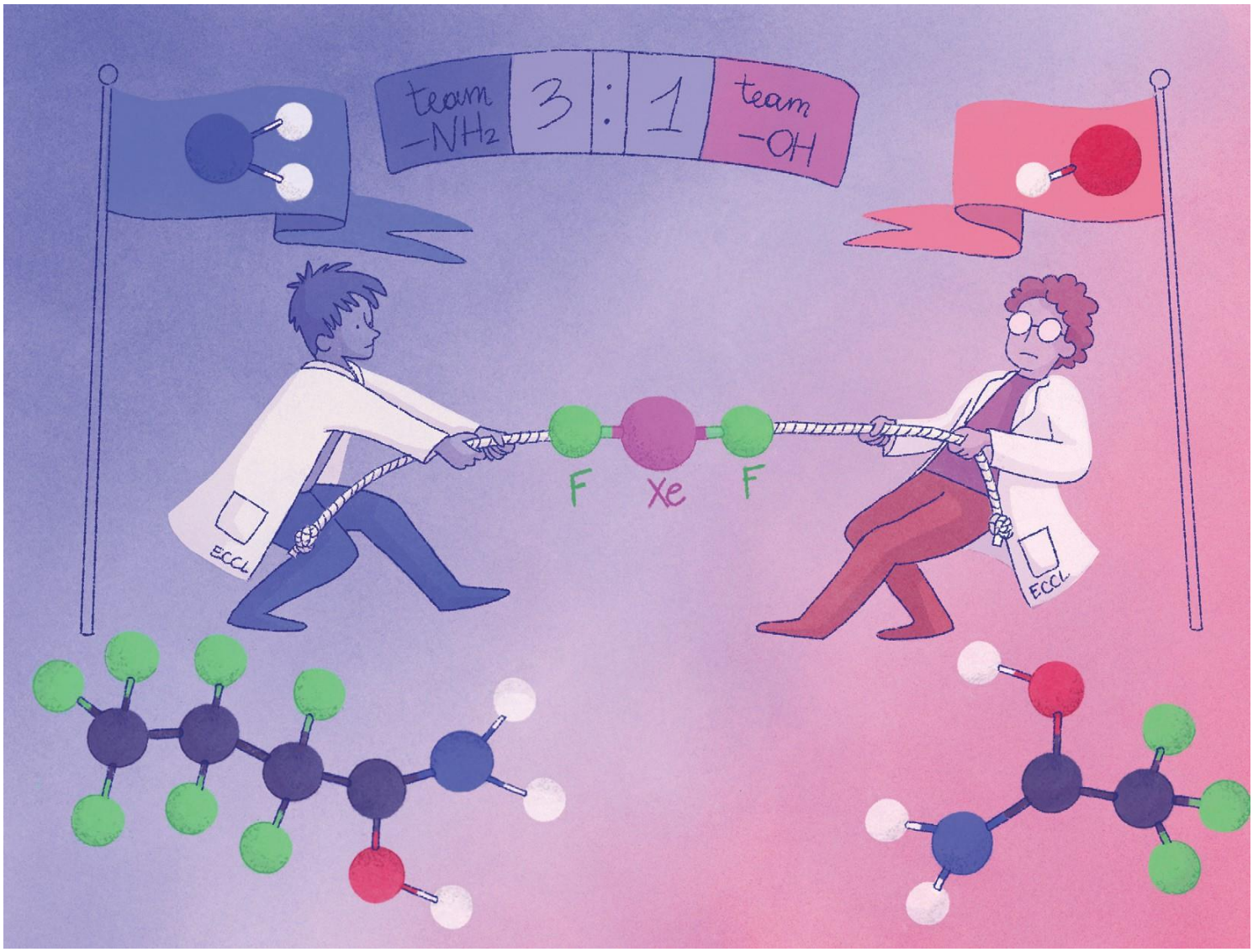
The XeF_2 salt cocrystals feature xenon difluoride acting as a hydrogen-bond acceptor with O—H and N—H groups. These structures represent the first examples in which N—H···F(Xe) hydrogen bonds are crystallographically characterized, and it has been shown that such bonds are preferentially formed, with the O—H···F(Xe) hydrogen bond observed only in $(CF_3C(OH)NH_2)[AsF_6]\cdot XeF_2$. Analysis of Xe—F bond lengths, combined with low-temperature Raman spectroscopy, indicates that XeF_2 is only slightly distorted due to the hydrogen bonding, consistent with other examples of XeF_2 acting as a hydrogen-bond acceptor.

In the following pages, only the most relevant information from the Supplementary Information is given.

Volume 27
Number 48
28 December 2025
Pages 7745–7984

CrystEngComm

rsc.li/crystengcomm



ISSN 1466-8033

ROYAL SOCIETY OF CHEMISTRY

PAPER
Erik Uran and Matic Lozinšek
Hydrogen-bonded salt cocrystals of xenon difluoride and protonated perfluoroamides

CrystEngComm

ROYAL SOCIETY OF CHEMISTRY

PAPER

View Article Online
View Journal | View Issue

Check for updates

Cite this: *CrystEngComm*, 2025, **27**, 7776

Hydrogen-bonded salt cocrystals of xenon difluoride and protonated perfluoroamides†

Erik Uran [ab] and Matic Lozinšek [*ab]

Received 3rd October 2025,
Accepted 31st October 2025

DOI: 10.1039/d5ce00956a

rsc.li/crystengcomm

The hydrogen-bonding ability of XeF_2 is an important factor influencing its chemical properties and reactivity, yet structurally characterised examples of hydrogen-bonded xenon fluorides remain rare. In this work, three salt cocrystals containing hydrogen-bonded xenon difluoride and hexafluoridoarsenate salts of protonated perfluoroamides—$CF_3C(OH)NH_2[AsF_6]\cdot XeF_2$, $C_2F_5C(OH)NH_2[AsF_6]\cdot XeF_2$, and $C_3F_7C(OH)NH_2[AsF_6]\cdot XeF_2$—were synthesised and structurally characterised. Diverse hydrogen-bonding motifs were observed, and the first crystallographically characterised examples of N–H···FXeF hydrogen bonds are presented. In total, eleven new crystal structures are reported, including two perfluoroamides, three protonated and two hemiprotonated perfluoroamides, and one salt cocrystal containing an oxonium ion. The XeF_2-containing cocrystals demonstrate that XeF_2 reliably functions as a hydrogen-bond acceptor and readily forms hydrogen-bonded cocrystals. These findings broaden the scope of noble-gas chemistry and highlight the potential of noble-gas fluorides for cocrystal formation.

Open Access Article. Published on 04 November 2025. Downloaded on 12/9/2025 10:41:59 AM.
This article is licensed under a Creative Commons Attribution 3.0 Unported Licence.

Introduction

Xenon difluoride (XeF_2) is the most common and extensively studied binary noble-gas fluoride and serves as a precursor to a wide range of xenon compounds.[1,2] It is a nonpolar molecular compound with linear geometry. XeF_2 is a good fluoride-ion donor[3] and thus forms a variety of Lewis acid–base adducts[4] and a plethora of coordination compounds with metal cations.[1,2,5]

The ability of XeF_2 to act as a hydrogen-bond acceptor strongly influences its physical and chemical properties. As a nonpolar molecule, it is highly soluble in the polar protic solvent anhydrous HF (aHF) (167 g/100 g at 30 °C).[6] This unusually high solubility arises from the formation of FXe–F···HF hydrogen bonds.[7–9] Furthermore, XeF_2 dissolved in aHF is a considerably more potent oxidiser than pure XeF_2, and even trace amounts of HF can catalyse its reactions with organic substrates through the hydrogen-bonding induced polarisation [$FXe^{\delta+}$–$F^{\delta-}$···HF].[10] HF also facilitates fluorine exchange in XeF_2, enabling the synthesis of ^{18}F-radiolabelled XeF_2.[11,12] In certain cases, the influence of HF is so pronounced that it can unexpectedly alter reaction outcomes, even when inadvertently generated by reaction with the vessel material.[13]

Despite the ability of XeF_2 to act as a hydrogen-bond acceptor, systematic crystallographic investigations are absent, and reported solid-state examples remain scarce. To date, only a handful of crystallographically characterised examples of hydrogen-bonded XeF_2 have been described. These include O–H···FXeF hydrogen bonds observed in $H_3O[AsF_6]\cdot 2XeF_2$ and in $HNO_3\cdot XeF_2$ cocrystals,[14,15] as well as an F–H···FXeF interaction observed in the coordination complex $[Cd(HF)_2(XeF_2)(MF_6)_2]$ (M = Ta, Nb).[5,16]

It has also been shown spectroscopically that protonated trifluoroacetamide (CF_3CONH_2) forms a hydrogen-bonded salt cocrystal[17] with XeF_2, $CF_3C(OH)NH_2[AsF_6]\cdot XeF_2\cdot xHF$.[18] This cocrystal is particularly noteworthy, as it may feature both $=OH^+$ and $-NH_2$ groups as hydrogen-bond donors,[18] potentially offering insight into the hydrogen-bonding preferences of XeF_2.

To investigate the hydrogen-bonding propensity of XeF_2 in the solid state and its tendency to form cocrystals with NH and OH hydrogen-bond donors, the crystal structures of XeF_2 salt cocrystals with protonated CF_3CONH_2, $C_2F_5CONH_2$, and $C_3F_7CONH_2$ were studied in this work. The perfluoroamides were selected because of their anticipated resistance to oxidative-fluorination by XeF_2.

Results and discussion

Crystal structures of $CF_3CF_2CONH_2$ and $CF_3CF_2CF_2CONH_2$

The crystal structures of pentafluoropropionamide ($C_2F_5CONH_2$) and heptafluorobutyramide ($C_3F_7CONH_2$) were elucidated by low-temperature single-crystal X-ray diffraction (LT SCXRD)

[a] *Extreme Condition Chemistry Laboratory (ECCL K2), Jožef Stefan Institute, Jamova cesta 39, 1000 Ljubljana, Slovenia. E-mail: matic.lozinsek@ijs.si*
[b] *Jožef Stefan International Postgraduate School, Jamova cesta 39, 1000 Ljubljana, Slovenia*

† Dedicated to Professor Resnati, celebrating a career in fluorine and noncovalent chemistry on the occasion of his 70th birthday.

This journal is © The Royal Society of Chemistry 2025

View Article Online
CrystEngComm Paper

Open Access Article. Published on 04 November 2025. Downloaded on 12/9/2025 10:41:59 AM.
This article is licensed under a Creative Commons Attribution 3.0 Unported Licence.

Table 1 Summary of crystal data and refinement results for crystal structures of amides and protonated amides

Compound	$C_2F_5CONH_2$	$C_3F_7CONH_2$	$CF_3C(OH)NH_2[AsF_6]$	$C_2F_5C(OH)NH_2[AsF_6]$	$C_3F_7C(OH)NH_2[AsF_6]$
Space group	$C2/c$	$P\bar{1}$	$P2_1/c$	$Pccn$	$P2_1/c$
a (Å)	21.7871(5)	5.11713(18)	9.81910(18)	8.12957(13)	6.17592(15)
b (Å)	5.11704(12)	5.27137(14)	7.90095(13)	25.2768(4)	7.94187(19)
c (Å)	10.0754(3)	12.7768(3)	20.5015(4)	9.34322(16)	21.7914(5)
α (°)	90	95.467(2)	90	90	90
β (°)	98.140(2)	91.890(3)	98.6498(18)	90	96.014(2)
γ (°)	90	105.584(3)	90	90	90
V (Å^3)	1111.94(5)	329.847(18)	1572.42(5)	1919.93(5)	1062.95(4)
M	163.06	213.07	302.97	352.98	402.99
Z	8	2	8	8	4
T (K)	100	100	100	100	100
$R[F^2 > 2\sigma(F^2)]$	0.048	0.028	0.033	0.027	0.027
$wR(F^2)$	0.138	0.076	0.087	0.058	0.068

(Tables 1 and S1), whereas the crystal structure of CF_3CONH_2 has been previously reported at 295 K and 110 K.[19,20] For comparison of bond lengths (Table S2), only the structure obtained at 110 K was considered.[20]

$C_2F_5CONH_2$ (Fig. 1a and S1) crystallizes in the monoclinic space group $C2/c$ with Z = 8. The C=O bond length (1.2323(19) Å) is comparable to the distances observed in the crystal structures of other primary amides, and the same applies to the C–N bond (1.317(2) Å).[21] Two N–H···O hydrogen bonds (2.912(2) Å, 171(2)°; 2.8396(17) Å, 149(2)°; Table S3) in the crystal structure form $R_2^2(8)$ and $R_6^4(16)$ hydrogen-bonding motifs,[22] which assemble into a corrugated layer parallel to the bc plane (Fig. S2 and S3).

$C_3F_7CONH_2$ (Fig. 1b and S4) crystallizes in the triclinic space group $P\bar{1}$ with Z = 2. The C=O bond distance (1.2293(15) Å) is essentially identical to that in $C_2F_5CONH_2$, as is the C–N bond (1.3162(16) Å). These bond distances are shorter than the corresponding ones observed in non-fluorinated secondary amides, such as capsaicin.[23] Two N–H···O hydrogen bonds

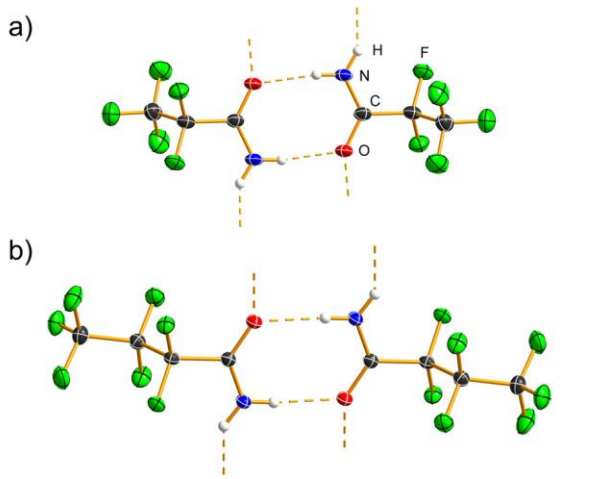


Fig. 1 $R_2^2(8)$ hydrogen-bonding motifs in the crystal structures of (a) $C_2F_5CONH_2$ and (b) $C_3F_7CONH_2$. Hydrogen bonds are shown as dashed orange lines. Displacement ellipsoids are drawn at the 50% probability level, and hydrogen atoms are represented as spheres of arbitrary radius.

(Table S4) are present in the crystal structure (2.9313(14) Å, 174.3(16)°; 2.8495(14) Å, 140.4(15)°), which fall within the typical range for amide molecules.[21] The $R_2^2(8)$ and $R_4^2(8)$ hydrogen-bond motifs link the molecules into a ladder along the a-crystallographic axis (Fig. S5).

Protonation of amides in superacidic media HF–AsF_5

All amides are soluble in aHF and readily undergo protonation upon addition of AsF_5. In all cases, protonation occurs at the oxygen atom, consistent with previous observations.[18,24–26] Low-temperature crystallisation from aHF afforded crystals of suitable quality for SCXRD.

$CF_3C(OH)NH_2[AsF_6]$ (Tables 1, S1 and S2; Fig. S6) crystallises in the monoclinic space group $P2_1/c$ with Z = 8 and Z' = 2. Upon protonation, the C=O bonds (1.2795(19), 1.282(2) Å) lengthen and the C–N bonds (1.279(2), 1.281(2) Å) shorten relative to those in CF_3CONH_2 (1.2304(12) and 1.3164(13) Å, respectively).[20] These changes in the C=O and C–N bond lengths are consistent with previous crystallographic studies of protonated amides.[25–27] The O–H···F hydrogen bonds (2.5860(16) Å, 2.6530(18) Å; Table S5) bracket the value observed in $CF_3C(OH)NH_2[SbF_6]$ (2.600(1) Å), whereas the N–H···F hydrogen bonds (2.8236(18)–3.0797(18) Å) are comparable to those in $CF_3C(OH)$-$NH_2[SbF_6]$ (2.884(2), 2.933(2) Å).[26] All hydrogen-bond angles (121(2)–179(3)°) fall within the typical range. The $[AsF_6]^-$ anions deviate from ideal octahedral geometry, with the longest As–F bonds (1.7524(10), 1.7557(10) Å) participating in hydrogen bonding with $=OH^+$ group. In the crystal structure, cations and anions are linked through O–H···F and N–H···F hydrogen-bonded chains (Fig. 2a and S7).

$C_2F_5C(OH)NH_2[AsF_6]$ (Tables 1, S1 and S2) crystallises in the orthorhombic space group $Pccn$ with Z = 8 and features a disordered $-C_2F_5$ moiety (Fig. S8). Perfluorinated alkyl chains frequently exhibit disorder in the crystalline state,[28] as F···F interactions are relatively weak,[29] and can therefore adopt various conformations. The C=O (1.2821(15) Å) and C–N (1.2772(16) Å) bonds are longer and shorter, respectively, than those in $C_2F_5CONH_2$. The $[AsF_6]^-$ anion deviates from ideal octahedral geometry, with the *mer*-As–F bonds involved

Open Access Article. Published on 04 November 2025. Downloaded on 12/9/2025 10:41:59 AM.
This article is licensed under a Creative Commons Attribution 3.0 Unported Licence.

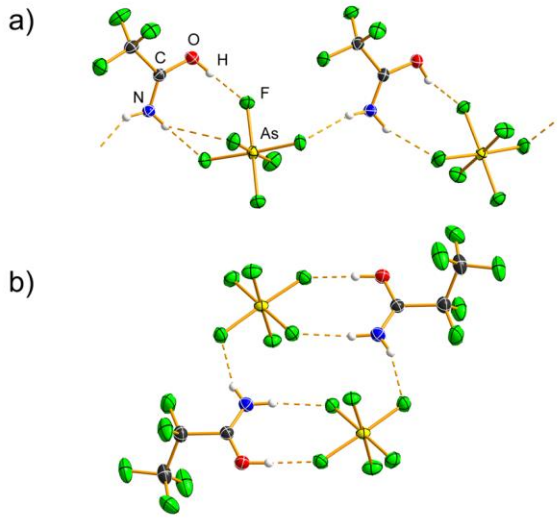


Fig. 2 Crystal structure of (a) the hydrogen-bonded chain in $CF_3C(OH)NH_2[AsF_6]$ and (b) the discrete hydrogen-bonded cluster in $C_2F_5C(OH)NH_2[AsF_6]$ (only one orientation of the disordered $-C_2F_5$ unit is shown). Hydrogen bonds are shown as dashed orange lines. Displacement ellipsoids are drawn at the 50% probability level, and hydrogen atoms are represented as spheres of arbitrary radius.

in hydrogen bonding being longer (1.7253(8)–1.7453(8) Å) than the remaining As–F bonds (1.6976(8)–1.7111(8) Å). The hydrogen bonds (Table S6) between the $=OH^+$ and $-NH_2$ groups and the $[AsF_6]^-$ anions (O(H)···F, 2.6006(12) Å, 172(2)°; N(H)···F, 2.8309(13) Å, 174(2)° and 2.8316(14) Å, 161.3(19)°) lead to the formation of discrete units (Fig. 2b, S8 and S9), exhibiting $R_2^2(8)$ and $R_4^4(12)$ hydrogen-bonding motifs.

$C_3F_7C(OH)NH_2[AsF_6]$ (Tables 1, S1 and S2) crystallises in the monoclinic space group $P2_1/c$ with $Z = 4$, with the $[AsF_6]^-$ anion disordered over two positions (Fig. S10). The C=O bond (1.2797(14) Å) is elongated, and the C–N bond (1.2841(16) Å) is shortened compared to those in $C_3F_7CONH_2$. A similar C=O(H) bond distance (1.274(2) Å) was observed in the crystal structure of $(C_6F_5)_2COH[AsF_6]$.[30] Hydrogen bonds (Table S7) are formed between the $=OH^+$ group (2.541(3), 2.557(3) Å; 157(3), 165(3)°) or the $-NH_2$ group (2.737(4)–3.179(5) Å, 118.0(19)–168.1(19)°) and the $[AsF_6]^-$ anions. The O···F hydrogen bond is the shortest among the protonated amides in this study, and also shorter than those in $CH_3C(OH)NH_2[AsF_6]$[25] and $CF_3C(OH)NH_2[SbF_6]$.[26] The $[AsF_6]^-$ anion deviates from ideal octahedral geometry (1.642(3)–1.795(2) Å). The $C_3F_7C(OH)NH_2^+$ cations and $[AsF_6]^-$ anions are linked into a hydrogen-bonded ribbon (Fig. 3 and S11), exhibiting conjoined $R_4^4(12)$, $R_2^4(8)$ and $R_2^2(8)$ motifs.

Two hemiprotonated salts, $(CF_3CONH_2)_2H[AsF_6]$ and $(C_3F_7CONH_2)_2H[AsF_6]$ (Fig. 4 and S12–S17; Tables 2, S1 and S2), were also crystallographically characterised. The former was inadvertently found during the low-temperature crystal selection and mounting of the $CF_3C(OH)NH_2[AsF_6]\cdot XeF_2$ sample, whereas the latter was identified as an impurity in

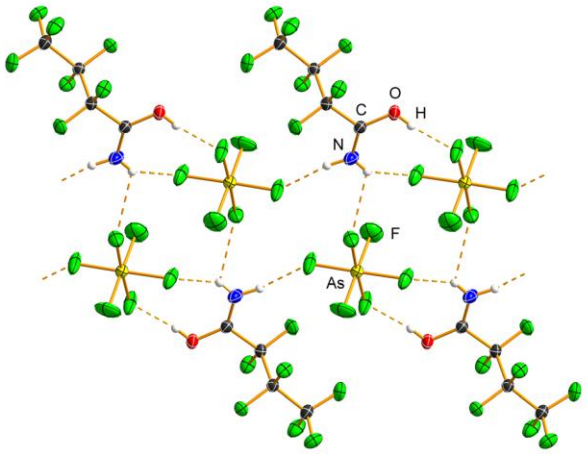


Fig. 3 Hydrogen-bonded ribbon in $C_3F_7C(OH)NH_2[AsF_6]$ (only one orientation of the disordered $[AsF_6]^-$ anion is shown). Hydrogen bonds are shown as dashed orange lines. Displacement ellipsoids are drawn at the 50% probability level, and hydrogen atoms are represented as spheres of arbitrary radius.

the sample of $C_3F_7C(OH)NH_2[AsF_6]\cdot XeF_2$ salt cocrystals. Both compounds crystallise in the triclinic space group $P\bar{1}$ with $Z = 2$. In both structures, the C=O bonds are elongated (1.283(6) Å in $(CF_3CONH_2)_2H[AsF_6]$; 1.2652(9), 1.2459(9) Å in $(C_3F_7CONH_2)_2H[AsF_6]$), whereas the C–N bonds are shortened (1.274(7) Å in $(CF_3CONH_2)_2H[AsF_6]$; 1.2942(10), 1.3027(10) Å in $(C_3F_7CONH_2)_2H[AsF_6]$) compared to the non-protonated amides.[20] The values for one of the amide molecules in $(CF_3CONH_2)_2H[AsF_6]$ fall within the

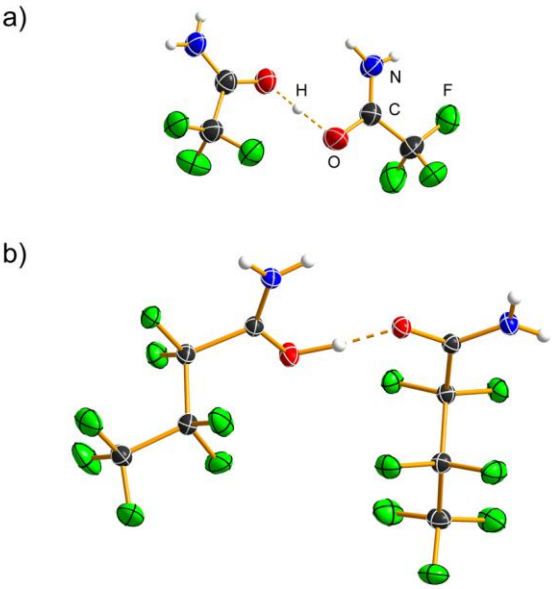


Fig. 4 Hydrogen-bonded dimers in the crystal structure of (a) $(CF_3CONH_2)_2H[AsF_6]$ and (b) $(C_3F_7CONH_2)_2H[AsF_6]$. The short O–H···O=C hydrogen bonds are shown as dashed orange lines. Displacement ellipsoids are drawn at the 50% probability level, and hydrogen atoms are represented as spheres of arbitrary radius.

 This journal is © The Royal Society of Chemistry 2025

View Article Online

Open Access Article. Published on 04 November 2025. Downloaded on 12/9/2025 10:41:59 AM.
This article is licensed under a Creative Commons Attribution 3.0 Unported Licence.

Table 2 Summary of crystal data and refinement results for hemiprotonated amides and $H_3O[AsF_6]\cdot 2CF_3CONH_2$ salt cocrystal

Compound	$(CF_3CONH_2)_2H[AsF_6]$	$(C_3F_7CONH_2)_2H[AsF_6]$	$H_3O[AsF_6]\cdot 2CF_3CONH_2$
Space group	$P\bar{1}$	$P\bar{1}$	*Pnma*
a (Å)	5.2815(3)	5.32051(4)	11.5349(2)
b (Å)	10.1517(6)	10.45222(9)	14.0649(3)
c (Å)	12.4911(6)	16.10170(12)	7.78994(14)
α (°)	108.936(5)	90.5740(6)	90
β (°)	93.107(5)	90.8760(6)	90
γ (°)	102.904(5)	103.0402(7)	90
V (Å^3)	611.63(6)	872.156(12)	1263.82(4)
M	416.02	616.06	434.04
Z	2	2	4
T (K)	100	100	100
$R[F^2 > 2\sigma(F^2)]$	0.047	0.022	0.037
w$R(F^2)$	0.125	0.055	0.085

range for neutral amide,[20] owing to the relatively high standard uncertainties of the bond lengths. The O(H)···O hydrogen bond length in $(CF_3CONH_2)_2H[AsF_6]$ (2.426(5) Å, 170(8)°) is essentially identical to that in $(C_3F_7CONH_2)_2H[AsF_6]$ (2.4174(9) Å, 172(2)°) (Tables S8 and S9), and comparable to literature values for such hydrogen-bonded systems.[21] The nearly equidistant position of the hydrogen atom (O–H, H···O: 1.13(9), 1.31(9) Å in $(CF_3CONH_2)_2H[AsF_6]$; 1.06(2), 1.36(2) Å in $(C_3F_7CONH_2)_2H[AsF_6]$), together with the relatively short O···O distances, indicates strong, positive charge-assisted hydrogen bonding, (+)CAHB.[31] These structures represent rare examples of proton sharing between two primary amide molecules,[21,32] a motif more commonly observed in secondary and tertiary amides.[21] The $-NH_2$ groups are hydrogen-bonded to $[AsF_6]^-$ anions (N···F, 2.644(5)–3.005(5) Å in $(CF_3CONH_2)_2H[AsF_6]$; 2.8168(9)–3.1046(9) Å in $(C_3F_7CONH_2)_2H[AsF_6]$) (Fig. S13–S17), resulting in the formation of ribbons that are further interconnected by the anions into layers parallel to the *ab* plane.

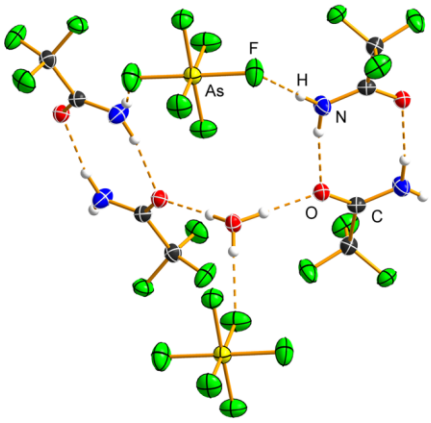


Fig. 5 $R_6^4(14)$ hydrogen-bonded cluster in the crystal structure of the $H_3O[AsF_6]\cdot 2CF_3CONH_2$ salt cocrystal. Hydrogen bonds are shown by dashed orange lines. Displacement ellipsoids are drawn at the 50% probability level, and hydrogen atoms are represented as spheres of arbitrary radius.

A crystal of $H_3O[AsF_6]\cdot 2CF_3CONH_2$ (Tables 2, S1 and S2; Fig. 5 and S18–S20) was fortuitously found during the low-temperature crystal selection and mounting of the $CF_3C(OH)NH_2[AsF_6]\cdot XeF_2$ sample. It crystallises in the orthorhombic space group *Pnma* with $Z = 4$. The amide molecule is not protonated, resulting in C=O (1.236(4) Å) and C–N (1.304(4) Å) bond lengths that are close to those in CF_3CONH_2.[20] The amide molecule acts as both a hydrogen-bond donor and acceptor (Table S10, Fig. S19), forming N–H···F(As) and N–H···O(C) hydrogen bonds. An $R_2^2(8)$ motif is observed between two amide molecules, with the N···O hydrogen bond (2.959(4) Å, 171(4)°) comparable to that found in CF_3CONH_2.[20] The H_3O^+ cation forms three hydrogen bonds: two symmetrically equivalent O–H···O(C) (2.525(3) Å, 167(4)°) and one O–H···F hydrogen bond (2.657(5) Å, 173(7)°) with the $[AsF_6]^-$ anion. Together, these hydrogen bonds form a hydrogen-bonded cluster represented by $R_6^6(20)$, $R_6^4(14)$ and $R_2^2(8)$ graph-set motifs[22] (Fig. 5), which further extend into a layer parallel to the *bc* plane (Fig. S20).

Hydrogen-bonded salt cocrystals of XeF_2

The reaction of amides with equimolar amounts of $[XeF][AsF_6]$ at temperatures down to −30 °C leads to the formation of $RC(OH)NH_2[AsF_6]\cdot XeF_2$ salt cocrystals. This indicates that a proton from HF is transferred to the amide, generating a protonated amide, while the resulting fluoride anion reacts with $[XeF]^+$ to form XeF_2. This behaviour was also reported in a previous study of the CF_3CONH_2–$[XeF][AsF_6]$ system.[18]

The salt cocrystals (Tables 3, S1 and S2) thus feature protonated amides cocrystallised with XeF_2 and exhibit a rare O–H···FXeF hydrogen bond, as well as the first crystallographically characterised examples of N–H···FXeF hydrogen bonds.

$CF_3C(OH)NH_2[AsF_6]\cdot XeF_2$ (Fig. 6 and S21) crystallises in the monoclinic space group $P2_1/n$ with $Z = 4$. The XeF_2 molecule exhibits slight asymmetry in Xe–F bond distances (1.9669(10), 2.0237(9) Å) compared to pure XeF_2 (1.999(4) Å),[33] and it remains linear (178.10(5) Å). The asymmetry of XeF_2 is slightly smaller than that observed in $XeF_2\cdot HNO_3$ (1.9737(8), 2.0506(8) Å).[15]

View Article Online
Paper CrystEngComm

Open Access Article. Published on 04 November 2025. Downloaded on 12/9/2025 10:41:59 AM. This article is licensed under a Creative Commons Attribution 3.0 Unported Licence.

Table 3 Summary of crystal data and refinement results for salt cocrystals of protonated amides with XeF_2

Compound	$CF_3C(OH)NH_2[AsF_6]\cdot XeF_2$	$C_2F_5C(OH)NH_2[AsF_6]\cdot XeF_2$	$C_3F_7C(OH)NH_2[AsF_6]\cdot XeF_2$
Space group	$P2_1/n$	$Aea2$	$Pnna$
a (Å)	7.41785(9)	8.67561(10)	8.62011(14)
b (Å)	9.84875(11)	31.0125(4)	35.5418(5)
c (Å)	14.90113(17)	8.65174(9)	8.71910(12)
α (°)	90	90	90
β (°)	99.4517(11)	90	90
γ (°)	90	90	90
V (Å^3)	1073.85(2)	2327.77(4)	2671.31(7)
M	472.27	522.28	572.29
Z	4	8	8
T (K)	100	100	100
$R[F^2 > 2\sigma(F^2)]$	0.025	0.018	0.026
w$R(F^2)$	0.067	0.038	0.066

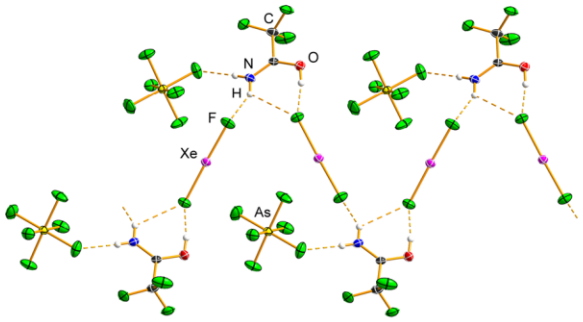


Fig. 6 Hydrogen-bonded ribbon in the crystal structure of the salt cocrystal $CF_3C(OH)NH_2[AsF_6]\cdot XeF_2$. Only one orientation of the disordered $-CF_3$ moiety is shown. Hydrogen bonds are shown as dashed orange lines. Displacement ellipsoids are drawn at the 50% probability level, and hydrogen atoms are represented as spheres of arbitrary radius.

$CF_3C(OH)NH_2[AsF_6]\cdot XeF_2$ is the only salt cocrystal in this series that exhibits both O–H···F(Xe) and N–H···F(Xe) hydrogen bonds. One fluorine atom of XeF_2 is acting as a bifurcated acceptor (Fig. 6 and S21; Table S11). The O–H···F(Xe) hydrogen bond (2.5467(14) Å, 171(3)°) is shorter than that in $H_3O[AsF_6]\cdot 2XeF_2$ (2.571(3) Å)[14] and $HNO_3\cdot XeF_2$ (2.690(1) Å).[15] It is also significantly shorter than the O–H···F(As) hydrogen bonds in $CF_3C(OH)NH_2[AsF_6]$ and $C_2F_5C(OH)NH_2[AsF_6]$, but comparable to that in $C_3F_7C(OH)NH_2[AsF_6]$. The N–H···F(Xe) hydrogen bonds (2.7865(15) Å, 151(3)°; 3.0894(16), 124(2)°), which involve a single bifurcated donor, are longer than those observed in the other two salt cocrystals described in this study. The C=O (1.2773(15) Å) and C–N (1.2772(16) Å) bond lengths are essentially identical to those in the protonated salts,[26] indicating a negligible influence of hydrogen bonding on the overall geometry of the $CF_3C(OH)NH_2^+$ cation. The $-CF_3$ moiety is disordered, as also observed in the crystal structure of CF_3CONH_2.[20] The $[AsF_6]^-$ anion participates in hydrogen bonding with the $-NH_2$ group (2.8270(18) Å, 176(3)°; 3.0594(15) Å, 111(2)°), resulting in a slight deviation from ideal octahedral geometry (As–F, 1.7006(12)–1.7417(11) Å).

Hydrogen bonds between $CF_3C(OH)NH_2^+$ and XeF_2 form a zigzag chain parallel to the b-crystallographic axis, with pendant $[AsF_6]^-$ anions connected to the chain *via* N–H···F(As) hydrogen bonds, giving rise to a ribbon-like structure (Fig. 6 and S22).

Both $C_2F_5C(OH)NH_2[AsF_6]\cdot XeF_2$ and $C_3F_7C(OH)NH_2[AsF_6]\cdot XeF_2$ (Tables 3, S1 and S2; Fig. S23–S26) crystallise in orthorhombic space groups, *Aea*2 and *Pnna*, respectively, with $Z = 8$. The asymmetry of the Xe–F bond lengths in $C_2F_5C(OH)NH_2[AsF_6]\cdot XeF_2$ (1.9734(14), 2.0061(15) Å) and in $C_3F_7C(OH)NH_2[AsF_6]\cdot XeF_2$ (1.9674(15), 2.0135(16) Å) is comparable. The shorter Xe–F bonds are similar to that observed in the trifluoroacetamide analogue, whereas the longer Xe–F bonds are significantly shorter. In both cocrystals, the F–Xe–F angle is essentially linear (179.88(9)°; 179.57(7)°).

The N–H···F(Xe) hydrogen bonds (Tables S12 and S13) in $C_2F_5C(OH)NH_2[AsF_6]\cdot XeF_2$ (2.688(3), 2.729(3) Å) and $C_3F_7C(OH)NH_2[AsF_6]\cdot XeF_2$ (2.692(3), 2.737(3) Å) are comparable and are significantly shorter than the corresponding hydrogen bonds in $CF_3C(OH)NH_2[AsF_6]\cdot XeF_2$. The C=O (1.289(2), 1.285(3) Å) and C–N (1.279(3), 1.280(3) Å) bond lengths in $C_2F_5C(OH)NH_2[AsF_6]\cdot XeF_2$ and $C_3F_7C(OH)NH_2[AsF_6]\cdot XeF_2$ are almost identical to those observed in the corresponding protonated salts.

The protonated oxygen atom acts as a hydrogen-bond donor towards the $[AsF_6]^-$ anions, forming bifurcated hydrogen bonds (Fig. 7, S23 and S25), which are longer than the O–H···F(As) hydrogen bonds observed in the parent protonated salts.

The packing in both $C_2F_5C(OH)NH_2[AsF_6]\cdot XeF_2$ and $C_3F_7C(OH)NH_2[AsF_6]\cdot XeF_2$ consists of hydrogen-bonded ribbons composed of alternating protonated amide and XeF_2 molecules, similar to those observed in $CF_3C(OH)NH_2[AsF_6]\cdot XeF_2$. These ribbons are further connected by O–H···F(As) hydrogen bonds, and in the case of $C_3F_7C(OH)NH_2[AsF_6]\cdot XeF_2$, also by N–H···F(As) hydrogen bonds (Fig. S24 and S26).

The relatively small difference in Xe–F bond lengths in the present XeF_2 cocrystals suggests that hydrogen bonding has only a minor influence on XeF_2 ionisation ($XeF_2 \rightarrow XeF^+ +$

 This journal is © The Royal Society of Chemistry 2025

Open Access Article. Published on 04 November 2025. Downloaded on 12/9/2025 10:41:59 AM.
This article is licensed under a Creative Commons Attribution 3.0 Unported Licence.

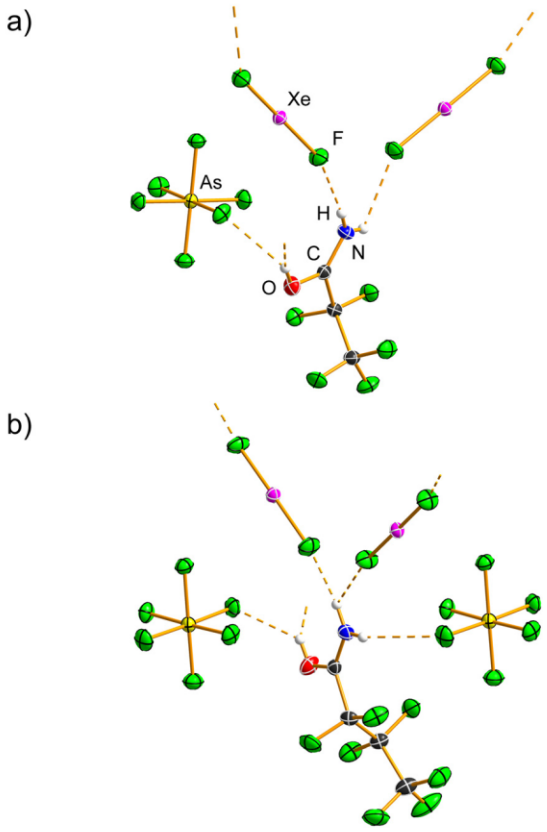


Fig. 7 Hydrogen bonds (dashed orange lines) in the crystal structures of the salt cocrystals (a) $C_2F_5C(OH)NH_2[AsF_6]\cdot XeF_2$ and (b) $C_3F_7C(OH)NH_2[AsF_6]\cdot XeF_2$. The OH groups are bifurcated hydrogen-bond donors; however, two $[AsF_6]^-$ anions have been omitted for clarity. Displacement ellipsoids are drawn at the 50% probability level, and hydrogen atoms are represented as spheres of arbitrary radius.

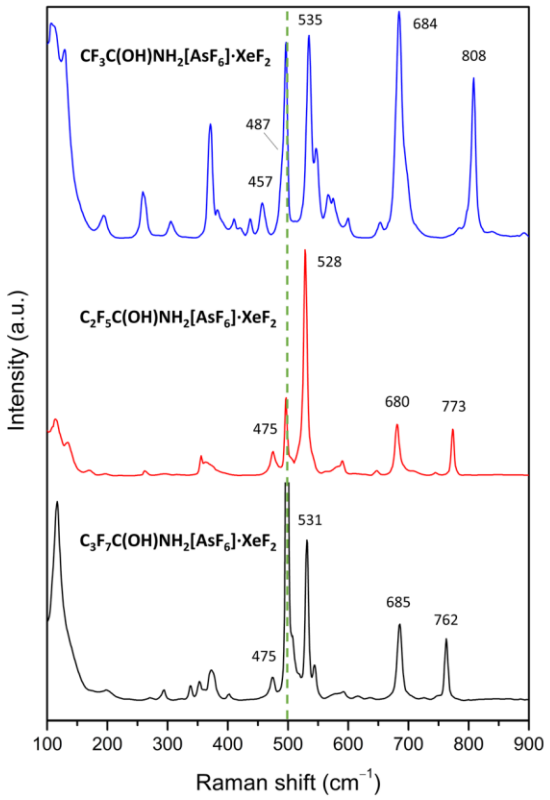


Fig. 8 Raman spectra of XeF_2 salt cocrystals with protonated amides recorded at low temperatures (−90 °C). The green dashed line is placed at the position of free XeF_2 (497 cm^{-1})[41] which was observed as an impurity in the reactions.

F^-).[34] In particular, the shorter Xe–F bonds (1.9669(10)–1.9734(14) Å) are considerably longer than those found in $[XeF]^+$ tight ion pairs[33,35,36] and in $[Xe_2F_3]^+$ salts.[35,37] They are comparable to the shortest Xe–F bond lengths in XeF_2 adduct-salts with $[BrOF_2]^+$ (1.956(5), 1.960(4) Å)[38] and $[BrO_2]^+$ cations (1.970(4)–1.978(3) Å).[39] Nevertheless, the distortion of hydrogen-bonded XeF_2 observed in the present salt cocrystals is significant when compared with Xe–F bond distances observed in the crystal structures containing cocrystallised XeF_2, *e.g.*, $3XeF_2\cdot 2MnF_4$ (1.9933(7) Å),[36] and in the molecular cocrystals $XeF_2\cdot XeF_4$ (1.9940(9) Å)[37] and $XeF_2\cdot XeOF_4$ (2.014(5) Å),[40] in which XeF_2 is centrosymmetric.

Vibrational spectroscopy

To corroborate the findings from LT SCXRD and to gain further insight into the ionisation of XeF_2, low-temperature Raman spectra were measured (Fig. 8 and S27–S40). Two bands at 457–475 and 528–535 cm^{-1} are observed in all XeF_2 salt cocrystals in this study, corresponding to the elongated and shortened Xe–F bond, respectively. These bands are significantly shifted from that of pure XeF_2 (497 cm^{-1})[41] and from values observed when cocrystallised XeF_2 does not participate in significant intermolecular interactions, such as in $XeF_2\cdot XeOF_4$ (494, 503 cm^{-1}),[40] $XeF_2\cdot XeF_4$ (505 cm^{-1}),[42] $3XeF_2\cdot 2MnF_4$ (508 cm^{-1}),[36] and $XeF_2\cdot N_2O_4$ (509 cm^{-1}).[15] The value of the higher-frequency band is comparable to the Raman shifts reported for the adduct salts $[BrOF_2][AsF_6]\cdot XeF_2$ (531, 543, 559 cm^{-1}),[38] $[BrO_2][AsF_6]\cdot nXeF_2$ (n = 1, 2; 516–546 cm^{-1}),[39] and for the hydrogen-bonded cocrystals $H_3O[AsF_6]\cdot 2XeF_2$ (552 cm^{-1})[14] and $HNO_3\cdot XeF_2$ (529 cm^{-1}).[15] However, these shifts are significantly smaller than those observed in $[XeF]^+$ tight-ion pair salts (>600 cm^{-1}) and $[Xe_2F_3]^+$ cations (580–600 cm^{-1}).[1,33,35,36,43,44] The band around 535 cm^{-1} is particularly noteworthy, as this value coincides with that observed for XeF_2 dissolved in aHF, which has been attributed to the FXe–F···HF hydrogen bonds.[7–9]

In addition to the bands attributed to XeF_2, those arising from $[AsF_6]^-$ anions are observed around 375 and 680 cm^{-1}.[18,25,26,45] Vibrations from the protonated amide molecules are also present, including an intense band around 800 cm^{-1} corresponding to ν(C–C),[25,26] and peaks near 1100 cm^{-1} attributed to C–F vibrations.[18,26,46] In all protonated amides, the N–H stretching vibrations were observed in 3150–3400 cm^{-1} range.[18,26,46]

View Article Online
Paper CrystEngComm

Open Access Article. Published on 04 November 2025. Downloaded on 12/9/2025 10:41:59 AM.
This article is licensed under a Creative Commons Attribution 3.0 Unported Licence.

Experimental

Caution! Anhydrous HF, AsF_5, XeF_2, $[XeF][AsF_6]$ and the compounds prepared in this study are highly reactive and hazardous. The amides used may cause skin, eye, and respiratory irritation. Contact with the skin must be avoided, and all compounds should be handled exclusively in a well-ventilated fume hood.

Appropriate safety precautions must be observed at all times, and working with minimal quantities is strongly recommended.

Materials and methods

Reactions were carried out in fluorinated ethylene propylene (FEP) vessels equipped with Kel-F or PTFE valves. All vessels were passivated with fluorine prior to use. Volatile substances were handled using a fluorine-resistant metal vacuum line, whereas solids were manipulated inside an N_2-filled glovebox. Detailed synthetic procedures are provided in the SI. Characterisation was performed by low-temperature single-crystal X-ray diffraction and low-temperature Raman spectroscopy. Single-crystal selection and mounting were carried out using a low-temperature crystal-mounting apparatus, as described previously (SI).[30,36,47] Low-temperature Raman spectra were recorded directly on the aluminium trough used for mounting single crystals for X-ray diffraction measurements.

Conclusions

In this work, the perfluoroamides trifluoroacetamide (CF_3CONH_2), pentafluoropropionamide ($C_2F_5CONH_2$), and heptafluorobutyramide ($C_3F_7CONH_2$), were protonated in superacidic medium HF–AsF_5, and the crystal structures of the resulting salts, $CF_3C(OH)NH_2[AsF_6]$, $C_2F_5C(OH)NH_2[AsF_6]$, and $C_3F_7C(OH)NH_2[AsF_6]$ were elucidated. Protonation at the carbonyl oxygen atom is consistently observed. In addition, the crystal structures of the amides $C_2F_5CONH_2$ and $C_3F_7CONH_2$, the hemiprotonated salts $(CF_3CONH_2)_2H[AsF_6]$ and $(C_3F_7CONH_2)_2H[AsF_6]$, and the oxonium salt cocrystal $H_3O[AsF_6]{\cdot}2CF_3CONH_2$ were determined. Low-temperature reactions of the perfluoroamides with $[XeF][AsF_6]$ in aHF yielded rare XeF_2-containing salt cocrystals: $CF_3C(OH)NH_2[AsF_6]{\cdot}XeF_2$, $C_2F_5C(OH)NH_2[AsF_6]{\cdot}XeF_2$ and $C_3F_7C(OH)NH_2[AsF_6]{\cdot}XeF_2$. Their crystal structures reveal a rare example of O–H···FXeF and the first crystallographically characterised cases of N–H···FXeF hydrogen bonding. The XeF_2 molecule is slightly polarised, as indicated by the differences observed in Xe–F bond lengths compared with those in free XeF_2; this finding is corroborated by low-temperature Raman spectroscopy. The reported crystal structures display diverse hydrogen-bonding motifs involving O–H···F(Xe), N–H···F(Xe), O–H···F(As) and N–H···F(As) interactions. The salt cocrystals prepared and structurally characterised in this study demonstrate that XeF_2 readily forms hydrogen-bonded cocrystals and serves as a reliable hydrogen-bond acceptor. These results open new possibilities for the exploration of cocrystal formation with noble-gas fluorides and the expansion of noble-gas chemistry.

Author contributions

Conceptualization, data curation, formal analysis, investigation, visualization, writing – original draft: EU; funding acquisition, methodology, project administration, resources, supervision: ML; validation, writing – review & editing: EU, ML. Both authors agreed on the final version of the article.

Conflicts of interest

There are no conflicts to declare.

Data availability

Supplementary information: crystallographic details, Raman spectra, experimental details. See DOI: https://doi.org/10.1039/d5ce00956a.

Crystallographic data for all reported crystal structures has been deposited at the Cambridge Crystallographic Data Centre (CCDC) under deposition numbers 2493130–2493140.[48a–k]

Data for this article, including SCXRD datasets and Raman spectra are available at Zenodo open repository at https://doi.org/10.5281/zenodo.17432981.

Acknowledgements

Financial support from the European Research Council (ERC) under the European Union's Horizon 2020 Research and Innovation Programme (Starting Grant No. 950625), the Slovenian Research and Innovation Agency (ARIS, Project No. J1-60022), and the Jožef Stefan Institute Director's Fund is gratefully acknowledged.

Notes and references

1 M. Tramšek and B. Žemva, *Acta Chim. Slov.*, 2006, **53**, 105–116.
2 D. S. Brock, G. J. Schrobilgen and B. Žemva in *Comprehensive Inorganic Chemistry II, From Elements to Applications*, ed. J. Reedijk and K. Poeppelmeier, Elsevier, Netherlands, 2013, vol. 1, pp. 755–822.
3 N. Bartlett and F. O. Sladky, *J. Am. Chem. Soc.*, 1968, **90**, 5316–5317.
4 B. Žemva, *Croat. Chem. Acta*, 1988, **61**, 163–187.
5 G. Tavčar and M. Tramšek, *J. Fluorine Chem.*, 2015, **174**, 14–21.
6 J. G. Malm, H. Selig, J. Jortner and S. A. Rice, *Chem. Rev.*, 1965, **65**, 199–236.
7 S. S. Nabiev and I. I. Ostroukhova, *Spectrochim. Acta, Part A*, 1993, **49**, 1537–1546.
8 S. S. Nabiev, *Russ. Chem. Bull.*, 1998, **47**, 535–559.

Open Access Article. Published on 04 November 2025. Downloaded on 12/9/2025 10:41:59 AM.
This article is licensed under a Creative Commons Attribution 3.0 Unported Licence.

9 S. M.-J. Yeh, *PhD Thesis*, University of California, 1984, (available at: https://escholarship.org/uc/item/9b1195zf).
10 M. A. Tius, *Tetrahedron*, 1995, **51**, 6605–6634.
11 G. Schrobilgen, G. Firnau, R. Chirakal and E. S. Garnett, *J. Chem. Soc., Chem. Commun.*, 1981, 198–199.
12 N. Vasdev, B. E. Pointner, R. Chirakal and G. J. Schrobilgen, *J. Am. Chem. Soc.*, 2002, **124**, 12863–12868.
13 M. M. Nielsen and C. M. Pedersen, *Chem. Sci.*, 2022, **33**, 6181–6196.
14 M. Gerken, M. D. Moran, H. P. A. Mercier, B. E. Pointner, G. J. Schrobilgen, B. Hoge, K. O. Christe and J. A. Boatz, *J. Am. Chem. Soc.*, 2009, **131**, 13474–13489.
15 M. D. Moran, D. S. Brock, H. P. A. Mercier and G. J. Schrobilgen, *J. Am. Chem. Soc.*, 2010, **132**, 13823–13839.
16 M. Lozinšek, *PhD Thesis*, University of Ljubljana, 2013.
17 S. Aitipamula, R. Banerjee, A. K. Bansal, K. Biradha, M. L. Cheney, A. R. Choudbury, G. Desiraju, A. Dikundwar, R. Dubey, N. Duggirala, P. P. Ghogale, S. Ghosh, P. K. Goswami, N. R. Goud, R. K. R. Jetti, P. Karpinski, P. Kaushik, D. Kumar, V. Kumar, B. Moulton, A. Mukherjee, H. Mukherjee, A. S. Myerson, V. Puri, A. Ramanan, T. Rajamannar, C. M. Reddy, N. Rodriguez-Horned, R. D. Rogers, T. N. G. Row, P. Sanphui, N. Shan, A. Singh, C. C. Sun, J. A. Swift, R. Thaimattam, T. S. Thakur, R. K. Thaper, S. P. Thomas, S. Tothadi, V. R. Vangala, P. Vishweshwar, D. R. Weyna and M. J. Zaworotko, *Cryst. Growth Des.*, 2012, **12**, 2147–2152.
18 G. J. Schrobilgen and J. M. Whalen, *Inorg. Chem.*, 1994, **33**, 5207–5218.
19 B. Kalyanaraman, L. D. Kispert and J. L. Atwood, *Acta Crystallogr., Sect. B*, 1978, **34**, 1131–1136.
20 F. R. Fronczek and N. H. Fischer, CCDC 174252: Experimental Crystal Structure Determination, 2002, DOI: 10.5517/cc5vb1c.
21 C. R. Groom, I. J. Bruno, M. P. Lightfoot and S. C. Ward, *Acta Crystallogr., Sect. B: Struct. Sci., Cryst. Eng. Mater.*, 2016, **72**, 171–179.
22 M. C. Etter, J. C. MacDonald and J. Bernstein, *Acta Crystallogr., Sect. B: Struct. Sci.*, 1990, **46**, 256–262.
23 M. Lozinšek, *Acta Crystallogr., Sect. C: Struct. Chem.*, 2025, **81**, 188–192.
24 R. J. Gillespie and T. Birchall, *Can. J. Chem.*, 1963, **41**, 148–155.
25 J. Axhausen, C. Ritter, K. Lux and A. Kornath, *Z. Anorg. Allg. Chem.*, 2013, **639**, 65–72.
26 T. Saal, R. Haiges and K. O. Christe, *Dalton Trans.*, 2023, **52**, 18143–18147.
27 M. C. Bayer, N. Greither, V. Bockmair, A. Nitzer and A. J. Kornath, *Eur. J. Inorg. Chem.*, 2022, **2022**, e202200501.
28 A. Dey, P. Metrangolo, T. Pilati, G. Resnati, G. Terraneo and I. Wlassics, *J. Fluorine Chem.*, 2009, **130**, 816–823.
29 Sakshi, Y. Gupta, C. M. Robertson, P. Munshi and A. R. Choudhury, *CrystEngComm*, 2025, **27**, 478–487.
30 E. Uran and M. Lozinšek, *Acta Crystallogr., Sect. C: Struct. Chem.*, 2025, **81**, 577–583.
31 P. Gilli, L. Pretto, V. Bertolasi and G. Gilli, *Acc. Chem. Res.*, 2009, **42**, 33–44.
32 A. I. Gubin, M. Z. Buranbaev and N. N. Nurakhmetov, *Kristallografiya*, 1988, **33**, 506–508.
33 H. S. A. Elliot, J. F. Lehmann, H. P. A. Mercier, H. D. B. Jenkins and G. J. Schrobilgen, *Inorg. Chem.*, 2010, **49**, 8504–8523.
34 B. Žemva, A. Jesih, D. H. Templeton, A. Zalkin, A. K. Cheetham and N. Bartlett, *J. Am. Chem. Soc.*, 1987, **109**, 7420–7427.
35 K. Radan, E. Goreshnik and B. Žemva, *Angew. Chem., Int. Ed.*, 2014, **53**, 13715–13719 (*Angew. Chem.*, 2014, **126**, 13935–13939).
36 K. Motaln, K. Gurung, P. Brázda, A. Kokalj, K. Radan, M. Dragomir, B. Žemva, L. Palatinus and M. Lozinšek, *ACS Cent. Sci.*, 2024, **10**, 1733–1741.
37 M. R. Bortolus, H. P. A. Mercier, B. Nguyen and G. J. Schrobilgen, *Angew. Chem., Int. Ed.*, 2021, **60**, 23678–23686 (*Angew. Chem.*, 2021, **133**, 23871–23879).
38 D. S. Brock, J. J. Casalis de Puty, H. P. A. Mercier, G. J. Schrobilgen and B. Silvi, *Inorg. Chem.*, 2010, **49**, 6673–6689.
39 M. R. Bortolus, G. J. LaChapelle, H. P. A. Mercier, J. Haner and G. J. Schrobilgen, *Inorg. Chem.*, 2023, **62**, 8761–8771.
40 M. J. Hughes, D. S. Brock, H. P. A. Mercier and G. J. Schrobilgen, *J. Fluorine Chem.*, 2011, **132**, 660–668.
41 P. A. Agron, G. M. Begun, H. A. Levy, A. A. Mason, C. G. Jones and D. F. Smith, *Science*, 1963, **139**, 842–844.
42 C. J. Adams, *J. Raman Spectrosc.*, 1974, **2**, 391–397.
43 F. O. Sladky, P. A. Bulliner and N. Bartlett, *J. Chem. Soc. A*, 1969, 2179–2188.
44 K. Motaln, K. Gurung, M. Dragomir, D. Kurzydlowski, L. Palatinus and M. Lozinšek, *Inorg. Chem.*, 2025, **64**, 14968–14976.
45 K. Nakamoto, *Infrared and Raman Spectra of Inorganic and Coordination Compounds: Part A: Theory and Application in Inorganic Chemistry*, John Wiley & Sons, Hoboken, New Jersey, 2009.
46 E. K. Murthy and G. R. Rao, *J. Raman Spectrosc.*, 1988, **19**, 359–363.
47 M. Lozinšek, H. P. A. Mercier and G. J. Schrobilgen, *Angew. Chem., Int. Ed.*, 2021, **60**, 8149–8156 (*Angew. Chem.*, 2021, **133**, 8230–8237).
48 (*a*) CCDC 2493130: Experimental Crystal Structure Determination, 2025, DOI: 10.5517/ccdc.csd.cc2pp9k8; (*b*) CCDC 2493131: Experimental Crystal Structure Determination, 2025, DOI: 10.5517/ccdc.csd.cc2pp9l9; (*c*) CCDC 2493132: Experimental Crystal Structure Determination, 2025, DOI: 10.5517/ccdc.csd.cc2pp9mb; (*d*) CCDC 2493133: Experimental Crystal Structure Determination, 2025, DOI: 10.5517/ccdc.csd.cc2pp9nc; (*e*) CCDC 2493134: Experimental Crystal Structure Determination, 2025, DOI: 10.5517/ccdc.csd.cc2pp9pd; (*f*) CCDC 2493135: Experimental Crystal Structure Determination, 2025, DOI: 10.5517/ccdc.csd.cc2pp9qf; (*g*) CCDC 2493136: Experimental Crystal Structure Determination, 2025, DOI: 10.5517/ccdc.csd.cc2pp9rg; (*h*) CCDC 2493137: Experimental Crystal Structure Determination, 2025, DOI: 10.5517/ccdc.csd.cc2pp9sh; (*i*)

CCDC 2493138: Experimental Crystal Structure Determination, 2025, DOI: 10.5517/ccdc.csd.cc2pp9tj; (*j*) CCDC 2493139: Experimental Crystal Structure Determination, 2025, DOI: 10.5517/ccdc.csd.cc2pp9vk; (*k*) CCDC 2493140: Experimental Crystal Structure Determination, 2025, DOI: 10.5517/ccdc.csd.cc2pp9wl.

Open Access Article. Published on 04 November 2025. Downloaded on 12/9/2025 10:41:59 AM.
This article is licensed under a Creative Commons Attribution 3.0 Unported Licence.



 This journal is © The Royal Society of Chemistry 2025

Supplementary Information (SI) for CrystEngComm.
This journal is © The Royal Society of Chemistry 2025

Supplementary Information

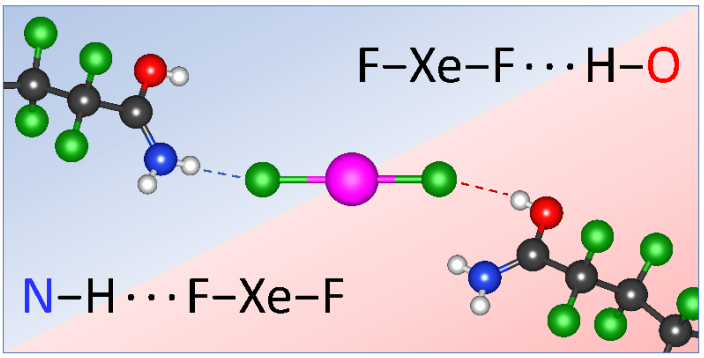
Hydrogen-Bonded Salt Cocrystals of Xenon Difluoride and Protonated Perfluoroamides

Erik Uran,[a,b] Matic Lozinšek*[a,b]

[a] *Extreme Condition Chemistry Laboratory (ECCL K2), Jožef Stefan Institute, Jamova cesta 39, 1000 Ljubljana, Slovenia*

[b] *Jožef Stefan International Postgraduate School, Jamova cesta 39, 1000 Ljubljana, Slovenia*

* Corresponding author: matic.lozinsek@ijs.si



DOI: 10.1039/D5CE00956A

Table S2. C=O, C–N, (O)C–C bond lengths (Å) and N–C–O angles (°)

Compound	C=O	C–N	(O)C–C	N–C–O
CF_3CONH_2[1]	1.2304 (12)	1.3164 (13)	1.5395 (14)	126.71 (9)
$C_2F_5CONH_2$	1.2323 (19)	1.317 (2)	1.536 (2)	125.71 (16)
$C_3F_7CONH_2$	1.2293 (15)	1.3162 (16)	1.5480 (16)	126.19 (11)
$CF_3C(OH)NH_2[AsF_6]$	1.282 (2) 1.2795 (19)	1.279 (2) 1.281 (2)	1.543 (2) 1.537 (2)	127.51 (16) 127.50 (15)
$C_2F_5C(OH)NH_2[AsF_6]$	1.2821 (15)	1.2772 (16)	1.5307 (17)	127.37 (11)
$C_3F_7C(OH)NH_2[AsF_6]$	1.2797 (14)	1.2841 (16)	1.5370 (15)	127.81 (11)
$(CF_3CONH_2)_2H[AsF_6]$	1.283 (6) 1.247 (6)	1.274 (7) 1.293 (7)	1.516(7) 1.518 (7)	125.8 (5) 124.1 (5)
$(C_3F_7CONH_2)_2H[AsF_6]$	1.2652 (9) 1.2459 (9)	1.2942 (10) 1.3027 (10)	1.5369 (10) 1.08 (10)	126.65 (7) 123.81 (7)
$H_3O[AsF_6]\cdot 2CF_3CONH_2$	1.236 (4)	1.304 (4)	1.545(4)	125.5 (3)
$CF_3C(OH)NH_2[AsF_6]\cdot XeF_2$	1.2773 (15)	1.2772 (16)	1.5342 (15)	127.37 (11)
$C_2F_5C(OH)NH_2[AsF_6]\cdot XeF_2$	1.289 (2)	1.279 (3)	1.531 (3)	126.4 (2)
$C_3F_7C(OH)NH_2[AsF_6]\cdot XeF_2$	1.285 (3)	1.280 (3)	1.531 (3)	126.1 (2)

2. Low-temperature Raman spectra

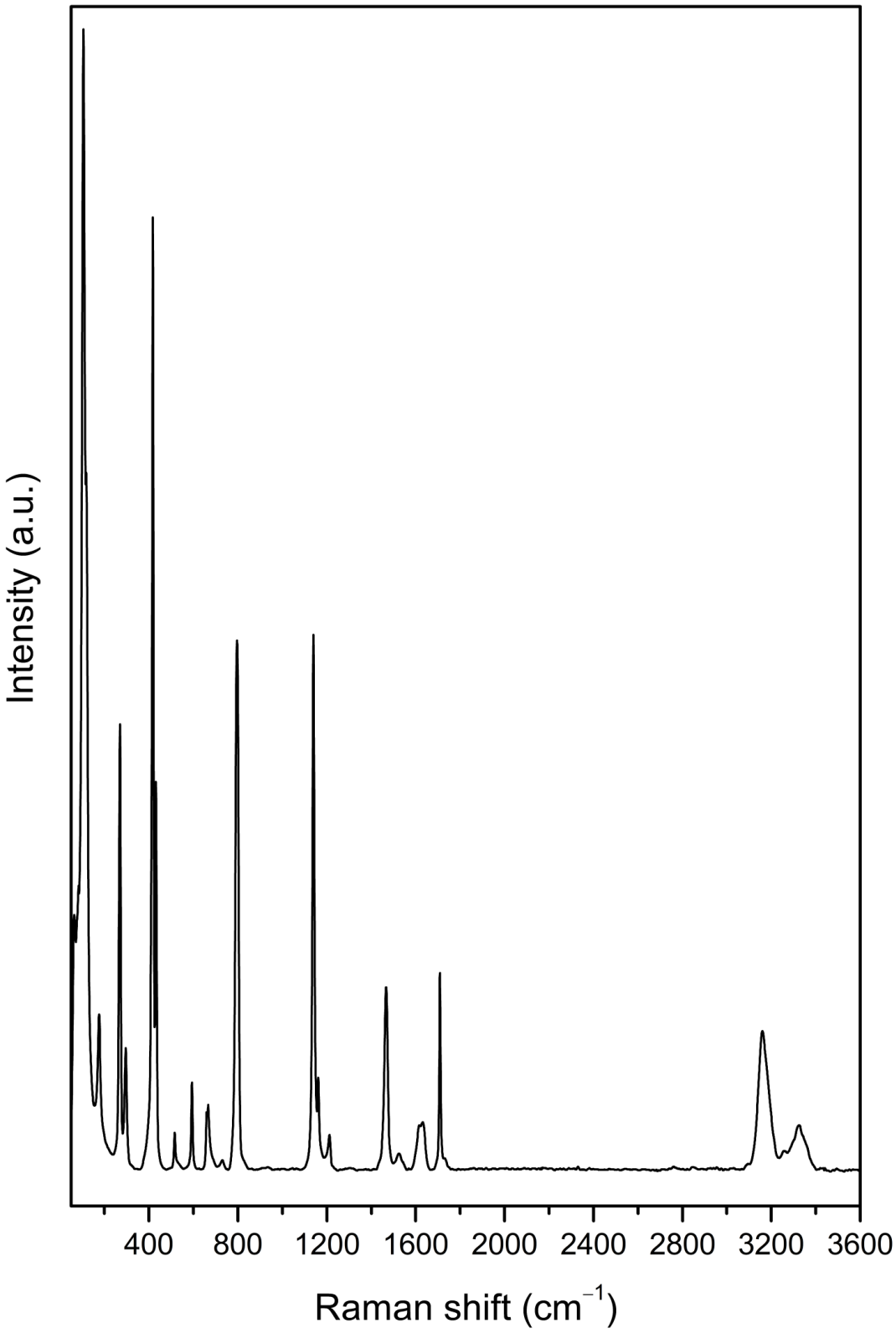


Figure S27. Raman spectrum of CF_3CONH_2 (–90 °C).

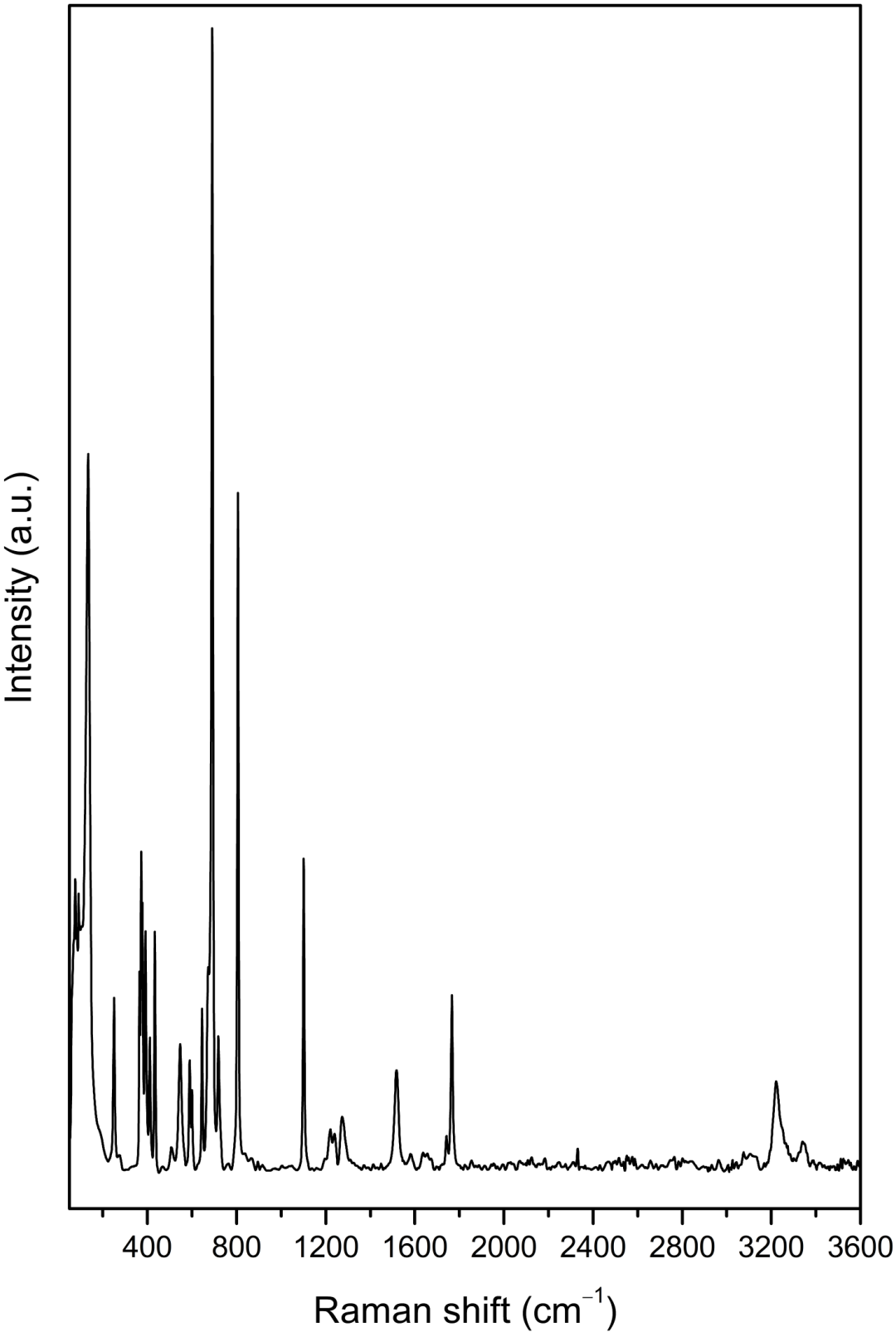


Figure S28. Raman spectrum of $CF_3C(OH)NH_2[AsF_6]$ (−100 °C).

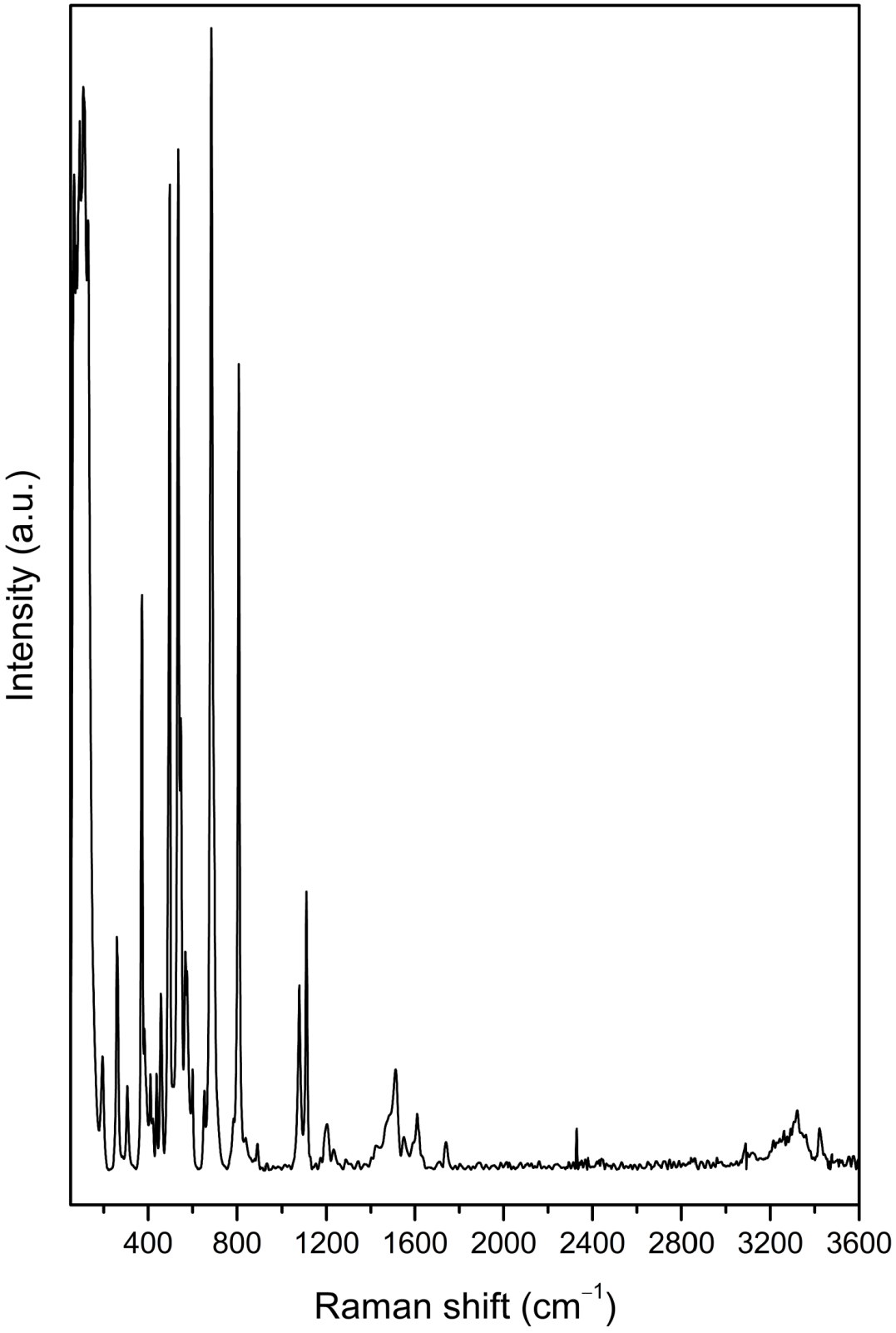


Figure S29. Raman spectrum of $CF_3C(OH)NH_2[AsF_6]\cdot XeF_2$ (−90 °C). Peak at 2327 cm^{-1} corresponds to N_2 from the nitrogen stream.

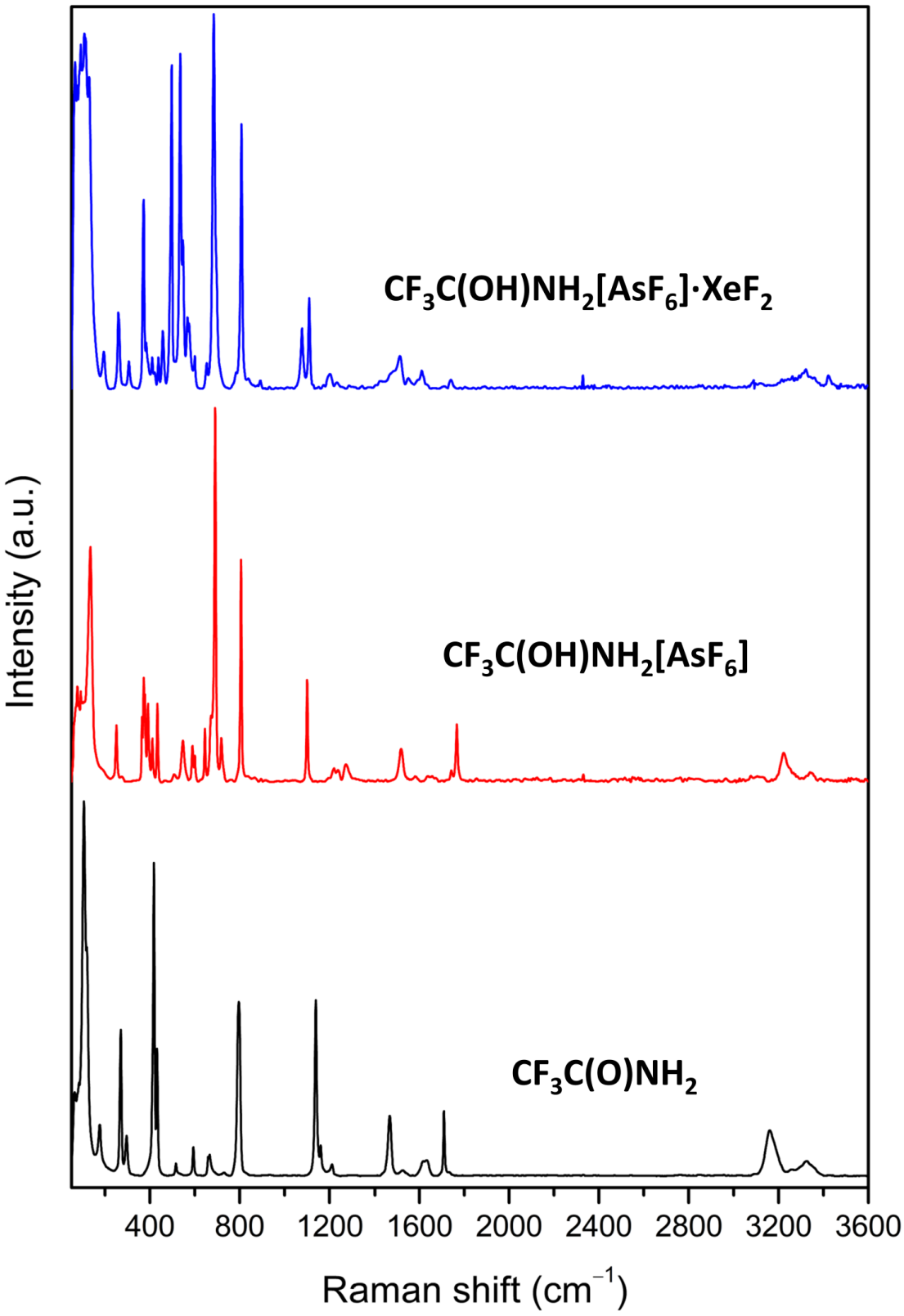


Figure S30. Comparison of Raman spectra of CF_3CONH_2, $CF_3C(OH)NH_2[AsF_6]$, and $CF_3C(OH)NH_2[AsF_6]\cdot XeF_2$.

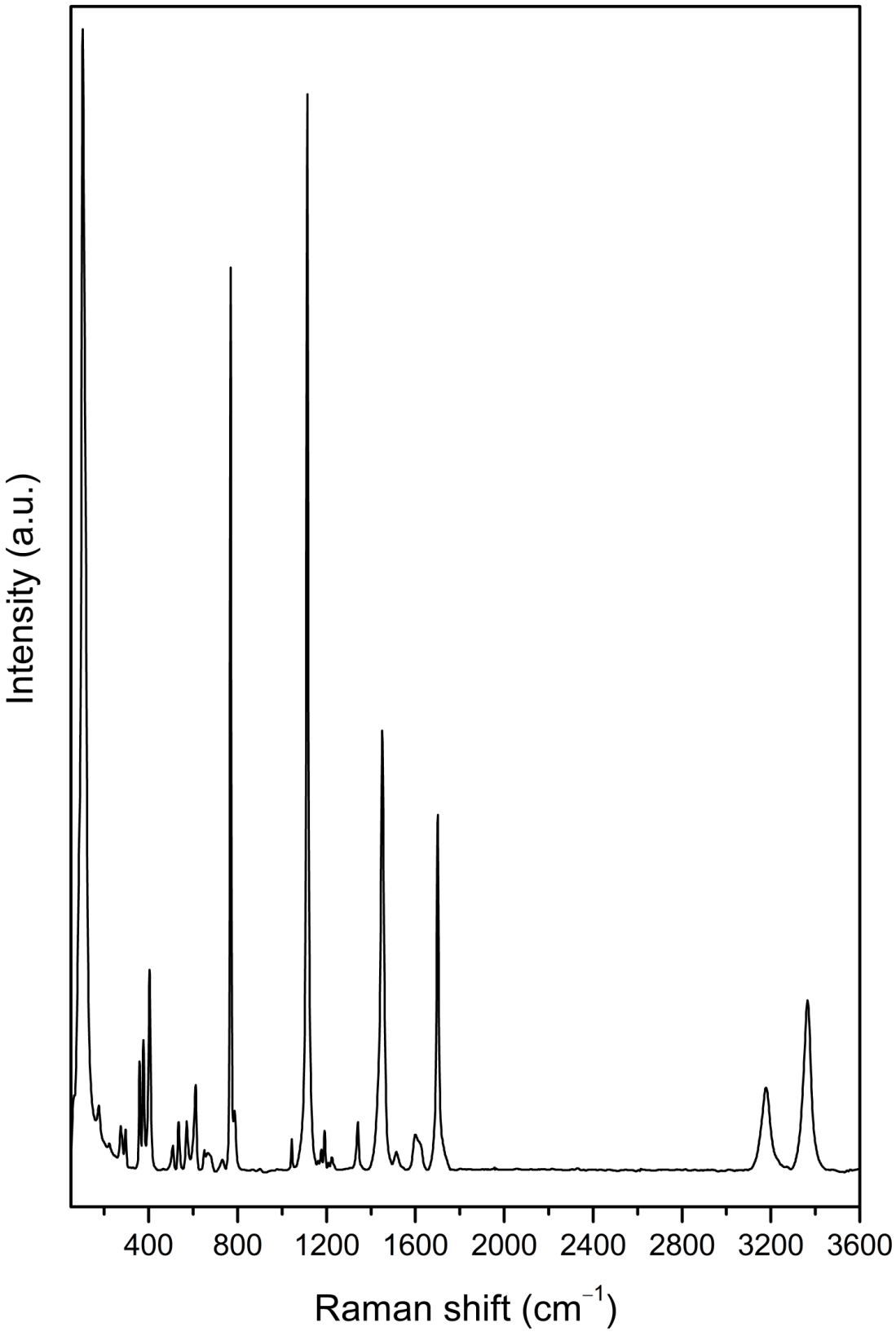


Figure S31. Raman spectrum of $C_2F_5CONH_2$ (−90 °C).

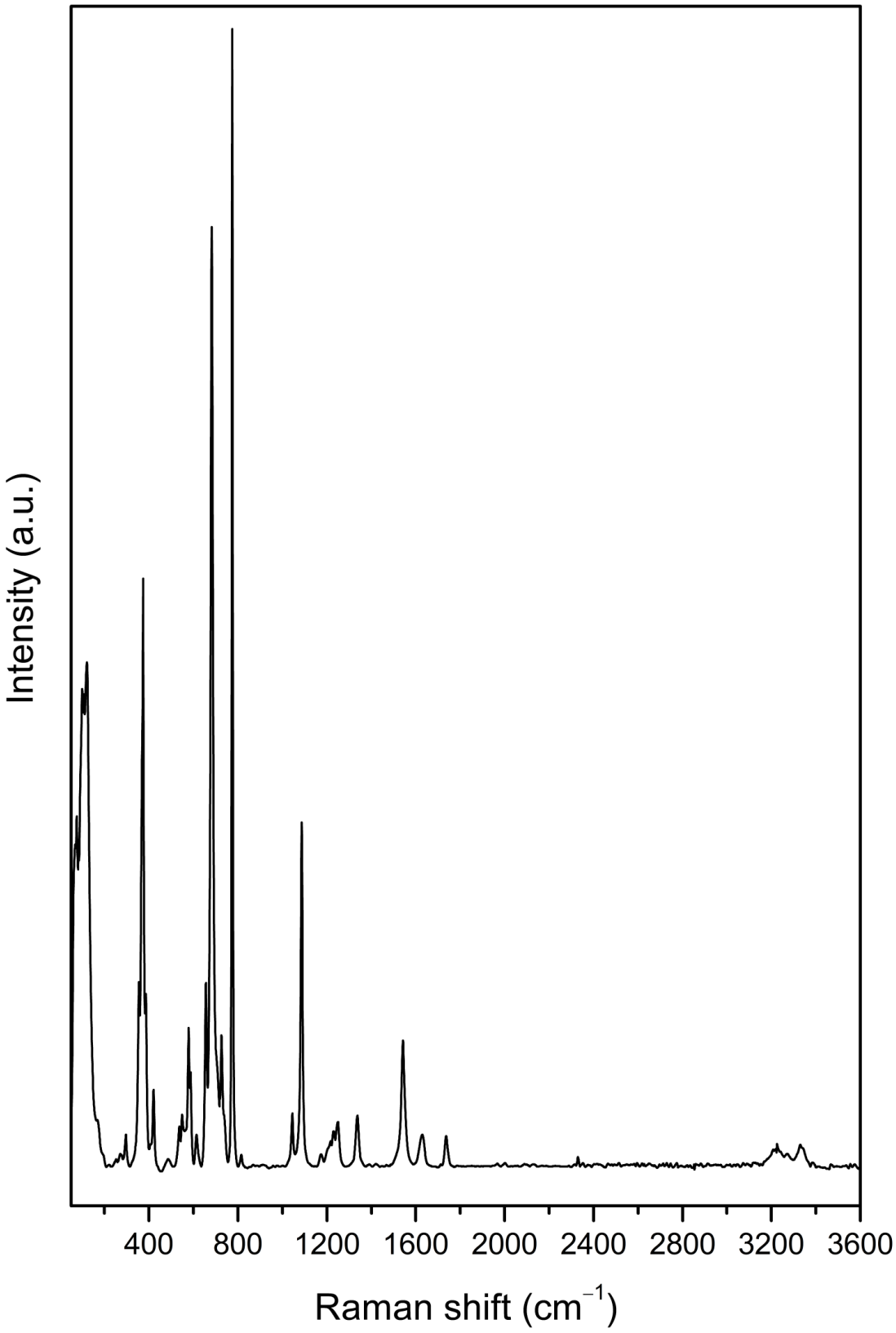


Figure S32. Raman spectrum of $C_2F_5C(OH)NH_2[AsF_6]$ (−50 °C).

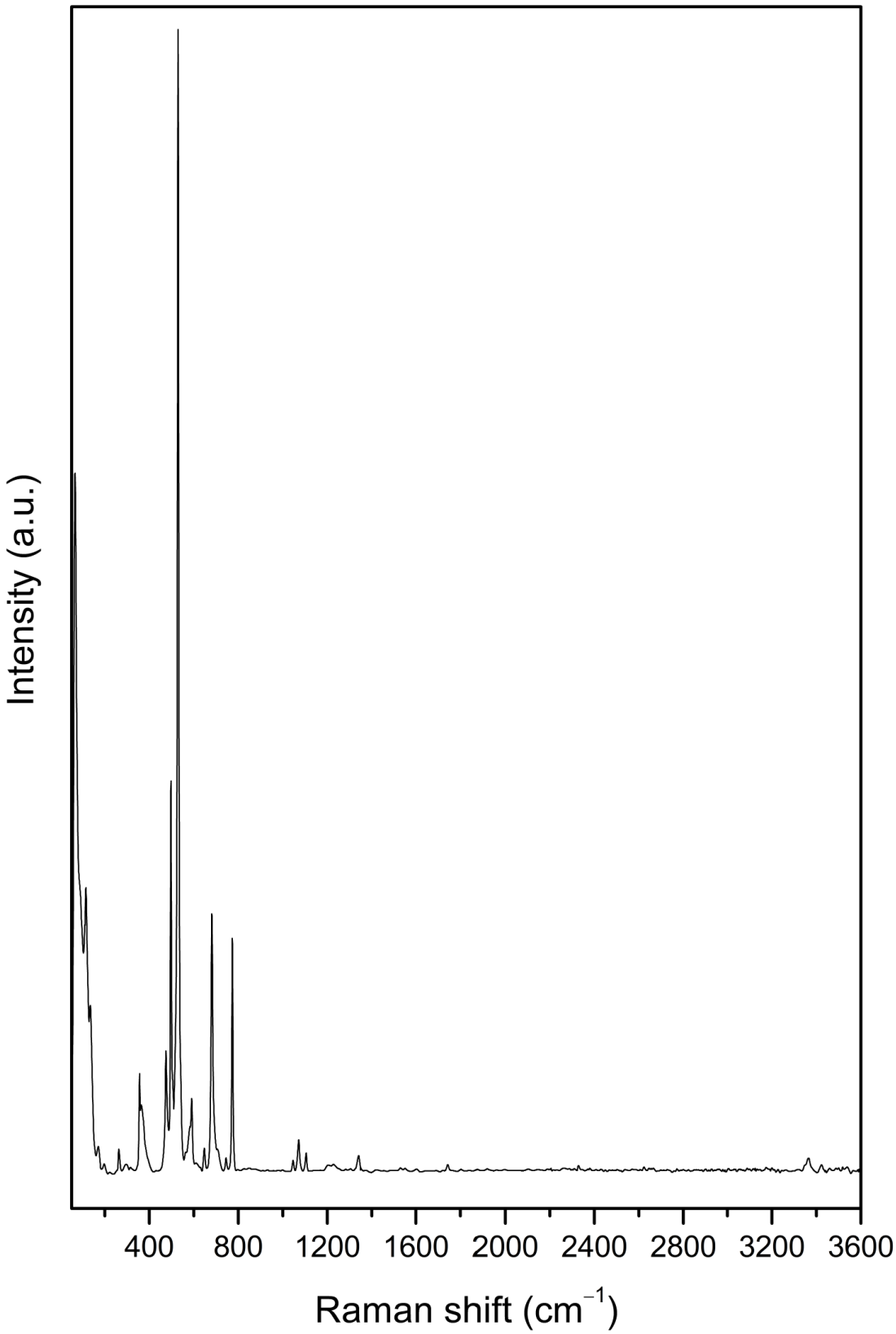


Figure S33. Raman spectrum of $C_2F_5C(OH)NH_2[AsF_6]\cdot XeF_2$ (−90 °C).

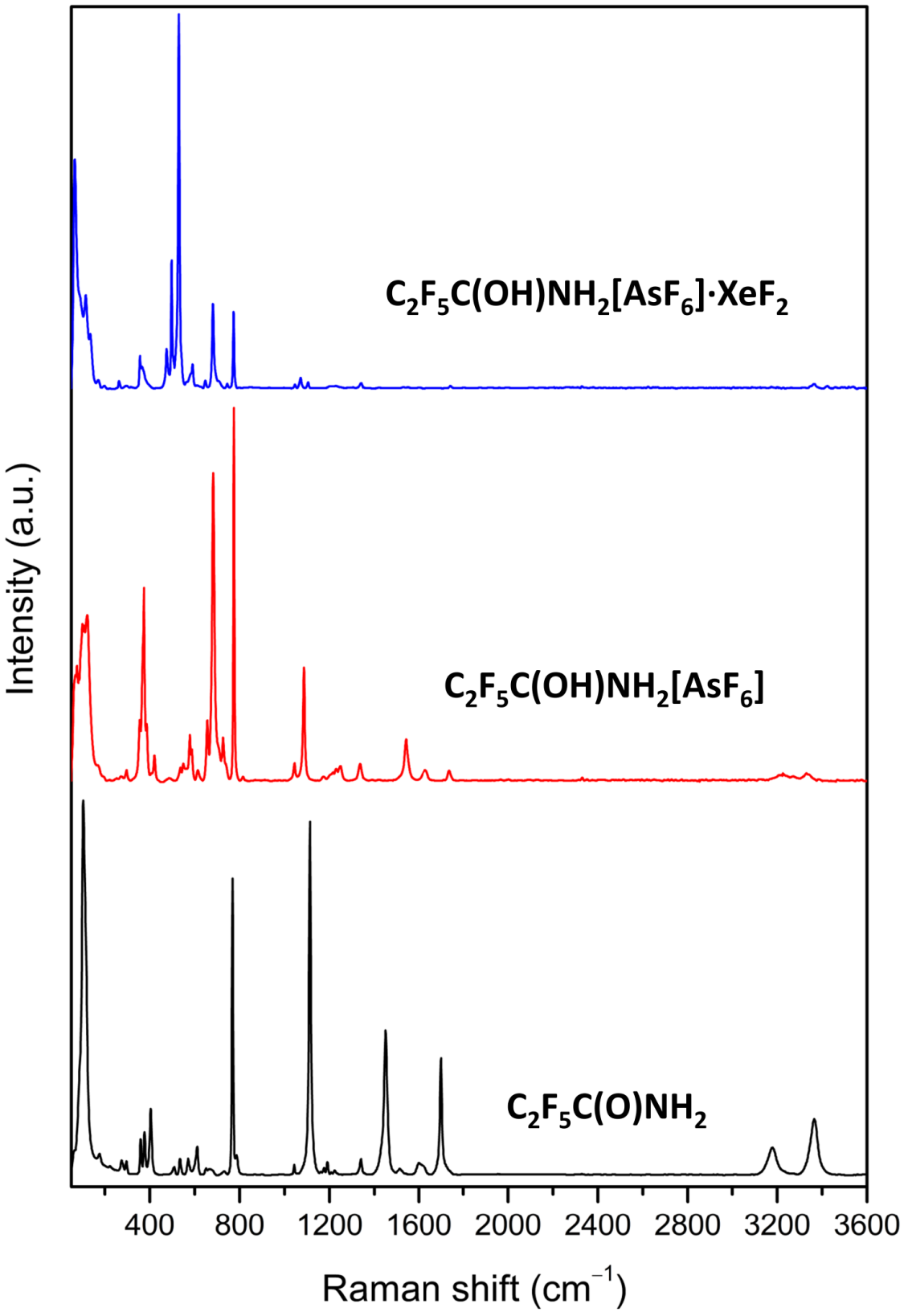


Figure S34. Raman spectra of $C_2F_5CONH_2$, $C_2F_5C(OH)NH_2[AsF_6]$, and $C_2F_5C(OH)NH_2[AsF_6]\cdot XeF_2$.

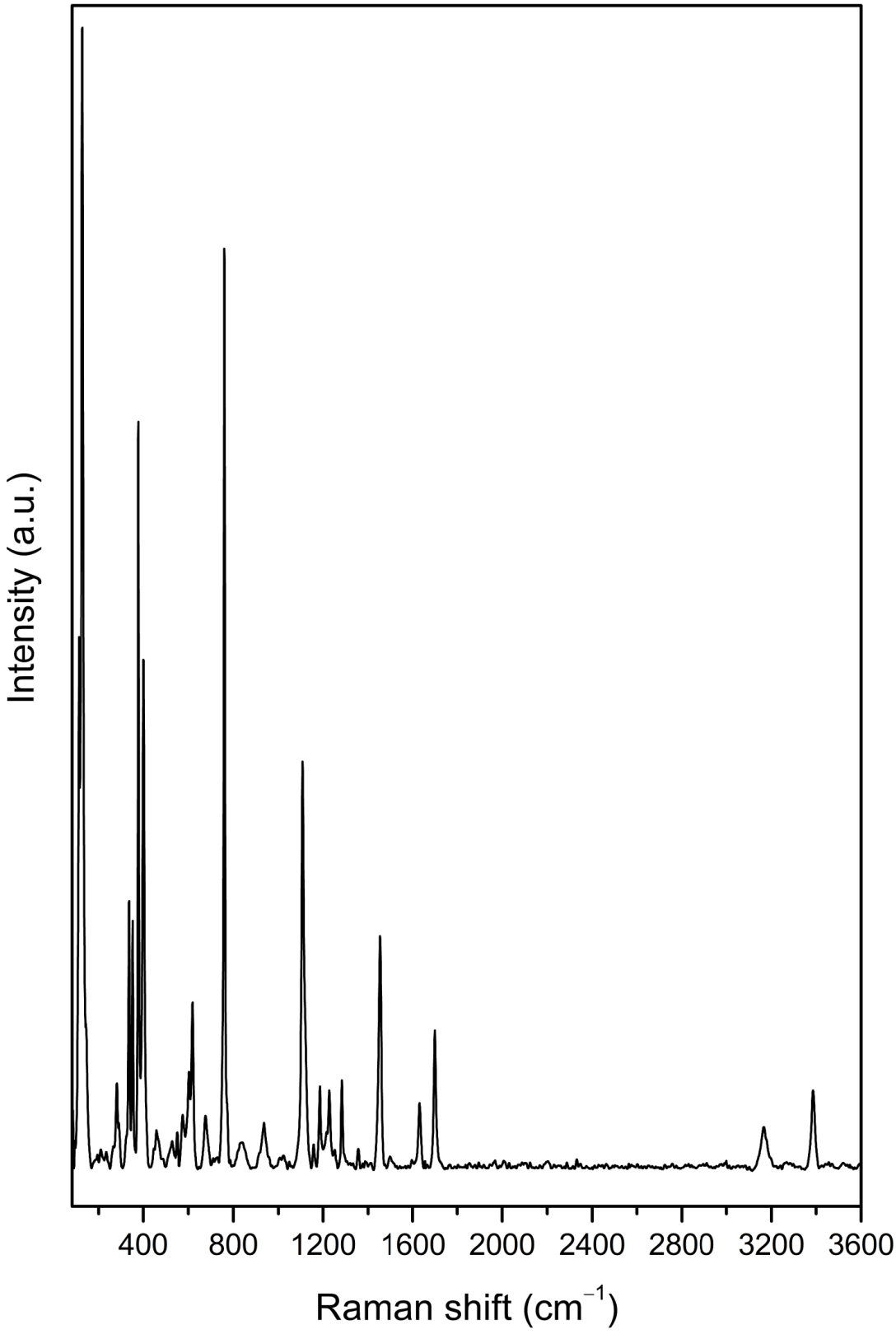


Figure S35. Raman spectrum of $C_3F_7CONH_2$ (−90 °C).

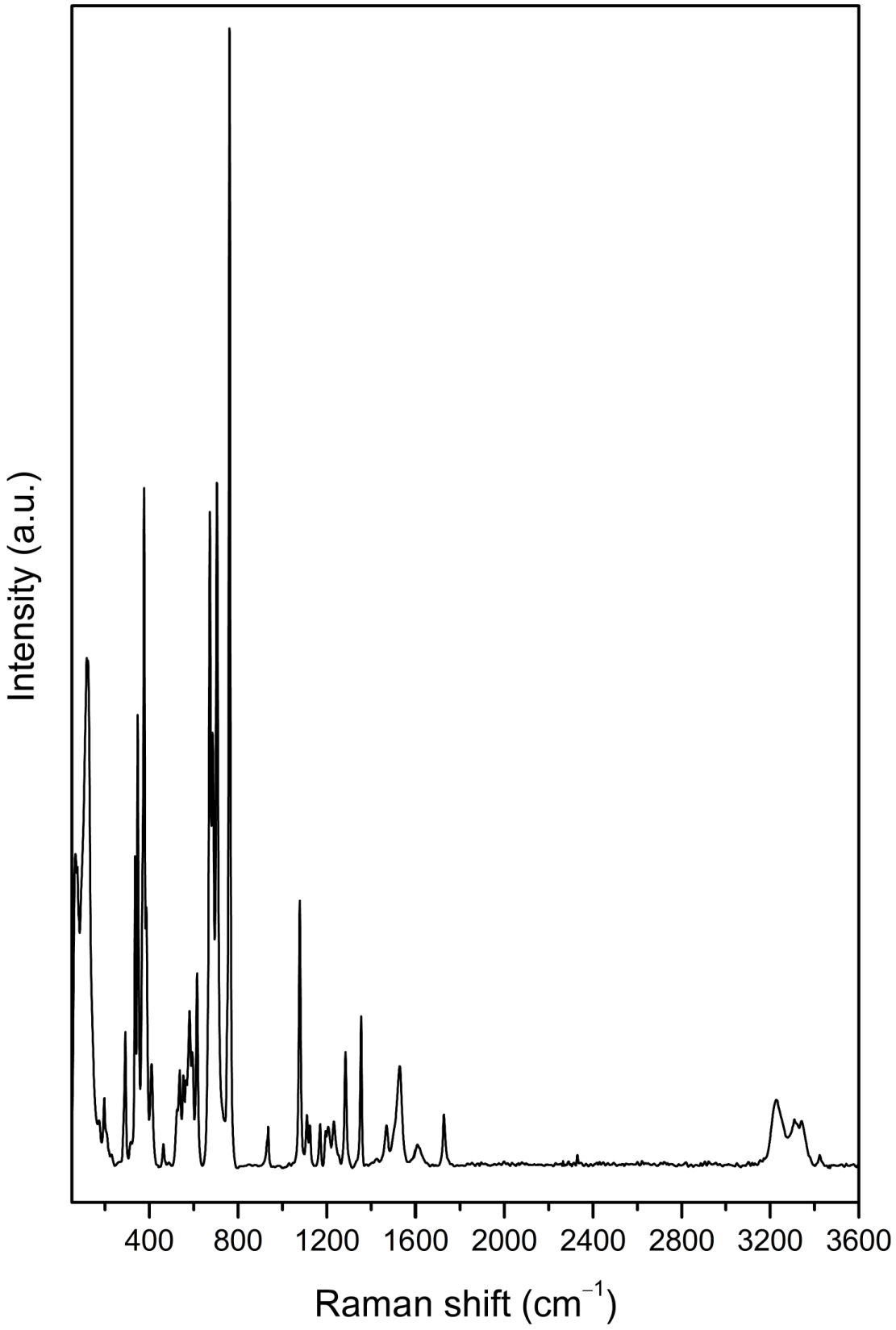


Figure S36. Raman spectrum of $C_3F_7C(OH)NH_2[AsF_6]$ (−100 °C).

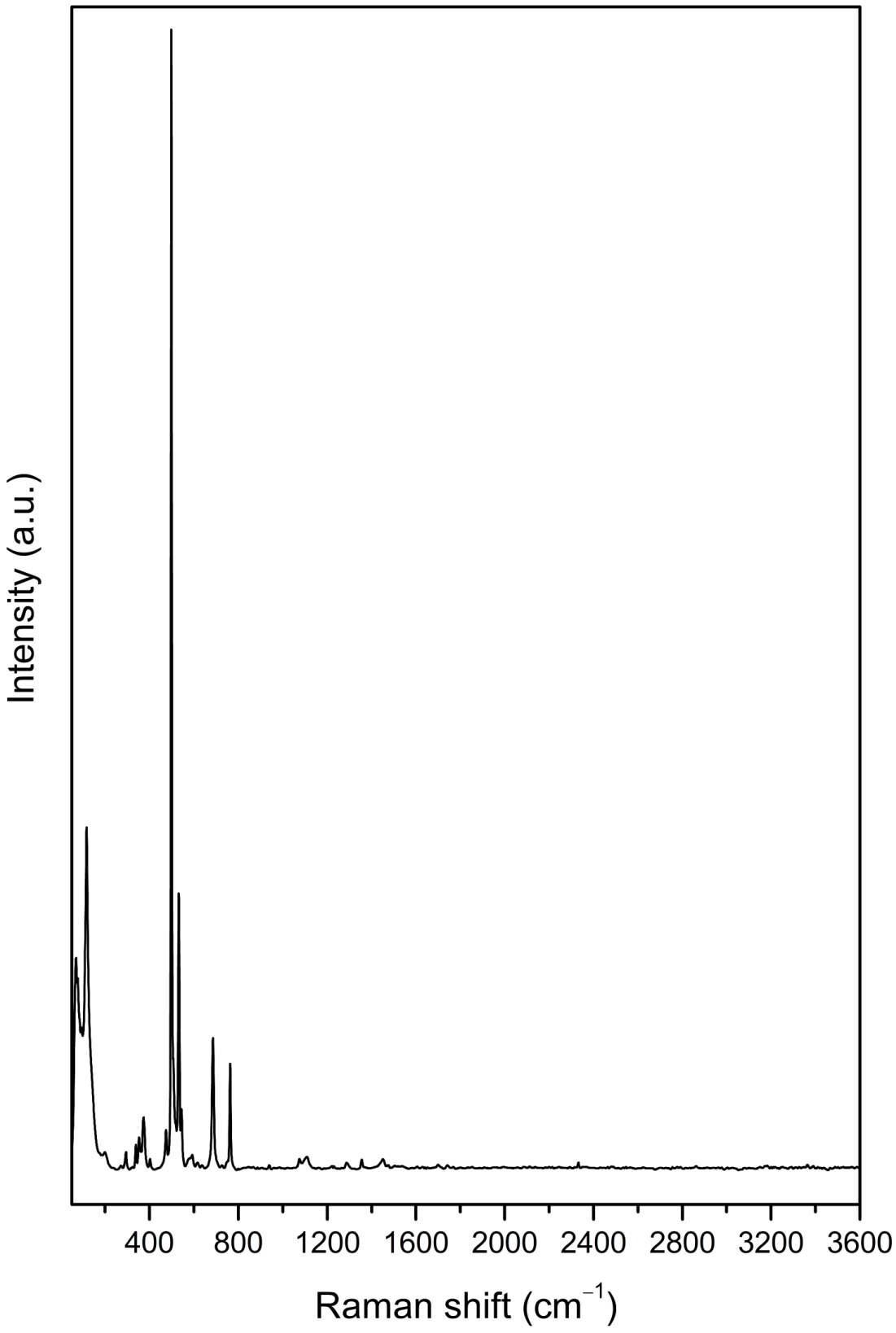


Figure S37. Raman spectrum of a mixture of $(C_3F_7CONH_2)_2H[AsF_6]$ and $C_3F_7C(OH)NH_2[AsF_6]\cdot XeF_2$ (–93 °C).

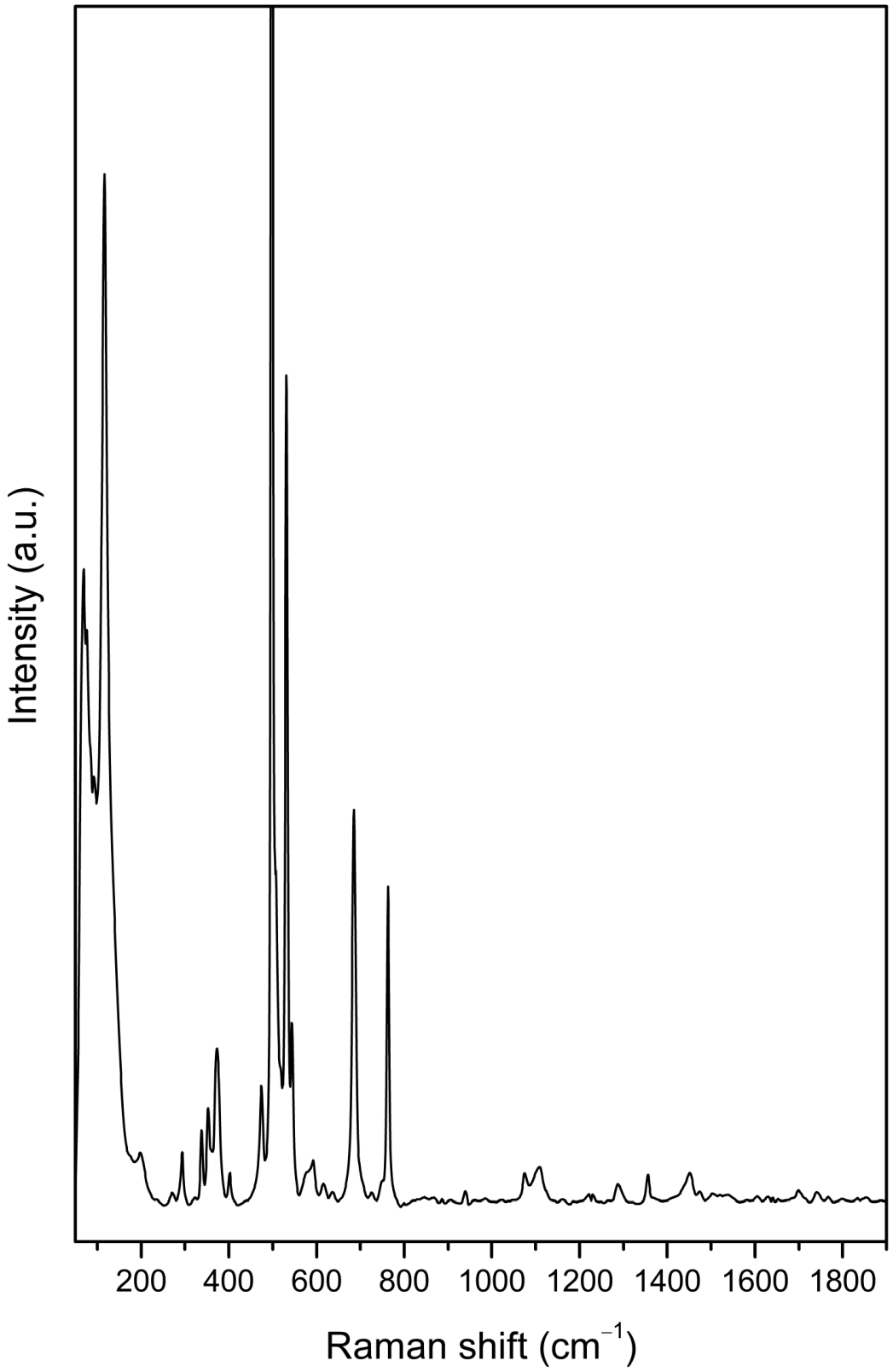


Figure S38. Enlarged Raman spectrum from Figure S37.

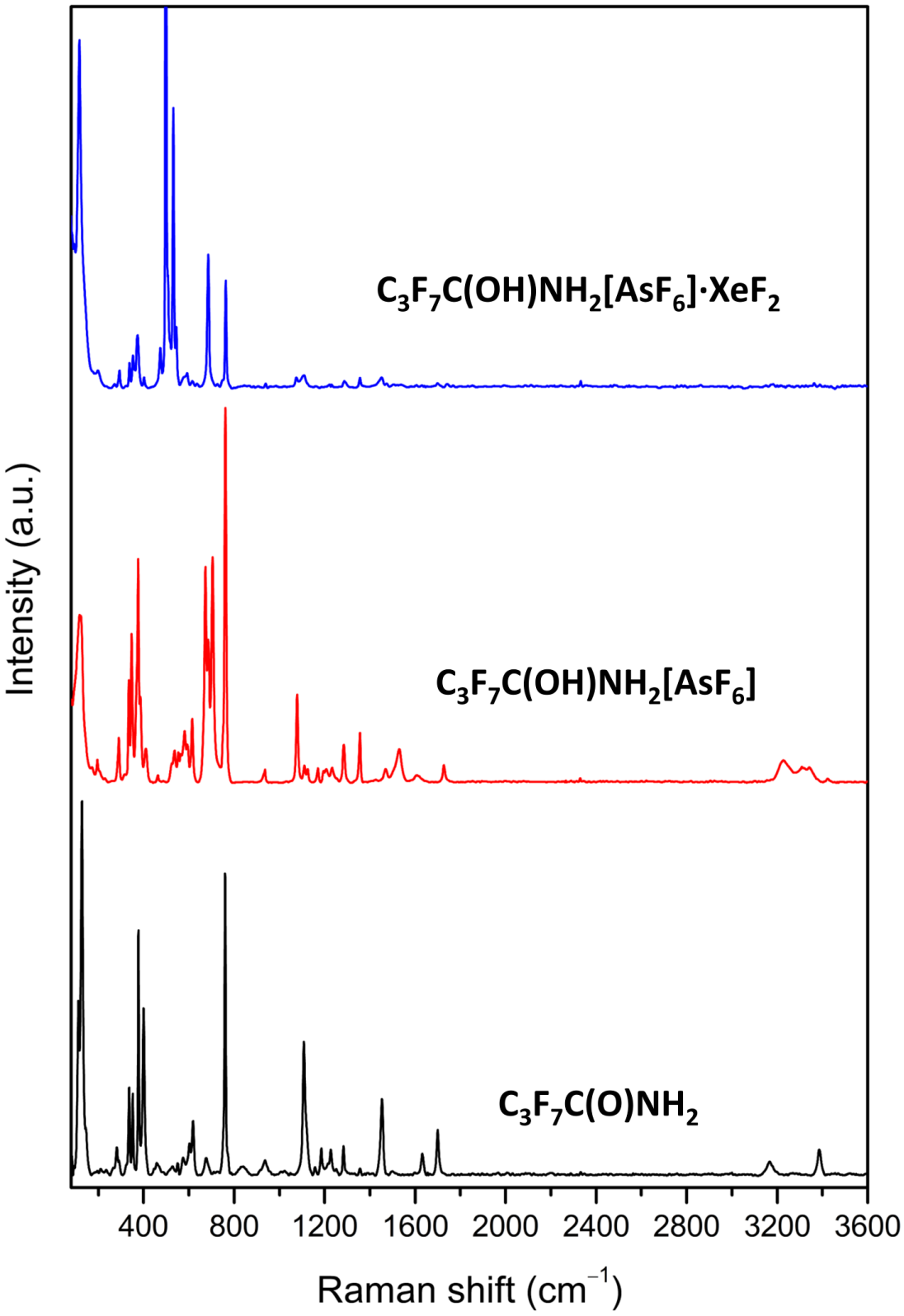


Figure S39. Comparison of Raman spectra of $C_3F_7CONH_2$, $C_3F_7C(OH)NH_2[AsF_6]$, and a mixture of $C_3F_7C(OH)NH_2[AsF_6]\cdot XeF_2$ and $(C_3F_7CONH_2)_2H[AsF_6]$.

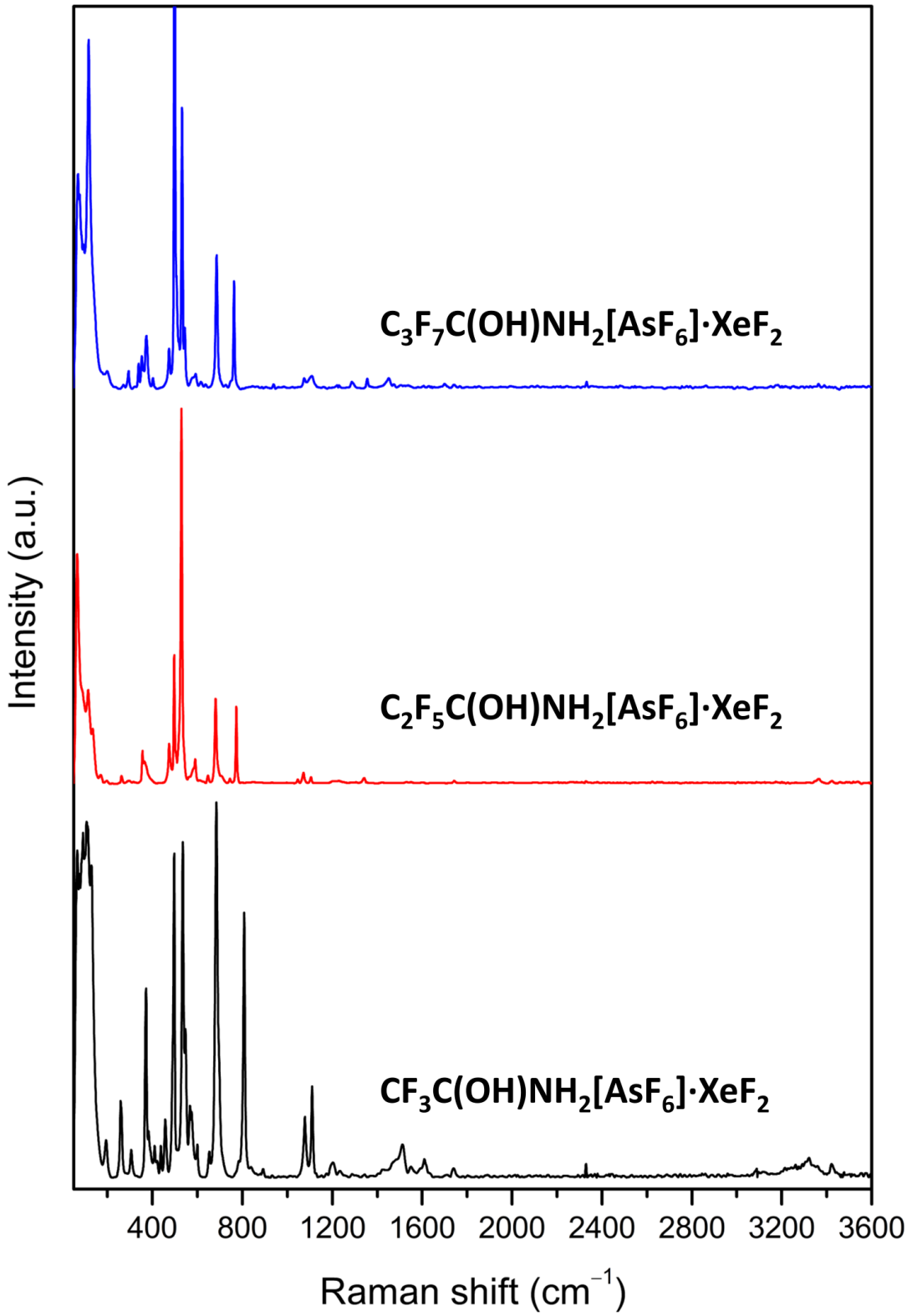


Figure S40. Comparison of Raman spectra (−90 °C) of $CF_3C(OH)NH_2[AsF_6]\cdot XeF_2$, $C_2F_5C(OH)NH_2[AsF_6]\cdot XeF_2$, and $C_3F_7C(OH)NH_2[AsF_6]\cdot XeF_2$. $(C_3F_7CONH_2)_2H[AsF_6]$ compound is also present in the Raman spectrum of $C_3F_7C(OH)NH_2[AsF_6]\cdot XeF_2$. Small peak at 2327 cm^{-1} originates from the nitrogen stream.

3. Experimental details

Caution: *All reagents (XeF_2, [XeF][AsF_6], anhydrous HF, K_2NiF_6, AsF_5, F_2) are toxic and highly corrosive and should be handled with extreme caution by trained personnel wearing appropriate protective clothing. Suitable first-aid equipment must be available at all times.*[2–4]

Apparatus

All manipulations involving solid reagents were performed in a nitrogen-filled glovebox (Vigor SG1200/750E–SG1500/750E), whereas syntheses involving volatile materials were carried out on a fluorine-resistant metal vacuum line equipped with FEP (copolymer of tetrafluoroethylene and hexafluoroethylene) manifolds, a Monel Helicoid pressure gauge, a soda-lime scrubber, liquid-nitrogen-cooled traps, and a two-stage rotary vane pump. All reaction vessels were made of FEP, while the valves were made of either polychlorotrifluoroethylene (Kel-F) with an aluminium casing or polytetrafluoroethylene (PTFE) encased in brass. All vessels were passivated with F_2 overnight prior to use.

Starting Materials

Fluorine gas (Solvay Fluor, 98–99%) was used without further purification. Commercial anhydrous HF (aHF, Linde, 99.995%) was distilled into a FEP vessel (outer diameter (o.d.) 19 mm, inner diameter (i.d.) 16 mm) and stored over K_2NiF_6 (Advanced Research Chemicals, 99.9%) prior to use. Trifluoroacetamide (Fluorochem, 99.0%), pentafluoropropionamide (Apollo Scientific, 97%) and heptafluorobutyramide (Fluorochem, 97.0%) were used as received. XeF_2 was synthesized photochemically from Xe and F_2 according to the literature procedure.[5] AsF_5 was synthesized by high-temperature fluorination of As_2O_3 and stored in a nickel vessel equipped with a nickel valve.[6] [XeF][AsF_6] was synthesized from XeF_2 and AsF_5 in aHF, following a procedure similar to that previously published.[7] Typically, XeF_2 (0.5 g, 2.95 mmol) was dissolved in aHF (1.6 mL) and AsF_5 (0.7 g, 4.43 mmol) was added at −196 °C. After thorough mixing at room temperature overnight, the excess aHF and remaining AsF_5 were removed at −65 ± 5 °C. The purity of the product was checked by powder X-ray diffraction and Raman spectroscopy.

CHARACTERISATION

Vibrational spectroscopy

Raman spectra were measured using a Horiba Jobin Yvon Labram-HR spectrometer coupled with an Olympus BXFM-ILHS microscope, employing either red or green lasers (633 or 532 nm, respectively). The typical spectral resolution was 4 cm^{-1}. The Raman spectra of all compounds were recorded directly on the aluminium trough used to mount the crystals for X-ray diffraction. The background subtraction was performed in the Bruker *OPUS* 8.7. software suite using concave rubberband correction (15 iterations, 50 baseline points).

Single crystal X-ray diffraction (SCXRD)

Crystals were isolated directly from the FEP reaction vessels employing the following procedure. After the complete removal of solvent, the vessel was backfilled with nitrogen (> 1 bar) at approximately −78 °C and then detached from the vacuum system. It was subsequently cooled to −196 °C and tapped with a plastic stick to dislodge the crystals from the vessel walls. The vessel was then cut open, allowing the crystals to fall onto the aluminium trough of the low-temperature crystal-mounting apparatus, which was cooled by a stream of cold nitrogen (−50 to −100 °C).[8–10] Suitable crystals were selected under a microscope and were mounted on the tip of a MiTeGen loop using Fomblin oil (Z25, SynQuest).[11] The loop assembly was picked up with cryo-pin

tongs cooled to −196 °C and quickly transferred to the goniometer head, where the crystal was protected by the stream of cold nitrogen at 100 K.

Crystals of pentafluoropropionamide and heptafluorobutyramide suitable for SCXRD were obtained from the commercial reagents. A small amount of amide, which was stored in the glovebox, was transferred into a short piece of FEP tube (o.d. 6.0 mm; i.d. 4.7 mm) closed by FEP stopper/cap (o.d. 8.0 mm; i.d. 6.0 mm), and was then deposited onto the aluminium trough.

All crystals and powder were measured on a Rigaku OD XtaLAB Synergy-S Dualflex diffractometer equipped with a Dectris Eiger2 R CdTe 1M detector, PhotonJet-S microfocus Cu and Ag X-ray sources, and an Oxford Cryosystems 800 Series Cryostream. All datasets were processed with empirical and numerical absorption corrections using *CrysAlisPro* software.[12] Crystal structures were solved by the charge flipping method using *olex2.solve*,[13] whereas $(CF_3CONH_2)_2H[AsF_6]$ was solved with *SHELXT*,[14] and subsequently refined using *SHELXL*[15] within *Olex2*.[16] Figures were drawn using the program *DIAMOND*.[17]

Crystal data, data collection details, and structure refinement parameters for the structures determined by SCXRD are summarized in Table S1.

Powder X-ray diffraction (PXRD)

The powder diffractogram of $CF_3C(OH)NH_2[AsF_6]\cdot XeF_2$ was measured at 100 K by mounting large amount of crystallites on the tip of a MiTeGen loop using Fomblin oil (Z25, SynQuest). Gandolfi movements were employed to enhance the random orientation of the crystallites. A measurement consisted of six frames, each with an exposure time of 300 s, with the detector positioned 90 mm away from the sample.

Calculated powder diffractogram of $CF_3C(OH)NH_2[AsF_6]\cdot XeF_2$ was obtained using *Mercury* 2025.2.0 (0.56087 Å, 2θ step = 0.01°, fwhm = 0.1).[18]

SYNTHESES

Synthesis of $CF_3C(OH)NH_2[AsF_6]$

An FEP vessel (4.7 mm i.d., 6 mm o.d.) was loaded with CF_3CONH_2 (76 mg, 0.67 mmol), and aHF (0.2 mL) was added at −196 °C. Upon warming to room temperature, a clear, colourless solution formed. The addition of Lewis acid AsF_5 (0.94 mmol) at −196 °C followed by warming to −45 °C yielded a clear solution. The solvent was removed under dynamic vacuum over the temperature range of −48 °C to −40 °C for one hour, affording a white, crystalline solid. The vessel was then backfilled with 900 Torr of N_2 at −78 °C and stored in dry ice prior to measurements. The material was subsequently transferred to an aluminium trough pre-cooled to −100 °C. The sample consisted of a white, chunky material, identified as $CF_3C(OH)NH_2[AsF_6]$.

Synthesis of $CF_3C(OH)NH_2[AsF_6]\cdot XeF_2$

An FEP vessel (4.7 mm i.d., 6 mm o.d.) was loaded with CF_3CONH_2 (24 mg, 0.21 mmol), followed by the addition of $[XeF][AsF_6]$ (61 mg, 0.18 mmol) at ca. −120 °C. The vessel was transferred in liquid nitrogen to the vacuum system, and aHF (0.2 mL) was added. Upon warming to −60 °C, the white solid dissolved, yielding a clear, colourless solution. Slow solvent removal from −65 °C to −50 °C over nearly five hours afforded colourless crystals. The vessel was backfilled with 900 Torr of N_2 at −70 °C, and the material was transferred to an aluminium trough pre-cooled to −90 °C. The product consisted of white, chunky material, identified as the $CF_3C(OH)NH_2[AsF_6]\cdot XeF_2$ salt cocrystal. During crystal mounting, crystals of $H_3O[AsF_6]\cdot 2CF_3CONH_2$ and $(CF_3CONH_2)_2H[AsF_6]$ were also discovered. Targeted synthesis of these phases was not attempted. The PXRD pattern measured at 100 K (Figure S41) shows that $CF_3C(OH)NH_2[AsF_6]\cdot XeF_2$ is obtained in nearly pure form.

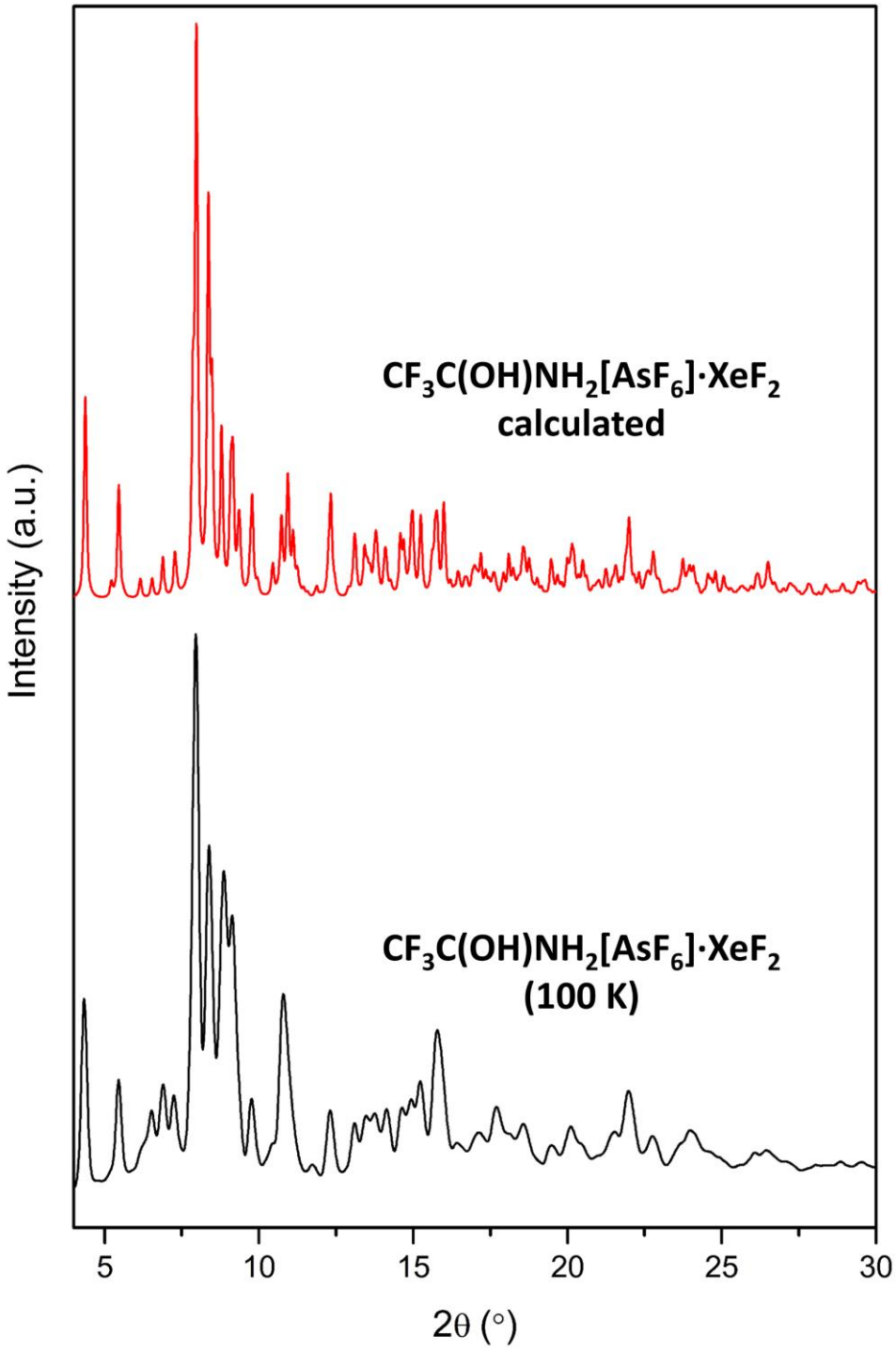


Figure S41. Experimental (black, measured at 100 K) and calculated (red) powder diffractogram of $CF_3C(OH)NH_2[AsF_6]\cdot XeF_2$.

Synthesis of $C_2F_5C(OH)NH_2[AsF_6]$

An FEP vessel (4.7 mm i.d., 6 mm o.d.) was loaded with $C_2F_5CONH_2$ (35 mg, 0.21 mmol), and aHF (0.3 mL) was added at −196 °C. Upon warming to room temperature a clear colourless solution formed. The addition of AsF_5 (0.25 mmol) at −196 °C, followed by warming to −30 °C, yielded a slightly turbid solution. Slow cooling to −78 °C afforded small, colourless needles. The solvent was removed under dynamic vacuum over the temperature range of −78 °C to −70 °C, affording a colourless, crystalline solid. The vessel was then backfilled with 900 Torr of N_2 at −70 °C, and the material was subsequently transferred to an aluminium trough pre-cooled to −50 °C. Although the material appeared dry inside the FEP vessel, residual HF was found adhering to the crystals. This layer evaporated after approximately one hour, leaving a considerable amount of powder on the crystals, which significantly diminished their quality.

Synthesis of $C_2F_5C(OH)NH_2[AsF_6]_2{\cdot}XeF_2$

An FEP vessel (4.7 mm i.d., 6 mm o.d.) was loaded with $C_2F_5CONH_2$ (9 mg, 0.055 mmol), followed by the addition of $[XeF][AsF_6]$ (18 mg, 0.053 mmol) at ca. −120 °C. The vessel was transferred in liquid nitrogen to the vacuum system, and aHF (0.2 mL) was added. The vessel was then removed from the cooling bath and vigorously shaken for several seconds, yielding a clear, colourless solution. The vessel was backfilled with 1000 Torr of N_2 at −78 °C. Over a period of two weeks, colourless plates crystallized at −78 °C. Slow solvent removal between −78 °C to −70 °C afforded additional colourless crystals. The vessel was then backfilled with 1000 Torr of N_2 at −78 °C, and the material was transferred to an aluminium trough pre-cooled to −90 °C. Single crystals analysis has shown both $C_2F_5C(OH)NH_2[AsF_6]{\cdot}XeF_2$ and XeF_2, which was also confirmed with Raman spectroscopy.

The same compound can also be obtained by the reaction of the protonated amide and XeF_2. An FEP vessel (4.7 mm i.d., 6 mm o.d.) was loaded with $C_2F_5CONH_2$ (17 mg, 0.10 mmol), and aHF (0.5 mL) was added at −196 °C. AsF_5 (0.28 mmol) was added at −196 °C, and the mixture was then warmed to −50 °C, which yielded a white powder. The solvent was removed under dynamic vacuum over the temperature range of −50 °C to −30 °C. To the dry powder, aHF (0.2 mL) was added, followed by the addition of XeF_2 (19 mg, 0.11 mmol) by sublimation, producing a white, powdery material that was difficult to dissolve; only part of the sample dissolved at −25 °C. During slow cooling to −78 °C, a few block-like crystals formed. The residual solution was removed at −63 °C. SCXRD analysis of block-like crystals revealed them to be $C_2F_5C(OH)NH_2[AsF_6]_2{\cdot}XeF_2$. The Raman spectrum of the powder material was in good agreement with the Raman spectrum of the product obtained from the reaction of $C_2F_5CONH_2$ with $[XeF][AsF_6]$.

Synthesis of $C_3F_7C(OH)NH_2[AsF_6]$:

An FEP vessel (4.7 mm i.d., 6 mm o.d.) was loaded with $C_3F_7CONH_2$ (39 mg, 0.18 mmol), and aHF (0.3 mL) was added at −196 °C. Upon warming to room temperature, a clear, colourless solution formed. AsF_5 (0.28 mmol) was added at −196 °C, and the mixture was then warmed to −25 °C, yielding a slightly turbid solution. Crystals formed at −78 °C after one hour. The solvent was removed under dynamic vacuum over the temperature range of −78 °C to −60 °C. The vessel was then backfilled with 1000 Torr of N_2 at −78 °C. The material was subsequently transferred to an aluminium trough pre-cooled to −100 °C. The sample consisted of a block-shaped crystals of $C_3F_7C(OH)NH_2[AsF_6]$. Even at 90 K, the anion remained disordered.

Synthesis of $C_3F_7C(OH)NH_2[AsF_6]{\cdot}XeF_2$ and $(C_3F_7CONH_2)_2H[AsF_6]$:

An FEP vessel (4.7 mm i.d., 6 mm o.d.) was loaded with $C_3F_7CONH_2$ (19 mg, 0.09 mmol), followed by the addition of $[XeF][AsF_6]$ (27 mg, 0.08 mmol) at ca. −120 °C. The vessel was transferred in liquid nitrogen to the vacuum system, and aHF (0.2 mL) was added. Upon warming to −50 °C, the white solid dissolved, yielding a

clear, colourless solution. Slow cooling to −55 °C resulted in growth of large, colourless blocks, and further cooling to −65 °C afforded thin plates. The solvent was slowly removed under dynamic vacuum over the temperature range of −78 °C to −60 °C. The vessel was backfilled with 1000 Torr of N_2 at −78 °C, and the material was transferred to an aluminium trough pre-cooled to −93 °C. The product consisted of colourless, block-shaped crystals of $(C_3F_7CONH_2)_2H[AsF_6]$ and thin plates identified as the $C_3F_7C(OH)NH_2[AsF_6]\cdot XeF_2$ salt cocrystal. No attempts were made to isolate either component in phase-pure form.

4. References

[1] F. R. Fronczek and N. H. Fischer, CCDC 174252: Experimental Crystal Structure Determination, 2002, DOI: 10.5517/cc5vb1c.

[2] D. Peters and R. Miethchen, *J. Fluorine Chem.*, 1996, **79**, 161–165.

[3] E. B. Segal, *Chem. Health Saf.*, 2000, **7**, 18–23

[4] M. Möbs and F. Kraus, *ACS Chem. Health Saf.*, 2025, **32**, 662–672.

[5] A. Šmalc and K. Lutar, *Inorg. Synth.*, 1992, **29**, 1–4.

[6] Z. Mazej and B. Žemva, *J. Fluorine Chem.,* 2005, **126**, 1432–1434.

[7] R. J. Gillespie and B. Landa, *Inorg. Chem.,* 1973, **12**, 1383–1388.

[8] M. Veith and H. Bärnighausen, *Acta Crystallogr.,* 1974, B**30**, 1806–1813.

[9] M. Lozinšek, H. P. A. Mercier and G. J. Schrobilgen, *Angew. Chem. Int. Ed.,* 2021, **60**, 8149–8156.

[10] K. Motaln, K. Gurung, P. Brazda, A. Kokalj, K. Radan, M. Dragomir, B. Žemva, L. Palatinus and M. Lozinšek, *ACS Cent. Sci.,* 2024, **10**, 1733–1741.

[11] K. Motaln, E. Uran, N. Giordano, S. Parsons and M. Lozinšek, *J. Appl. Crystallogr.*, 2025, **58**, 221–226.

[12] Rigaku OD, CrysAlis PRO. Rigaku Corporation, Wrocław, Poland, 2025.

[13] L. J. Bourhis, O. V. Dolomanov, R. J. Gildea, J. A. K. Howard and H. Puschmann, *Acta Crystallogr.*, 2015, A**71**, 59–75.

[14] G. M. Sheldrick, *Acta Crystallogr.,* 2015, A**71**, 3–8.

[15] G. M. Sheldrick, *Acta Crystallogr.,* 2015, C**71**, 3–8.

[16] O. V. Dolomanov, L. J. Bourhis, R. J. Gildea, J. A. K. Howard and H. Puschmann, *J. Appl. Crystallogr.*, 2009, **42**, 339–341.

[17] K. Brandeburg, Diamond – Crystal and Molecular Structure Visualization, Crystal Impact GbR, Bonn, Germany, 2022.

[18] C. F. Macrae, I. Sovago, S. J. Cottrell, P. T. A. Galek, P. McCabe, E. Pidcock, M. Platings, G. P. Shields, J. S. Stevens, M. Towler and P. A. Wood, *J. Appl. Crystallogr.*, 2020, **53**, 226–235.

4.4 Synthesis of Protonated Decafluorobenzophenone and Decafluorobenzophenone—AsF_5 Adduct

In this chapter, the results of the structural investigation of protonated decafluorobenzophenone (perfluorobenzophenone, $(C_6F_5)_2CO$) as the $[AsF_6]^-$ salt, $(C_6F_5)_2COH^+[AsF_6]^-$, and of the adduct $(C_6F_5)_2CO{\cdot}AsF_5$ are presented. These results have been published in *Acta Cryst.* (2025), C**81**, 557–583, which is attached to this Chapter. Erik Uran performed experiments, analyzed the data, and contributed to both data interpretation, as well as to writing of the manuscript.

The original aim of this work was to prepare either the $[(C_6F_5)_2CO{-}XeF]^+$ adduct cation or a hydrogen-bonded cocrystal featuring XeF_2 as a hydrogen-bond acceptor toward $(C_6F_5)_2COH^+$ by reacting $[XeF][AsF_6]$ with $(C_6F_5)_2CO$ in aHF at low temperatures. However, neither of these target compounds was obtained under the applied conditions; instead, only $(C_6F_5)_2COH^+[AsF_6]^-$ was isolated.

The reaction of $(C_6F_5)_2COH^+[AsF_6]^-$ with XeF_2 was also unsuccessful. Warming the solution above −55 °C resulted in the formation of a yellow-green amorphous compound, whereas the only crystalline product identified was $(C_6F_5)_2COH^+[AsF_6]^-$. Raman spectroscopy similarly showed only signals corresponding to protonated decafluorobenzophenone, along with unreacted XeF_2.

A subsequent literature survey and search of the Cambridge Structural Database (Groom, Bruno, Lightfoot, & Ward, 2016) showed that protonated ketones have been well characterized in the solid state, with [C−(C=OH)−C] fragment present in 61 entries.[2] The $(C_6F_5)_2COH^+$ cation has been observed, but only in solution (Chambers & Spring, 1969; Olah & Mo, 1973). In contrast, no crystal structure of a ketone—AsF_5 adduct could be found in the Cambridge Structural Database (CSD) (Groom, Bruno, Lightfoot, & Ward, 2016), despite the fact that ketones have been investigated as Lewis bases towards AsF_5 (Stuart, Wetmore, & Gerken, 2019).

Although $(C_6F_5)_2CO$ is only sparingly soluble in aHF, the addition of AsF_5 leads to its dissolution, accompanied by the appearance of a yellow coloration. From such solution, yellow $(C_6F_5)_2COH^+[AsF_6]^-$ is isolated. The crystal structure reveals protonated $(C_6F_5)_2CO$, in which both the C=O and C(O)−C bond lengths are significantly longer than those observed in the crystal structure of neutral decafluorobenzophenone. The $[AsF_6]^-$ is hydrogen-bonded to the cation through a short O−H···F contact, which induces a distortion of its octahedral geometry.

Dissolution of $(C_6F_5)_2CO$ in SO_2 at room temperature, followed by the addition of AsF_5, results in the formation of a yellow solution, from which a yellow $(C_6F_5)_2CO{\cdot}AsF_5$ crystallized at −78 °C. The ketone moiety closely resembles neutral $(C_6F_5)_2CO$, except for an elongated C=O bond, which is comparable to that observed in the $(C_6F_5)_2COH^+$ cation, whereas only one C(O)−C bond is significantly changed. The AsF_5 is coordinated to the oxygen atom and exhibits a distorted octahedral geometry with a nearly linear O−As−F_{trans} angle.

[2] The search was performed in CSD database (November, 2025) using *Conquest*. The crystal structure of $(C_6F_5)_2COH^+[AsF_6]^-$, obtained in this study, was not taken into the account. The C−C(=OH)−C fragment was searched. 3D coordinates of all atoms had to be determined using single-crystal X-ray diffraction, R factor had to be below 7.5 % and the structure should not contain any errors.

research papers

STRUCTURAL CHEMISTRY

ISSN 2053-2296

Protonated decafluorobenzophenone and the decafluorobenzophenone–arsenic pentafluoride adduct

Erik Uran[a,b] and Matic Lozinšek[a,b]*

[a]Extreme Conditions Chemistry Laboratory (ECCL K2), Jožef Stefan Institute, Jamova cesta 39, 1000 Ljubljana, Slovenia, and [b]Jožef Stefan International Postgraduate School, Jamova cesta 39, 1000 Ljubljana, Slovenia. *Correspondence e-mail: matic.lozinsek@ijs.si

Received 28 July 2025
Accepted 28 August 2025

Edited by R. I. Cooper, University of Oxford, United Kingdom

Keywords: superacid medium; protonation; decafluorobenzophenone; AsF_5 adduct; crystal structure; protonated ketone.

CCDC references: 2483527; 2483526; 2483525; 2483524

Supporting information: this article has supporting information at journals.iucr.org/c

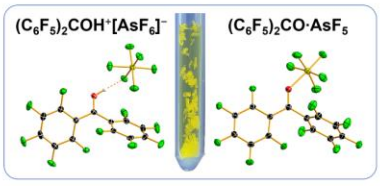
The reaction of decafluorobenzophenone [perfluorobenzophenone, $(C_6F_5)_2CO$] with AsF_5 in anhydrous HF yields the protonated salt [bis(2,3,4,5,6-pentafluorophenyl)methylidene]oxidanium hexafluoridoarsenate, $(C_6F_5)_2COH^+$-$[AsF_6]^-$, whereas its reaction with AsF_5 in SO_2 affords the Lewis acid–base adduct decafluorobenzophenone–arsenic pentafluoride, $(C_6F_5)_2CO{\cdot}AsF_5$. In both compounds, the decafluorobenzophenone moiety exhibits an elongated C=O bond [1.274 (2) and 1.2526 (15) Å in the salt and adduct, respectively]. The crystal structure of $(C_6F_5)_2COH^+[AsF_6]^-$ features a short O—H···F hydrogen bond between the cation and the anion, and the crystal structure of $(C_6F_5)_2CO{\cdot}AsF_5$ represents a rare example of a ketone coordinated to the strong Lewis acid AsF_5.

1. Introduction

Protonation of small molecules plays an important role in investigating and elucidating the reaction mechanisms of acid-catalysed organic reactions. These reactive cations are typically generated in superacidic media (Olah *et al.*, 2009) and a wide range of compounds has been shown to undergo protonation under such conditions. Examples include nitriles (Haiges *et al.*, 2016; Goetz *et al.*, 2016), organic azides (Saal *et al.*, 2020), carboxylic acids (Saal *et al.*, 2023; Hollenwäger *et al.*, 2024), acyl halides (Steiner *et al.*, 2024*a*), amides (Axhausen *et al.*, 2013; Saal *et al.*, 2023), esters (Hollenwäger *et al.*, 2025) and amino sulfonic acids (Bockmair *et al.*, 2024).

The protonation of aldehydes and ketones in solution has been studied in detail by low-temperature NMR spectroscopy. For example, the protonation of aliphatic aldehydes (Olah *et al.*, 1967*b*) and aliphatic ketones (Olah *et al.*, 1967*a*) was studied in the superacidic media HSO_3F–SbF_5–SO_2, protonated alicyclic ketones in HSO_3F–SbF_5–SO_2 and HSO_3F–SO_2 (Olah & Calin, 1968), protonated acetophenones in HSO_3F (Birchall & Gillespie, 1965) and benzophenones in HSO_3F–SbF_5 (Sekuur & Kranenburg, 1966; van der Linde *et al.*, 1968). The reaction of hexafluoroacetone in an HF–SbF_5 mixture, however, results in HF addition to the ketone, followed by protonation, yielding a rare example of a protonated alcohol (Minkwitz & Reinemann, 1999).

Several crystallographically characterized examples of protonated ketones (Childs *et al.*, 1982, 1990; Chadda *et al.*, 1986; Stuart *et al.*, 2017; Schickinger *et al.*, 2018) and protonated aldehydes (Hwang *et al.*, 2010; Heo *et al.*, 2011; Hayatifar *et al.*, 2014; Stuart *et al.*, 2017) have been reported. The crystal structure of protonated benzophenone has been reported in



OPEN ACCESS
Published under a CC BY 4.0 licence

Table 1
Experimental details.

Experiments were carried out at 100 K using a Rigaku OD XtaLAB Synergy-S Dualflex diffractometer with an Eiger2 R CdTe 1M detector. The absorption correction was Gaussian (*CrysAlis PRO*; Rigaku OD, 2025).

	$(C_6F_5)_2CO$	$(C_6F_5)_2COH^+[AsF_6]^-$	$(C_6F_5)_2CO{\cdot}AsF_5$
Crystal data			
Chemical formula	$C_{13}F_{10}O$	$C_{13}HF_{10}O^+AsF_6^-$	$C_{13}AsF_{15}O$
M_r	362.13	552.06	532.05
Crystal system, space group	Monoclinic, *C*2	Monoclinic, $P2_1/n$	Orthorhombic, *Pbca*
a, *b*, *c* (Å)	20.1460 (4), 5.39987 (10), 5.47058 (14)	8.19207 (7), 21.17409 (18), 9.28475 (9)	12.39109 (18), 12.04038 (17), 20.8754 (3)
α, β, γ (°)	90, 95.912 (2), 90	90, 98.2086 (8), 90	90, 90, 90
V (Å^3)	591.96 (2)	1594.03 (2)	3114.47 (8)
Z	2	4	8
Radiation type	Cu *K*α	Cu *K*α	Ag *K*α, λ = 0.56087 Å
μ (mm^{-1})	2.18	4.70	1.25
Crystal size (mm)	0.43 × 0.1 × 0.07	0.09 × 0.05 × 0.03	0.58 × 0.29 × 0.22
Data collection			
T_{min}, T_{max}	0.491, 1.000	0.842, 1.000	0.290, 1.000
No. of measured, independent and observed [$I > 2\sigma(I)$] reflections	10783, 1212, 1193	26147, 3336, 3134	97292, 8537, 7132
R_{int}	0.056	0.032	0.033
(sin $\theta/\lambda)_{max}$ (Å^{-1})	0.629	0.630	0.914
Refinement			
$R[F^2 > 2\sigma(F^2)]$, $wR(F^2)$, *S*	0.034, 0.095, 1.11	0.025, 0.066, 1.05	0.031, 0.081, 1.09
No. of reflections	1212	3336	8537
No. of parameters	110	285	271
No. of restraints	1	0	0
H-atom treatment	–	All H-atom parameters refined	–
$\Delta\rho_{max}$, $\Delta\rho_{min}$ (e Å^{-3})	0.28, −0.24	0.30, −0.49	0.53, −0.64
Absolute structure	Flack *x* determined using 514 quotients $[(I^+) - (I^-)]/[(I^+) + (I^-)]$ (Parsons *et al.*, 2013)	–	–
Absolute structure parameter	0.05 (10)	–	–

Computer programs: *CrysAlis PRO* (Rigaku OD, 2025), *olex2.solve* (Bourhis *et al.*, 2015), *SHELXL* (Sheldrick, 2015), *DIAMOND* (Brandenburg, 2022) and *OLEX2* (Dolomanov *et al.*, 2009).

the form of $[HCB_{11}H_5Cl_6]^-$ carborane (Stasko *et al.*, 2002) and $[TaF_6]^-$ salts (Marchetti *et al.*, 2007), both featuring a hydrogen-bonded dimer, $[(C_6H_5)_2C{=}O{-}H\cdots O{=}C(C_6H_5)_2]^+$.

The protonation of decafluorobenzophenone, $(C_6F_5)_2CO$, in solution was previously studied in H_2SO_4 and HSO_3F (Chambers & Spring, 1969), and in HF–SbF_5–SO_2ClF mixtures (Olah & Mo, 1973) by NMR spectroscopy. Research on Lewis acid–base adducts of AsF_5 with ketones remains scarce (Stuart *et al.*, 2019) and no crystal structures containing a C_2CO–AsF_5 fragment have been reported in the Cambridge Structural Database (CSD, Version 6.00, April 2025; Groom *et al.*, 2016).

In this work, the synthesis and structural characterization of the protonated decafluorobenzophenone (perfluorobenzophenone) salt $(C_6F_5)_2C{=}OH^+[AsF_6]^-$ and a Lewis acid–base adduct of arsenic pentafluoride and decafluorobenzophenone, *i.e.* $(C_6F_5)_2CO{\cdot}AsF_5$, are reported.

2. Experimental

2.1. Synthesis and crystallization

A fluorinated ethylene propylene (FEP) vessel (outer diameter: 6 mm; inner diameter: 4.6 mm), equipped with an aluminium-encased polychlorotrifluoroethylene (PCTFE) valve, was passivated with fluorine overnight prior to use. In a nitrogen-filled glovebox (Vigor SG1200/750E–SG1500/750E; H_2O < 0.02 ppm, O_2 < 2 ppm), the vessel was loaded with $(C_6F_5)_2CO$ (23 mg, 0.064 mmol; Thermo Scientific, 97%). Anhydrous HF (0.2 ml; Linde, 99.995%; stored over K_2NiF_6) was then condensed into it using a vacuum line designed for handling elemental fluorine, resulting in a suspension of $(C_6F_5)_2CO$ at room temperature. Upon addition of AsF_5 (0.137 mmol), synthesized as described previously (Mazej & Žemva, 2005), a yellow precipitate formed that dissolved completely upon warming to room temperature. Slow cooling to −30 °C yielded canary-yellow crystals of $(C_6F_5)_2COH^+$-$[AsF_6]^-$. The solvent aHF was removed under dynamic vacuum at −78 °C, leaving a yellow crystalline solid. Another synthesis was performed on a slightly larger scale [113 mg, 0.312 mmol $(C_6F_5)_2CO$; 0.4 ml aHF; 0.936 mmol AsF_5] (Figs. 1–3).

For the synthesis of $(C_6F_5)_2CO{\cdot}AsF_5$, $(C_6F_5)_2CO$ (14 mg, 0.039 mmol) was dissolved in dry SO_2 (0.3 ml; Ruše, stored over CaH_2 in a glass bulb) at room temperature. AsF_5 (0.168 mmol) was added at −196 °C. Upon thawing of the SO_2–AsF_5 mixture, a yellow coloration appeared immediately. The vessel was then stored at −78 °C under a nitrogen overpressure (~1000 Torr). Large yellow crystals of $(C_6F_5)_2CO{\cdot}AsF_5$ formed over a period of ten days. Volatiles, SO_2 and

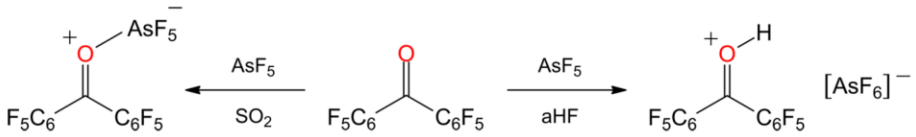


Figure 1
Synthesis of the $(C_6F_5)_2COH^+[AsF_6]^-$ salt and the $(C_6F_5)_2CO{\cdot}AsF_5$ adduct.

excess AsF_5 were removed under dynamic vacuum between −78 and −50 °C, yielding a yellow solid (Figs. 1 and 2).

A crystalline sample was quickly deposited from the FEP reaction vessel into an aluminium trough of the low-temperature crystal-mounting apparatus, designed and employed for mounting highly reactive moisture-sensitive noble-gas compounds (Lozinšek *et al.*, 2021; Motaln *et al.*, 2024), which was cooled using a stream of cold nitrogen to temperatures ranging from −80 to −100 °C. Suitable crystals were selected under a stereomicroscope and mounted on the tip of a MiTeGen loop using Fomblin oil (Z25, SynQuest) (Motaln *et al.*, 2025). The loop assembly was picked up with cryo-pin tongs cooled to −196 °C and quickly transferred to the magnetic holder on the goniometer head, where the crystal was protected by a cold nitrogen stream at 100 K.

2.2. Refinement

Crystal data, data collection and structure refinement details are summarized in Table 1. The position of the H atom in the crystal structure of $(C_6F_5)_2COH^+[AsF_6]^-$ was located in a difference electron-density map and refined freely, including its isotropic displacement parameter (Cooper *et al.*, 2010).

2.3. Raman spectroscopy

Raman spectroscopy was performed using either a Horiba Jobin Yvon LabRAM HR spectrometer coupled with an Olympus BXFM-ILHS microscope or a Bruker Senterra II confocal Raman microscope equipped with a Linkam LTS420 low-temperature stage. Red (633 and 785 nm) and green (532 nm) lasers were tested, with the laser power adjusted to the sample. The Raman spectra of $(C_6F_5)_2COH^+[AsF_6]^-$ and $(C_6F_5)_2CO{\cdot}AsF_5$ exhibited fluorescence regardless of the excitation wavelength used. The low-temperature (−90 °C) spectrum of solid $(C_6F_5)_2CO$ (Fig. 2), which is in good agreement with the previously published Raman spectrum (Anandhi & Umapathy, 2000), was recorded using the Bruker spectrometer with a 785 nm red laser at 1.5 cm^{-1} resolution. Low-temperature Raman spectra of the $(C_6F_5)_2COH^+[AsF_6]^-$ salt and the $(C_6F_5)_2CO{\cdot}AsF_5$ adduct (Fig. 2) were acquired on the Horiba system using a 633 nm red laser at 4 cm^{-1} resolution from crystalline material protected by a cold nitrogen stream of the crystal-mounting apparatus. Background subtraction from the spectra was performed using the Bruker *OPUS8.7* software suite, with 15 iterations of concave rubber-band correction and 50 baseline points.

3. Results and discussion

To facilitate a comparison of structural changes in the decafluorobenzophenone moiety upon protonation and coordination to AsF_5, the crystal structure of $(C_6F_5)_2CO$ was redetermined at 100 K (Table 1; Figs. S1 and S2 in the supporting information). The current structural parameters [C=O = 1.197 (4) Å; C—CO = 1.498 (3) Å; C—C = 1.373 (3)–1.392 (3) Å; C—F = 1.331 (3)–1.341 (3) Å] are in excellent agreement with the previously reported crystal structure measured at 153 K [C=O = 1.201 (8) Å; C—CO = 1.489 (6) Å; C—C = 1.361 (6)–1.403 (5) Å; C—F = 1.329 (5)–1.351 (4) Å; Schwarzer *et al.*, 2004]. Decafluorobenzophenone crystallizes in the Sohncke space group *C*2 and the molecule exhibits axial chirality owing to sterically hindered rotation of the C_6F_5 rings about the $C_{aryl}—C(O)—C_{aryl}$ bonds (Farmer & Walker, 1967). Similarly,

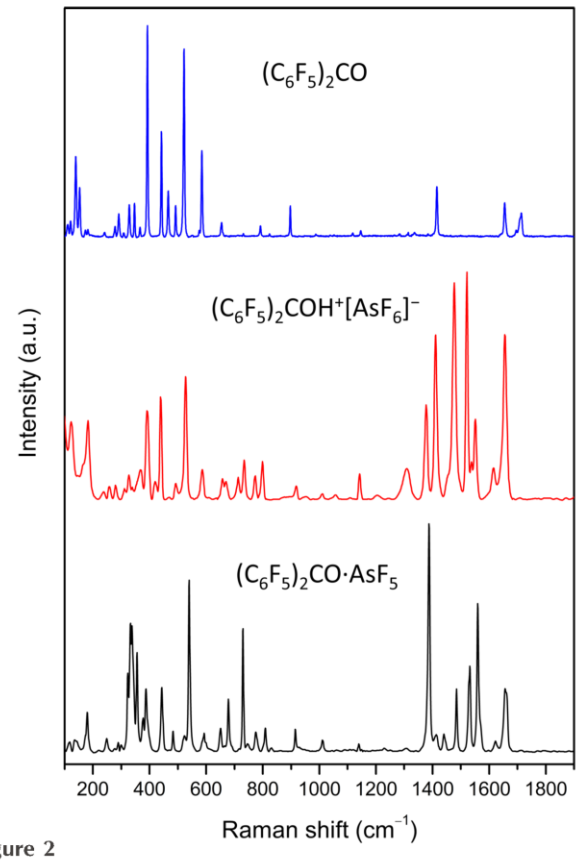


Figure 2
The low-temperature Raman spectra of $(C_6F_5)_2CO$ (top), $(C_6F_5)_2COH^+[AsF_6]^-$ (middle) and $(C_6F_5)_2CO{\cdot}AsF_5$ (bottom) measured at −90, −90 and −93 °C, respectively.

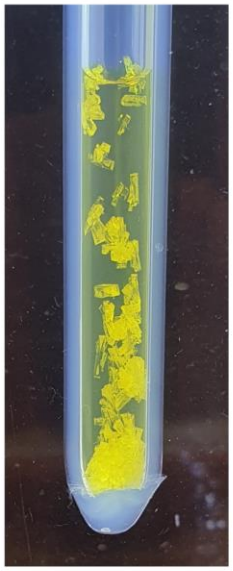


Figure 3
Canary-yellow crystals of $(C_6F_5)_2COH^+[AsF_6]^-$ that formed upon cooling a solution of $(C_6F_5)_2CO$ and AsF_5 in anhydrous HF to about −10 °C using an ethanol bath. The outer diameter of the FEP tube is 6 mm.

chiral crystallization has also been reported for achiral benzophenone (Matsumoto *et al.*, 2016).

The synthetic procedure for the preparation of $(C_6F_5)_2COH^+[AsF_6]^-$ and $(C_6F_5)_2CO{\cdot}AsF_5$ involved the reaction of $(C_6F_5)_2CO$ with AsF_5 in anhydrous HF (aHF) and in liquid SO_2 solvent, respectively (Fig. 1). Although decafluorobenzophenone was poorly soluble in aHF, the addition of AsF_5 resulted in its dissolution at room temperature, accompanied by the development of a yellow coloration. Upon cooling the reaction mixture, canary-yellow plank-shaped crystals began to form (Fig. 3). Slow removal of the aHF solvent yielded a crystalline canary-yellow solid, identified as $(C_6F_5)_2COH^+[AsF_6]^-$.

Table 2
Hydrogen-bond geometry (Å, °) for $(C_6F_5)_2COH^+[AsF_6]^-$.

D—H···A	D—H	H···A	D···A	D—H···A
O1—H1···F16	0.90 (3)	1.63 (3)	2.5279 (16)	178 (3)

The protonated salt $(C_6F_5)_2COH^+[AsF_6]^-$ crystallizes in the monoclinic space group $P2_1/n$ and contains one $(C_6F_5)_2COH^+$ cation and one $[AsF_6]^-$ anion in the asymmetric unit (Table 1 and Figs. 4 and S3).

In $(C_6F_5)_2COH^+[AsF_6]^-$ (Fig. 4), the C=O bond length [1.274 (2) Å] is elongated compared to that in $(C_6F_5)_2CO$ [1.197 (4) Å], and is comparable to values observed in the protonated ketones: acetone, $C_3H_6OH^+$ [1.271 (3) and 1.273 (3) Å]; adamantan-2-one, $C_{10}H_{14}OH^+$ [1.274 (2) Å]; and cyclopentanone, $C_5H_8OH^+$ [1.266 (3) and 1.267 (2) Å] (Stuart *et al.*, 2017). Similar C=O bond lengths have been reported for the crystal structures of the hemiprotonated benzophenone salts $[(C_6H_5)_2CO]_2H^+[CHB_{11}H_5Cl_6]^-$ [1.274 (4) Å; Stasko *et al.*, 2002] and $[(C_6H_5)_2CO]_2H^+[TaF_6]^-$ [1.259 (3) Å; Marchetti *et al.*, 2007]. The C—C(=O) bonds in $(C_6F_5)_2COH^+$ [1.443 (2) and 1.455 (2) Å] are shorter than the corresponding bonds in $(C_6F_5)_2CO$ [1.498 (3) Å]. The remaining C—F and C—C bonds in the $(C_6F_5)_2COH^+$ cation [C—C = 1.370 (2)–1.406 (2) Å; C—F = 1.322 (2)–1.334 (2) Å] remain within the range of those observed in the crystal structure of $(C_6F_5)_2CO$. The angle between the plane normals of the two arene rings [76.58 (6)°] is very similar to that in $(C_6F_5)_2CO$ [77.22 (9)°]. The angles between the arene-ring-plane normals and the plane normal of the carbonyl-bond-containing $C_2C{=}O$ fragment [36.93 (7) and 44.90 (7)°] are smaller than the corresponding value observed in the crystal structure of $(C_6F_5)_2CO$ [47.97 (7)°].

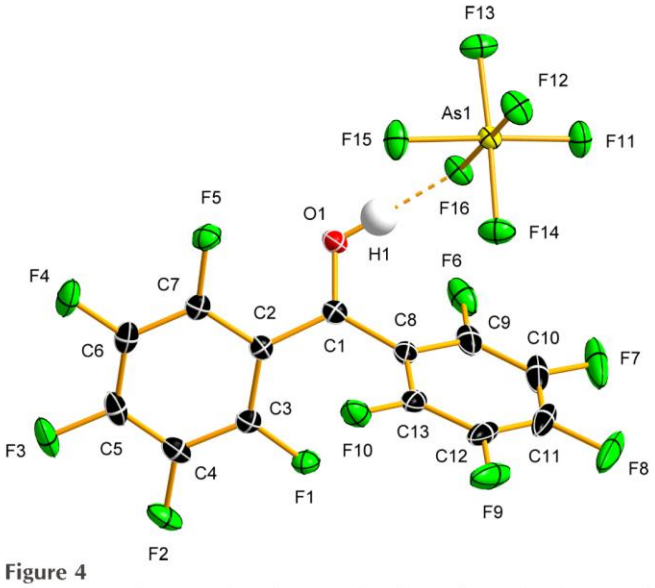


Figure 4
The asymmetric unit with the atom-labelling scheme in the crystal structure of $(C_6F_5)_2COH^+[AsF_6]^-$. The O—H···F hydrogen bond is shown as an orange dashed line. Displacement ellipsoids are depicted at the 50% probability level.

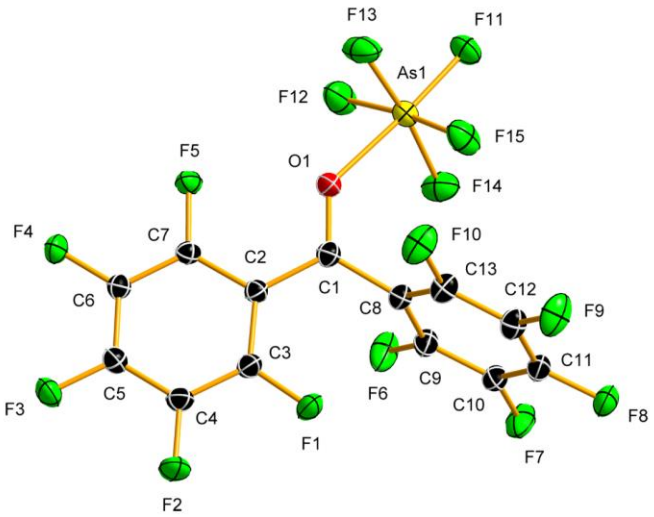


Figure 5
The asymmetric unit with the atom-labelling scheme in the crystal structure of adduct $(C_6F_5)_2CO{\cdot}AsF_5$. Displacement ellipsoids are depicted at the 50% probability level.

Table 3
Selected geometric parameters (Å, °) for crystallographically characterized compounds featuring AsF_5 coordinated to a carbonyl group.

S_2N_2CO = 5-oxo-1,3λ^4,2,4-dithiadiazole, $C_4H_2F_2O_2$ = fumaryl fluoride, CH_2ClCFO = chloroacetyl fluoride and CH_2FCFO = fluoroacetyl fluoride.

Compound (moiety)	C=O	O—As	As—F_{ax}	C—O—As	Reference
$(C_6F_5)_2CO{\cdot}AsF_5$	1.2526 (15)	1.9897 (10)	1.6890 (8)	133.83 (8)	This work
$S_2N_2CO{\cdot}AsF_5$	1.279 (4)	1.879 (7)	1.695 (6)	127.3 (1)	Gieren *et al.* (1980)
$C_4H_2F_2O_2{\cdot}4(C_4H_2F_2O_2{\cdot}AsF_5){\cdot}(C_4H_2F_2O_2{\cdot}2AsF_5)$					Bayer *et al.* (2021)
$(C_4H_2F_2O_2{\cdot}AsF_5)$	1.221 (2)	2.0367 (15)	1.6840 (14)	132.33 (15)	
$(C_4H_2F_2O_2{\cdot}AsF_5)$	1.220 (2)	2.0472 (14)	1.6835 (13)	130.67 (14)	
$(C_4H_2F_2O_2{\cdot}2AsF_5)$	1.215 (3)	2.0444 (14)	1.6926 (13)	130.83 (14)	
$CH_2ClCFO{\cdot}AsF_5$	1.213 (3)	2.0418 (16)	1.6854 (14)	128.96 (17)	Steiner *et al.* (2024*b*)
$CH_2FCFO{\cdot}AsF_5$	1.210 (3)	2.0306 (15)	1.6835 (13)	130.49 (15)	Steiner *et al.* (2024*b*)

The crystal structure exhibits a short hydrogen bond between the $(C_6F_5)_2COH^+$ cation and the $[AsF_6]^-$ anion (Table 2). The H atom lies only slightly out of the $C_2C{=}O$ plane [0.14 (3) Å]. The O···F hydrogen-bond distance [2.5279 (16) Å] is shorter than those observed in the crystal structures of $[PnF_6]^-$ (Pn = As or Sb) salts of protonated ketones – acetone, cyclopentanone and adamantan-2-one [2.560 (3)–2.6233 (16) Å; Stuart *et al.*, 2017] – due to the greater Brønsted acidity of the perfluorinated conjugate acid $(C_6F_5)_2COH^+$. The hydrogen-bonded As—F bond is elongated [As—F(H) = 1.7853 (10) Å; As—F = 1.6943 (10)–1.7237 (11) Å], resulting in a distortion of the $[AsF_6]^-$ anion from idealized octahedral geometry. Interestingly, similar $As{-}F_{bridging}$ bond lengths have been observed in metal complexes where the $[AsF_6]^-$ anion is coordinated to a metal centre, for example, in $[Mg(KrF_2)_4(AsF_6)_2]$ [1.7856 (14) and 1.7965 (13) Å] (Lozinšek *et al.*, 2017).

The supporting information includes an additional crystal structure determination of $(C_6F_5)_2COH^+[AsF_6]^-$ employing Ag *Kα* radiation, providing results essentially similar to those presented in the text.

The reaction of decafluorobenzophenone with an excess of AsF_5 in SO_2 at low temperature (Fig. 1) resulted in the formation of a yellow solution, from which large yellow plate-like crystals of the Lewis acid–base adduct $(C_6F_5)_2CO{\cdot}AsF_5$ crystallized at −78 °C over a period of ten days. The compound crystallizes in the orthorhombic space group *Pbca* (Table 1) and represents a rare crystallographically characterized example of a ketone coordinated to AsF_5 (Figs. 5 and S4).

The C=O bond length [1.2526 (15) Å] in the crystal structure of the adduct is elongated compared to that in $(C_6F_5)_2CO$ [1.197 (4) Å], although to a lesser extent than in the protonated salt [1.274 (2) Å]. A similar C=O bond length was observed in the benzophenone adduct with $TaCl_5$ [1.265 (3) Å; Marchetti *et al.*, 2007], in the adducts of BF_3 with ethylene carbonate [1.2486 (14) Å], dimethyl carbonate [1.2559 (14) Å], diethyl carbonate [1.2562 (18) Å] and γ-butyrolactone [1.2541 (16) Å] (Bodin *et al.*, 2023), and in the amide moiety of capsaicin [1.2459 (19) Å; Lozinšek, 2025]. The elongation of the C=O bond is accompanied by a significant shortening of the *anti*-C—C(=O) bond [1.4549 (16) Å], whereas the *syn*-C—C(=O) bond length remains virtually unchanged [1.4879 (16) Å] compared to the corresponding distance observed in $(C_6F_5)_2CO$ [1.498 (3) Å]. All other bond lengths in the $(C_6F_5)_2CO$ moiety within $(C_6F_5)_2CO{\cdot}AsF_5$ [C—C = 1.3788 (17)–1.4133 (15) Å; C—F = 1.3162 (13)–1.3359 (15) Å] are similar to those observed in $(C_6F_5)_2COH^+[AsF_6]^-$ and $(C_6F_5)_2CO$. The angle between the plane normals of the two arene rings [81.57 (4)°] differs from those in the crystal structures of $(C_6F_5)_2CO$ and $(C_6F_5)_2COH^+[AsF_6]^-$. Of the two rings, one is almost coplanar with the plane formed by the $C_2C{=}O$ moiety [9.44 (5)°], while the other is nearly perpendicular [75.63 (5)°].

The O—As bond [1.9897 (10) Å] in the crystal structure of $(C_6F_5)_2CO{\cdot}AsF_5$ is substantially longer than that reported for the adduct of Roesky's ketone, $S_2N_2CO{\cdot}AsF_5$ [1.879 (7) Å; Gieren *et al.*, 1980], and shorter than the O—As bond lengths (Table 3) observed in the limited number of crystal structures of compounds featuring a $C{=}O{-}AsF_5$ linkage, involving acyl

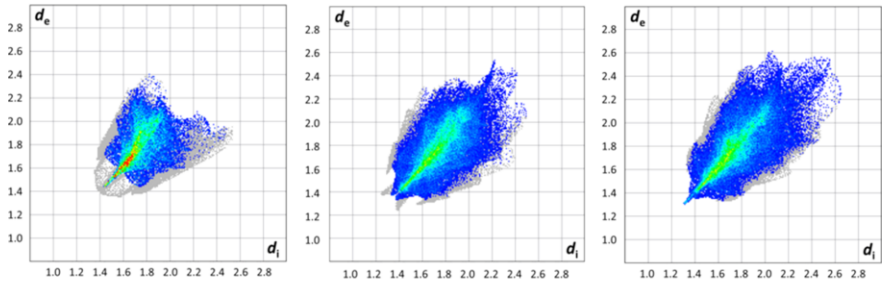


Figure 6
Hirshfeld fingerprint plots of (*a*) $(C_6F_5)_2CO$ (56.8%), (*b*) $(C_6F_5)_2COH^+[AsF_6]^-$ (69.6%) and (*c*) $(C_6F_5)_2CO{\cdot}AsF_5$ (72.8%), showing the prevalent F···F intermolecular contacts.

fluorides (Bayer *et al.*, 2021; Steiner *et al.*, 2024*b*). The As atom resides slightly out of the $C_2C{=}O$ plane [0.417 (2) Å]. The C=O—As bond angle [133.83 (8)°] is comparable to those in other compounds where a C=O group acts as a ligand to AsF_5 (Table 3). The As—F_{ax} (ax is axial) bond *trans* to As—O is somewhat shorter [1.6890 (8) Å] than the As—F_{eq} (eq is equatorial) bonds in the AsF_5 moiety [1.6960 (10)–1.7018 (9) Å]. The O—As—F_{ax} angle [176.30 (5)°] is close to linear. The acute O—As—F_{eq} angles [83.84 (5)–89.06 (5)°], the obtuse F_{ax}—As—F_{eq} angles [92.94 (5)–94.16 (5)°] and the *trans*-F_{eq}—As—F_{eq} angles deviating from linearity [171.85 (5) and 172.89 (5)°] reflect the smaller bond domain (Gillespie, 2008) and lower bond order (Stuart *et al.*, 2019) of the As—O bond compared to the As—F bonds.

In all three crystal structures, *i.e.* $(C_6F_5)_2CO$, $(C_6F_5)_2COH^+[AsF_6]^-$ and $(C_6F_5)_2CO{\cdot}AsF_5$, the dominant intermolecular contacts are F···F (Figs. 6 and S5), which involve contributions of 56.8, 69.6 and 72.8%, respectively, whereas the C···F contacts (Fig. S6) cover 30.7, 23.7 and 25.2% of the surface area, respectively. The similarity in the intermolecular interactions between $(C_6F_5)_2COH^+[AsF_6]^-$ and $(C_6F_5)_2CO{\cdot}AsF_5$ is evident from a comparison of their Hirshfeld fingerprint plots (Figs. 6 and S5–S7) (Spackman & McKinnon, 2002; Spackman *et al.*, 2021). In the crystal structure of $(C_6F_5)_2CO$, O···F contacts (Fig. S7) also contribute to the packing, accounting for 8.5% of the surface area. However, in the crystal structures of $(C_6F_5)_2COH^+[AsF_6]^-$ and $(C_6F_5)_2CO{\cdot}AsF_5$, this contribution is reduced to 4.4 and 1.9%, respectively, as the O atom is bonded to hydrogen and arsenic, respectively. In the protonated salt, F···H contacts involve 2.3% of the surface area (Fig. S8).

4. Conclusion

In this work, the syntheses, crystal structure determination and Raman spectra of a protonated decafluorobenzophenone salt, $(C_6F_5)_2COH^+[AsF_6]^-$, and a Lewis acid–base adduct, $(C_6F_5)_2CO{\cdot}AsF_5$, are reported. The crystal structure of $(C_6F_5)_2CO$ was also redetermined at 100 K. These crystal structures represent rare examples of a protonated perfluorinated aromatic ketone and a ketone–arsenic pentafluoride adduct.

Funding information

Funding for this research was provided by: European Research Council (ERC) under the European Union's Horizon 2020 Research and Innovation Programme (Starting Grant No. 950625); Jožef Stefan Institute Director's Fund.

References

Anandhi, R. & Umapathy, S. (2000). *J. Raman Spectrosc.* **31**, 331–338.
Axhausen, J., Ritter, C., Lux, K. & Kornath, A. (2013). *Z. Anorg. Allg. Chem.* **639**, 65–72.
Bayer, M. C., Jessen, C. & Kornath, A. J. (2021). *Z. Anorg. Allg. Chem.* **647**, 258–265.
Birchall, T. & Gillespie, R. J. (1965). *Can. J. Chem.* **43**, 1045–1051.
Bockmair, V., Klöck, A., Hollenwäger, D. & Kornath, A. J. (2024). *Acta Cryst.* C**80**, 781–786.
Bodin, C., Forero Saboya, J., Jankowski, P., Radan, K., Foix, D., Courrèges, C., Yousef, I., Dedryvère, R., Davoisne, C., Lozinšek, M. & Ponrouch, A. (2023). *Batteries Supercaps* **6**, e202200433.
Bourhis, L. J., Dolomanov, O. V., Gildea, R. J., Howard, J. A. K. & Puschmann, H. (2015). *Acta Cryst.* A**71**, 59–75.
Brandenburg, K. (2022). *DIAMOND*. Crystal Impact GbR, Bonn, Germany.
Chadda, S. K., Childs, R. F., Faggiani, R. & Lock, C. J. L. (1986). *J. Am. Chem. Soc.* **108**, 1694–1695.
Chambers, R. D. & Spring, D. J. (1969). *Tetrahedron* **25**, 565–572.
Childs, R. F., Kostyk, M. D., Lock, C. J. L. & Mahendran, M. (1990). *J. Am. Chem. Soc.* **112**, 8912–8920.
Childs, R. F., Varadarajan, A., Lock, C. J. L., Faggiani, R., Fyfe, C. A. & Wasylishen, R. E. (1982). *J. Am. Chem. Soc.* **104**, 2452–2456.
Cooper, R. I., Thompson, A. L. & Watkin, D. J. (2010). *J. Appl. Cryst.* **43**, 1100–1107.
Dolomanov, O. V., Bourhis, L. J., Gildea, R. J., Howard, J. A. K. & Puschmann, H. (2009). *J. Appl. Cryst.* **42**, 339–341.
Farmer, D. B. & Walker, S. (1967). *Trans. Faraday Soc.* **63**, 966–973.
Gieren, A., Dederer, B., Martin, R., Schanda, F., Roesky, H. W. & Eiser, M. (1980). *Chem. Ber.* **113**, 3904–3909.
Gillespie, R. J. (2008). *Coord. Chem. Rev.* **252**, 1315–1327.
Goetz, N. R., Axhausen, J. A. H., Soltner, T., Rotter, C. & Kornath, A. J. (2016). *ChemistrySelect* **1**, 5517–5520.
Groom, C. R., Bruno, I. J., Lightfoot, M. P. & Ward, S. C. (2016). *Acta Cryst.* B**72**, 171–179.
Haiges, R., Baxter, A. F., Goetz, N. R., Axhausen, J. A., Soltner, T., Kornath, A. & Christe, K. O. (2016). *Dalton Trans.* **45**, 8494–8499.
Hayatifar, M., Marchetti, F., Pampaloni, G. & Zacchini, S. (2014). *Polyhedron* **70**, 6–10.
Heo, S. W., Hwang, I.-C., Chun, Y., Lee, J. W., Singh, N. J., Kim, S. B. & Kim, K. S. (2011). *Chem. Asian J.* **6**, 2055–2061.
Hollenwäger, D., Bockmair, V. & Kornath, A. J. (2025). *Acta Cryst.* C**81**, 31–37.
Hollenwäger, D., Thamm, S., Bockmair, V., Nitzer, A. & Kornath, A. J. (2024). *J. Org. Chem.* **89**, 11421–11428.
Hwang, I.-C., Heo, S. W., Singh, N. J., Lee, J. W., Chun, Y., Baek, S. B., Jin, K. S., Ree, M., Lee, H. C., Kim, S. B. & Kim, K. S. (2010). *J. Phys. Chem. B* **114**, 7216–7221.
Lozinšek, M. (2025). *Acta Cryst.* C**81**, 188–192.
Lozinšek, M., Mercier, H. P. A., Brock, D. S., Žemva, B. & Schrobilgen, G. J. (2017). *Angew. Chem. Int. Ed.* **56**, 6251–6254.
Lozinšek, M., Mercier, H. P. A. & Schrobilgen, G. J. (2021). *Angew. Chem. Int. Ed.* **60**, 8149–8156.
Marchetti, F., Pampaloni, G. & Zacchini, S. (2007). *Dalton Trans.* pp. 4343–4351.
Matsumoto, A., Tsuchiya, S., Hagiwara, Y., Ishikawa, K., Koshima, H., Asahi, T. & Soai, K. (2016). *Chem. Lett.* **45**, 526–528.
Mazej, Z. & Žemva, B. (2005). *J. Fluorine Chem.* **126**, 1432–1434.
Minkwitz, R. & Reinemann, S. (1999). *Z. Anorg. Allg. Chem.* **625**, 121–125.
Motaln, K., Gurung, K., Brázda, P., Kokalj, A., Radan, K., Dragomir, M., Žemva, B., Palatinus, L. & Lozinšek, M. (2024). *ACS Cent. Sci.* **10**, 1733–1741.
Motaln, K., Uran, E., Giordano, N., Parsons, S. & Lozinšek, M. (2025). *J. Appl. Cryst.* **58**, 221–226.
Olah, G. A. & Calin, M. (1968). *J. Am. Chem. Soc.* **90**, 938–943.
Olah, G. A., Calin, M. & O'Brien, D. H. (1967*a*). *J. Am. Chem. Soc.* **89**, 3586–3590.
Olah, G. A. & Mo, Y. K. (1973). *J. Org. Chem.* **38**, 2682–2685.
Olah, G. A., O'Brien, D. H. & Calin, M. (1967*b*). *J. Am. Chem. Soc.* **89**, 3582–3586.
Olah, G. A., Prakash, G. K. S., Molnár, A. & Sommer, J. (2009). *Superacid Chemistry*, 2nd ed. Chichester: John Wiley & Sons.
Parsons, S., Flack, H. D. & Wagner, T. (2013). *Acta Cryst.* B**69**, 249–259.

Rigaku OD (2025). *CrysAlis PRO*. Rigaku Corporation, Wrocław, Poland.
Saal, T., Blastik, Z. E., Haiges, R., Nirmalchandar, A., Baxter, A. F., Christe, K. O., Vasiliu, M., Dixon, D. A., Beier, P. & Prakash, G. K. S. (2020). *Angew. Chem. Int. Ed.* **59**, 12520–12526.
Saal, T., Haiges, R. & Christe, K. O. (2023). *Dalton Trans.* **52**, 18143–18147.
Schickinger, M., Siegert, M., Morgenstern, Y., Zischka, F., Stierstorfer, K. & Kornath, A. (2018). *Z. Anorg. Allg. Chem.* **644**, 1564–1569.
Schwarzer, A., Seichter, W., Weber, E., Stoeckli-Evans, H., Losada, M. & Hulliger, J. (2004). *CrystEngComm* **6**, 567–572.
Sekuur, Th. J. & Kranenburg, P. (1966). *Tetrahedron Lett.* **7**, 4793–4795.
Sheldrick, G. M. (2015). *Acta Cryst.* C**71**, 3–8.
Spackman, M. A. & McKinnon, J. J. (2002). *CrystEngComm* **4**, 378–392.
Spackman, P. R., Turner, M. J., McKinnon, J. J., Wolff, S. K., Grimwood, D. J., Jayatilaka, D. & Spackman, M. A. (2021). *J. Appl. Cryst.* **54**, 1006–1011.
Stasko, D., Hoffmann, S. P., Kim, K.-C., Fackler, N. L. P., Larsen, A. S., Drovetskaya, T., Tham, F. S., Reed, C. A., Rickard, C. E. F., Boyd, P. D. W. & Stoyanov, E. S. (2002). *J. Am. Chem. Soc.* **124**, 13869–13876.
Steiner, S., Djordjevic, K., Bockmair, V., Hollenwäger, D. & Kornath, A. J. (2024*a*). *Acta Cryst.* C**80**, 792–797.
Steiner, S., Jessen, C., Nitzer, A., Bockmair, V. & Kornath, A. J. (2024*b*). *J. Org. Chem.* **89**, 14399–14407.
Stuart, D., Wetmore, S. D. & Gerken, M. (2017). *Angew. Chem. Int. Ed.* **56**, 16380–16384.
Stuart, D., Wetmore, S. D. & Gerken, M. (2019). *J. Fluorine Chem.* **221**, 9–16.
van der Linde, R., Dornseiffen, J. W., Veenland, J. U. & de Boer, Th. J. (1968). *Spectrochim. Acta A* **24**, 2115–2119.

Acta Cryst. (2025). C**81**, https://doi.org/10.1107/S2053229625007697 Supporting information, sup-1

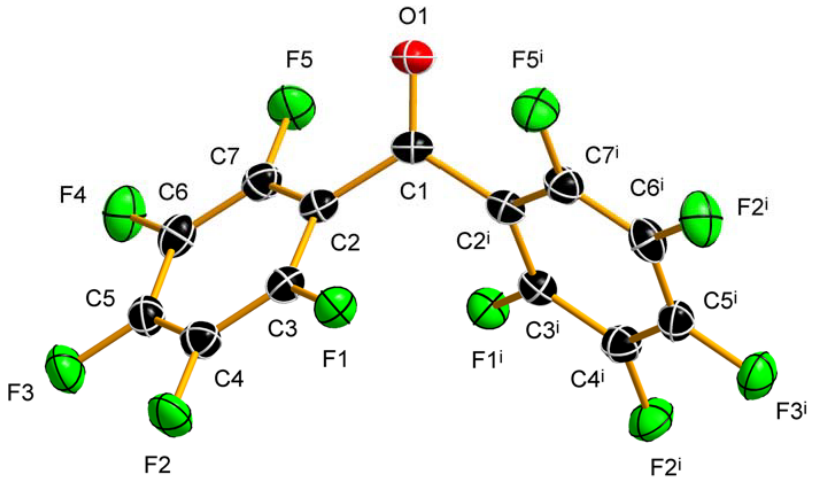


Figure S1 Expanded asymmetric unit with atom-labelling scheme in the crystal structure of $(C_6F_5)_2CO$. Displacement ellipsoids are depicted at the 50% probability level. Symmetry code: (i) $-x+1, y, -z$.

Acta Cryst. (2025). C81, https://doi.org/10.1107/S2053229625007697 Supporting information, sup-2

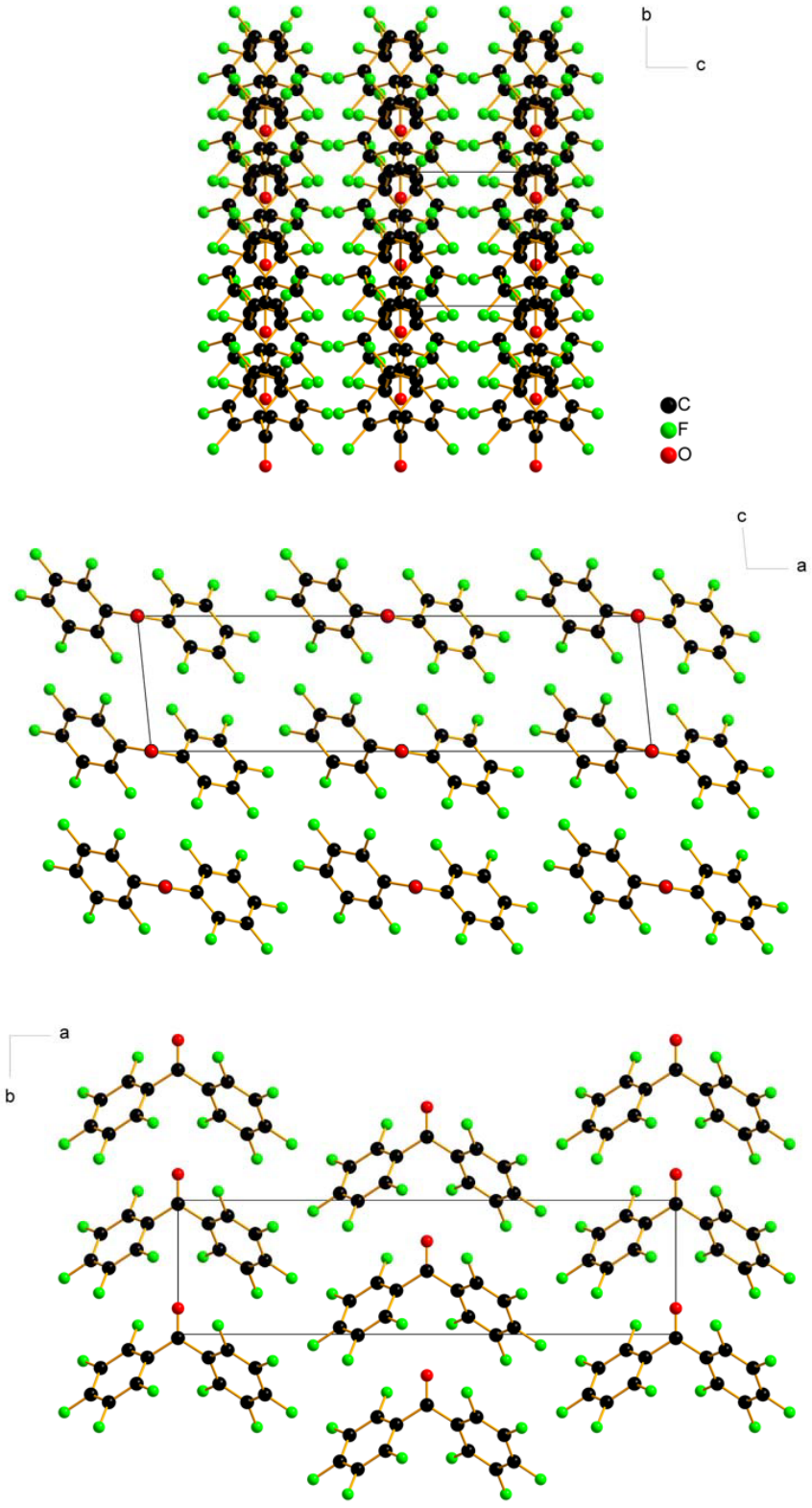


Figure S2 Packing diagrams and the unit cell of the $(C_6F_5)_2CO$ crystal structure viewed along the crystallographic *a*- (top), *b*- (middle) and *c*-axis (bottom).

Acta Cryst. (2025). C81, https://doi.org/10.1107/S2053229625007697 Supporting information, sup-3

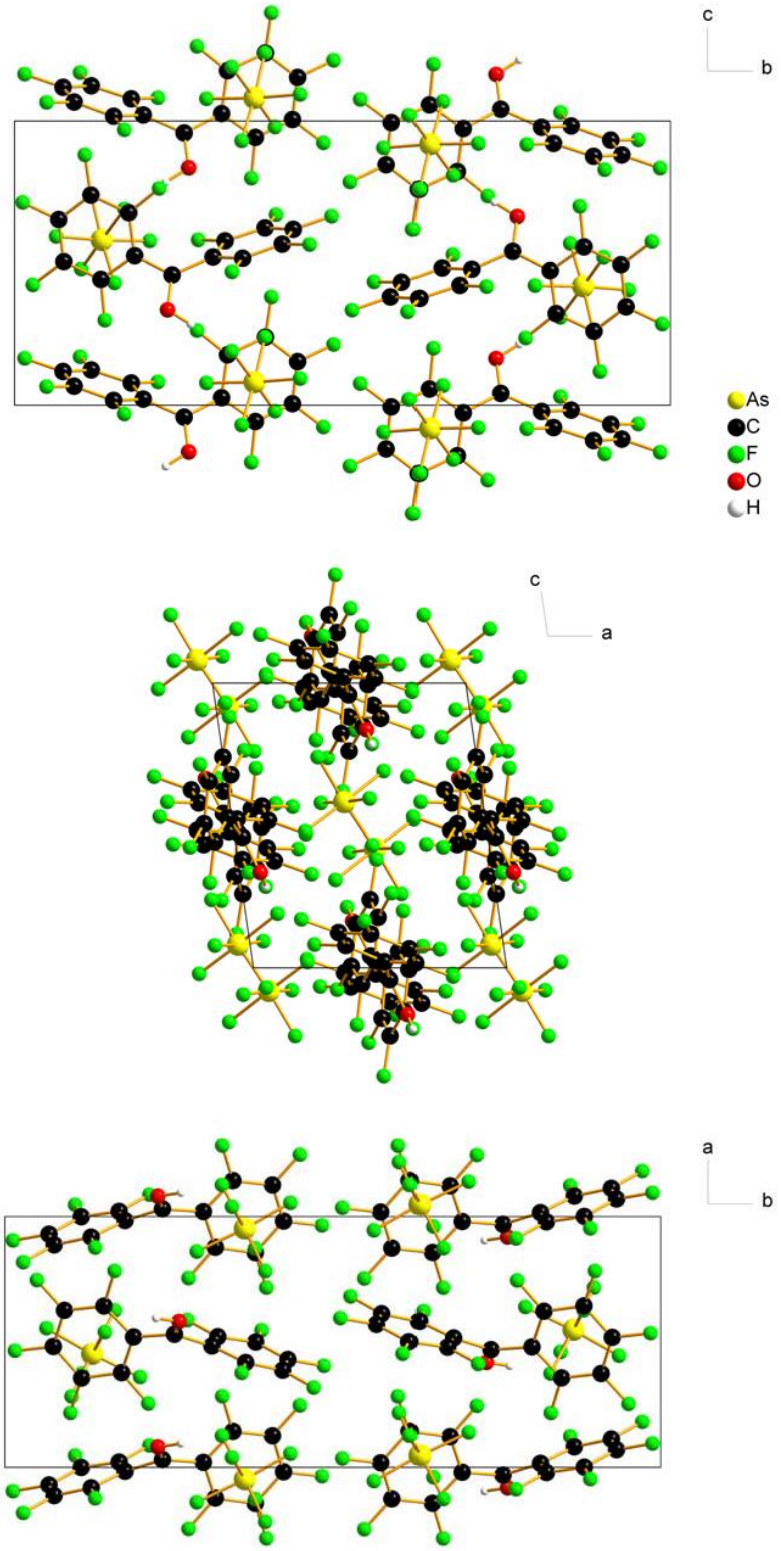


Figure S3 Packing diagrams and the unit cell of the $(C_6F_5)_2COH^+[AsF_6]^-$ crystal structure viewed along the crystallographic *a*- (top), *b*- (middle) and *c*-axis (bottom).

Acta Cryst. (2025). C81, https://doi.org/10.1107/S2053229625007697 Supporting information, sup-4

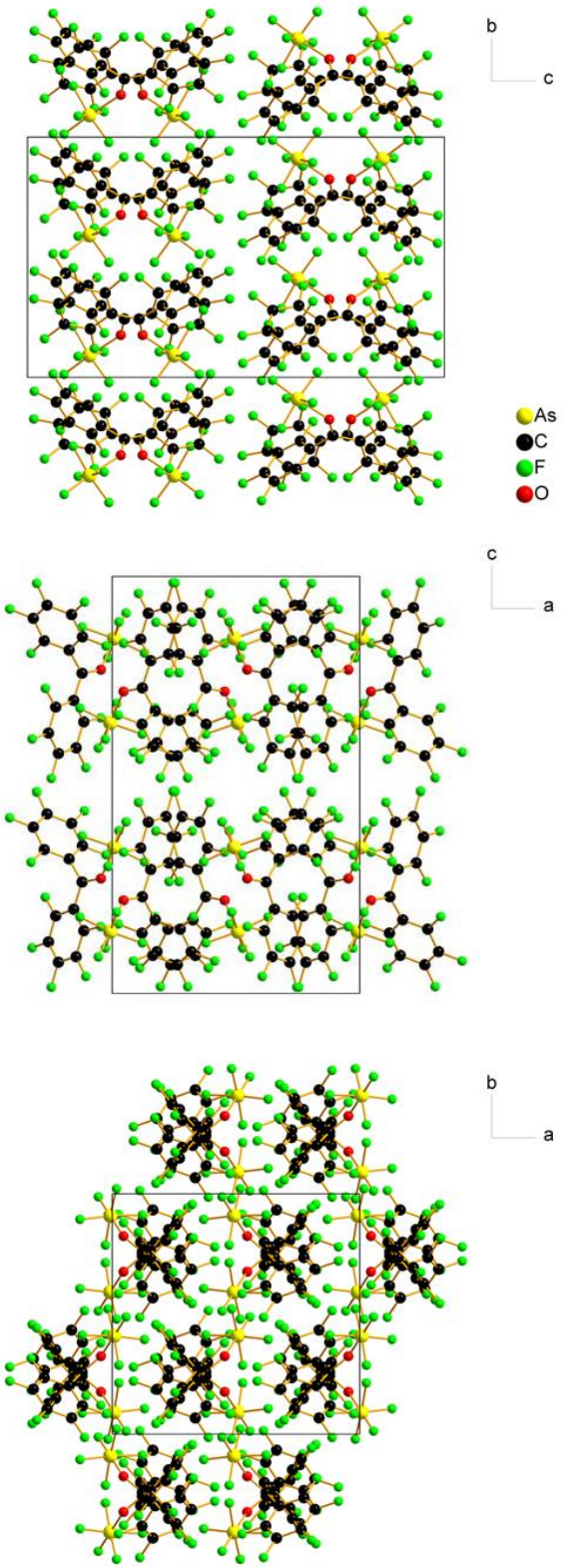


Figure S4 Packing diagrams and the unit cell of the $(C_6F_5)_2CO{\cdot}AsF_5$ crystal structure viewed along the crystallographic *a*- (top), *b*- (middle) and *c*-axis (bottom).

Acta Cryst. (2025). C81, https://doi.org/10.1107/S2053229625007697 Supporting information, sup-5

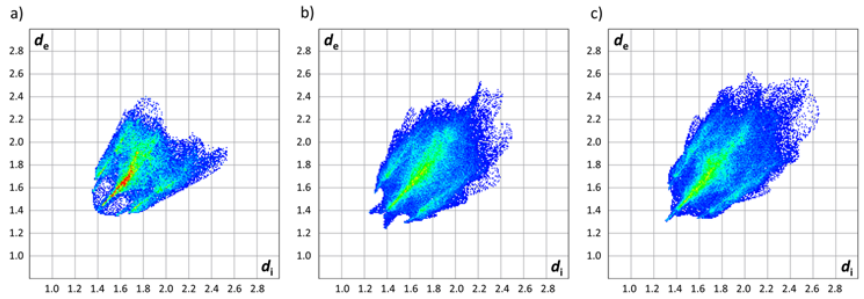


Figure S5 Hirshfeld fingerprint plots of (a) $(C_6F_5)_2CO$, (b) $(C_6F_5)_2COH^+[AsF_6]^-$, and (c) $(C_6F_5)_2CO{\cdot}AsF_5$.

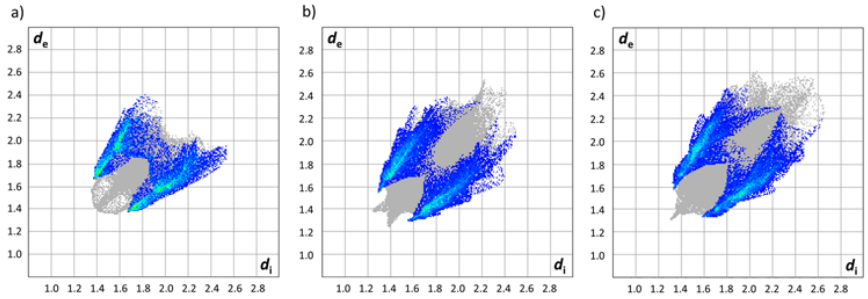


Figure S6 Hirshfeld fingerprint plots for C···F intermolecular contacts of (a) $(C_6F_5)_2CO$ (30.7%), (b) $(C_6F_5)_2COH^+[AsF_6]^-$ (23.7%), and (c) $(C_6F_5)_2CO{\cdot}AsF_5$ (25.2%).

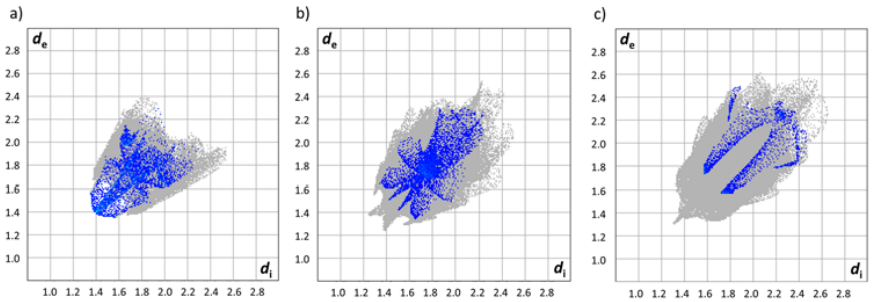


Figure S7 Hirshfeld fingerprint plots for O···F intermolecular contacts of (a) $(C_6F_5)_2CO$ (8.5%), (b) $(C_6F_5)_2COH^+[AsF_6]^-$ (4.4%), and (c) $(C_6F_5)_2CO{\cdot}AsF_5$ (1.9%).

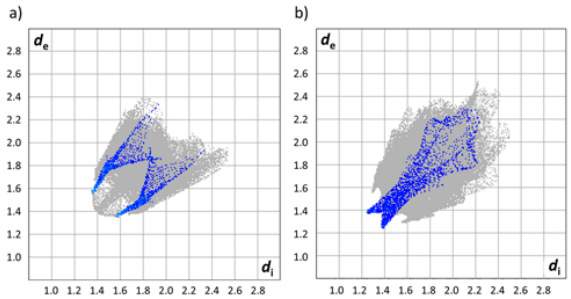


Figure S8 Hirshfeld fingerprint plots for C···O intermolecular contacts of (a) $(C_6F_5)_2CO$ (3.9%) and for H···F contacts of (b) $(C_6F_5)_2COH^+[AsF_6]^-$ (2.3%).

4.5 Hydrostatic Limits of Selected Inert Fluids

In this chapter, the results of the investigation into the hydrostatic behavior of selected inert fluids are presented. The findings of this work have been published in *J. Appl. Cryst.* (2025), **58**, 221–226. Klemen Motaln performed the experiments, whereas Erik Uran performed preliminary measurements and provided procedure for data analysis. Both authors contributed to data analysis, as well as to writing and editing of the manuscript.

High-pressure investigations of many materials have led to important discoveries in physics, chemistry, geoscience, and materials research. As most of these discoveries rely on structure–function correlations, knowledge of the structure at high pressure is crucial. Therefore, single-crystal X-ray diffraction remains the primary method of structural analysis up to 10 GPa in many laboratories (Katrusiak, 2019).

Single-crystal high-pressure diffraction is particularly dependent on the maintenance of hydrostatic conditions, which ensures uniform pressure within the gasket hole. Such conditions are important not only for preserving the overall crystal quality, which deteriorates under non-hydrostatic conditions, but also for accurately elucidating the effects of pressure. Specifically, phase transitions can be either suppressed or promoted by shear or strain arising from non-hydrostaticity, and under such conditions, the observed phase transition may not correlate solely with the applied pressure (Takemura, 2021).

Hydrostaticity is achieved through the use of a pressure-transmitting medium (PTM). Many media have been explored, with solidified gases such as helium, neon, and nitrogen being the most effective, as they remain hydrostatic above 10 GPa. However, their loading requires gas compressors, which are not readily available in most laboratories. Nitrogen can also be loaded as a liquid, although this requires cryogenic temperatures (Klotz, Chervin, Munsch, & Le Marchand, 2009).

Ambient-pressure liquid mixtures, such as ethanol–methanol (4:1) or pentane–isopentane (1:1), also exhibit good hydrostatic properties up to 10 GPa. They are, however, reactive with many materials and can dissolve a wide variety of compounds. Inert media, such as silicone oils and the Daphne series of oils, can also be used, although their application is limited to non-oxidizing compounds, and only Daphne 7474 remains hydrostatic up to approximately 4 GPa. Fluorocarbon-based fluids, such as Fluorinerts, are hydrostatic only up to 1.5 GPa (Klotz, Chervin, Munsch, & Le Marchand, 2009). Therefore, further exploration of inert, oxidatively-resistant, fluorine-based hydrostatic media for high-pressure experiments is required.

For this reason, the following fluorine-based inert fluids were investigated: Fomblin Z60, Fomblin Z25, Fomblin Y LVAC 06/6, and Halocarbon Oil 11-14. They were selected because they demonstrate resistance to XeF_2 under ambient conditions and may serve as promising candidates for high-pressure studies of noble-gas compounds.

The ruby fluorescence method (Klotz, Chervin, Munsch, & Le Marchand, 2009) was used to monitor the evolution of pressure gradients across the DAC sample chamber during compression and decompression. To validate the methodology, a test measurement was performed using N_2 as the PTM.

Fomblin Z60 and Fomblin Z25 perfluoropolyethers were hydrostatic up to 1.7 and 1.5 GPa, respectively. Halocarbon Oil 11-14 followed, with a hydrostatic limit of 1.2 GPa, whereas the Fomblin Y LVAC 06/6 exhibited non-hydrostatic behavior above 0.6 GPa. Slight pressure gradients observed above the hydrostatic limits suggest that these media may still be usable at pressures exceeding 5 GPa.

research papers

JOURNAL OF APPLIED CRYSTALLOGRAPHY

ISSN 1600-5767

Hydrostatic behaviour of highly inert Fomblin and Halocarbon fluids as pressure-transmitting media in high-pressure experiments

Klemen Motaln,[a,b]‡ Erik Uran,[a,b]‡ Nico Giordano,[c] Simon Parsons[d] and Matic Lozinšek[a,b]*

[a]Jožef Stefan Institute, Jamova cesta 39, 1000 Ljubljana, Slovenia, [b]Jožef Stefan International Postgraduate School, Jamova cesta 39, 1000 Ljubljana, Slovenia, [c]Deutsches Elektronen-Synchrotron DESY, Notkestr. 85, 22607 Hamburg, Germany, and [d]EaStCHEM School of Chemistry and Centre for Science at Extreme Conditions, University of Edinburgh, King's Buildings, W. Mains Road, Edinburgh EH9 3FJ, United Kingdom. *Correspondence e-mail: matic.lozinsek@ijs.si

Received 20 November 2024
Accepted 14 January 2025

Edited by S. Moggach, The University of Western Australia, Australia

‡ These authors contributed equally to this work.

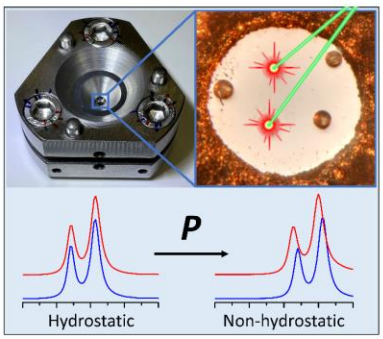
Keywords: pressure-transmitting media; ruby fluorescence measurements; high-pressure crystallography; single-crystal X-ray diffraction; diamond anvil cells; DACs; hydrostaticity.

Supporting information: this article has supporting information at journals.iucr.org/j

A pressure-transmitting medium (PTM) plays an important role in diamond anvil cell (DAC) experiments as it ensures that the sample is exposed to hydrostatic pressure. Although PTMs that are liquids under ambient conditions are the easiest to handle and load, the selection of chemically inert liquid media with established hydrostatic properties is limited. To widen the choice of highly inert PTMs for high-pressure experiments, the hydrostatic behaviours of Fomblin Z60, Fomblin Z25, Fomblin Y LVAC 06/6 and Halocarbon Oil 11-14 were investigated. The ruby fluorescence method was used to monitor the evolution of pressure gradients across the DAC sample chamber during compression and decompression. Fomblin Z60 and Fomblin Z25 perfluoropolyethers, which are hydrostatic to 1.7 and 1.5 GPa, respectively, exhibited the best hydrostatic performance, followed by Halocarbon Oil 11-14 with a limit of 1.2 GPa, whereas the non-hydrostatic behaviour of Fomblin Y LVAC 06/6 was observed above only 0.6 GPa.

1. Introduction

The application of high-pressure research is increasingly prevalent across a diverse range of scientific disciplines, including physics, chemistry, materials research and geoscience (Hemley, 2000; Duffy, 2005; Zhang *et al.*, 2017; Mao *et al.*, 2018; Miao *et al.*, 2020; Moggach & Oswald, 2020). In the field of chemistry, advances in laboratory-based diffractometer technology, access to dedicated high-pressure synchrotron beamlines and the increased availability of diamond anvil cells (DACs) have prompted a surge in investigations focusing on the analysis of pressure-induced structural changes by single-crystal X-ray diffraction (SCXRD) (Katrusiak, 2008, 2019; Tidey *et al.*, 2014; Zakharov & Boldyreva, 2019). In such investigations, it is highly desirable that uniform pressure is exerted on all of the surfaces of the crystal (Miletich *et al.*, 2000). The presence of non-hydrostatic conditions can influence the occurrence of pressure-induced phase transitions and may also induce structural changes that are not necessarily related solely to pressure, but rather also to shear strain and deviatoric and uniaxial stresses (Takemura, 2021). It is also well established that non-hydrostatic conditions can be responsible for degradation and amorphization of single crystals (Gillet *et al.*, 1995; Machon *et al.*, 2003). Furthermore, precise information regarding the pressure in the DAC experiments is vital not only for ensuring experimental accuracy and reproducibility but also for facilitating



OPEN ACCESS
Published under a CC BY 4.0 licence

comparisons with the results of theoretical modelling that assume hydrostatic compression (Takemura, 2021).

Hydrostatic conditions within the sample chamber of the DAC are achieved through the use of a pressure-transmitting medium (PTM). A variety of PTMs are currently utilized for high-pressure experiments, encompassing materials that are either gaseous, liquid or solid under ambient conditions. Liquid or solidified gases typically demonstrate the highest hydrostatic limits. Among these, helium, neon and nitrogen are popular for accessing pressures beyond 10 GPa and for their high degree of inertness (Klotz *et al.*, 2009). Nevertheless, the loading of gases typically requires the use of specialized gas-loading systems, which are mainly accessible at synchrotron facilities or specially equipped laboratories (Rivers *et al.*, 2008; Kurnosov *et al.*, 2008). The commonly utilized PTMs employed in high-pressure SCXRD experiments are organic solvent mixtures, such as 5:1 isopentane–*n*-pentane and 4:1 methanol–ethanol, which are usually straightforward to handle and load and can remain hydrostatic up to 7.4 and 10.5 GPa, respectively (Klotz *et al.*, 2009). A liquid PTM is not suitable if it dissolves or reacts with the sample. In the case of porous materials, the PTM may also penetrate the pores, changing the chemical composition and structure of the material (McKellar & Moggach, 2015; Collings & Goodwin, 2019). Reactions with the sample can be avoided using a chemically inert PTM; popular examples include silicone oils, Daphne series oils (7373, 7474 and 7575), and Fluorinert fluids and their mixtures. Among these, Daphne 7474 has been found to exhibit one of the highest hydrostatic limits of approximately 4 GPa (Murata *et al.*, 2008; Klotz *et al.*, 2009), whereas the hydrostatic limits of other Daphne oils studied are lower (Varga *et al.*, 2003; Sidorov & Sadykov, 2005; Klotz *et al.*, 2009; Staško *et al.*, 2020). Among Fluorinerts, which are perfluorinated compounds and thus offer the greatest chemical inertness, the highest hydrostatic limit of 2.3 GPa was reported for the Fluorinert FC84–FC87 1:1 mixture (Sidorov & Sadykov, 2005; Klotz *et al.*, 2009), whereas the hydrostatic limits of other examined Fluorinert PTMs typically lie below 2.2 GPa (Varga *et al.*, 2003; Sidorov & Sadykov, 2005; Torikachvili *et al.*, 2015). Another class of highly chemically inert fluids are the Fomblin series of perfluoropolyether (PFPE) synthetic polymer liquid lubricants. Prior investigations into the hydrostatic behaviour of one type of Fomblin oil, Fomblin Y HVAC 140/13, revealed that it is essentially non-hydrostatic above 1 GPa (Koyama-Nakazawa *et al.*, 2007; Osakabe & Kakurai, 2008). Moreover, perhalogenated PTMs that contain no hydrogen can be employed for high-pressure neutron experiments, as these media typically exhibit only very small neutron incoherent scattering (Varga *et al.*, 2003; Sidorov & Sadykov, 2005).

To widen the selection of highly inert fluids which could serve as PTMs and demonstrate satisfactory hydrostatic performance, Fomblin Z60, Fomblin Z25 and Fomblin Y LVAC 06/6 perfluoropolyethers, as well as the poly(chlorotrifluoroethylene) Halocarbon Oil 11-14, have been investigated in this work. The hydrostatic behaviour of selected fluids was studied by the ruby fluorescence technique, which enables the determination of the pressure distribution experienced by ruby balls located at different positions within a DAC (Piermarini *et al.*, 1973; Klotz *et al.*, 2009). The specific fluids were selected because of their exceptional inertness, which is reflected in the fact that Fomblin Z25 can be used for mounting single crystals of highly reactive and strongly oxidizing noble-gas compounds (Lozinšek *et al.*, 2021; Motaln *et al.*, 2024).

2. Experimental

Perfluoropolyethers Fomblin Z60 (Synquest), Fomblin Z25 (Synquest), Fomblin Y LVAC 06/6 (Aldrich) and the poly(chlorotrifluoroethylene) Halocarbon Oil 11-14 (Halocarbon Products Corp.) were used as supplied (Fig. S1 of the supporting information). The Raman (Fig. S2) and attenuated total reflectance IR spectra (Fig. S3) of the fluids, along with the relevant measurement details, are provided in the supporting information. The inertness of the fluids was tested by bringing them into contact with XeF_2 in an inert atmosphere: no reaction or evolution of Xe gas was observed in any case. In all experiments, Merrill–Bassett type cell bodies (Fig. 1) (Merrill & Bassett, 1974) were paired with Boehler–Almax

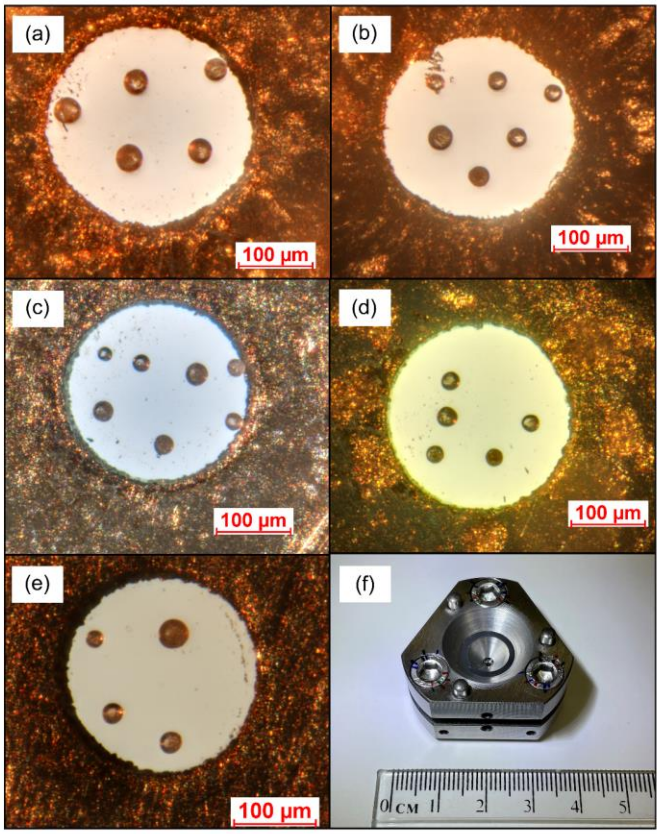


Figure 1
DAC pressure chambers showing the distribution of the ruby balls loaded with the following fluids: (*a*) Fomblin Z60, (*b*) Fomblin Z25, (*c*) Fomblin Y LVAC 06/6, (*d*) Halocarbon Oil 11-14 and (*e*) N_2. The differences in colour are an artefact of illumination. (*f*) Merrill–Bassett DAC, as used in this study.

design type Ia or IIas diamonds (Boehler & Hantsetters, 2004) with 600 μm diameter culets and tungsten carbide seats (Moggach *et al.*, 2008) (Almax easyLab). Inconel X750 (Goodfellow, Ni74/Cr15/Fe7/Ti/Al/Nb, annealed) plates, with a starting thickness of 250 μm, were employed as gaskets and pre-indented to a thickness of approximately 100 μm. Subsequently, the gasket holes with a 250 μm diameter were drilled using a spark eroder (LOTO-eng SEC-400). Prior to use, the gaskets were cleaned in an ultrasonic bath containing ethanol. In order to load the cells, 4–7 ruby balls [BETSA, Al_2O_3:Cr^{3+}, 3600 p.p.m. Cr^{3+}, 3–50 μm mean diameter (Chervin *et al.*, 2001)] were placed on the culet of the upper diamond, with the investigated PTM placed within the gasket hole. The DAC was then closed, ensuring that no air bubbles remained trapped within. Care was taken to ensure that the ruby balls were distributed throughout the sample chamber (Fig. 1).

Ruby fluorescence spectra (Syassen, 2008) were recorded at room temperature (23 ± 1 °C) using a Bruker Sentera II confocal Raman microscope. Rubies were excited by the 532 nm laser with a power output of 0.5 mW. The fluorescence spectra were recorded in the range 635–725 nm by accumulation of ten acquisitions with an exposure time of 1 ms per acquisition. The spectrum of each ruby in the DAC was measured four times in the course of each measurement cycle. The first measurement cycle of the spectra was conducted 15 min after the pressure in the cell was increased, with an additional measurement cycle following at least 24 h later in order to account for mechanical equilibration and creep effects (Piermarini *et al.*, 1973). If a significant change in the measured pressure was observed, the measurement cycle was repeated one day later until no further change was observed. Further compression was only performed once the pressure at various points within the cell fully stabilized. The fluorescence spectra measured just before a new round of compression were used for the calculation of pressure deviation. When differences of >1 GPa were detected between different ruby balls, typically at pressures of 7–9 GPa, the cells were gradually decompressed in a manner analogous to the compression cycle, with measurements taken at each step of the decompression.

Prior to spectrum analysis, background subtraction was performed in the Bruker *Opus* 8.7 software suite, utilizing a concave rubber band correction with three iterations and 1024 baseline points. The spectra were fitted with Pearson VII functions in the *Fityk* program (Wojdyr, 2010), with optimization by the *VAR2* method (Vlček & Lukšan, 2006) from the *NLopt* library (Johnson, 2007). Under markedly non-hydrostatic conditions, a shoulder began to emerge in the R_1 line which significantly compromised the fit. This issue was addressed by incorporating a third Pearson VII function into the optimization, which enabled the fitting of this shoulder and led to an improvement of the overall fit. The fitting yielded the position of the R_1 and R_2 peaks and their respective full width at half-maximum values (fwhm). The separation between R_1 and R_2 peak positions was calculated as $\Delta R = R_1 - R_2$. The reference position of the R_1 line under ambient conditions was obtained by measuring the fluorescence spectra of five rubies kept under ambient conditions and adhered to a microscope slide by the use of Fomblin Z25 twice prior to and twice after each measurement cycle. The spectra were processed and analysed in accordance with the aforementioned methodology, and the mean value of all extracted R_1 peak positions was employed as the reference wavelength of the R_1 line in subsequent pressure calculations during the corresponding measurement cycle. Pressures were calculated with the Ruby2020 pressure gauge equation (Shen *et al.*, 2020).

The onset of non-hydrostatic conditions was monitored by plotting the standard deviation of the measured pressures (σ_P), the averaged values of ΔR and the fwhm of the R_1 peaks as a function of the average pressure in the cell P_{avg}, as previously outlined (Klotz *et al.*, 2009). The value of P_{avg} is the mean of all the pressures obtained in a single cycle of measurement, individually calculated from the position of the R_1 peak of each ruby in the cell, each measured four times (see Section S3 in the supporting information). Similarly, the mean values of ΔR and fwhm of the R_1 peak were obtained by averaging all the individual ΔR and fwhm(R_1) values obtained in a single measurement cycle. The σ_P value is calculated as the standard deviation of the mean pressures of all loaded rubies.

In order to benchmark the employed methodology, an experimental run utilizing N_2 as the PTM, for which the hydrostatic behaviour is well established (LeSar *et al.*, 1979; Klotz *et al.*, 2009), was also conducted. A Merrill–Bassett cell body with 600 μm culet type Ia Boehler–Almax diamond anvils was employed in conjunction with a stainless-steel gasket [with a thickness of 250 μm, preindented to approximately 70 μm with a 250 μm-diameter hole; Fig. 1(*e*)]. N_2 was loaded into the DAC by submerging a partially opened cell that had been pre-loaded with ruby balls into a bath of liquid nitrogen. Once the DAC had cooled to the temperature of liquid nitrogen, it was closed and fully tightened, trapping the liquid nitrogen within the sample chamber.

3. Results

A reliable indicator for the appearance of non-hydrostaticity is the onset of an increase in the standard deviation of pressure (σ_P) observed in the pressure dependence of σ_P plots (Klotz *et al.*, 2009) (Figs. 2 and S4). The pressure dependences of ΔR and fwhm(R_1) plots are depicted in the supporting information (Figs. S5 and S6).

Among the perhalogenated fluids examined, the highest hydrostatic limit was observed for Fomblin Z60 and Z25 fluids, with the initial pressure gradients appearing above 1.7 and 1.5 GPa, respectively (Figs. 2 and S4; Table 1). These conclusions are corroborated by the pressure dependences of the ΔR and fwhm(R_1) plots (Figs. S5 and S6), which also exhibit a large sudden increase in both parameters above the pressures identified in the pressure dependence of σ_P plots (Fig. 2).

While σ_P steadily rises as the pressure is increased in the non-hydrostatic regime in the case of Fomblin Z60, more complex behaviour is seen for Fomblin Z25. Following the initial increase, the σ_P value rises relatively slowly and nearly

Table 1
Selected physical properties of the evaluated halogenated fluids and their observed hydrostatic limits.

The values for Fomblin Z and Fomblin Y fluids were sourced from the respective product data sheet brochures: Fomblin PFPE Lubricants, Syensqo, R 06/2017, version 2.2, and Fomblin PFPE Lubes for Vacuum Applications, Syensqo, R 10/2017, version 2.7, respectively.

	Fomblin Z60	Fomblin Z25	Fomblin Y LVAC 06/6	Halocarbon Oil 11-14
Average molecular weight (g mol^{-1})	21500	17100	1800	–
Density at 20 °C (g cm^{-3})	1.85	1.85	1.88	1.90†
Kinematic viscosity at 20 °C (cSt)	600	223	64	–
Pour point (°C)	−63	−75	−50	–
Hydrostatic limit (GPa)	≃1.7	≃1.5	≃0.6	≃1.2

† Density was determined at 20 °C using a pycnometer.

reaches a plateau at the interval between 1.5 and 4 GPa, followed by a more rapid increase at higher pressures. Such a pattern is not evident in the ΔR and fwhm(R_1) plots, which show a pronounced increase in the values of both ΔR and fwhm(R_1) as the pressure is increased above 1.5 GPa (Figs. S5 and S6).

Halocarbon Oil 11-14 exhibits a sharp rise in σ_P above 1.2 GPa, suggesting that this is the hydrostatic limit. However, as the pressure increase was continued in the non-hydrostatic regime, the increase of σ_P was considerably more gradual than in other media, reaching 0.45 GPa (5%) at the final pressure point of 9.1 GPa. Such a standard deviation was observed in other fluids at considerably lower pressures, specifically at 5.0 GPa for Fomblin Z60, above 6.7 GPa for Fomblin Z25 and at 5.7 GPa for Fomblin Y LVAC 06/6.

The poorest hydrostatic performance was demonstrated by Fomblin Y LVAC 06/6, where pressure gradients appeared above only 0.6 GPa.

A benchmark experiment with N_2 as the pressure medium revealed a hydrostatic behaviour up to a maximum attained pressure of 10.5 GPa, as shown from the pressure dependences of the σ_P, ΔR and fwhm(R_1) plots (Figs. 2, S4, S5 and S6). In addition, the pressure dependence plots of ΔR and fwhm(R_1) show a slight decrease with P_{avg}. These results are consistent with the previous findings (Klotz *et al.*, 2009).

Pressure measurements were also conducted during the stepwise decompression of the cells, and the results were compared with compression cycles. For Fomblin Z60 and Fomblin Y, the pressure dependences of σ_P during the compression and decompression cycles corresponded very

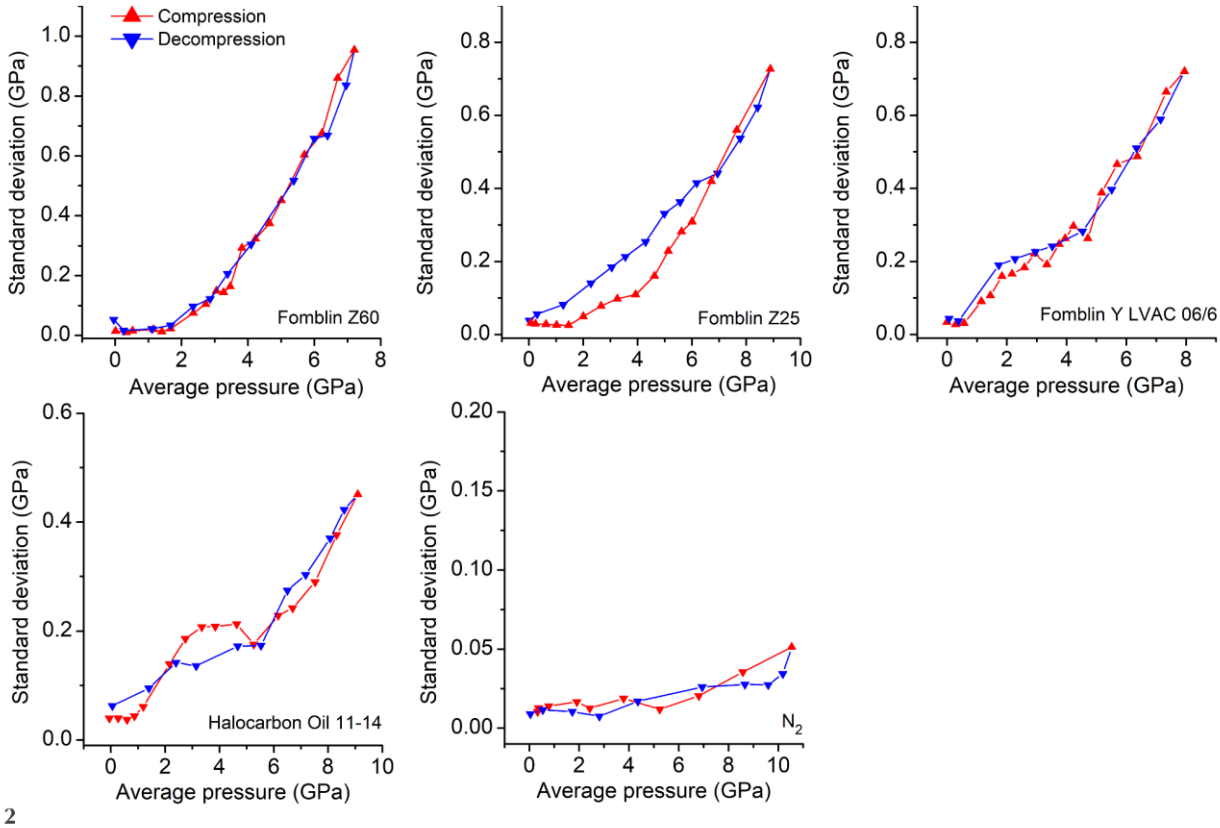


Figure 2
Plots displaying the pressure dependence of the standard deviation of pressure (σ_P) from which the hydrostatic limits of the fluids were deduced. As the pressure is increased, there is a sudden increase in σ_P. This suggests that, at this point, the hydrostatic limit is reached.

closely, but in the case of Fomblin Z25 a clear hysteresis was observed. Similarly, hysteresis was also noted in the majority of the pressure dependences of the ΔR and fwhm(R_1) plots, with the exception of the pressure dependences of ΔR for Fomblin Z60 and Halocarbon Oil 11-14, which show reasonable agreement between the compression and decompression. Moreover, the values of ΔR and fwhm(R_1) obtained after decompression to ambient pressure were higher than the values measured at the start of the compression for all fluids. The increase in the final fwhm(R_1) values in comparison with the initial ones ranged from 0.04 nm in the case of Fomblin Z60 to 0.17 nm in the case of Halocarbon Oil 11-14 (Fig. S5), whereas the ΔR values after decompression increased between 0.01 nm in the case of Fomblin Z60 and 0.04 nm in the case of Fomblin Y LVAC 06/6 when compared with the initial measurements taken at the beginning of the compression cycle (Fig. S6). In the absence of any observable increase in the ΔR and fwhm(R_1) parameter values obtained at ambient pressure after decompression when N_2 was used as a PTM and subjected to an even higher pressure, it can be surmised that these effects may be due to the prolonged exposure of rubies to non-homogenous pressure (Adams *et al.*, 1976).

4. Conclusions

In this study, the hydrostatic behaviour of Fomblin Z60, Fomblin Z25, Fomblin Y LVAC 06/6 and Halocarbon Oil 11-14 under high-pressure conditions was investigated by following the pressure distribution across the sample chamber employing the ruby fluorescence technique, thereby expanding the selection of highly inert fluids for which the hydrostatic behaviour was examined. Among these fluids, the highest hydrostatic limit of 1.7 GPa has been established for Fomblin Z60. An onset of non-hydrostatic behaviour was observed at 1.5 GPa for Fomblin Z25, at 0.6 GPa for Fomblin Y LVAC 06/6 and at 1.2 GPa for Halocarbon Oil 11-14. Although the hydrostatic limits of the media investigated in this study are relatively low, they are nonetheless considered useful for high-pressure experiments with samples whose reactivity precludes the use of more conventional PTMs. This is supported by other recent results from our laboratories, whereby the use of Fomblin Z25 and Halocarbon Oil 11-14 as PTMs provided useful SCXRD data at pressures above 5 GPa and Halocarbon Oil 11-14 was used as the PTM in neutron powder diffraction measurements up to 5 GPa (Clough *et al.*, 2025). Moreover, by mixing two or more of the fluids examined in this study a PTM mixture with an even higher hydrostatic limit might be obtained, as evidenced in the case of other well established PTM mixtures (*e.g.* Fluorinert FC84–FC87, methanol–ethanol, isopentane–*n*-pentane).

Conflict of interest

The authors declare no conflicts of interest.

Data availability

The supporting information includes figures depicting the vibrational spectra of the evaluated fluids and descriptions of their acquisitions, the procedure used for the calculation of the parameter values at each measurement cycle, and plots showing the pressure dependences of the σ_P, ΔR and fwhm(R_1) values for the PTMs studied. A full cohort of raw experimental data and processed, fitted spectra is available upon request.

Funding information

The following funding is acknowledged: European Research Council Starting Grant under the European Union's Horizon 2020 research and innovation programme (grant No. 950625); Engineering and Physical Sciences Research Council (grant No. EP/R042845/1); Royal Society of Chemistry Researcher Mobility Grant (grant No. RM1802-9455); Jožef Stefan Institute Director's Fund; Slovenian Research and Innovation Agency research equipment co-financing (grant No. P20-050).

References

Adams, D. M., Appleby, R. & Sharma, S. K. (1976). *J. Phys. E Sci. Instrum.* **9**, 1140–1144.
Boehler, R. & De Hantsetters, K. (2004). *High Pressure Res.* **24**, 391–396.
Chervin, J. C., Canny, B. & Mancinelli, M. (2001). *High Pressure Res.* **21**, 305–314.
Clough, L. A., Funnell, N. P., Ridley, C. J., Daisenberger, D., Hriljac, J. A., Lozinšek, M., Angel, R. J. & Parsons, S. (2025). *J. Appl. Cryst.* **58**, 227–232.
Collings, I. E. & Goodwin, A. L. (2019). *J. Appl. Phys.* **126**, 181101.
Duffy, T. S. (2005). *Rep. Prog. Phys.* **68**, 1811–1859.
Gillet, P., Badro, J., Varrel, B. & McMillan, P. F. (1995). *Phys. Rev. B*, **51**, 11262–11269.
Hemley, R. J. (2000). *Annu. Rev. Phys. Chem.* **51**, 763–800.
Johnson, S. G. (2007). *The NLopt nonlinear-optimization package*, https://github.com/stevengj/nlopt.
Katrusiak, A. (2008). *Acta Cryst.* A**64**, 135–148.
Katrusiak, A. (2019). *Acta Cryst.* B**75**, 918–926.
Klotz, S., Chervin, J.-C., Munsch, P. & Le Marchand, G. (2009). *J. Phys. D Appl. Phys.* **42**, 075413.
Koyama-Nakazawa, K., Koeda, M., Hedo, M. & Uwatoko, Y. (2007). *Rev. Sci. Instrum.* **78**, 066109.
Kurnosov, A., Kantor, I., Boffa-Ballaran, T., Lindhardt, S., Dubrovinsky, L., Kuznetsov, A. & Zehnder, B. H. (2008). *Rev. Sci. Instrum.* **79**, 045110.
LeSar, R., Ekberg, S. A., Jones, L. H., Mills, R. L., Schwalbe, L. A. & Schiferl, D. (1979). *Solid State Commun.* **32**, 131–134.
Lozinšek, M., Mercier, H. P. A. & Schrobilgen, G. J. (2021). *Angew. Chem. Int. Ed.* **60**, 8149–8156.
Machon, D., Dmitriev, V. P., Bouvier, P., Timonin, P. N., Shirokov, V. B. & Weber, H.-P. (2003). *Phys. Rev. B*, **68**, 144104.
Mao, H.-K., Chen, X.-J., Ding, Y., Li, B. & Wang, L. (2018). *Rev. Mod. Phys.* **90**, 015007.
McKellar, S. C. & Moggach, S. A. (2015). *Acta Cryst.* B**71**, 587–607.
Merrill, L. & Bassett, W. A. (1974). *Rev. Sci. Instrum.* **45**, 290–294.
Miao, M., Sun, Y., Zurek, E. & Lin, H. (2020). *Nat. Rev. Chem.* **4**, 508–527.
Miletich, R., Allan, D. R. & Kuhs, W. F. (2000). *Rev. Mineral. Geochem.* **41**, 445–519.

Moggach, S. A., Allan, D. R., Parsons, S. & Warren, J. E. (2008). *J. Appl. Cryst.* **41**, 249–251.
Moggach, S. A. & Oswald, I. D. H. (2020). *21st century challenges in chemical crystallography I: History and technical developments*, Structure and bonding, Vol. 185, edited by D. M. P. Mingos & P. R. Raithby. pp. 141–198. Cham: Springer.
Motaln, K., Gurung, K., Brázda, P., Kokalj, A., Radan, K., Dragomir, M., Žemva, B., Palatinus, L. & Lozinšek, M. (2024). *ACS Cent. Sci.* **10**, 1733–1741.
Murata, K., Yokogawa, K., Yoshino, H., Klotz, S., Munsch, P., Irizawa, A., Nishiyama, M., Iizuka, K., Nanba, T., Okada, T., Shiraga, Y. & Aoyama, S. (2008). *Rev. Sci. Instrum.* **79**, 085101.
Osakabe, T. & Kakurai, K. (2008). *Jpn. J. Appl. Phys.* **47**, 6544–6547.
Piermarini, G. J., Block, S. & Barnett, J. D. (1973). *J. Appl. Phys.* **44**, 5377–5382.
Rivers, M., Prakapenka, V. B., Kubo, A., Pullins, C., Holl, C. M. & Jacobsen, S. D. (2008). *High Pressure Res.* **28**, 273–292.
Shen, G., Wang, Y., Dewaele, A., Wu, C., Fratanduono, D. E., Eggert, J., Klotz, S., Dziubek, K. F., Loubeyre, P., Fat'yanov, O. V., Asimow, P. D., Mashimo, T., Wentzcovitch, R. M. M., Bass, J., Bi, Y., He, D., Khishchenko, K. V., Leinenweber, K., Li, B., Mezouar, M., Sakai, T., Tsuchiya, T., Shimizu, K. & Yamazaki, D. (2020). *High Pressure Res.* **40**, 299–314.
Sidorov, V. A. & Sadykov, R. A. (2005). *J. Phys. Condens. Matter*, **17**, S3005–S3008.
Staško, D., Prchal, J., Klicpera, M., Aoki, S. & Murata, K. (2020). *High Pressure Res.* **40**, 525–536.
Syassen, K. (2008). *High Pressure Res.* **28**, 75–126.
Takemura, K. (2021). *High Pressure Res.* **41**, 155–174.
Tidey, J. P., Wong, H. L. S., Schröder, M. & Blake, A. J. (2014). *Coord. Chem. Rev.* **277–278**, 187–207.
Torikachvili, M. S., Kim, S. K., Colombier, E., Bud'ko, S. L. & Canfield, P. C. (2015). *Rev. Sci. Instrum.* **86**, 123904.
Varga, T., Wilkinson, A. P. & Angel, R. J. (2003). *Rev. Sci. Instrum.* **74**, 4564–4566.
Vlček, J. & Lukšan, L. (2006). *J. Comput. Appl. Math.* **186**, 365–390.
Wojdyr, M. (2010). *J. Appl. Cryst.* **43**, 1126–1128.
Zakharov, B. A. & Boldyreva, E. V. (2019). *CrystEngComm*, **21**, 10–22.
Zhang, L., Wang, Y., Lv, J. & Ma, Y. (2017). *Nat. Rev. Mater.* **2**, 17005.

J. Appl. Cryst. (2025). 58, https://doi.org/10.1107/S1600576725000342 Supporting information, sup-1

S1. Experimental details – Materials



Figure S1 Perfluoropolyether fluids Fomblin Z60 (Synquest Laboratories; Item: 2108-2-60; Lot: Q152-148; CAS: 69991-61-3), Fomblin Z25 (Synquest Laboratories; Item: 2108-2-49; Lot: 00013201; CAS: 69991-61-3), Fomblin Y LVAC 06/6 (Aldrich; Item: 317926; Lot: MKCM2271; CAS: 69991-67-9) and the poly(chlorotrifluoroethylene) Halocarbon Oil 11-14 (Halocarbon Products Corp.; Batch: 81178) used in this work.

S2. Experimental details – Vibrational spectroscopy

S2.1. Raman spectroscopy

Ambient condition Raman spectra of the fluids (Figure S2) were recorded using a Bruker Senterra II confocal Raman microscope with a 785-nm emission line operating at a power output of 100 mW. Attempts to record the Raman spectra of fluids placed directly onto glass microscope slides resulted in the acquisition of spectra with a strong, broad signal of glass in the range 1000–2000 cm^{-1} and a maximum at ~1380 cm^{-1}. Therefore, a sheet of aluminium foil, which produces a minimal Raman background signal, was placed on the microscope slide, and the fluid drops were deposited on the foil using a dropper pipette. The spectra were recorded in the 50–3630 cm^{-1} range with a resolution of 4 cm^{-1} by accumulation of two acquisitions with an exposure time of 20 s per acquisition. The background was subtracted from the spectra using the Bruker *Opus* 8.7 software suite, employing three iterations of a concave rubber band correction with 64 baseline points.

S2.2. ATR-Infrared spectroscopy

Infrared spectra (Figure S3) were measured on a Bruker Alpha II FT-IR spectrometer, equipped with a Platinum Diamond-ATR sampling module, which was operated within an N_2 atmosphere glovebox (Vigor SG1500/750E). The spectra were recorded in the range of 400–4000 cm^{-1} with a resolution of 4 cm^{-1} and 24 scans were taken per measurement.

J. Appl. Cryst. (2025). 58, https://doi.org/10.1107/S1600576725000342 Supporting information, sup-2

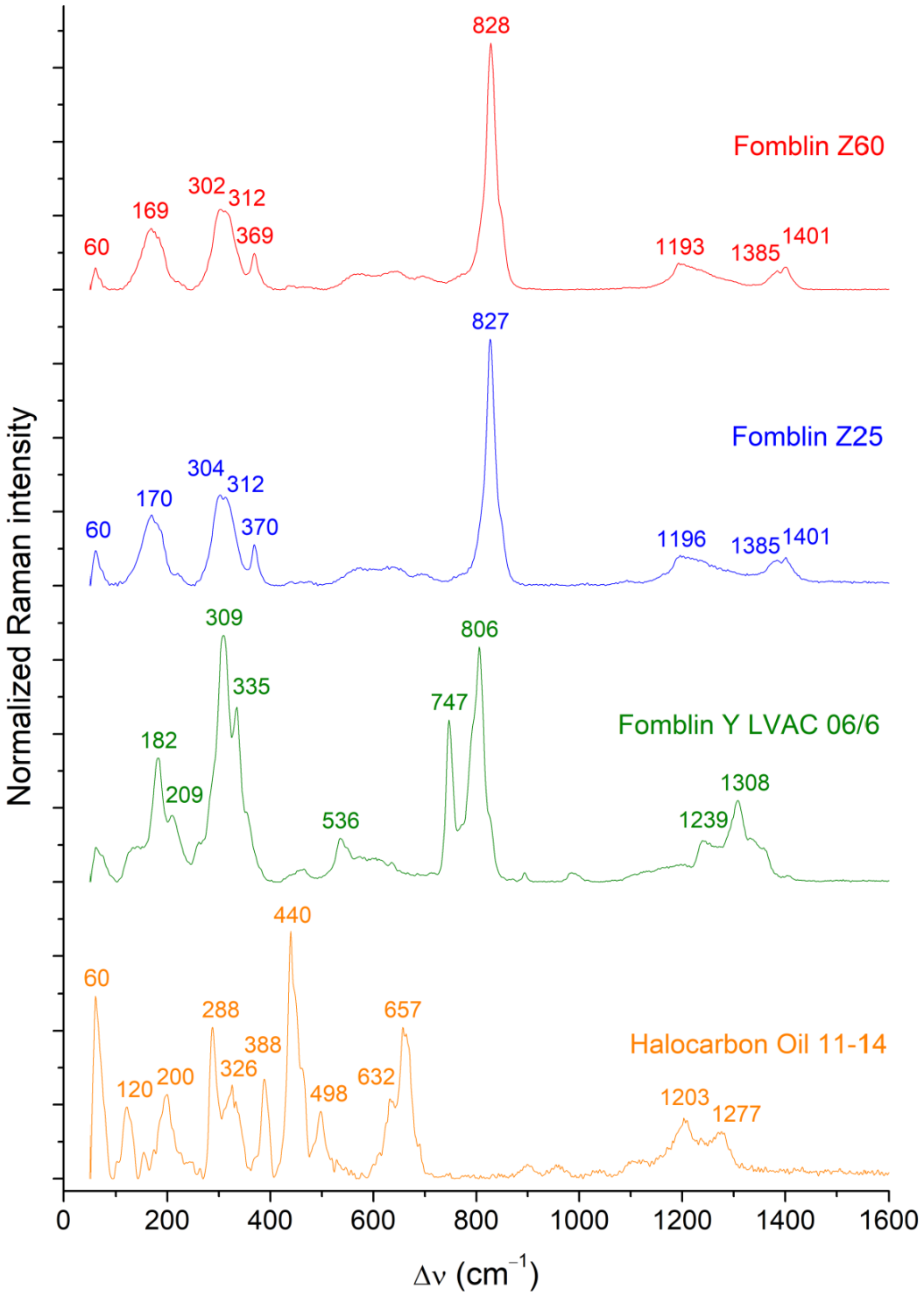


Figure S2 Ambient condition Raman spectra of the inert perhalogenated fluids evaluated in this work (Fomblin Z60, Fomblin Z25, Fomblin Y LVAC 06/6, and Halocarbon Oil 11-14). The spectra show no additional bands in the region 1600–3630 cm^{-1}.

J. Appl. Cryst. (2025). 58, https://doi.org/10.1107/S1600576725000342 Supporting information, sup-3

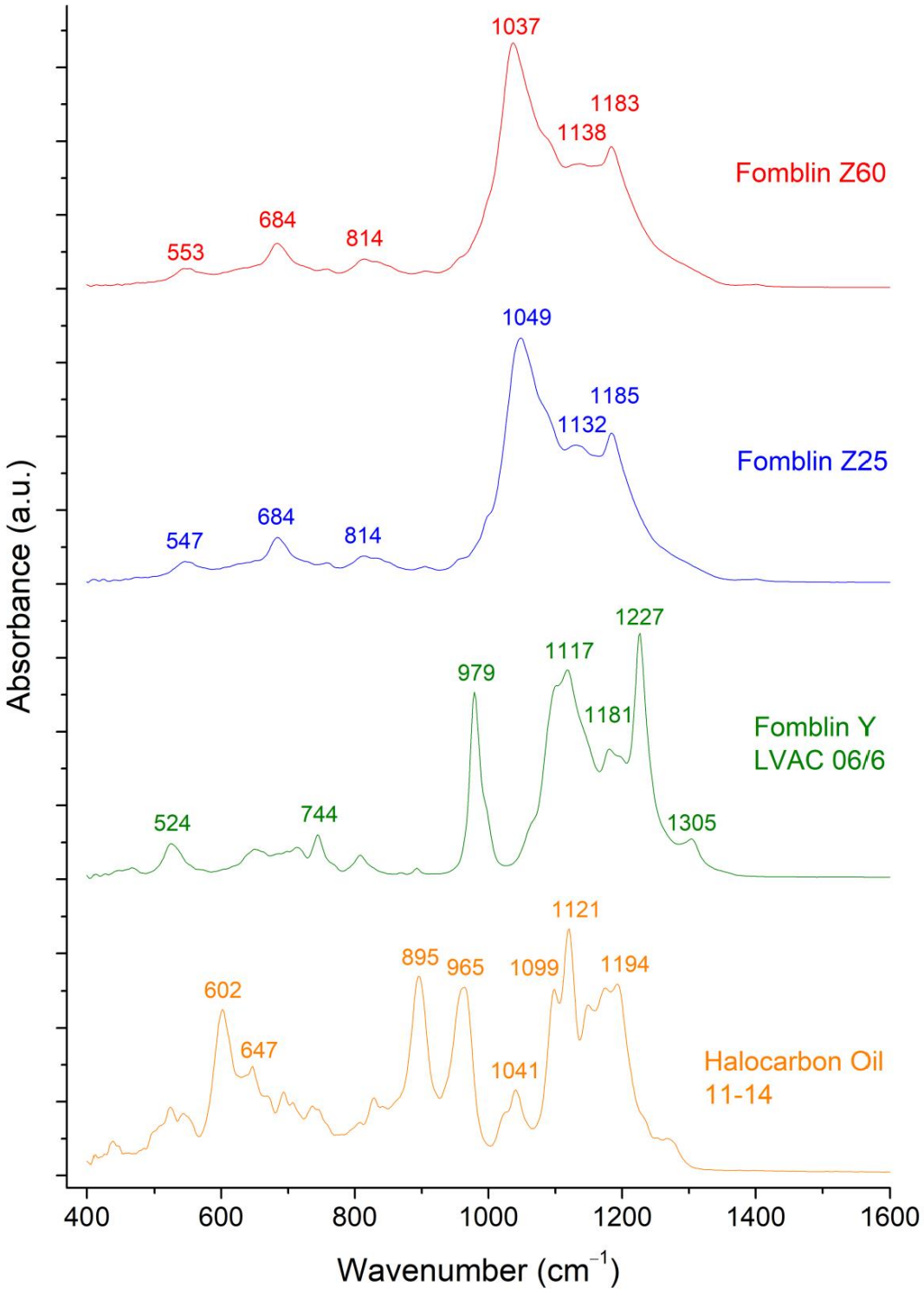


Figure S3 ATR-IR spectra of the inert perhalogenated fluids evaluated in this work (Fomblin Z60, Fomblin Z25, Fomblin Y LVAC 06/6, and Halocarbon Oil 11-14). The spectra show no additional features in the range 1600–4000 cm^{-1}.

J. Appl. Cryst. (2025). 58, https://doi.org/10.1107/S1600576725000342 Supporting information, sup-4

S3. Experimental details – Calculations

The mean pressure within a cell at a specific measurement cycle was calculated as:

$$P_{\mathrm{avg}} = \frac{1}{4n}\sum_{i=1}^{n}\sum_{j=1}^{4} P_{ij}$$

where n is the number of rubies and P_{ij} represents the pressure measured on the i-th ruby at the j-th acquisition, each individually calculated from the position of the respective $(R_1)_{ij}$ using the Ruby2020 pressure gauge equation. Number of rubies varied from 4 to 7 between the different experiments whereas each measurement cycle consisted of four separate spectra acquisitions at each ruby.

Standard deviation of the pressure in a specific measurement cycle was calculated as:

$$\sigma_P = \sqrt{\frac{\sum_{i=1}^{n}(\bar{P}_i - P_{\mathrm{avg}})^2}{n}}$$

where n is the number of rubies and $\bar{P}_i$ represents the mean pressure at the i-th ruby calculated as the average of four acquisitions, for which the pressure was individually calculated from the position of the respective $(R_1)_{ij}$ using the Ruby2020 pressure gauge equation:

$$\bar{P}_i = \frac{1}{4}\sum_{j=1}^{4} P_{ij}$$

Mean full width at half maximum of the R_1 line, fwhm(R_1), and the mean difference between the positions of the R_1 and R_2 lines, $\Delta R = R_1 - R_2$, at a specific measurement cycle were calculated as:

$$\mathrm{fwhm}(R_1) = \frac{1}{4n}\sum_{i=1}^{n}\sum_{j=1}^{4} \mathrm{fwhm}(R_1)_{ij}$$

$$\Delta R = \frac{1}{4n}\sum_{i=1}^{n}\sum_{j=1}^{4} \Delta R_{ij}$$

where n is the number of rubies and $\mathrm{fwhm}(R_1)_{ij}$ and ΔR_{ij} represent the fwhm of the R_1 line and ΔR values in the fluorescence spectrum of the i-th ruby at the j-th acquisition, respectively.

J. Appl. Cryst. (2025). 58, https://doi.org/10.1107/S1600576725000342 Supporting information, sup-5

S4. Results

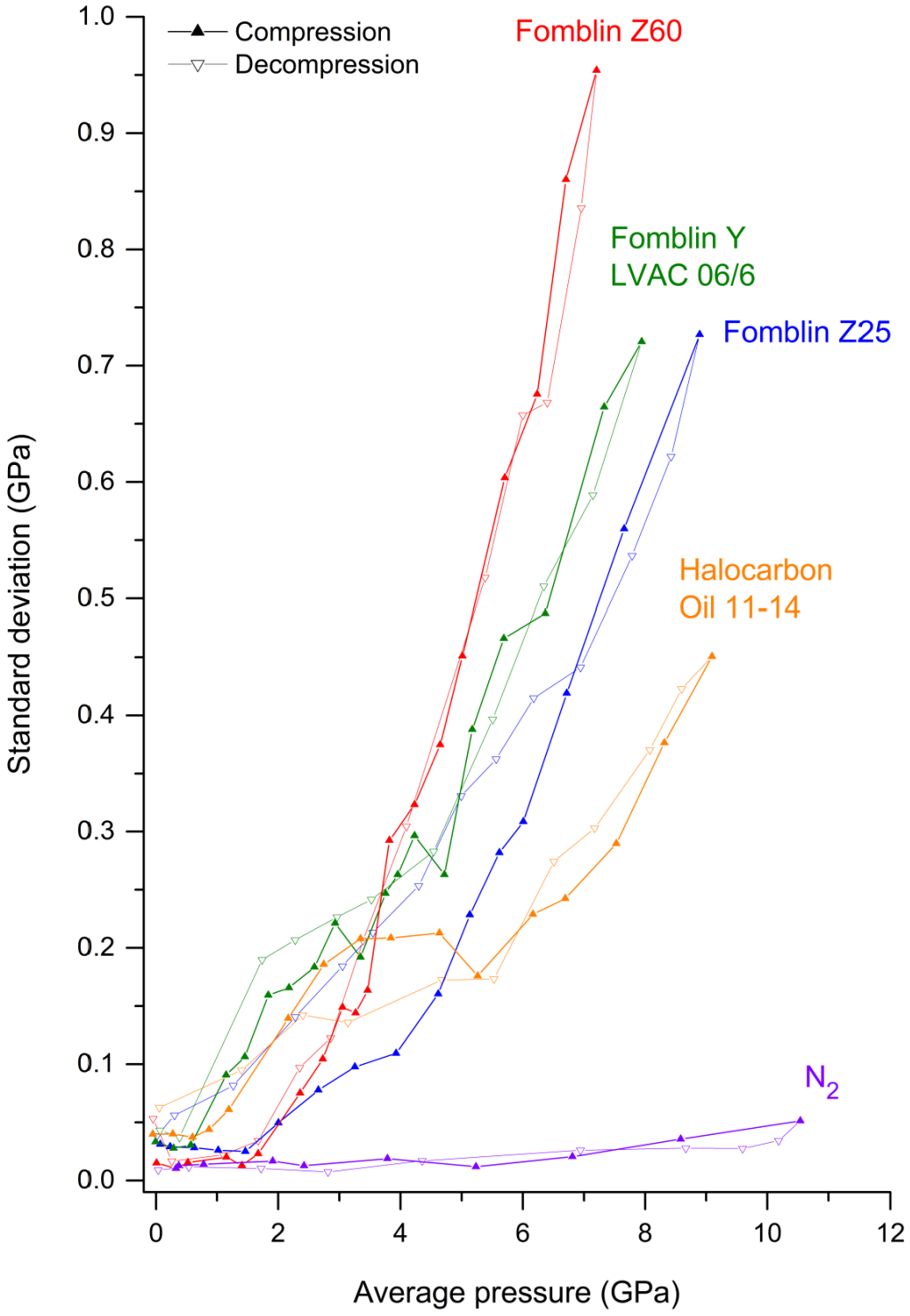


Figure S4 Pressure dependence of the standard deviation of pressure (σ_P) plot for Fomblin Z60, Fomblin Z25, Fomblin Y LVAC 06/6, Halocarbon Oil 11-14, and nitrogen.

J. Appl. Cryst. (2025). 58, https://doi.org/10.1107/S1600576725000342 Supporting information, sup-6

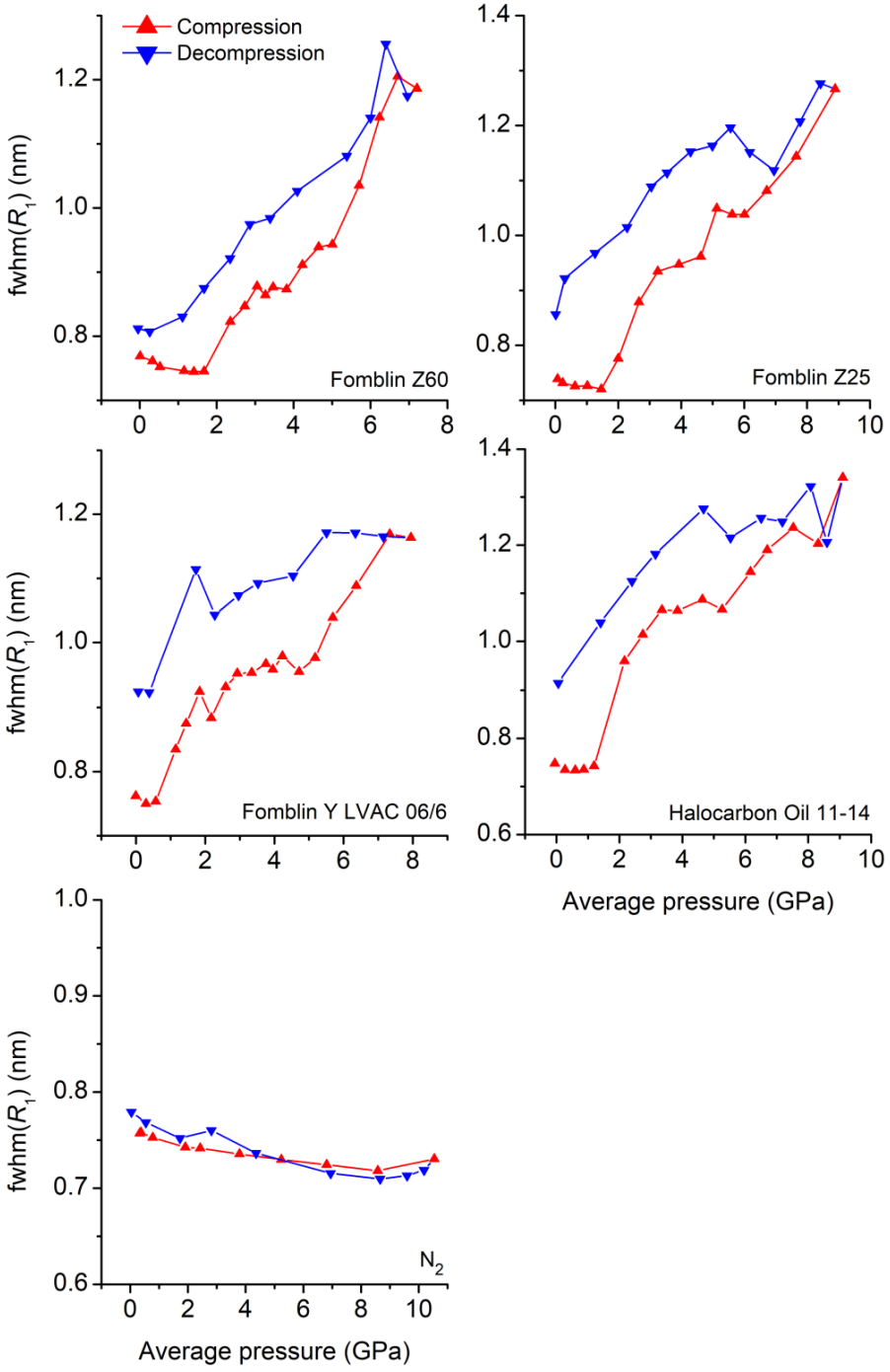


Figure S5 Pressure dependence of fwhm(R_1) plots for Fomblin Z60, Fomblin Z25, Fomblin Y LVAC 06/6, Halocarbon Oil 11-14, and nitrogen.

J. Appl. Cryst. (2025). 58, https://doi.org/10.1107/S1600576725000342 Supporting information, sup-7

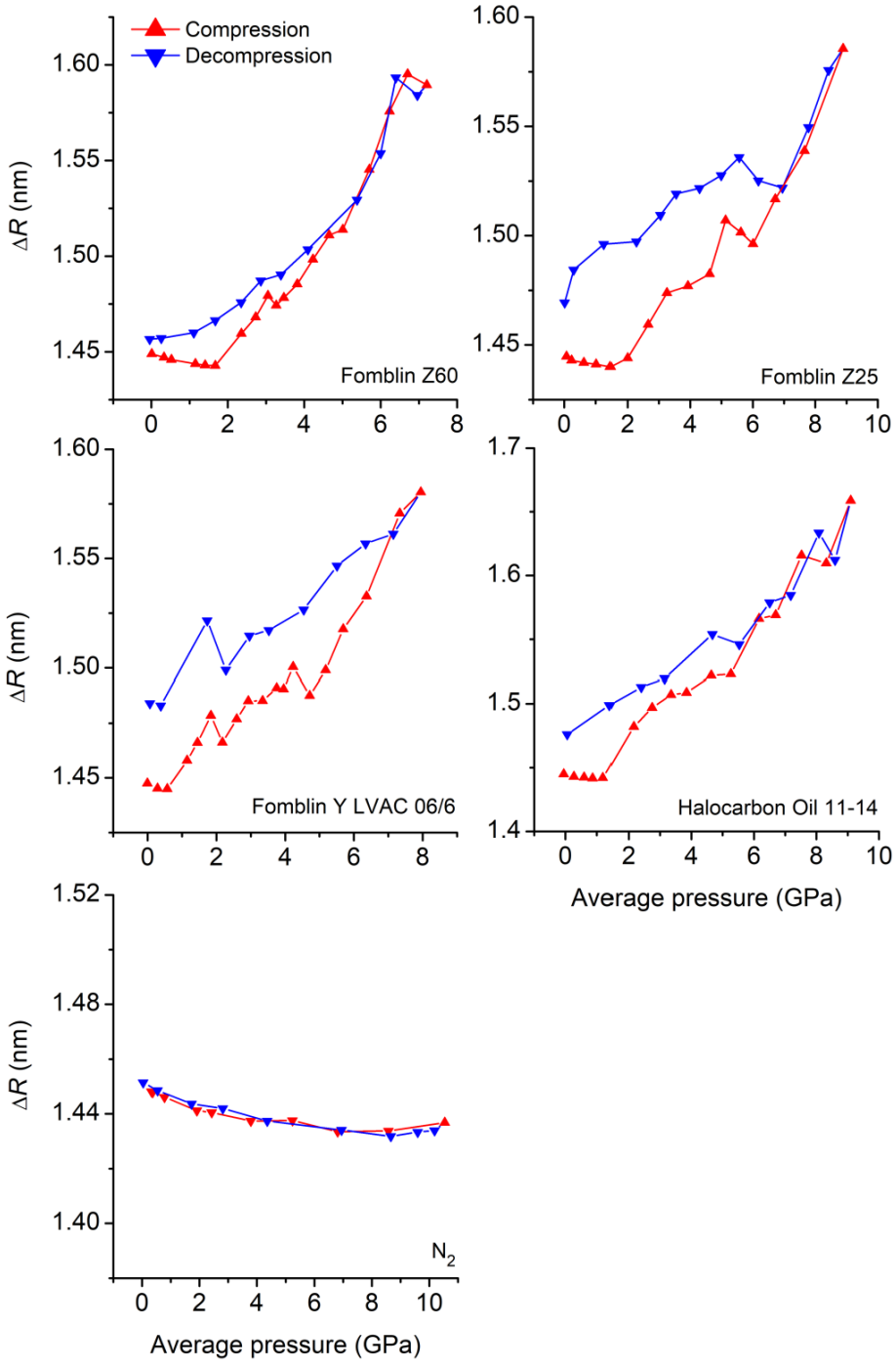


Figure S6 Pressure dependence of ΔR plots for Fomblin Z60, Fomblin Z25, Fomblin Y LVAC 06/6, Halocarbon Oil 11-14, and nitrogen.

4.6 High-Pressure Behavior of Noble-Gas Fluorides

Currently, XeF_2 is the only xenon fluoride that has been investigated under high pressure. It was originally found that XeF_2 undergoes monotonic compression up to 50 GPa (Schwarz & Syassen, 1992). In the following study, it has been reported that XeF_2 metallizes at 80 GPa (Kim, Debessai, & Yoo, 2010), but this has not been substantiated. Instead, calculations predicted ionization to XeF^+ and F^- (Kurzydłowski, Zaleski-Ejgierd, Grochala, & Hoffmann, 2011). Subsequent experimental reinvestigation demonstrated the presence of two new polymorphs (Wu, et al., 2017), and showed that, at 80 GPa and upon laser heating, XeF_2 undergoes disproportionation to form a high-pressure phase of XeF_4 together with $XeF_2{\cdot}2Xe$, as evidenced by PXRD and Raman spectroscopy (Liu, et al., 2024).

These findings motivate further investigation of other xenon fluorides to elucidate their behavior under high pressure. XeF_6 appears to be a particularly compelling candidate, as it represents the highest oxidation state of xenon in an exclusively fluorine environment and exhibits rich structural chemistry, as evidenced by the presence of several polymorphs at ambient pressure (Burbank & Jones, 1970; Burbank & Jones, 1974; Hoyer, Emmler, & Seppelt, 2006). Finally, its relatively high vapor pressure (*ca.* 30 Torr at 25 °C) (Malm, Sheft, & Chernick, 1963) and high reactivity mean that, if a successful loading procedure is implemented, the same methodology could be applied to the loading of other volatile and highly oxidizing compounds in a DAC.

4.6.1 High-pressure behavior of XeF_6

XeF_6 was loaded in a Merrill–Bassett cell in a nitrogen-filled glovebox. Due to its volatility, XeF_6 was loaded by cooling the sample, stored in an FEP vessel equipped with polychlorotrifluoroethylene (PCTFE) valve, to approximately −40 °C and rapidly transferring it into the pre-cooled cell (*ca.* −20 °C), which was then quickly closed. Three ruby spheres were placed inside the cell prior to loading to enable pressure determination. According to the Raman spectra, no evidence for the formation of $XeOF_4$ or other Xe−O compounds was observed, as indicated by the absence of Xe=O vibrations near 900 cm^{-1}.

Interestingly, at the lowest pressure investigated (0.20 GPa, Figure 4.12), XeF_6 has similar spectrum to that of liquid XeF_6 (Gasner & Claassen, 1967; Adams & Bartlett, 1978). Crystallization is observed only above 0.4 GPa, as evidenced by the formation of small crystalline grains in the cell (Figure 4.12). Raman spectra collected up to 1.68 GPa indicate the presence of $[XeF_5]^+$ cations, as evidenced by bands in the 500–700 cm^{-1} region, which are similar to those observed in liquid XeF_6 (Gasner & Claassen, 1967; Adams & Bartlett, 1978) and in $[XeF_5]^+$ and $[Xe_2F_{11}]^+$ salts (Adams & Bartlett, 1978; Milićev, 1995).

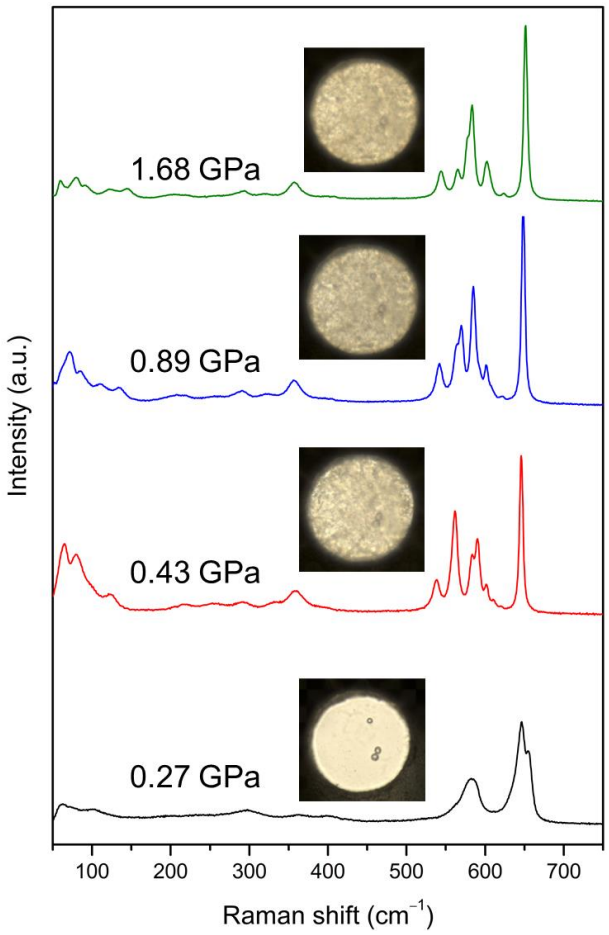


Figure 4.12: Raman spectra of XeF_6 collected up to 1.68 GPa. Insets show the photographs of the sample chamber at the indicated pressure points.

Upon increasing the pressure to 1.68 GPa, tiny crystalline grains remained. Although the sample was polycrystalline, the elucidation of two high-pressure polymorphs of XeF_6 (Table 4.3) using synchrotron multigrain micro-single-crystal X-ray diffraction was possible. These polymorphs crystallize in the $P\bar{1}$ and $P2_1/m$ space groups and exhibit one-dimensional (1D) polymeric structure consisting of $[XeF_5]^+F^-$ units (Figure 4.13). Heating the sample for one hour at 100 °C led to partial recrystallization (Figure 4.14), with only a slight pressure increase to 1.9 GPa. The two previously identified polymorphs were still present, alongside a new polymorph crystallizing in the $P2_1/c$ space group (Table 4.3), which also consists of chains composed of $[XeF_5]^+F^-$ units (Figure 4.13).

These polymorphs represent the first examples of a noble-gas fluoride having extended, polymeric structure in the solid state and constitute examples of one-dimensional fluorides (Leblanc, Maisonneuve, & Tressaud, 2014). They are among few one-dimensional fluorides observed in the p-block of the periodic table, such as BiF_5 (Hebecker, 1971; Wassermann & Kraus, 2024), in which the chain is linear, and GeF_2 (Usvyat, et al., 2012) where *zig-zag* chains, due to electron pair on germanium atom, are present.

The difference between these polymorphs appears to lie primarily in the $F_5Xe\cdots F\cdots XeF_5$ angles, which range from 167(16)° in the $P2_1/m$, 172.6(4)° in $P2_1/c$, to 180(4)° in the $P\bar{1}$ polymorph. Due to the possible twinning in the $P\bar{1}$ and $P2_1/m$ polymorphs, the data quality was relatively poor, and therefore the observed angles fall essentially within the $\pm 3\sigma$ range. After accounting for twinning in the $P2_1/c$ polymorph, the Xe—F bond lengths of the $[XeF_5]^+$ cation (1.832(5)–1.899(10) Å) could be estimated more accurately. These

bond lengths are within $\pm 3\sigma$ of those observed in $[XeF_5]^+$ cations at ambient conditions, whereas the Xe···F bridging bonds (2.240(6), 2.283(7) Å) are similar to those found in $[Xe_2F_{11}]^+$ cations (Leary, Zalkin, & Bartlett, 1973; Mazej & Goreshnik, 2019; Goettel, Bortolus, Stuart, Mercier, & Schrobilgen, 2019; Bortolus, Mercier, & Schrobilgen, 2020; Bortolus, Mercier, & Schrobilgen, 2024). The Xe···F bond lengths are shorter than in XeF_6·HF (2.372(3), 2.403(3) Å), XeF_6·1.5HF (2.387(5), 2.413(5) Å) (Hoyer, Emmler, & Seppelt, 2006), and in the XeF_6·$XeOF_4$·HF cocrystal (2.3974(8), 2.4459(8) Å) (Goettel, 2017).

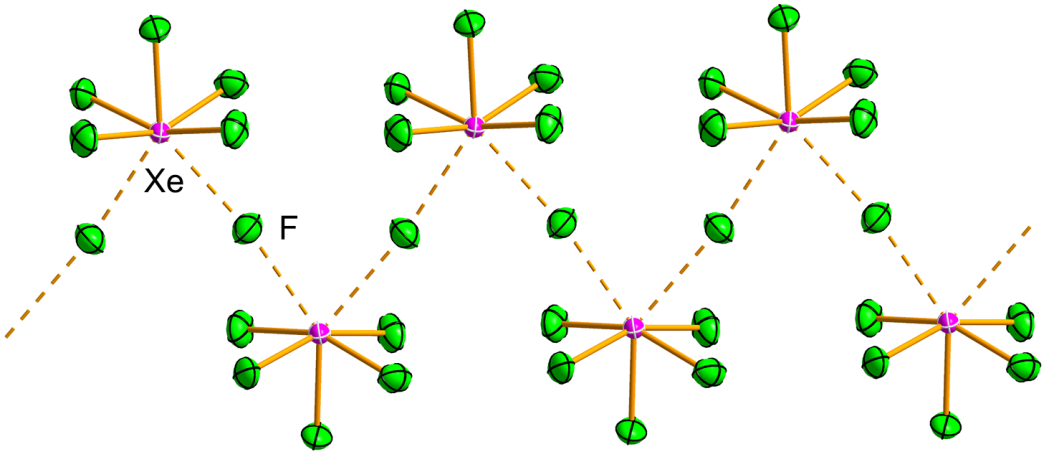


Figure 4.13: One-dimensional polymer in the $P2_1/c$ polymorph of XeF_6 at 1.9 GPa. Essentially the same 1D polymer is observed in the $P\bar{1}$ and $P2_1/m$ polymorphs.

Table 4.4: Summary of crystal data and structure refinements for different polymorphs of XeF_6 obtained at 1.68 GPa ($P\bar{1}$ and $P2_1/m$) and 1.90 GPa ($P2_1/c$). The radiation wavelength for all measurements was 0.2898 Å.

Compound	**XeF_6**	**XeF_6**	**XeF_6**§
Chemical formula	XeF_6	XeF_6	XeF_6
M_r	245.30	240.30	490.60
Crystal system	Triclinic	Monoclinic	Monoclinic
Space group	$P\bar{1}$	$P2_1/m$	$P2_1/c$
T / K	293(2)	293(2)	293(2)
a / Å	4.843(4)	5.3304(7)	8.189(4)
b / Å	5.3426(12)	8.357(5)	5.355(3)
c / Å	7.610(2)	8.2733(13)	9.315(3)
α / °	80.16(2)	90	90
β / °	79.40(4)	90.873(13)	115.92(5)
γ / °	73.61(4)	90	90
V / Å^3	184.21(16)	368.5(2)	367.4(3)
Z	2	4	2
$R[F^2 > 2\sigma(F^2)]$, $wR(F^2)$, S	0.088, 0.22	0.081, 0.263	0.067, 0.182
No. of reflections	237	413	1234
No. of parameters	31	62	65
$\Delta\rho_{max}$, $\Delta\rho_{min}$ / e Å^{-3}	2.16, −1.23	3.13, −1.77	4.308, −2.899

§ Refined as two-component twin; scales: 0.297(4), 0.703(4); structure solution and subsequent refinement of the twin was performed by Prof. Maxim Bykov.

The packing in these polymorphs is also quite similar, as all structures contain fluoride-bridged zig-zag chains of $[XeF_5]^+$ cations and F^- anions (Figure 4.14) that interact through long Xe···F contacts (3.255(14) Å and 3.299(10) Å in the $P2_1/c$ polymorph), which are only slightly shorter than the sum of the van der Waals radii of xenon (2.06 Å) and fluorine (1.46 Å) (Alvarez, 2013).

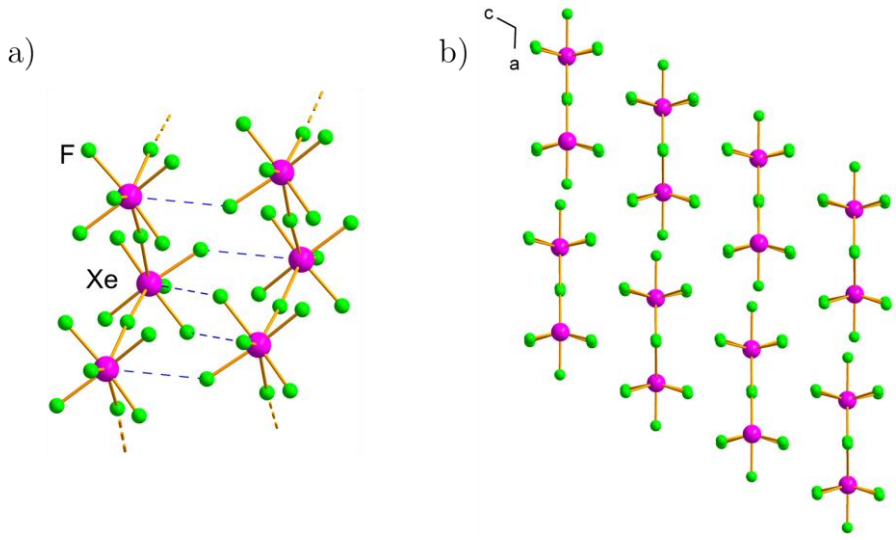


Figure 4.14: a) Interchain Xe···F contacts (blue dashed lines) and b) packing in the $P2_1/c$ polymorph. In a), orange dashed lines indicate the continuation of the 1D polymer.

As all of these polymorphs contain $[XeF_5]^+$ units and are structurally very similar, the Raman spectrum in the 500–700 cm^{-1} region does not differ significantly from polymorph to polymorph, nor does it differ appreciably from the Raman spectrum of liquid (Gasner & Claassen, 1967; Adams & Bartlett, 1978) and solid XeF_6 (Gasner & Claassen, 1967), where $[XeF_5]^+$ units are also tetramers or hexamers bridged by fluoride anions (Burbank & Jones, 1970; Burbank & Jones, 1974; Hoyer, Emmler, & Seppelt, 2006). The Raman spectrum of the recrystallized portion of the sample is likewise very similar to that of the portion that remained unchanged.

Further increase of the pressure to approximately 8 GPa resulted in a slight blue-shift of the Raman bands, although their overall features remained largely unchanged (Figure 4.15). X-ray diffraction data became progressively weaker, and although laser-heating induced some recrystallization of the sample, it also caused some decomposition, as indicated by Raman peaks attributable to XeF_2 (Liu, et al., 2024) (Figure 4.16). Unfortunately, the data quality was insufficient to elucidate the crystal structure of either XeF_2 or any other polymorph of XeF_6 at these pressures.

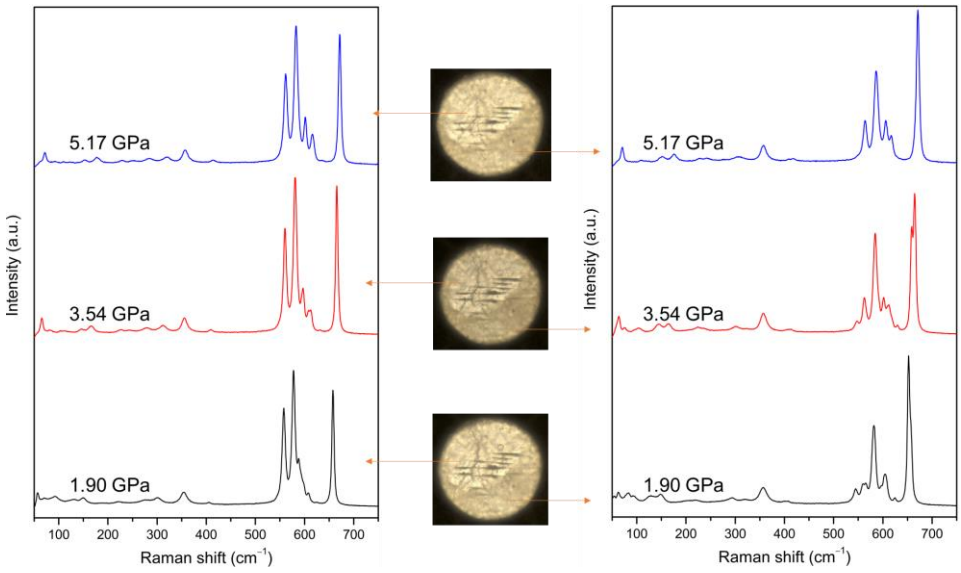


Figure 4.15: Raman spectra of XeF_6 collected up to 5.17 GPa. Insets show the sample chamber. Black streaks observed in the sample are attributed to synchrotron radiation damage.

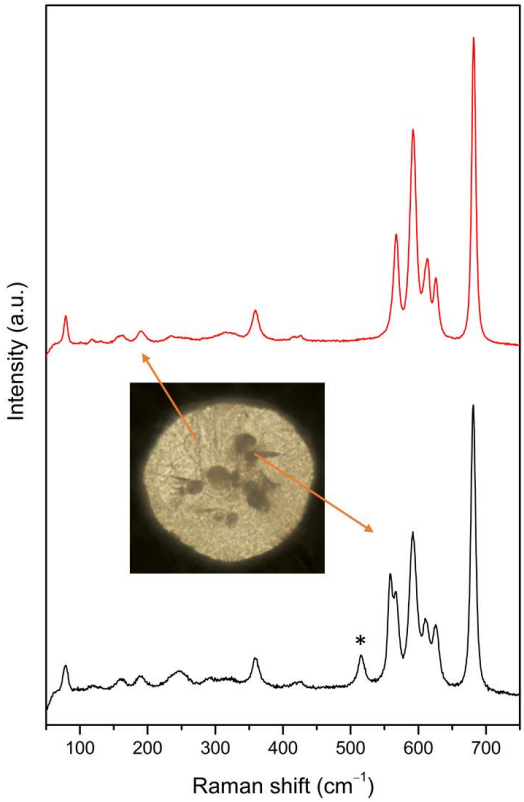


Figure 4.16: Raman spectra of the sample at 7.8 GPa. Inset shows the sample chamber. Arrows indicate the areas from which the Raman spectra were collected. The asterisk (*) denotes the XeF_2 peak, which is in good agreement with the values reported in literature (Liu, et al., 2024).

4.6.2 High-pressure behavior of $XeF_2{\cdot}XeF_4$

To investigate the behavior of the $XeF_2{\cdot}XeF_4$ cocrystal under high pressure, it was compressed in an SSDAC-80 cell up to 30 GPa. The cell was prepared and loaded with the sample at Cardinal Stefan Wyszyński University in Warsaw in the group of Prof. Dominik Kurzydłowski, whereas the Raman spectra were measured at Jožef Stefan Institute.

Comparison of the Raman spectrum from ambient pressure to 7.12 GPa suggests that structural changes may have occurred upon compression (Figure 4.17). This is particularly evident in the 100–200 cm^{-1} region and may indicate the presence of polymorphic transition. The Xe—F vibrations observed in the region 500—600 cm^{-1} show a shift upon compression, but the overall spectral features remain largely unchanged. These observations indicate that, at such relatively low pressures, both XeF_2 and XeF_4 in the cocrystal retain their molecular character.

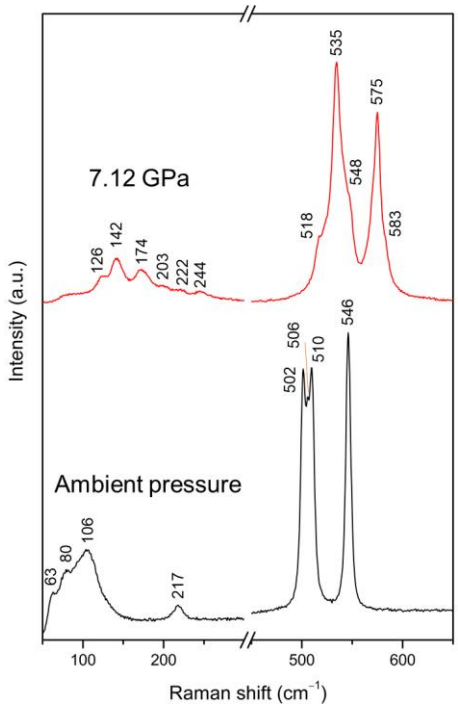


Figure 4.17: Comparison of Raman spectra of the $XeF_2 \cdot XeF_4$ cocrystal at ambient pressure and at 7.12 GPa.

Further compression up to 32 GPa resulted in broadening and weakening of the peak intensities (Figure 4.18 a), with all bands typically attributed to Xe−F stretches merging into a broad peak. Upon decompression (Figure 4.18 b), the intensity and shape of the peaks were partially restored, indicating that the structural changes are at least partially reversible.

In a separate experiment, the cocrystal was compressed up to the similar pressure and was laser heated in order to induce recrystallization. However, only XeF_2, XeF_4 and XeF_6 could be identified, indicating that the cocrystal decomposes under high-temperature high-pressure conditions. This work was carried out by the group of Prof. Maxim Bykov and Prof. Elena Bykova from Goethe University Frankfurt.

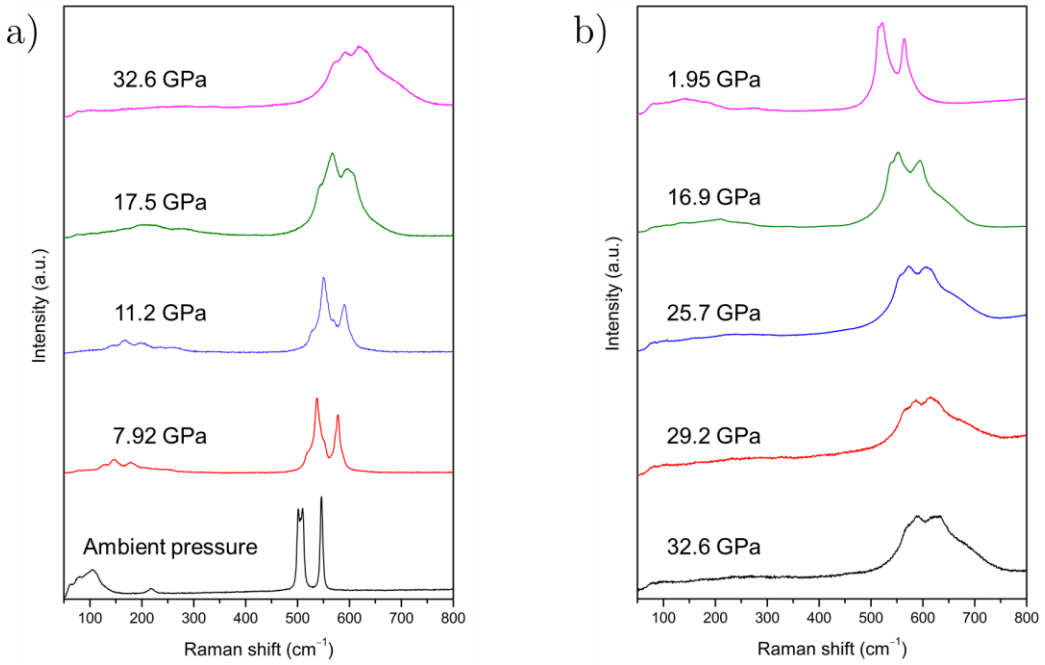


Figure 4.18: a) Raman spectra of the $XeF_2 \cdot XeF_4$ cocrystal during compression up to 32 GPa; b) Raman spectra of the $XeF_2 \cdot XeF_4$ cocrystal during decompression down to 1.95 GPa.

Chapter 5

Conclusions

Several conclusions can be drawn from the research presented herein, and they are presented in accordance with the structure of the thesis chapters.

Mechanochemistry has been demonstrated to be a viable method for synthesizing noble-gas compounds, offering both efficiency and simplicity. The mechanochemically obtained products in the XeF_2–TaF_5 system, $[XeF][Ta_2F_{11}]$, $[XeF][TaF_6]$ and $[Xe_2F_3][TaF_6]$, exhibit purity comparable to that produced by solid-state or solution-based methods. Reaction time and the initial molar ratio of reactants were shown to be important parameters in these systems. The crystal structures of these products were also elucidated, and the results agree well with those of other compounds typically obtained in XeF_2–MF_5 systems. Mechanochemistry also enabled the straightforward synthesis of the dixenon cation, $[Xe_2]^+$, as well as pure $[Xe_2F_3][SbF_6]$. The compound containing dixenon cation is amorphous, precluding its analysis by X-ray diffraction, which precluded the elucidation of its structure, particularly with respect to the anion present.

Chemistry of xenon in oxidation state +4 has also been explored mechanochemically. The $XeF_2{\cdot}XeF_4$ cocrystal can be obtained as a phase-pure material in only 20 minutes, and the resulting powder has been shown to be suitable for analysis by 3D ED. To explore the potential of mechanochemical approach for the synthesis of new compounds featuring xenon in oxidation state +4, the previously unknown $[XeF_3][Ta_2F_{11}]$ was also synthesized and crystallographically characterized.

With those results, introduction of mechanochemistry to the noble-gas chemistry can not only lead to isolation of novel noble-gas compounds, but can also potentially lead to investigation of the correlation of mechanochemical and high-pressure effects on the noble-gas compounds. These can therefore give a valuable insight into solid-state chemistry of these compounds, which has until now received scarce attention.

Low-temperature reactions of $[XeF][AsF_6]$ with NCCN in aHF afforded $[NCCNXeF][AsF_6]$ and $[FXeNCCNXeF][AsF_6]_2$, the latter representing the first example in which nitrogen base acts as a ligand to two $[XeF]^+$ cations. Both $[NCCNXeF]^+$ and $[FXeNCCNXeF]^{2+}$ cations contain the most strongly ionized $[XeF]^+$ fragment within the known series of $[RNXeF]^+$ adduct-cations. To assess the influence of a Lewis acid on the geometry of NCCN, the astrochemically important $NCCNH^+$ cation was also crystallographically characterized as its $[AsF_6]^-$ salt.

At room temperature, $[FXeNCCNXeF][AsF_6]_2$ undergoes fluoride-rearrangement to yield $[XeNC(F)C(F)NXe][AsF_6]_2$, the first compound exhibiting a C=N−Xe bonding modality. This compound is stable at room temperature and features a σ-hole on the xenon atoms, which was exploited in the synthesis of the adduct-cations $[RCN{\cdots}XeNC(F)C(F)NXe{\cdots}NCR][AsF_6]_2$ (R = H, CH_3), which are rare examples of an N−Xe−N linkage. The isolation of these compounds, alongside the room-temperature stability of $[XeNC(F)C(F)NXe][AsF_6]_2$, demonstrates its potential use of as a potent noble-gas Lewis acid.

Reaction of perfluorinated amides with [XeF][AsF_6] yielded hydrogen-bonded salt cocrystals, ($RC(OH)NH_2$)[AsF_6]·XeF_2 (R = CF_3, C_2F_5, C_3F_7) featuring the first crystallographically characterized NH···FXeF hydrogen bonds, which are preferentially formed. Only in ($CF_3C(OH)NH_2$)[AsF_6]·XeF_2 does XeF_2 also participate in a hydrogen bond with the $=OH^+$ moiety. The crystal structures of protonated perfluorinated amides, ($RC(OH)NH_2$)[AsF_6] (R = CF_3, C_2F_5, C_3F_7), were also elucidated, showing that protonation occurs at the oxygen atom in all cases. The crystal structures of hemiprotonated amide salts, (CF_3CONH_2)$_2$H[AsF_6] and ($C_3F_7CONH_2$)$_2$H[AsF_6], exhibit short but asymmetric O–H···O hydrogen bonds. Additionally, the crystal structure of salt cocrystal H_3O[AsF_6]·$2CF_3CONH_2$ was also determined. These compounds demonstrate the further use of XeF_2 as a hydrogen-bond acceptor in crystal engineering, and encourage the use of other noble-gas compounds in the similar manner.

The crystal structure of protonated decafluorobenzophenone as a hexafluoridoarsenate(V) salt, (C_6F_5)$_2$$COH^+$[$AsF_6$]$^-$, represents a rare example of a protonated benzophenone moiety that does not form a hydrogen-bonded dimer, i.e., a hemiprotonated salt. The compound was shown to be stable at room temperature. Decafluorobenzophenone was reacted with arsenic pentafluoride in SO_2, which provided a rare example of a crystallographically characterized ketone acting as a ligand toward AsF_5. In both compounds, the C=O and *anti*-C–C(O) bonds are significantly shorter than in (C_6F_5)$_2$CO. Conversely, *syn*-C–C(O) is shorter in (C_6F_5)$_2$$COH^+$[$AsF_6$]$^-$ than in (C_6F_5)$_2$CO·AsF_5, in which it is essentially the same as in (C_6F_5)$_2$CO.

The hydrostatic properties of oxidatively resistant fluorinated liquids under high pressure have been investigated. Fomblin Y LVAC 06/6 was hydrostatic only below 0.6 GPa, whereas Fomblin Z25 and Fomblin Z60 perfluoropolyethers were hydrostatic up to 1.5 and 1.7 GPa, respectively. Halocarbon Oil 11-14 was truly hydrostatic up to 1.2 GPa. Slight pressure gradients observed above these hydrostatic limits indicate that these media might still be usable as hydrostatic media at pressures exceeding 5 GPa. Moreover, all of these media were found to be unreactive toward XeF_2, suggesting that they can be safely used for high-pressure studies of noble-gas compounds.

XeF_6 has been shown to form new polymorphs up to 10 GPa. They represent the first examples of a polymeric noble-gas fluorides and feature $[XeF_5]^+$ cations connected into chains via bridging fluoride anions. These findings significantly expand the structural chemistry of noble-gas fluorides under high pressure.

Compression of the XeF_2·XeF_4 cocrystal indicates structural changes at low pressure based on Raman spectrum. Upon further compression to 30 GPa, only broadening and weakening of the bands in the Raman spectrum is observed. Upon decompression of the sample, the bands are only partially restored. Upon laser heating, the cocrystal decomposes to XeF_2, XeF_4, and XeF_6.

References

Adam, S., Ellern, A., & Seppelt, K. (1996). Structural Principles of the Coordination Number Eight: WF_8^{2-}, ReF_8^{2-}, and XeF_8^{2-}. *Chemistry - A European Journal, 2*(4), 398-402.

Adams, C. J. (1974). The Raman spectra of solid xenon tetrafluoride and its adduct with xenon difluoride. *Journal of Raman Spectroscopy, 2*(4), 391-397.

Adams, C. J., & Bartlett, N. (1978). Tautomerism in Xenon Hexafluoride: An Investigation of Xenon Hexafluoride and its Complexes by Raman Spectroscopy. *Israel Journal of Chemistry, 17*(1-2), 114-125.

Adeleke, A. A., Kunz, M., Greenberg, E., Prakapenka, V. B., Yao, Y., & Stavrou, E. (2019). A high-pressure compound of argon and nickel: noble gas in the Earth's core. *ACS Earth and Space Chemistry, 3*(11), 2517-2524.

Akahama, Y., & Kawamura, H. (2010). Pressure calibration of diamond anvil Raman gauge to 410 GPa. *Journal of Physics: Conference Series, 215*, 012195.

Alvarez, S. (2013). A cartography of the van der Waals territories. *Dalton Transactions, 42*(24), 8617-8636.

Anzellini, S., & Boccato, S. (2020). A Practical Review of the Laser-Heated Diamond Anvil Cell for University Laboratories and Synchrotron Applications. *Crystals, 10*(6), 459.

Aslandukov, A., Aslandukov, M., Dubrovinskaia, N., & Dubrovinsky, L. (2022). Domain Auto Finder (DAFi) program: the analysis of single-crystal X-ray diffraction data from polycrystalline samples. *Journal of Applied Crystallography, 55*(5), 1383-1391.

Axhausen, J., Ritter, C., & Kornath, A. (2013). The Protonation of Acetamide and Thioacetamide in Superacidic Solutions: Crystal Structures of $[H_3CC(OH)NH_2]^+AsF_6^-$ and $[H_3CC(SH)NH_2]^+AsF_6^-$. *Zeitschrift für anorganische und allgemeine Chemie*, 65-72.

Baláž, P., Achimovičova, M., Baláž, M., Billik, P., Cherkezoca-Zheleva, Z., Criado, J. M., . . . Wieczorek-Ciurowa, K. (2013). Hallmarks of mechanochemistry: from nanoparticles to technolog. *Chemical Society Reviews, 42*(18), 7571-7637.

Ball, P. (2005). *Elegant Solutions: Ten Beautiful Experiments in Chemistry.* Great Britain: Royal Society of Chemistry.

Bartell, L. S., & Powell, B. M. (1992). Crystal structures of the low temperature phases of TeF6. *Molecular Physics, 75*(3), 689-698.

Bartlett, N. (1962). Xenon Hexafluoroplatinate(v) $Xe^+[PtF_6]^-$. *Proceedings of the Chemical Society* , 218.

Bartlett, N., & Rao, P. R. (1963). Xenon hydroxide: an experimental hazard. *Science, 139*(3554), 506.

Bartlett, N., & Wechsberg, M. (1971). The Xenon Difluoride Complexes $XeF_2 \cdot XeOF_4$; $XeF_2 \cdot XeF_6 \cdot AsF_5$ and $XeF_2 \cdot 2\ XeF_6 \cdot 2\ AsF_5$ and Their Relevance to Bond Polarity and Fluoride Ion Donor Ability of XeF_2 and XeF_6. *Zeitschrift für anorganische und allgemeine Chemie, 385*(1-2), 5-17.

Bartlett, N., Žemva, B., & Graham, L. (1976). Redox reactions in the XeF_2/platinum fluoride and XeF_2/palladium fluoride systems and the conversion of XeF_2 to XeF_4 and Xe. *Journal of Fluorine Chemistry, 7*(1-3), 301-320.

Beattie, I. R., Livingston, K. M., Ozin, G. A., & Reynolds, D. J. (1969). Single-crystal Raman Spectrum of Bismuth Pentafluoride and of Antimony Tetrachloride Fluoride and the Vibrational Spectrum of Vanadium, Niobium, Tantalum, and Antimony Pentafluorides. *Journal of the Chemical Society A: Inorganic, Physical, Theoretical*, 958-956.

Beck, J., & Zink, M. (2009). Donor-Acceptor Complexes of Tellurium Polycationic Clusters with Cyanogen. *Zeitschrift für anorganische und allgemeine Chemie*, 692-699.

Belak Vivod, M., Jagličić, Z., King, G., Hansen, T., Lozinšek, M., & Dragomir, M. (2024). Mechanochemical Synthesis and Magnetic Properties of the Mixed-Valent Binary Silver(I,II) Fluorides, $Ag^{I}_2Ag^{II}F_4$ and $Ag^{I}Ag^{II}F_3$. *Journal of American Chemical Society, 146*(44), 30510-30517.

Bezmel'nitsyn, V. N., Legasov, V. A., & Chaivanov, B. B. (1977). Synthesis of krypton difluoride using a. *Doklady Akademii Nauk SSSR, 235*, 273-274.

Bilir, V., Blaser, D., Boese, R., & Frohn, H.-J. (2009). Bis(pentafluorophenylxenonium) tetrafluoroterephthalate, p-$C_6F_5XeO(O)CC_6F_4C(O)OXeC_6F_5$, a hypervalent compound with two xenon–carbon bonds. *Journal of Fluorine Chemistry, 130*(9), 824-829.

Boehler, R. (2000). Laser heating in the diamond cell: techniques and applications. *Hyperfine Interactions, 128*, 307-321.

Boldyrev, V. V. (2006). Mechanochemistry and mechanical activation of solids. *Russian Chemical Reviews, 75*(3), 177-189.

Bortolus, M. R., Ellwanger, M., Haner, J., & Schrobilgen, G. J. (2021). Syntheses and Structural Characterizations of the Cl(V) Coordination Complex, $[O_2Cl(FXeF)_2][AsF_6]$, and β-$[ClO_2][AsF_6]$. *Journal of Fluorine Chemistry, 250*, 109814.

Bortolus, M. R., LaChapelle, G. J., Mercier, H. P., Haner, J., & Schrobilgen, G. J. (2023). XeF_2 Coordination Complexes of the $[BrO_2]^+$ Cation, $[O_2Br(FXeF)_n][AsF_6]$ (n = 1, 2) and $[O_2Br(FXeF)_2][SbF_6]$; Their Syntheses and Structural Characterizations. *Inorganic Chemistry, 62*(23), 8761-8771.

Bortolus, M. R., Mercier, H. P., & Schrobilgen, G. J. (2020). Group 6 Oxyfluoro-Anion Salts of $[XeF_5]^+$ and $[Xe_2F_{11}]^+$: Syntheses and Structures of $[XeF_5][M_2O_2F_9]$ (M=Mo, W), $[Xe_2F_{11}][M'OF_5]$ (M′=Cr, Mo, W), $[XeF_5][HF_2]\cdot CrOF_4$, and $[XeF_5][WOF_5]\cdot XeOF_4$. *Chemistry - A European Journal, 26*(41), 8935-8950.

Bortolus, M. R., Mercier, H. P., & Schrobilgen, G. J. (2022). Synthesis, Structure, and Bonding of a XeIV Transition-Metal Coordination Complex, F_3XeF_b- - -WOF_4. *Angewandte Chemie International Edition, 61*(45), e202211699.

Bortolus, M. R., Mercier, H. P., & Schrobilgen, G. J. (2024). Chromium(VI) Oxyfluoride Dianions, $[Cr_2O_4F_6]^{2-}$ and $[CrO_2F_4]^{2-}$; Syntheses and Structures of $[XeF_5]_2[Cr_2O_4F_6]$, $[XeF_5]_2[Cr_2O_4F_6]\cdot n$X (X=HF, n=4; X=$XeOF_4$, n=2), and $[XeF_5][Xe_2F_{11}][CrO_2F_4]$. *Chemistry - A European Journal, 30*(10), e202303059.

Bortolus, M. R., Mercier, H. P., Brock, D. S., & Schrobilgen, G. J. (2022). Noble-Gas Difluoride Complexes of MOF_4 (M=Mo, W); Syntheses, Structures and Bonding of $NgF_2\cdot MOF_4$ and $XeF_2\cdot 2MOF_4$ (Ng=Kr, Xe). *Chemistry - A European Journal, 28*(15), e202103729.

Bortolus, M. R., Mercier, H. P., Nguyen, B., & Schrobilgen, G. J. (2021). Syntheses and Characterizations of the Mixed Noble-Gas Compounds,

$[FKr^{II}FXe^{II}F][AsF_6]\cdot 0.5\,Kr^{II}F_2\cdot 2\,HF$, $([Kr^{II}_2F_3][AsF_6])2\cdot Xe^{IV}F_4$, and $Xe^{IV}F_4\cdot Kr^{II}F_2$. *Angewandte Chemie International Edition, 60*(44), 23678-23686.

Bourhis, L. J., Dolomanov, O. V., Gildea, R. J., Howard, J. A., & Puschmann, H. (2015). The anatomy of a comprehensive constrained, restrained refinement program for the modern computing environment – *Olex2* dissected. *Acta Crystallographica A, Foundations and Advances*, 59-75.

Brandenburg, K. (2022). *Diamond, Crystal Impact GbR.* Hamburg.

Brewer, S. A., Brisdon, A. K., Fawcett, J., Holliman, P. J., Holloway, J. H., Hope, E. G., & Russell, D. R. (2005). Re-evaluation of the X-ray Crystal Structure of $[Ta_4F_{20}]$ and the Synthesis and Characterization of a Series of Mixed-Metal Pentafluorides of Niobium and Tantalum. *Zeitschrift für anorganische und allgemeine Chemie, 632*(2), 325-329.

Britvin, S. N., Kashtanov, S. A., Krivovichev, S. V., & Chukanov, N. V. (2016). Xenon in Rigid Oxide Frameworks: Structure, Bonding and Explosive Properties of Layered Perovskite $K_4Xe_3O_{12}$. *Journal of American Chemical Society, 138*(42), 13838-13841.

Britvin, S. N., Kashtanov, S. A., Krzhizhanovskaya, M. G., Gurinov, A. A., Glumov, O. V., Strekopytov, S., . . . Krivovichev, S. V. (2015). Perovskites with the Framework-Forming Xenon. *Angewandte Chemie International Edition, 54*(48), 14340-14344.

Brock, D. S., & Schrobilgen, G. J. (2011). Synthesis of the Missing Oxide of Xenon, XeO_2, and Its Implications for Earth's Missing Xenon. *Journal of American Chemical Society, 133*(16), 6265-6269.

Brock, D. S., Bilir, V., Mercier, H. P., & Schrobilgen, G. J. (2007). $XeOF_2$, $F_2OXeN{\equiv}CCH_3$, and $XeOF_2\cdot n$HF: Rare Examples of Xe(IV) Oxide Fluorides. *Journal of American Chemical Society*, 3598-3611.

Brock, D. S., Casalis de Pury, J. J., Mercier, H. P., Schrobilgen, G. J., & Silvi, B. (2010). XeF_2 Coordination to a Halogen Center; Raman Spectra (n = 1, 2) and X-ray Crystal Structures (n = 2) of $[BrOF_2][AsF_6]\cdot n XeF_2$ and $[XOF_2][AsF_6]$ (X = Cl, Br). *Inorganic Chemistry, 49*(14), 6673-6689.

Brock, D. S., Mercier, H. P., & Schrobilgen, G. J. (2013). $[H(OXeF_2)_n][AsF_6]$ and $[FXe^{II}(OXe^{IV}F_2)n][AsF_6]$ (n = 1, 2): Examples of Xenon(IV) Hydroxide Fluoride and Oxide Fluoride Cations and the Crystal Structures of $[F_3Xe{-}{-}{-}FH][Sb_2F_{11}]$ and $[H_5F_4][SbF_6]\cdot 2[F_3Xe{-}{-}{-}FH][Sb_2F_{11}]$. *Journal of American Chemical Society, 135*(13), 5089-5104.

Brock, D. S., Schrobilgen, G. J., & Žemva, B. (2013). Main-Group Elements, Including Noble Gases. In J. Reedjik, & K. Poeppelmeier, *Comperhensive Inorganic Chemistry II, From Elements to Applications* (pp. 785-822). Amsterdam, Netherlands: Elsevier.

Brown, D. R., Clegg, M. J., Downs, A. J., Fowler, R. C., Minihan, A. R., Norris, J. R., & Stein, L. (1992). The Dixenon(1+) Cation: Formation in the Condensed Phases and Characterization by ESR, UV-Visible and Raman Spectroscopy. *Inorganic Chemistry, 31*(24), 5041-5052.

Bruker. (2022). *OPUS 8.7 Build: 8, 7, 41 (20220611 x64).* Massachusetts: Bruker Optics GmbH & Co. KG.

Brüning, L., Jena, N., Bykova, E., Jurzick, P. L., Flosbach, N. T., Mezouar, M., . . . Bykov, M. (2023). Stabilization of Guanidinate Anions $[CN_3]^{5-}$ in Calcite-Type $SbCN_3$. *Angewandte Chemie International Edition, 62*(47), e202311519.

Burbank, R. D., & Jones, G. R. (1970). Xenon Hexafluoride: Structural Crystallography of Tetrameric Phases. *Science, 171*(3970), 485-487.

Burbank, R. D., & Jones, G. R. (1974). Structure of the cubic phase of xenon hexafluoride at 193.deg.K. *Journal of American Chemical Society, 96*(1), 43-48.

Burbank, R. D., Falconer, W. E., & Sunder, W. A. (1972). Crystal Structure of Krypton Difluoride at -80°C. *Science, 178*(4067), 1285-1286.

Burla, M. C., Caliandro, R., Carrozzini, B., Cascarano, G. L., Cuocci, C., Giacovazzo, C., . . . Poliodri, G. (2015). Crystal structure determination and refinement via SIR2014. *Journal of Applied Crystallography, 48*(1), 306-309.

Burns, J. H. (1963). A Second Crystalline Phase of Xenon Tetrafluoride. *The Journal of Physical Chemistry, 67*(2), 536.

Burns, J. H., Ellison, R. D., & Levy, H. A. (1965). The Crystal Structure of the Molecular Addition Compound Xenon Difluoride-Xenon Tetrafluoride. *Acta Crystallographica, 18*, 11-16.

Chambers, R. D., & Spring, D. J. (1969). Polyfluoroaryl organometallic compounds—X : Nucleophilic substitution in octafluorofluoren-9-one. *Tetrahedron*, 565-572.

Christe, K. O., & Wilson, W. W. (1988). New Syntheses and Properties of XeO_2F_2, $Cs^+XeO_2F_3$, and $NO_2^+[XeO_2F_3nXeO_2F_2]$. *Inorganic Chemistry, 27*(21), 3763-3768.

Christe, K. O., Curtis, E. C., Dixon, D. A., Mercier, H. P., Sanders, J. C., & Schrobilgen, G. J. (1991). The pentafluoroxenate(IV) anion, XeF_5^-: the first example of a pentagonal planar AX5 species. *Journal of American Chemical Society, 113*(9), 3351-3361.

Claassen, H. H., & Huston, J. L. (1971). Matrix-Isolation Raman and Infrared Spectra, Molecular Structure, and Force Constants for XeO_3F_2. *The Journal of Chemical Physics, 55*(4), 1505-1507.

Colacino, E., Carta, M., Pia, G., Porcheddu, A., Ricci, P. C., & Delogu, F. (2018). Processing and Investigation Methods in Mechanochemical Kinetics. *ACS Omega, 3*(8), 9196-9209.

Corain, B. (1982). The Coordination Chemistry of Hydrogen Cyanide, Cyanogen and Cyanogen Halides. *Coordination Chemistry Reviews*, 165-200.

Crawford, D. E., & Casaban, J. (2016). Recent Developments in Mechanochemical Materials Synthesis by Extrusion. *Advanced Materials, 28*(27), 5747-5754.

Dalladay-Simpsons, P., Binns, J., Pena-Alvarez, M., Donnelly, M.-E., Greenberg, E., Prakapenka, V., . . . Howie, R. T. (2019). Band gap closure, incommensurability and molecular dissociation of dense chlorine. *Nature Communications, 10*(1), 1134.

De Backere, J. R., & Schrobilgen, G. J. (2018). A Homoleptic KrF2 Complex, $[Hg(KrF_2)_8][AsF_6]_2{\cdot}2\,HF$. *Angewandte Chemie International Edition, 57*(40), 13167-13171.

De Backere, J. R., Bortolus, M. R., & Schrobilgen, G. J. (2016). Synthesis and Characterization of $[XeOXe]^{2+}$ in the Adduct-Cation Salt, $[CH_3CN{-}{-}{-}XeOXe{-}{-}{-}NCCH_3][AsF_6]_2$. *Angewandte Chemie International Edition, 55*(39), 11917-11920.

DesMarteau, D. D., LeBlond, R. D., Hossain, S. F., & Nothe, D. (1981). Xenon-nitrogen bonds. The synthesis and characterization of [imidobis(sulfuryl fluoride)]xenon(II) derivatives $Xe[N(SO_2F)_2]_2$, $FXeN(SO_2F)_2$ and $[(FSO_2)_2NXe]_2F^+AsF_6^-$ and the radical $\cdot N(SO_2F)_2$. *Journal of the American Chemical Society, 103*(26), 7734-7739.

Dewaele, A., Pepin, C. M., Geneste, G., & Gabarino, G. (2017). Reaction between nickel or iron and xenon under high pressure. *High Pressure Research, 37*, 137-146.

Dewaele, A., Worth, N., Pickards, C. J., Needs, R. J., Pascarelli, S., Mathon, O., . . . Irifune, T. (2016). Synthesis and stability of xenon oxides Xe_2O_5 and Xe_3O_2 under pressure. *Nature Chemistry, 8*(8), 784-790.

Dolomanov, O. V., Bourhis, L. J., Gildea, R. J., Howard, J. A., & Puschmann, H. (2009). OLEX2: a complete structure solution, refinement and analysis program. *Journal of Applied Crystallography*, 339-341.

Dong, X., Oganov, A. R., Goncharov, A. F., Stavrou, E., Lobanov, S., Saleh, G., . . . Wang, H.-T. (2017). A stable compound of helium and sodium at high pressure. *Nature Chemistry, 9*(5), 440-445.

Drews, T., & Seppelt, K. (1997). The Xe_2^+ Ion - Preparation and Structure. *Angewandte Chemie International Edition, 36*(8), 273-274.

Drews, T., Seidel, S., & Seppelt, K. (2002). Gold-Xenon Complexes. *Angewandte Chemie International Edition, 41*(3), 454-456.

Drozdov, A. P., Eremets, M. I., Troyan, I. A., Ksenofontov, V., & Shylin, S. I. (2015). Conventional superconductivity at 203 kelvin at high pressures in the sulfur hydride system. *Nature, 523*, 73-76.

Družina, B., & Žemva, B. (1986). On the synthesis of xenon(II) fluorostannates(IV). *Journal of Fluorine Chemistry, 34*(2), 233-239.

Edwards, A. J. (1964). The structures of niobium and tantalum pentafluorides. *Journal of the Chemical Society (Resumed)*(0), 3714-3718.

Edwards, A. J., & Taylor, P. (1971). Crystal structure of antimony pentafluoride. *Journal of the Chemical Society D: Chemical Communications*(21), 1376-1377.

Edwards, A. J., Holloway, J. H., & Peacock, R. D. (1963). New Fluorine Compounds of Xenon. *Proc. Chem. Soc*, 275-276.

Ehlers, A. W., Frenking, G., & Baerends, E. J. (1997). Carbonyl Complexes $M(CO)_5$—Ng (M = Cr, Mo, W and Ng = Ar, Kr, Xe). *Organometallics, 16*(22), 4896-4902.

Ellern, A., & Seppelt, K. (1995). $XeOF_5^-$, an Anion with Pentagonal-Pyramidal Structure. *Angewandte Chemie International Edition, 34*(15), 1586-1587.

Ellern, A., Mahjoub, A.-R., & Seppelt, K. (1996). Structures of XeF_7^- and $Xe_2F_{13}^-$. *Angewandte Chemie International Edition, 35*(10), 1123-1125.

Elliot, H. S., Lehmann, J. F., Mercier, H. P., Jenkins, H. D., & Schrobilgen, G. J. (2010). X-ray Crystal Structures of $[XeF][MF_6]$ (M = As, Sb, Bi), $[XeF][M_2F_{11}]$ (M = Sb, Bi) and Estimated Thermochemical Data and Predicted Stabilities for Noble-Gas Fluorocation Salts using Volume-Based Thermodynamics. *Inorganic Chemistry, 49*, 8504-8523.

Emara, A. A. (1991). *Lewis Acid Properties of the XeF^+ Cation and its Adducts with Organic Nitrogen Bases.* Ontario: McMaster University.

Emara, A. A., & Schrobilgen, G. J. (1987). Fluoro(nitrile)xenon(II) cations, $RC{\equiv}N{-}XeF^+$ $AsF6^-$(R = H, CH_3, CH_2F, C_2H_5, C_2F_5, C_3F_7, or C_6F_5); novel examples of xenon–nitrogen bonds and ^{129}Xe–^{13}C, ^{129}Xe–^{1}H, and ^{129}Xe–^{14}N nuclear spin-spin couplings. *Journal of the Chemical Society, Chemical Communications*, 1644-1646.

Emara, A. A., & Schrobilgen, G. J. (1992). The fluoro(hydrogen cyanide)xenon(II) cation. Preparation of $HC{\equiv}NXeF^+AsF_6^-$: a multinuclear magnetic resonance and Raman spectroscopic study. *Inorganic Chemistry, 31*(8), 1323-1332.

Eremets, M. I., Gavriliuk, A. G., Serebryanaya, N. R., Trojan, I. A., Dzivenko, D. A., Boehler, R., . . . Hemley, R. J. (2004). Structural transformation of molecular nitrogen to a single-bonded atomic state at high pressures. *Journal of Chemical Physics, 121*(22), 11296-11300.

Eremets, M. I., Gavriliuk, A. G., Trojan, I. A., Dzivenko, D. A., & Boehler, R. (2004). Single-bonded cubic form of nitrogen. *Nature Materials, 3*, 558-563.

Eremets, M. I., Minkov, V. S., Kong, P. P., Drozdov, A. P., Chariton, S., & Prakapenka, V. B. (2023). Universal diamond edge Raman scale to 0.5 terapascals and implications for the metallization of hydrogen. *Nature Communications, 14*, 907.

Eugene Weaver, E., Weinstock, B., & Knop, C. P. (1963). Xenon Hexafluoride. *Journal of American Chemical Society, 85*(1), 111-112.

Ewing, G. E. (1975). Structure and properties of van der Waals molecules. *Accounts of Chemical Research, 8*(6), 185-192.

Fir, B. A. (1999). *X-ray Crystal Structures of Xe(II)−N and Xe(II)−O bonded compounds, and the syntheses of $OTeF_5$ derivatives of As(III) and Sb(III).* Hamilton, Ontario: McMaster University.

Fir, B. A., Gerken, M., Pointner, B. E., Mercier, H. P., Dixon, D. A., & Schrobilgen, G. J. (2000). An X-ray crystallographic study of $[Xe_2F_3][SbF_6]$ and dimorphism in $[Xe_2F_3][AsF_6]$; and a density functional theory study of the $Xe_2F_3^+$ cation. *Journal of Fluorine Chemistry, 105*(1), 159-167.

Fir, B., Whalen, J. M., Mercier, H. P., Dixon, D. A., & Schrobilgen, G. J. (2006). Syntheses of $[F_5TeNH_3][AsF_6]$, $[F_5TeN(H)Xe][AsF_6]$, and F_5TeNF_2 and Characterization by Multi-NMR and Raman Spectroscopy and by Electronic Structure Calculations: The X-ray Crystal Structures of α- and β-F_5TeNH_2, $[F_5TeNH_3][AsF_6]$, and $[F_5TeN(H)Xe][AsF_6]$. *Inorganic Chemistry, 45*(5), 1978-1996.

Flosbach, N. T., Brüning, L., Jurzick, P. L., Bykova, E., Ekholm, M., Abrikosov, I. A., . . . Bykov, M. (2025). High Pressure Synthesis of Pr_2O_5 – A Unique Lanthanoid(IV) Oxide. *Angewandte Chemie International Edition, 64*(11), e202422929.

Forgeron, M. A., Wasylishen, R. E., Gerken, M., & Schrobilgen, G. J. (2007). Solid-State ^{129}Xe and ^{131}Xe NMR Study of the Perxenate Anion XeO_6. *Inorganic Chemistry, 46*(9), 3585-3592.

Forman, R. A., Piermarini, G. J., Barnett, J. D., & Block, S. (1972). Pressure Measurement Made by the Utilization of Ruby Sharp-Line Luminescence. *Science, 176*(4032), 284-285.

Foropoulos, J. J., & DesMarteau, D. D. (1982). Bis[bis(trifluoromethanesulfonyl)imido]xenon: a new compound possessing xenon-nitrogen bonds. *Journal of the American Chemical Society, 104*(15), 4260-4261.

Friščić, T., Mottillo, C., & Titi, H. M. (2020). Mechanochemistry for Synthesis. *Angewandte Chemie International Edition, 59*(3), 1018-1029.

Frlec, B., & Holloway, J. H. (1973). New krypton difluoride adducts. *Journal of the Chemical Society, Chemical Communications*(11), 370-371.

Frlec, B., & Holloway, J. H. (1974). Preparation of $2KrF_2{\cdot}SbF_5$ and $KrF_2{\cdot}SbF_5$: the $Kr_2F_3^+$ and KrF^+ cations. *Journal of the Chemical Society, Chemical Communications*(3), 89-90.

Frlec, B., & Holloway, J. H. (1975). The XeF_2—MF_5 (M = Sb, Ta, or Nb) Systems: Vibrational Spectra of Solid Xenon Difluoride Adducts. *Journal of Chemical Society, Dalton Transactions*, 535-540.

Frlec, B., & Holloway, J. H. (1976). Preparation and characterization of $2KrF_2{\cdot}SbF_5$, $KrF_2{\cdot}MF_5$ (M = antimony, tantalum), and $KrF_2{\cdot}2MF_5$ (M = antimony, tantalum, niobium): the trifluorodikrypton(1+) and fluorokrypton(1+) cations. *Inorganic Chemistry, 15*(6), 1263-1270.

Frlec, B., & Holloway, J. H. (1976). The XeF_2—MF_5 (M = Sb, Ta or Nb) Systems: Raman Spectra of Melts. *Journal of Inorganic and Nuclear Chemistry Supplement*, 167-171.

Frohn, H.-J., & Bardin, V. V. (2001). Preparation and Reactivity of Compounds Containing a Carbon−Xenon Bond. *Organometallics, 20*(23), 4750-4762.

Frohn, H.-J., Jakobs, S., & Henkel, G. (1989). The Acetonitrile(pentafluorophenyl)xenon(II) Cation, $[MeCNXe–C_6F_5]^{\oplus}$: The First Structural Characterization of a Xenon Carbon Bond. *Angewandte Chemie International Edition, 28*(11), 1506-1507.

Frohn, H.-J., LeBlond, N., Lutar, K., & Žemva, B. (2000). The First Organoxenon(IV) Compound: Pentafluorophenyldifluoroxenonium(IV) Tetrafluoroborate. *Angewandte Chemie International Edition, 39*(2), 391-393.

Frohn, H.-J., Schroer, T., & Henkel, G. (1999). C_6F_5XeCl and $[(C_6F_5Xe)_2Cl][AsF_6]$: The First Isolated and Unambigously Characterized Xenon(II) Chlorine Compounds. *Angewandte Chemie International Edition, 38*(17), 2554-2556.

Gasner, E. L., & Claassen, H. H. (1967). Raman spectrum of xenon hexafluoride. *Inorganic Chemistry, 6*(10), 1937-1938.

Gawrilow, M., Beckers, H., Riedel, S., & Cheng, L. (2018). Matrix-Isolation and Quantum-Chemical Analysis of the C_{3v} Conformer of XeF_6, $XeOF_4$, and Their Acetonitrile Adducts. *The Journal of Physical Chemistry A, 122*(1), 119-129.

Gerken, M. (2000). *Syntheses and Characterization of XeO_4 and Oxide Fluorides of Xenon(VIII), Osmium(VIII), Iodine(VII), and Xenon(II)* . Hamilton: McMaster University.

Gerken, M., & Schrobilgen, G. J. (2000). The impact of multi-NMR spectroscopy on the development of noble-gas chemistry. *Coordination Chemistry Reviews, 197*(1), 335-395.

Gerken, M., Moran, M. D., Mercier, H. P., Pointner, B. E., Schrobilgen, G. J., Hoge, B., . . . Boatz, J. A. (2009). On the XeF^+/H2O System: Synthesis and Characterization of the Xenon(II) Oxide Fluoride Cation, $FXeOXeFXeF^+$. *Journal of American Chemical Society*, 13474-13489.

Gillespie, R. J., & Hargittai, I. (2012). *The VSEPR Model of Molecular Geometry.* Boston: Dover Publications.

Gillespie, R. J., & Schrobilgen, G. J. (1974). Preparation of the KrF^+, $Kr_2F_3^+$, and BrF_6^+ ions and their characterisation by ^{19}F nuclear magnetic resonance and Raman spectroscopy. *Journal of the Chemical Society, Chemical Communications*(3), 90-92.

Gillespie, R. J., & Schrobilgen, G. J. (1977). Preparation and Raman spectra of $XeOF_2$, $XeOF_3^-$, and $XeO_2F_3^-$. *Journal of the Chemical Society, Chemical Communications*(17), 595-597.

Gillespie, R. J., Martin, D., Schrobilgen, G. J., & Slim, D. R. (1977). The Crystal Structure of Trifluoroxenon(1v) Hexafluorobismuthate(v): the Fluoride-acceptor Strength of Bismuth Pentafluoride. *Journal of the Chemical Society, Dalton Transactions*(22), 2234-2237.

Goettel, J. T. (2017). *Oxide And Oxide Fluoride Chemistry of Xenon(VIII), Xenon(VI), and Iridium.* Ontario: McMaster University.

Goettel, J. T., & Schrobilgen, G. J. (2016). Solid-State Structures of XeO_3. *Inorganic Chemistry, 55*(24), 12975-12981.

Goettel, J. T., Bortolus, M. R., Stuart, D. G., Mercier, H. P., & Schrobilgen, G. J. (2019). Chromium Oxide Tetrafluoride and Its Reactions with Xenon Hexafluoride; the $[XeF_5]^+$ and $[Xe_2F_{11}]^+$ Salts of the $[Cr^{VI}OF_5]^-$, $[Cr^{V}OF_5]^{2-}$, $[Cr^{V}{}_2O_2F_8]^{2-}$, and $[Cr^{IV}F_6]^{2-}$ Anions. *Chemistry - A European Journal, 25*(69), 15815-15829.

Goettel, J. T., Haensch, V. G., & Schrobilgen, G. J. (2017). Stable Chloro- and Bromoxenate Cage Anions; $[X_3(XeO_3)_3]^{3-}$ and $[X_4(XeO_3)_4]^{4-}$ (X = Cl or Br). *Journal of American Chemical Society, 139*(25), 8725-8733.

Goettel, J. T., Matsumoto, K., Mercier, H. P., & Schrobilgen, G. J. (2016). Syntheses and Structures of Xenon Trioxide Alkylnitrile Adducts. *Angewandte Chemie International Edition, 54*(44), 13780-13783.

Graham, L., Graudejus, O., Jha, N. J., & Bartlett, N. (2000). Concerning the nature of XePtF6. *Coordination Chemistry Reviews*, 321-334.

Grochala, W. (2007). Atypical compounds of gases, which have been called "noble". *Chemical Society Reviews, 36*(10), 1632-1655.

Grochala, W., Hoffmann, R., Feng, J., & Ashcroft, N. W. (2007). The Chemical Imagination at Work in Very Tight Places. *Angewandte Chemie International Edition, 46*(20), 3620-3642.

Groom, C. R., Bruno, I. J., Lightfoot, M. P., & Ward, S. C. (2016). The Cambridge Structural Database. *Acta Crystallographica Section B, Structural Science, Crystal Engineering and Materials*, 171-179.

Guan, R., Liu, J., Wang, X., Bao, K., Yu, H., & Cui, T. (2024). In Situ Synthesis of WF_6 and ReF_6 in a Diamond Anvil Cell and Phase Separation of Products. *The Journal of Physical Chemistry C, 128*(33), 14113-14117.

Hagiwara, R., Hollander, F., Maines, C., & Bartlett, N. (1991). The crystal structure of $[Ag(XeF_2)_2][AsF_6]$ formed in the Oxidation of Xe by $AgFAsF_6$. *European Journal of Solid State and Inorganic Chemistry, 28*, 855-866.

Hamilton, W. C., Ibers, J. A., & Mackenzie, D. R. (1963). Geometry of the Perxenate Ion. *Science, 141*(3580), 532-534.

Haner, J., & Schrobilgen, G. J. (2015). The Chemistry of Xenon(IV). *Chemical Reviews, 115*(2), 1255-1295.

Hattori, M., Saha, D., Bacho, M. Z., & Shibata, N. (2025). Mechanochemical pathway for converting fluoropolymers to fluorochemicals. *Nature Chemistry, 17*, 1480-1487.

Hebecker, C. (1971). Zur Kristallstruktur von Wismutpentafluorid. *Zeitschrift für anorganische und allgemeine Chemie , 384*(2), 111-114.

Hemley, R. J. (2000). Effect of High Pressure on Molecules. *Annual Reviews of Physical Chemistry, 51*, 763-800.

Hermann, A., & Schwerdtfeger, P. (2014). Xenon suboxides stable under pressure. *Journal of Physical Chemistry Letters, 5*(24), 4336-4342.

Hodgson, D. J., & Ibers, J. A. (1969). Crystal and molecular structure of potassium monofluoroxenate(VI), $KXeO_3F$. *Inorganic Chemistry, 8*(2), 326-331.

Holloway, J. H., & Knowles, J. G. (1969). Reactions of Xenon Difluoride with the Pentafluorides of Tantalum, Niobium, Ruthenium and Osmium. *Journal of the Chemical Society A: Inorganic, Physical, Theoretical*, 756-761.

Holloway, J. H., Kaučič, V., Martin-Rovet, D., Russell, D. R., Schrobilgen, G. J., & Selig, H. (1985). Crystal Structure of $Cs^+[(XeOF_4)_3F]$ and Vibrational Study of the 180-Enriched $[XeOF_5]^-$ and $[(XeOF_4)_3F]^-$ Anions. *Inorganic Chemistry, 24*(5), 678-683.

Horie, K., Baron, M., Fox, R. B., He, J., Hess, M., Kahovec, J., . . . Work, W. J. (2004). Definitions of terms relating to reactions of polymers and to functional polymeric materials. *Pure and Applied Chemistry, 76*(4), 889-906.

Hou, C., Wang, X., Botana, J., & Miao, M. (2017). Noble gas bond and the behaviour of XeO3 under pressure. *Physical Chemistry Chemical Physics, 19*(40), 27463-27467.

Howie, R. T., Turnbull, R., Binns, J., Frost, M., Dalladay-Simpson, P., & Gregoryanz, E. (2016). Formation of xenon-nitrogen compounds at high pressure. *Scientific Reports, 6*(1), 34896.

Hoyer, S., Emmler, T., & Seppelt, K. (2006). The structure of xenon hexafluoride in the solid state. *Journal of Fluorine Chemistry, 127*(10), 1415-1422.

Hughes, M. J. (2010). *Fluoride Ion Donor-Acceptor Properties of cis-$Os0_2F_4$ and Lewis Acid Properties of OsO_3F_2 and $XeOF_4$.* Ontario: McMaster University.

Hughes, M. J., Brock, D. S., Mercier, H. P., & Schrobilgen, G. J. (2011). A Raman spectroscopic study of the $XeOF_4/XeF_2$ system and the X-ray crystal structure of a-$XeOF_4 \cdot XeF_2$. *Journal of Fluorine Chemistry, 132*(10), 660-668.

Huston, J. L. (1967). Xenon dioxide difluoride: isolation and some properties. *The Journal of Physical Chemistry, 71*(10), 3339-3341.

Huston, J. L. (1968). Xenon Trioxide Difluoride: Mass Spectrum. *Inorg. Nucl. Chem. Lett., 4*(1), 29-30.

Huston, J. L. (1971). Xenon Dioxide Tetrafluoride. *Journal of American Chemical Society, 93*(20), 5255-5256.

Hwang, I.-C., Seidel, S., & Seppelt, K. (2003). Gold(I) and Mercury(II) Xenon Complexes. *Angewandte Chemie International Edition, 42*(36), 4392-4395.

Ivanova, M. V., Mercier, H. P., & Schrobilgen, G. J. (2015). $[XeOXeOXe]^{2+}$, the Missing Oxide of Xenon(II); Synthesis, Raman Spectrum, and X-ray Crystal Structure of $[XeOXeOXe][\mu\text{-}F(ReO_2F_3)_2]_2$. *Journal of American Chemical Society, 137*(41), 13398-13413.

Jacob, V. E., Lentz, D., Seppelt, K., & Simon, A. (1981). Edelgasverbindungen mit dem Liganden -$OTeF_5$. *Zeitschrift für anorganische und allgemeine Chemie, 472*(1), 7-25.

Jaselskis, B., Huston, J. L., & Spittler, T. M. (1969). Preparation and properties of alkali fluoroxenates, $M_x(FXeO_3)_x$. *Journal of the American Chemical Society, 91*(7), 1874-1875.

Katrusiak, A. (2019). Lab in a DAC – high-pressure crystal chemistry in a diamond-anvil cell. *Acta Crystallographica Section B - Structural Science, Crystal Engineering and Materials*, 918-926 .

Kim, M., Debessai, M., & Yoo, C.-S. (2010). Two- and three-dimensional extended solids and metallizazion of compressed XeF_2. *Nature Chemistry, 2*(2), 784-788.

Kinkead, S. A., FritzPatrcik, J. P., Foropoulos, J., Kissane, R. J., & Purson, J. D. (1994). Photochemical and Thermal Dissociation of Krypton Difluoride. In J. S. Thrasher, & J. S. Thrasher (Ed.), *Fluorine Chemistry Toward the 21st Century* (pp. 40-55). Washington DC: American Chemical Society.

Klar, P. B., Krysiak, Y., Xu, H., Steciuk, G., Cho, J., Zou, X., & Palatinus, L. (2023). Accurate structure models and absolute configuration determination using dynamical effects in continuous-rotation 3D electron diffraction data. *Nature Chemistry, 15*(6), 848-855.

Kleppe, A. K., Amboage, M., & Jephcoat, A. P. (2014). New high-pressure van der Waals compound Kr(H2)4 discovered in the krypton-hydrogen binary system. *Scientific Reports, 4*(1), 4989.

Klotz, S., Chervin, J.-C., Munsch, P., & Le Marchand, G. (2009). Hydrostatic limits of 11 pressure transmitting media. *Journal of Physics D: Applied Physics*, 075413.

Koppe, K., Haner, J., Mercier, H. P., Frohn, H.-J., & Schrobilgen, G. J. (2014). Xenon(IV)–Carbon Bond of $[C_6F_5XeF_2]^+$; Structural Characterization and Bonding of $[C_6F_5XeF_2][BF_4]$, $[C_6F_5XeF_2][BF_4] \cdot 2HF$, and $[C_6F_5XeF_2][BF_4] \cdot n NCCH_3$ ($n = 1, 2$); and the Fluorinating Properties of $[C6F_5XeF_2][BF_4]$. *Inorganic Chemistry, 53*(21), 11640-11661.

Kovalev, V., Spahr, D., Winkler, B., Bayarjargal, L., Wedek, L., Aslandukova, A., . . . Bykova, E. (2025). High-pressure synthesis and crystal structure of iron sp3-carbonate ($Fe_2[C_4O_{10}]$) featuring pyramidal $[C_4O_{10}]^{4-}$ anions. *Communications Chemistry, 8*, 66.

Koyama-Nakazawa, K., Koeda, M., Hedo, M., & Uwatoko, Y. (2007). In situ pressure calibration for piston cylinder cells via ruby fluorescence with fiber optics. *Review of Scientific Instruments*, 066109.

Kurzydlowski, D., & Zaleski-Ejgierd, P. (2015). High-pressure stabilization of argon fluorides. *Physical Chemistry Chemical Physics, 18*(4), 2309-2313.

Kurzydlowski, D., Soltysiak, M., Džoleva, A., & Zaleski-Ejgierd, P. (2017). High-pressure reactivity of Kr and F_2 - stabilization of krypton in the +4 oxidation state. *Crystals, 7*(11), 329.

Kurzydłowski, D., Zaleski-Ejgierd, P., Grochala, W., & Hoffmann, R. (2011). Freezing in Resonance Structures for Better Packing: XeF_2 Becomes $(XeF^+)(F^-)$ at Large Compression. *Inorganic Chemistry, 50*(8), 3832-3840.

LaBonville, P., Ferraro, J. R., & Spittler, T. M. (1971). Vibrational Investigations of Several Alkali Metal Haloxenates. *The Journal of Chemical Physics, 55*(2), 631-640.

Laniel, D., Weck, G., & Loubeyre, P. (2016). $Xe(N_2)_2$ compound up to 150 GPa: Reluctance to the formation of xenon nitride. *Physical Review B, 94*(17), 174109.

Lavina, B., Dera, P., Kim, E., Meng, Y., Downs, R. T., Weck, P. F., . . . Zhao, Y. (2011). Discovery of the recoverable high-pressure iron oxide Fe_4O_5. *Proceedings of the National Academy of Sciences, U.S.A, 108*(42), 17281-17285.

Leary, K., Zalkin, A., & Bartlett, N. (1973). Crystal structure of $[Xe_2F_{11}]^+[AuF_6]^-$. *Journal of the Chemical Society, Chemical Communications*(4), 131-132.

Leblanc, M., Maisonneuve, V., & Tressaud, A. (2014). Crystal Chemistry and Selected Physical Properties of Inorganic Fluorides and Oxide-Fluorides. *Chemical Reviews, 115*(2), 1191-1254.

LeBlond, R. D., & DesMarteu, D. D. (1974). Fluoro[imidobis(sulphuryl fluoride)]xenon. An Example of a Xenon-Nitrogen Bond. *Journal of the Chemical Society, Chemical Communications*(14), 555-556.

Lehmann, J. F., & Schrobilgen, G. J. (2003). Structural and vibrational characterization of $[KrF][AuF_6]$ and α-$[O_2][AuF_6]$ using single crystal X-ray diffraction, Raman spectroscopy and electron structure calculations. *Journal of Fluorine Chemistry, 119*(2), 109-124.

Lehmann, J. F., Mercier, H. P., & Schrobilgen, G. J. (2002). The chemistry of krypton. *Coordination Chemistry Reviews, 233-234*(1-39), 1-39.

Lehmann, J., Dixon, D. A., & Schrobilgen, G. J. (2001). X-ray Crystal Structures of α-KrF_2, $[KrF][MF_6]$ (M = As, Sb, Bi), $[Kr_2F_3][SbF_6] \cdot KrF_2$, $[Kr_2F_3]_2[SbF_6]_2 \cdot KrF_2$, and $[Kr_2F_3][AsF_6] \cdot [KrF][AsF_6]$; Synthesis and Characterization of $[Kr_2F_3][PF_6] \cdot n KrF_2$; and Theoretical Studies of KrF_2, KrF^+, $Kr_2F_3^+$, and the $[KrF][MF_6]$. *Inorganic Chemistry, 40*(13), 3002-3017.

Liermann, H.-P., Konopkova, Z., Morgenroth, W., Glazyrin, K., Bednarčik, J., McBride, E. E., . . . Franz, H. (2015). The Extreme Conditions Beamline P02.2 and the Extreme Conditions Science Infrastructure at PETRA III. *Journal of Synchrotron Radiation, 22*, 908-924.

Liu, J., Zhu, J., Yu, H., Zhang, Z., Wu, G., Yao, A., . . . Cui, T. (2024). Structural Phase Transition and Decomposition of XeF_2 under High Pressure and Its Formation of Xe-Xe covalent bonds. *Inorganic Chemistry, 63*(26), 12248-12254.

Loubeyre, P., Letoullec, R., & Pinceaux, J.-P. (1994). Compression of $Ar(H_2)_2$ up to 175 GPa: A new path for the dissociation of molecular hydrogen? *Physical Review Letters, 72*(9), 1360-1363.

Lowe, M. E., Gallant, B. M., Davison, N., Hopkinson, M. N., Kubicki, D. J., Lu, E., & Armstrong, R. J. (2025). A Reductive Mechanochemical Approach Enabling Direct Upcycling of Fluoride from Polytetrafluoroethylene (PTFE) into Fine Chemicals. *Journal of American Chemical Society, 147*(44), 40895-40899.

Lozinšek, M. (2013). *Sinteza in karakterizacija novih spojin šibko koordinirajočih fluoridoanionov.* Ljubljana: University of Ljubljana.

Lozinšek, M., Mercier, H. P., & Schrobilgen, G. J. (2021). Mixed Noble-Gas Compounds of Krypton(II) and Xenon(VI); $[F_5Xe(FKrF)AsF_6]$ and $[F_5Xe(FKrF)_2AsF_6]$. *Angewandte Chemie International Edition, 60*(15), 8149-8156.

Lozinšek, M., Mercier, H. P., Brock, D. S., Žemva, B., & Schrobilgen, G. J. (2017). Coordination of KrF_2 to a Naked Metal Cation, Mg^{2+}. *Angewandte Chemie International Edition, 56*(22), 6251-6254.

Lundegaard, L. F., Weck, G., McMahon, M. I., Desgreniers, S., & Loubeyre, P. (2006). Observation of O_8 molecular lattice in the e phase of solid oxygen. *Nature, 443*(7108), 201-204.

Lutar, K., & Šmalc, A. (1989). Fotokemična sinteza ksenonovega difluorida v večjem laboratorijskem merilu. *Kemija u industriji, 38*(12), 589-591.

Lutar, K., Borrmann, H., & Žemva, B. (1998). $XeF_2 \cdot 2CrF_4$ and $XeF_5^+CrF_5^-$: Syntheses, Crystal Structures, and Some Properties. *Inorganic Chemistry, 37*(12), 3002-3006.

Lutar, K., Leban, I., Ogrin, T., & Žemva, B. (1992). $XeF_2{\cdot}CrF_4$ and $(XeFCrF_5)_4$. XeF_4: Syntheses, crystal structures and some properties. *European Journal of Solid State and Inorganic Chemistry, 29*, 713-727.

MacDougall, P. J., Schrobilgen, G. J., & Bader, R. F. (1989). Properties of atoms in molecules: krypton and xenon and their bonds to nitrogen and fluorine in hydrogen cyanide complexes with noble gas fluorides, $HCN{-}NgF^+$, NgF^+ and NgF_2 (Ng = noble gas. *Inorganic Chemistry*, 763-769.

Malm, J. G., Sheft, I., & Chernick, C. L. (1963). Xenon Hexafluoride. *Journal of American Chemical Society, 85*(1), 110-111.

Marcus, Y., & Cohen, D. (1966). Americum(III) Perxenate. *Inorganic Chemistry, 5*(10), 1740-1743.

Marczenko, K. M., Mercier, H. P., & Schrobilgen, G. J. (2018). A Stable Crown Ether Complex with a Noble-Gas Compound. *Angewandte Chemie International Edition, 57*(38), 12448-12452.

Marczenko, K. M., Mercier, H. P., Goettel, J. T., & Schrobilgen, G. J. (2025). Xenon Trioxide Coordination Complexes of Crown Ethers: $(CH_2CH_2O)_4XeO_3$ and Xe(VI) Hydrates, $[(CH_2CH_2O)_6(H_2O)XeO_3]\cdot H_2O$ and $[(CH_2CH_2O)_6(H_2O)XeO_3]_2 \cdot 2H_2O \cdot HF$. *Angewandte Chemie International Edition, 64*(20), e20245216.

Marrett, J. M., Effaty, F., Ottenwaelder, X., & Friščić, T. (2025). Mechanochemistry for Metal–Organic Frameworks and Covalent–Organic Frameworks (MOFs, COFs): Methods, Materials, and Mechanisms. *Advaced Materials*, 2418707.

Martinez, V., Stolar, T., Karadeniz, B., Brekalo, I., & Užarević, K. (2022). Advancing mechanochemical synthesis by combining milling with different energy sources. *Nature Reviews Chemistry, 7*, 51-65.

Mateti, S., Mathesh, M., Liu, Z., Tao, T., Ramireddy, T., Glushenkov, A. M., . . . Chen, Y. I. (2024). Mechanochemistry: A force in disguise and conditional effects towards chemical reactions. *Chemical Communications, 57*(9), 1080-1092.

Matsumoto, K., Hagiwara, R., Ito, Y., & Tamada, O. (2002). Synthetic, structural and thermal studies of Ag(I)–XeF_2 complex salts. *Solid State Sciences, 4*(11-12), 1465-1469.

Matsumoto, K., Haner, J., Mercier, H. P., & Schrobilgen, G. J. (2015). Syntheses and Structures of $F_6XeNCCH_3$ and $F_6Xe(NCCH_3)_2$. *Angewandte Chemie International Edition, 54*(47), 14169-14173.

Mazej, Z. (2017). *Modern Synthesis Processes and Reactivity of Fluorinated Compounds.* Amsterdam: John Fedor.

Mazej, Z., & Goreshnik, E. (2019). Crystal Structures of Photochemically Prepared $(Xe_2F_{11})_2(MF_6)$ (M = Sn, Pb) and $(XeF_5)_4(Sn_5F_{24})$ Containing Six- and Seven-

Coordinated Tin(IV). *European Journal of Inorganic Chemistry, 2019*(9), 1265-1272.

Mazej, Z., & Goreshnik, E. (2023). Crystal Structures of Xenon(VI) Salts: $XeF_5Ni(AsF_6)_3$, XeF_5AF_6 (A = Nb, Ta, Ru, Rh, Ir, Pt, Au), and $XeF_5A_2F_{11}$ (A = Nb, Ta). *Molecules, 28*(8), 3370.

Mazej, Z., & Žemva, B. (2003). Synthesis of arsenic pentafluoride by static fluorination of As_2O_3 in a closed system. *Journal of Fluorine Chemistry*, 1432-1434.

Mazej, Z., Goreshnik, E., Jagličić, Z., Filinchuk, Y., Tumanov, N., & Akselrud, L. G. (2017). Photochemical Synthesis and Characterization of Xenon(VI) Hexafluoridomangantes(IV). *European Journal of Inorganic Chemistry, 2017*(14), 2130-2137.

McKee, D. E., Zalkin, A., & Bartlett, N. (1973). Crystal Structure of $[XeF_3]^+[Sb_2F_{11}]^-$. *Inorganic Chemistry, 12*(8), 1713-1717.

Mecier, H. P., Breddemann, U., Brock, D. S., Bortolus, M. R., & Schrobilgen, G. J. (2019). Syntheses, Structures, and Bonding of $NgF_2{\cdot}CrOF_4$, $NgF_2{\cdot}2CrOF_4$ (Ng=Kr, Xe), and $(CrOF4)_\infty$. *Chemistry - A European Journal, 25*(52), 12105-12119.

Mercier, H. P., Sanders, J. C., Schrobilgen, G. J., & Tsai, S. S. (1993). The oxotrifluoroxenon(VI) cation: x-ray crystal structure of $XeOF_3^+SbF_6^-$ and a solution oxygen-17 and xenon-129 nuclear magnetic resonance study of the ^{17,18}O-enriched $XeOF_3^+$ cation. *Inorganic Chemistry, 32*(4), 386-393.

Merrill, L., & Bassett, W. A. (1974). Miniature diamond anvil pressure cell for single crystal x-ray diffraction studies. *Review of Scientific Instruments, 45*(2), 290-294.

Mezouar, M., Gabarino, G., Bauchau, S., Morgenroth, M., Martel, K., Petitdemange, S., . . . Wehinger, B. (2024). The high flux nano-X-ray diffraction, fluorescence and imaging beamline ID27 for science under extreme conditions on the ESRF Extremely Brilliant Source. *High Pressure Research, 44*, 171-198.

Miao, M. (2020). Noble gases in solid compounds show a rich display of chemistry with enough pressure. *Frontiers in Chemistry, 8*, 1-8.

Miao, M., Sun, Y., Zurek, E., & Lin, H. (2020). Chemistry under high pressure. *Nature Reviews Chemistry, 4*, 508-527.

Mihailović, D., Kušar, P., Demšar, J., & Kabanov, V. V. (2006). The determination of length scales associated with dynamic inhomogeneity in cuprate superconductors. *Journal of Superconductivity, 19*(1/2), 43-47.

Milićev, S. (1995). Frequency and intensity relations in Raman spectra of XeF^5+ and $Xe_2F_{11}^+$ in their solid fluorometalate complexes. *Vibrational Spectroscopy, 8*(2), 309-314.

Minkwitz, R., & Molsbeck, W. (1992). The reaction of $XeF^+MF_6^-$ (M = As, Sb) with sulfuranes; preparation of $CF_3(O)F_2^+SbF_6^-$ and $(CF_3)_2SOXeF^+SbF_6^-$. *Z. Anorg. Allg. Chem, 612*(6), 35-39.

Möbs, M., & Kraus, F. (2025). Tips and Procedures for Safe Handling of Anhydrous Hydrogen Fluoride and Pure Elemental Fluorine in Chemical University Laboratories. *ACS Chemical Health & Safety, 32*(5), 662-672.

Moggach, S. A., Allan, D. R., Parsons, S., & Warren, J. E. (2008). Incorporation of a new design of backing seat and anvil in a Merrill-Bassett diamond anvil cell. *Journal of Applied Crystallography, 41*, 249-251.

Moran, M. D., Brock, D. S., Mercier, H. P., & Schrobilgen, G. J. (2010). $Xe_3OF_3^+$, a Precursor to a Noble-Gas Nitrate; Syntheses and Structural Characterizations of $FXeONO_2$, $XeF_2 \cdot HNO_3$, and $XeF_2 \cdot N_2O_4$. *Journal of American Chemical Society*, 13823-13839.

Motaln, K., Gurung, K., Brazda, P., Kokalj, A., Radan, K., Dragomir, M., . . . Lozinšek, M. (2024). Reactive Noble-Gas Compounds Explored by 3D Electron Diffraction: XeF_2–MnF_4 Adducts and a Facile Sample Handling Procedure. *ACS Central Science, 10*(9), 1733-1741.

Motaln, K., Gurung, K., Dragomir, M., Kurzydłowski, D., Palatinus, L., & Lozinšek, M. (2025). Crystal Structures of $XeF_2 \cdot 2PtF_4$ and $XeF_2 \cdot 2PdF_4$ Determined by 3D Electron Diffraction and Structural Models of $XePtF_6$. *Inorganic Chemistry, 64*(29), 14968-14976.

Motaln, K., Uran, E., Giordano, N., Parsons, S., & Lozinšek, M. (2025). Hydrostatic behaviour of highly inert Fomblin and Halocarbon fluids as pressure-transmitting media in high-pressure experiments. *Journal of Applied Crystallography*, 221-226.

Nabiev, S. S. (1998). Vibrational spectra and structural features of noble gas fluorides in cryogenic and nonaqueous solutions. *Russian Chemical Bulletin*, 535-559.

Niwa, K., Matsuzaki, F., & Hasegawa, M. (2017). Synthesis, crystal structure and phase transition of a Xe-N_2 compound at high pressure: experimental indication of orbital interaction between xenon and nitrogen. *Physical Chemistry Chemical Physics, 19*(1), 59-63.

O'Bannon III, E. F., Jenei, Z., Cynn, H., Lipp, M. J., & Jeffries, J. R. (2018). Culet diameter and the achievable pressure of a diamond anvil cell: Implications for the upper pressure limit of a diamond anvil cell. *Review of Scientific Instruments, 89*(11), 111501.

Ogrin, T., Bohinc, M., & Slivnik, J. (1973). Melting-Point Determinations of Xenon Difluoride-Xenon Tetrafluoride Mixtures. *Journal of Chemical and Engineering Data, 18*(4), 401-402.

Olah, G. A., & Mo, Y. K. (1973). table Carbocations. CLIII. Fluorinated Phenylcarbenium. *The Journal of Organic Chemistry*, 2682-2685.

Olah, G. A., Prakash, G. K., Molnar, A., & Sommer, J. (2009). *Superacid Chemistry* (2nd Edition ed.). New Jersey, United States of America: John Wiley & Sons.

Osakabe, T., & Kakurai, K. (2008). Feasibility Tests on Pressure-Transmitting Media for Single-Crystal Magnetic Neutron Diffraction under High Pressure. *Japan Journal of Applied Physics*, 6544-6547.

Osorio, J. G., & Muzzio, F. J. (2015). Evaluation of resonant acoustic mixing performance. *Powder Technology, 278*, 46-56.

Palatinus, L., Brazda, P., Jelinek, M., Hrda, J., Steciuk, G., & Klementova, M. (2019). Specifics of the data processing of precession electron diffraction tomography and their implementation in the program *PETS2.0. Acta Crystallographica B: Structural Science, Crystal Engineering and Materials, 75*, 512-522.

Palatinus, L., Petříček, V., & Corrêa, C. A. (2015). Structure refinement using precession electron diffraction tomography and dynamical diffraction: theory and implementation. *Acta Crystallographica A: Foundations and Advances, 71*(2), 235-244.

Patel, C., Joyaux-Andre, E., Leitch, J. A., de Irujo-Labalde, X. M., Ibba, F., Strujis, J., . . . Gouverneur, V. (2023). Fluorochemicals from fluorspar via a phosphate-enabled mechanochemical process that bypasses HF. *Science, 381*(6655), 302-306.

Peng, F., Botana, J., Wang, Y., Ma, Y., & Miao, M. (2016). Unexpected Trend in Stability of Xe–F Compounds under Pressure Driven by Xe–Xe Covalent Bonds. *The Journal of Physical Chemistry Letters, 7*(22), 4562-4567.

Peng, F., Wang, Y., Wang, H., Zhang, Y., & Ma, Y. (2015). Stable xenon-nitride at high pressure. *Physical Review B, 92*(9), 094104.

Peters, D., & Mietchen, R. (1996). Symptoms and treatment of hydrogen fluoride injuries. *Journal of Fluorine Chemistry, 79*(2), 161-165.

Peterson, S. W., Holloway, J. H., Coyle, B. A., & Williams, J. M. (1971). Antiprismatic Coordination about Xenon: The Structure of Nitrosonium Octafluoroxenate(VI). *Science, 173*(4003), 1238-1239.

Peterson, S. W., Willett, R. D., & Huston, J. L. (1973). Symmetry and structure of XeO_2F_2 by neutron diffraction. *The Journal of Chemical Physics, 59*(1), 453-459.

Petříček, V., Palatinus, L., Plašil, J., & Dušek, M. (2023). Jana2020 – a new version of the crystallographic computing system Jana. *Zeitschrift für Kristallographie - Crystalline Materials, 238*(7-8), 271-282.

Piermarini, G. J., Block, S., & Barnett, J. D. (1973). Hydrostatic limits in liquids and solids to 100 kbar. *Journal of Applied Physics, 44*(12), 5377-5382.

Pointner, B. E., Suontamo, R. J., & Schrobilgen, G. J. (2006). Syntheses and X-ray Crystal Structures of α- and β-$[XeO_2F][SbF_6]$, $[XeO_2F][AsF_6]$, $[FO_2XeFXeO_2F][AsF_6]$, and $[XeF_5][SbF_6] \cdot XeOF_4$ and Computational Studies of the XeO_2F^+ and $FO_2XeFXeO_2F^+$ Cations and Related Species. *Inorganic Chemistry, 45*(4), 1517-1534.

Politzer, P., Murray, J. S., Clark, T., & Resnati, G. (2017). The σ-hole revisited. *Physical Chemistry Chemical Physics, 19*(48), 32166-32178.

Popov, A. I., Scharabarin, A. V., Sukhoverkhov, V. F., & Tchumaevsky, N. A. (1989). Synthesis and Properties of Pentavalent Antimony and Bismuth Fluorides. *Zeitschrift für anorganische und allgemeine Chemie, 576*, 242-254.

Preishuber-Pflügl, F., & Wilkening, M. (2016). Mechanochemically synthesized fluorides: local structures and ion transport. *Dalton Transactions, 45*(21), 8675-8687.

Radan, K. (2017). *Interactions of xenon(II) fluoride with some metal tetrafluorides.* Ljubljana: Jozef Stefan International Postgraduate School.

Radan, K., Goreshnik, E., & Žemva, B. (2014). Xenon(II) Polyfluoridotitanates(IV): Synthesis and Structural Characterization of $[Xe_2F_3]^+$ and $[XeF]^+$ Salts. *Angewandte Chemie Internantional Edition, 53*(50), 13715-13719.

Radan, K., Lozinšek, M., Goreshnik, E., & Žemva, B. (2011). Syntheses, structures and Raman spectra of $Cd(BF_4)(AF_6)$ (A = Ta, Bi) compounds. *Journal of Fluorine Chemistry, 132*(10), 767-771.

Reynes, J. F., Isoni, V., & García, F. (2023). Tinkering with Mechanochemical Tools for Scale Up. *Angewandte Chemie International Edition, 62*(44), e202300819.

Reynes, J. F., Leon, F., & Garcia, F. (2024). Mechanochemistry for Organic and Inorganic Synthesis. *ACS Organic & Inorganic, 4*(5), 432-470.

Rigaku OD. Wroclaw, Poland: Rigaku Corporations (2025).

Rightmire, N. R., & Hanusa, T. P. (2016). Advances in organometallic synthesis with mechanochemical methods. *Dalton Transactions, 45*(6), 2352-2362.

Ruprecht, B., Wilkening, M., Feldhoff, A., Steuernagel, S., & Heitjans, P. (2009). High anion conductivity in a ternary non-equilibrium phase of BaF_2 and CaF_2 with mixed cations. *Physical Chemistry Chemical Physics, 11*(17), 3071-3081.

Saal, T., Haiges, R., & Christe, K. O. (2023). Synthesis and characterization of trifluoromethylcarboxonium salts. *Dalton Transactions*, 18143-18147.

Sanders, J. C., & Schrobilgen, G. J. (1989). Krypton bis[pentafluoro-oxotellurate(VI)], $Kr(OTeF_5)_2$, the first example of a Kr–O bond. *Journal of the Chemical Society, Chemical Communications*(20), 1576-1578.

Sawyer, J. F., Schrobilgen, G. J., & Sutherland, S. J. (1982). Crystal structure, Raman, and multinuclear NMR study of fluoro[imidobis(sulfuryl fluoride)]xenon(II)

($FXeN(SO_2F)_2$), an example of xenon-nitrogen bonding. *Inorganic Chemistry, 21*(11), 4064-4072.

Scheibe, B., Haiges, R., Ivlev, S. I., Karttunen, A. J., Muller, U., Christe, K. O., & Kraus, F. (2020). Difluorochloronium(III) Fluoridometallates – from Molecular Building Blocks to (Helical) Chains. *European Journal of Inorganic Chemistry, 2020*, 4483-4496.

Scholz, G. (2021). Mechanochemistry of fluoride solids: from mechanical activation to mechanically stimulated synthesis. *ChemTexts, 7*, 16.

Schreiner, F., Malm, J. G., & Hindman, J. C. (1965). The Preparation and Nuclear Magnetic Resonance of Krypton Fluoride. *Journal of American Chemical Society, 87*(1), 25-28.

Schrobilgen, G. J. (1988). The fluoro(hydrocyano)krypton(II) cation $[HC{\equiv}N{-}Kr{-}F]^+$; the first example of a krypton–nitrogen bond. *Journal of the Chemical Society, Chemical Communications*(13), 863-865.

Schrobilgen, G. J. (1988). The Fluoro(perfluoroalkyInitrile)noble-gas(li) Cations, R_FN-NgF^+ (Ng = Kr or Xe; R_F = CF_3, C_2F_5, *n*-C_3F_7), and the Fluoro(trifluoro-s-trazine)xenon(II) Cation, s-$C_3F_3N_2N$-XeF^+; Nobel Noble Gas-Nitrogen Bonds. *Journal of the Chemical Society, Chemical Communications*(22), 1506-1508.

Schrobilgen, G. J., & Whalen, J. M. (1994). The Xenon-Oxygen-Bonded Cation $CF_3C(OXeF)NH_2^+$ and Related $CF_3C(OH)NH_2^+AsF_6^-$ and $CF_3C(OH)NH_2^+AsF_6^-XeF_2$*n*HF salts. Their Syntheses and Characterization by Multi-NMR and Raman spectroscopy. *Inorganic Chemistry*, 5207-5218.

Schwarz, U., & Syassen, K. (1992). The behaviour of solid XeF_2 under pressure. *High Pressure Research, 9*(1-6), 47-50.

Segal, E. B. (2000). First aid for a unique acid, HF: A sequel. *Chemical Health & Safety, 7*(1), 18-23.

Seidel, S., & Seppelt, K. (2000). Xenon as a Complex Ligand: The Tetra Xenono Gold(II) Cation in $AuXe_4^{2+}(Sb_2F_{11}^-)_2$. *Science, 290*(5489), 117-118.

Seidel, S., & Seppelt, K. (2001). The $XeCl^+$ Ion: $[XeCl]^+[Sb_2F_{11}]^-$. *Angewandte Chemie International Edition, 40*(22), 4225-4227.

Seidel, S., Seppelt, K., van Wulle, C., & Sun, X. Y. (2007). The Blue Xe_4^+ Cation: Experimental Detection and Theoretical Characterization. *Angewandte Chemie International Edition, 46*(35), 6717-6720.

Selig, H., & Peacock, R. D. (1964). A Krypton Difluoride-Antimony Pentafluoride Complex. *Journal of the American Chemical Society, 86*(18), 3895.

Selig, H., Claassen, H. H., Chernick, C. L., Malm, J. G., & Huston, J. L. (1964). Xenon Tetroxide: Preparation and Some Properties. *Science, 143*(3612), 1322-1323.

Šepelak, V., Duvel, A., Wilkening, M., Becker, K.-D., & Heitjans, P. (2013). Mechanochemical reactions and syntheses of oxides. *Chemical Society Reviews, 42*(18), 7507-7520.

Seppelt, K. (1979). Recent developments in the chemistry of some electronegative elements. *Accounts of Chemical Research, 12*(6), 211-216.

Sheldrick, G. M. (2015). Crystal structure refinement with *SHELXL*. *Acta Crystallographica C, Structural Chemistry*, 3-8.

Sheldrick, G. M. (2015). *SHELXT* – Integrated space-group and crystalstructure determination. *Acta Crystallographica Section A: Foundations and Advances, 71*(1), 3-8.

Simpson, M. B., Poliakoff, M., Turner, J. J., Maier II, W. B., & McLaughlin, J. G. (1983). $[Cr(CO)_5Xe]$ in solution; the first spectroscopic evidence. *Journal of the Chemical Society, Chemical Communications*(22), 1355-1357.

Sladky, F. O., Bulliner, P. A., & Bartlett, N. (1969). Xenon Difluoride as a Fluoride Ion Donor. Evidence for the Salts $[Xe_2F_3]^+[MF_6]^-$, $[XeF]^+[MF_6]^-$ and $[XeF]^+[M_2F_{11}]^-$. *Journal of the Chemical Society A: Inorganic, Physical, Theoretical*(0), 2179-2188.

Slivnik, J., Brčić, B., Volavšek, B., Marsel, J., Vrščaj, V., Šmalc, A., . . . Zemljič, Z. (1962). Uber die Synthese von XeF_6. *Croatica Chemica Acta, 34*(4), 253.

Slivnik, J., Šmalc, A., Lutar, K., Žemva, B., & Frlec, B. (1975). A new method for the preparation of krypton difluoride. *Journal of Fluorine Chemistry, 5*(3), 273-274.

Slivnik, J., Šmalc, A., Žemva, B., & Mosevič, A. N. (1968). On the Synthesis of Xenon Di-, Tetra- and Hexafluoride. *Croatica Chemica Acta, 40*(1), 49-51.

Šmalc, A., Lutar, K., & Kinkead, S. A. (1992). Xenon difluoride (modfication). In R. N. Grimes, *Inorganic Syntheses* (Vol. 29, pp. 1-4). New York: John Wiley & Sons.

Smith, D. F. (1963). Xenon Trioxide. *Journal of American Chemical Society, 85*(6), 816-817.

Smith, G. L. (2010). *Noble Gas Chemistry Derived fron NSF3 and Related Sulfur-Nitrogen-Fluorine Chemistry.* Ontario: McMaster University.

Smith, G. L., & Schrobilgen, G. J. (2009). On the Reactivity of $F_3S{\equiv}NXeF+$: Syntheses and Structural Characterizations of $[F_4S{=}N{-}Xe{-}{-}{-}N{\equiv}SF_3][AsF_6]$, a Rare Example of a N−Xe−N Linkage, and $[F_3S(N{\equiv}SF_3)_2][AsF_6]$. *Inorganic Chemistry*, 7714-7728.

Smith, G. L., Mercier, H. P., & Schrobilgen, G. J. (2007). Synthesis of $[F_3S{:}NXeF][AsF_6]$ and Structural Study by Multi-NMR and Raman Spectroscopy, Electronic Structure Calculations, and X-ray Crystallography. *Inorganic Chemistry, 46*(4), 1369-1378.

Smith, G. L., Mercier, H. P., & Schrobilgen, G. J. (2008). F5SN(H)Xe+; a Rare Example of Xenon Bonded to sp3-Hybridized Nitrogen; Synthesis and Structural Characterization of $[F_5SN(H)Xe][AsF_6]$. *Inorganic Chemistry, 47*(10), 4173-4184.

Smith, G. L., Mercier, H. P., & Schrobilgen, G. J. (2009). Solid-State and Solution Rearrangements of $F_3S{\equiv}NXeF^+$ Leading to the $F_4S{=}NXe^+$ Cation; Syntheses, HF Solvolyses, and Structural Characterizations of $[F_4S{=}NXe][AsF_6]$ and $[F_4S{=}NH_2][AsF_6]$. *Journal of American Chemical Society, 131*(21), 7272-7286.

Somayazulu, M., Dera, P., Goncharov, A. F., Gramsch, S. A., Liermann, P., Yang, W., . . . Mao, H.-K. H. (2010). Pressure-induced bonding and compounds formation in xenon-hydrogen solids. *Nature Chemistry, 2*(1), 50-53.

Somayuzulu, M., Dera, P., Smith, J., & Hemley, R. J. (2015). Structure and stability of solid Xe(H2)n. *Journal of Chemical Physics, 142*(10), 104503.

Somayuzulu, M., Gramsch, S., Mao, H.-K., & Hemley, R. (2007). High pressure-high temperature reactions in xenon-chlorine system. *MRS Online Proceedings Library, 987*(1), 9870407.

Spitzin, V. I., Kiselev, Y. M., Fadeeva, N. E., Popov, A. I., & Tchumaevsky, N. A. (1988). Interaction between Xenon Di- and Tetrafluoride with Alkali Metal Fluorides. *Zeitschrift für anorganische und allgemeine Chemie, 559*(1), 171-181.

Stavrou, E., Yao, Y., Goncharov, A. F., Lobanov, S. S., Zaug, J. M., Liu, H., . . . Prakapenka, V. B. (2018). Synthesis of xenon and iron-nickel intermetallic compounds at Earth's core thermodynamic conditions. *Physical Review Letters, 120*, 096001.

Stein, L. (1983). The Chemistry of Radon. *Radiochimica Acta, 42*(1-3), 163-171.

Stuart, D., Wetmore, S. D., & Gerken, M. (2019). Syntheses, characterization, and computational study of AsF_5 adducts with ketones. *Journal of Fluorine Chemistry*, 9-16.

Syassen, K. (2008). Ruby under pressure. *High Pressure Research, 28*(2), 75-126.

Takacs, L. (2013). The historical development of mechanochemistry. *Chemical Society Reviews, 42*(18), 7649-7659.

Takahashi, R., Hu, A., Gao, P., Gao, Y., Pang, Y., Seo, T., . . . Ito, H. (2021). Mechanochemical synthesis of magnesium-based carbon nucleophiles in air and their use in organic synthesis. *Nature Communications*, 6691.

Takemura, K. (2021). Hydrostaticity in high pressure experiments: some generalobservations and guidelines for high pressure experimenters. *High Pressure Research*, 155-174.

Tan, D., & García, F. (2019). Main group mechanochemistry: from curiosity to established protocols. *Chemical Society Reviews, 48*(8), 2274-2292.

Tavčar, G., & Goreshnik, E. (2016). One dimensional group 12 metal undecafluoridoditantalates. *Journal of Fluorine Chemistry, 189*, 33-38.

Tavčar, G., & Tramšek, M. (2015). XeF_2 as a ligand to a metal center, an interesting field of noble gas chemistry. *Journal of Fluorine Chemistry*, 14-21.

Tavčar, G., & Žemva, B. (2009). XeF_4 as a Ligand for a Metal Ion. *Angewandte Chemie International Edition*, 1432-1434.

Tavčar, G., Goreshnik, E., & Mazej, Z. (2006). Homoleptic $[M(XeF_2)_6]^{2+}$ cations of copper(II) and zinc(II)—Syntheses and crystal structures of $[M(XeF_2)_6](SbF_6)_2$ (M = Cu, Zn). *Journal of Fluorine Chemistry, 127*(10), 1368-1373.

Tius, M. A. (1995). Xenon difluoride in synthesis. *Tetrahedron, 51*(24), 6605-6634.

Toby, B. H., & Von Dreele, R. B. (2013). GSAS-II: the genesis of a modern open-source all purpose crystallography software package. *Journal of Applied Crystallography*, 544-549.

Toraman, A. N., Fischer, L., Pérez-Bitrián, A., Wiesner, A., Hoffmann, K. F., & Riedel, S. (2024). $[Xe(OTeF_5)(pyF)]^+$: a strong oxidizing xenonium(ii) teflate cation with N-donor bases. *Chemical Communications, 60*(13), 1711-1714.

Tramšek, M., & Žemva, B. (2006). Synthesis, Properties and Chemistry of Xenon(II) Fluoride. *Acta Chimica Slovenica*, 105-116.

Tramšek, M., Benkič, P., & Žemva, B. (2004). The First Compound Containing a Metal Center in a Homoleptic Environment of XeF_2 Molecules. *Angewandte Chemie International Edition, 43*(26), 3456-3458.

Usvyat, D., Yin, C., Wälz, G., Mühle, C., Schütz, M., & Jansen, M. (2012). Phase transition in GeF_2 driven by change of type of intermolecular interaction. *Physical Review B, 86*(5), 054102.

Vasdev, N., Moran, M. D., Tuononen, H. M., Chirakal, R., Suontamo, R. J., Bain, A. D., & Schrobilgen, G. J. (2010). NMR Spectroscopic Evidence for the Intermediacy of XeF_3^- in XeF_2/F^- Exchange, Attempted Syntheses and Thermochemistry of XeF_3^- Salts, and Theoretical Studies of the XeF_3^- Anion. *Inorganic Chemistry, 49*(19), 8997-9004.

Veith, M., & Bärnighausen, H. (1974). Die Kristall- und Molekülstruktur von Bis(trimethylsilyl)diimin. *Acta Crystallogtaphic V: Structural Science, Crystal Engineering and Materials, B30*, 1806-1813.

Virant, M., & Lozinšek, M. (2025). CrimsonCalc: a software tool for pressure determination based on ruby fluorescence spectra. *Journal of Applied Crystallography, 58*(5), 1827-1833.

Wang, Y., Bykov, M., Chepkasov, I., Samtsevich, A., Bykova, E., Zhang, X., . . . Goncharov, A. F. (2022). Stabilization of hexazine rings in potassium polynitride at high pressure. *Nature Chemistry, 14*, 794-800.

Wassermann, T. B., & Kraus, F. (2024). Rerefinement of the crystal structure of BiF_5. *Acta Crystallographica E: Crystallographic Communications, 80*(8), 826-828.

Wechsberg, M., Bulliner, P. A., Sladky, F. O., Mews, R., & Bartlett, N. (1972). Fluorosulfates and perchlorates of xenon(II) and the salt $[(FXeO)_2S(O)F]^+[AsF_6]^-$. *Inorganic Chemistry, 11*(12), 3063-3070.

Weck, G., Dewaele, A., & Loubeyre, P. (2010). Oxygen/noble gas binary phase diagrams at 296 K and high pressures. *Physical Review B, 82*(1), 014112.

Weiller, B. H. (1992). Metal carbonyl complexes with xenon and krypton: IR spectra, carbon monoxide substitution kinetics, and bond energies. *Journal of American Chemical Society, 114*(27), 10910-10915.

Wells, J. R., & Weitz, E. (1992). Rare gas-metal carbonyl complexes: bonding of rare gas atoms to the Group VIB pentacarbonyls. *Journal of American Chemical Society, 114*(8), 2783-2787.

Willet, R. D., Peterson, S. W., & Coyle, B. A. (1977). Structural evidence for xenon-chlorine bonding: neutron and x-ray diffraction determinations of the structure of cesium and rubidium trioxodichloroxenate(VI) chloride, $Cs_9(XeO_3Cl_2)_4Cl$ and $Rb_9(XeO_3Cl_2)_4Cl$. *Journal of the American Chemical Society, 99*(25), 8202-8207.

Wu, G., Huang, X., Huang, Y., Pan, L., Li, F., Li, X., . . . Cui, T. (2017). Confirmation of the structural phase transitions of XeF_2 under high pressures. *The Journal of Physical Chemistry C, 121*(11), 6264-6271.

Yang, L., Chen, Z., Goult, C. A., Schlatzer, T., Paton, R. S., & Gouverneur, V. (2025). Phosphate-enabled mechanochemical PFAS destruction for fluoride reuse. *Nature, 640*, 100-106.

Zaelski-Ejgierd, P., & Lata, P. M. (2016). Krypton oxides under pressure. *Scientific Reports, 6*(1), 18938.

Zalkin, A., Forrester, J. D., Templeton, D. H., Williamson, S. M., & Koch, C. W. (1964). Potassium Perxenate Nonahydrate. *Journal of American Chemical Society, 86*(17), 3569-3571.

Zarifi, N., Liu, H., Tse, J. S., & Zurek, E. (2018). Crystal structures and electronic properties of Xe—Cl compounds at high pressure. *Journal of Physical Chemistry C, 122*(5), 2941-2950.

Žemva, B. (1988). Binary Fluorides of Noble-Gases and Their Compounds. *Croatica Chemica Acta, 61*(1), 163-187.

Žemva, B., Jesih, A., Templeton, D. H., Zalkin, A., Cheetham, A. K., & Bartlett, N. (1987). Phases in the system XeF_2/XeF_5AsF_6 and structural and vibrational evidence for the following ionization pathway: XeF_2 --> $XeF^+ + F^-$. *Journal of American Chemical Society, 109*(24), 7420-7427.

Zhang, W., Oganov, A. R., Goncharov, A. F., Zhu, Q., Boulfelfel, S. E., Lyakhov, A. O., . . . Konôpková, Z. (2013). Unexpected Stable Stoichiometries of Sodium Chlorides. *Science, 342*(6165), 1502-1505.

Zhu, Q., Jung, D. Y., Oganov, A. R., Glass, C. W., Gatti, C., & Lyakhov, A. O. (2013). Stability of xenon oxides at high pressures. *Nature Chemistry, 5*(1), 61-65.

Bibliography

Publications Related to the Thesis

Journal Articles

Motaln, K., Uran, E., Giordano, N., Parsons, S., & Lozinšek, M. (2025). Hydrostatic behaviour of highly inert Fomblin and Halocarbon fluids as pressure-transmitting media in high-pressure experiments. *J. Appl. Cryst., 19*(1), 221–226.

Uran, E., & Lozinšek, M. (2025). Protonated decafluorobenzophenone and the decafluorobenzophenone–arsenic pentafluoride adduct. *Acta Cryst., C81*(10), 577–583.

Uran, E., & Lozinšek, M. (2025). Hydrogen-bonded salt cocrystals of xenon difluoride and protonated perfluoroamides. *CrystEngComm, 27*(48) 7776–7784.

Conference Contributions*

E. Uran, K. Motaln, M. Lozinšek. (2022). Inert pressure transmitting media for high-pressure structural investigation of noble-gas compounds. *ISCoC, International School of Crystallography: 56th course: Crystallography under extreme conditions: the future is bright and very compressed*, Erice, Italy.

E. Uran, M. Dragomir, K. Radan, M. Lozinšek. (2022). Compounds from the XeF_2–TaF_5 system: novel synthesis and crystal structures. *4th International Congress of Chemists and Chemical Engineers of Bosnia and Herzegovina*, Sarajevo, Bosnia and Herzegovina.

E. Uran, M. Dragomir, K. Radan, M. Lozinšek. (2022). Crystal structures of compounds formed in the XeF_2–TaF_5 system. *7th European Crystallographic School, ECS7*, Lisbon, Portugal.

E. Uran, M. Dragomir, K. Radan, M. Lozinšek. (2022). Mechanochemical synthesis of XeF_2–TaF_5 noble-gas compounds. *ESFC 2022, 20th European Symposium on Fluorine Chemistry*. Berlin, Germany.

E. Uran, M. Dragomir, K. Radan, M. Lozinšek. (2022). Exploring the XeF_2–TaF_5 with mechanochemistry. *28th Croatian-Slovenian Crystallographic Meeting, CSCM28*, Poreč, Croatia.

E. Uran, M. Dragomir, K. Radan, M. Lozinšek. (2023). Mechanochemistry of noble-gas compounds. *15th Jožef Stefan International Postgraduate School Students' Conference*, Kamnik, Slovenia.

E. Uran, M. Dragomir, K. Radan, M. Lozinšek. (2023). Mechanochemical adventures in noble-gas chemistry. *Solid-State Science & Research 2023*, Zagreb, Croatia.

E. Uran, K. Motaln, M. Lozinšek. (2023). Hydrostatic behaviour of selected chemically inert pressure-transmitting media. *28th AIRAPT and 60th EHPRG International Conference 2023*, Edinburgh, United Kingdom.

E. Uran, K. Radan, M. Virant, M. Dragomir, M. Lozinšek. (2024). Cyanogen adduct of [XeF][AsF_6] and products thereof. *16th Jožef Stefan International Postgraduate School Students' Conference*, Piran, Slovenia.

E. Uran, K. Radan, M. Virant, M. Dragomir, M. Lozinšek. (2024). Reactivity of cyanogen towards $[XeF]^+$ cation. *30th Croatian-Slovenian Crystallographic Meeting*, Veli Lošinj, Croatia.

E. Uran, K. Radan, M. Virant, M. Dragomir, M. Lozinšek. (2024). Novel Xe^{II}–N-bonded compounds derived from cyanogen. *Fluorine Frontiers: A Symposium Honoring the Legacy of Boris Žemva*, Ljubljana, Slovenia.

E. Uran, K. Radan, M. Virant, M. Dragomir, M. Lozinšek. (2024). Chemistry of the cyanogen–[XeF][AsF_6]. *30th Annual Meeting of the Slovenian Chemical Society*, Portorož, Slovenia.

E. Uran, K. Radan, M. Virant, M. Dragomir, M. Lozinšek. (2025). Recent progress in xenon–nitrogen bonded compounds. *Solid-State Science & Research 2025*, Zagreb, Croatia.

E. Uran, M. Lozinšek. (2025). Xenon difluoride as a hydrogen-bond acceptor. *31st Annual Meeting of the Slovenian Chemical Society*, Portorož, Slovenia.

**Only contributions directly connected with PhD work and with Erik Uran as presenting author are listed.*

Other Publications

Uran, E., Fotović, L., Bedeković, N., Stilinović, V. & Cinčić, D. (2021). The amine group as halogen bond acceptor in cocrystals of aromatic diamines and perfluorinated iodobenzenes. *Crystals, 11*, 529.

Gurung, K., Uran, E., Motaln, K., Brázda, P., Radan, K., Lozinšek, M. & Palatinus, L. (2025). A simple cryo-transfer method for 3D electron diffraction measurements of highly sensitive samples. *J. Appl. Cryst., 58*(3), 1079–1084.

Uran, E., Cotman, A. E., & Lozinšek, M. (2025). Methyl 2-amino-4-(morpholin-4-yl)benzo[*d*]thiazole-6-carboxylate tetartohydrate. *IUCr Data, 10*, x241249.

Jakupec, N., Uran, E., Jabłońska, M., Užarević, K., Palčić, A. (2026). Thermo-mechanochemical interzeolite conversion in water-deficient systems. *Microporous Mesoporous Mater., 403*, 113981.

Biography

Erik Uran was born on February 27th, 1998 in Rijeka, Croatia. He finished elementary and high school in Buzet, and in 2016 he enrolled to Faculty of Science in Zagreb and graduated in 2021 with a master thesis "Aromatic diamines as halogen bond acceptors" (Aromatski diamini kao akceptori halogenske veze) under supervision of Prof. Vladimir Stilinović. During his undergraduate and graduate studies, he was a member of Crystal Materials Group led by Prof. Dominik Cinčić, where he was able to get insight into the mechanochemical synthesis, crystal growth and crystal structure analysis, with emphasis on the crystal engineering with hydrogen and halogen bonds.

In 2021, he joined the ECCL team as a PhD student under supervision of Asst. Prof. Matic Lozinšek at Jožef Stefan Institute. During his PhD, he explored mechanochemical and low-temperature synthesis of noble-gas compounds, as well as high-pressure (structural) chemistry of inorganic compounds.

Erik Uran was a co-leader alongside Dr. Nikola Jakupec on the HAZU project under the name "Nove metode sinteze cijanidnih kompleksa prijelaznih metala" (New methods of synthesis of cyano complexes of transition metals). He also participated in 1 month Erasmus+ research visit in the laboratory of Prof. Sebastian Riedel at Freie Universität (Berlin, Germany) in 2024 and was visiting and performing high-pressure work in the laboratory of Prof. Dominik Kurzydłowski in Warsaw (Poland) for two weeks.

Erik Uran performed experiments at DESY and ESRF synchrotrons and got insight into *in situ* PXRD measurements for mechanochemistry (principal investigator: Dr. Nikola Jakupec, 2022) and in the X-ray diffraction and laser heating at high pressure (principal investigators: Asst. Prof. Matic Lozinšek and Dr. Miha Virant, 2025).

During his studies, he also actively participated in the popularization of science.